



University  
of Glasgow

Murad, Masoud Kheder (2011) Integrated high brightness array semiconductor lasers incorporating multimode interference couplers

<http://theses.gla.ac.uk/4591>

Copyright and moral rights for this thesis are retained by the author

A copy can be downloaded for personal non-commercial research or study, without prior permission or charge

This thesis cannot be reproduced or quoted extensively from without first obtaining permission in writing from the Author

The content must not be changed in any way or sold commercially in any format or medium without the formal permission of the Author

When referring to this work, full bibliographic details including the author, title, awarding institution and date of the thesis must be given



University  
of Glasgow | School of  
Engineering

# **Integrated High Brightness Array Semiconductor Lasers Incorporating Multimode Interference Couplers**

**Masoud Kheder Murad**

**September 2011**

A thesis submitted in partial fulfilment for the degree of  
Doctor of Philosophy (Ph.D)

in the

College of Science & Engineering

School of Engineering

© Masoud Kheder Murad 2011

# Declaration of Authorship

I, Masoud kheder Murad, declare that this thesis titled, “Integrated High Brightness Array Semiconductor Lasers Incorporating Multimode Interference Couplers” and the work presented in it are my own. I confirm that:

- This work was done wholly or mainly while in candidature for a research degree at this University.
- Where any part of this thesis has previously been submitted for a degree or any other qualification at this University or any other institution, this has been clearly stated.
- Where I have consulted the published work of others, this is always clearly attributed.
- Where I have quoted from the work of others, the source is always given. With the exception of such quotations, this thesis is entirely my own work.
- I have acknowledged all main sources of help.
- Where the thesis is based on work done by myself jointly with others, I have made clear exactly what was done by others and what I have contributed myself.

Signed: Masoud Kheder Murad

Date: 6/ September / 2011

# Abstract

The research described work in this thesis is concerned with the development and realisation of high brightness array laser diodes operating in single spatial mode. The fabrication of the high brightness laser devices was carried out on 830 nm GaAs/AlGaAs material system. Broad area lasers were fabricated to evaluate the material quality. The material design was based on the high d/T concept, by which the optical power is maximised prior to thermal roll-over or the catastrophic optical mirror damage (COMD). A quantum well intermixing (QWI) process was developed for integrating the non absorbing mirrors (NAMs), the gain section, the MMI coupler and the single spatial mode output waveguide. The quantum well intermixing (QWI) was used to fabricate non-absorbing mirrors (NAMs) with a blue shift of 58 nm. The annealing for the optimum process was 810° C for 90 seconds. The QWI was evaluated using the photoluminescence method, band gap shift of 58 nm was realised. The fabricated NAMs ranged from 30 to 100 µm in length. The gain section length was set at 975 µm. In the passive sections, the MMI and output waveguide are 1 mm long. The total device length was around 2 mm. No COMD was observed in the fabricated devices meaning that the quantum well intermixing has worked well. The propagation loss measurement for 830 nm passive waveguide, intermixed with a QWI blue shifted 58 nm and 9.8 mm long was 4.48 dB/cm. This is comparable to the loss that was measured from broad area laser material, which had a loss of 6.9 dB/cm. Fimmwave and beam propagation method (BPM) were used for the modelling. The results of the modelling for the single mode ridge waveguide were that, a ridge depth of 1.84 µm supported a single mode. The selected ridge width was 2.5 µm. Modelling of a 1x4 MMI array laser and a 1x2 MMI array was undertaken using the beam propagation method (BPM). The optimum lateral spacing of the gain waveguides was found to be in a range of 2.5-3.5 µm for high power operation. In the 1x4 MMI array laser, the phase was modelled. The inner gain sections have a phase difference of  $\pi/2$  with respect to the outer gain sections, while the 1x2 MMI array laser has zero phase shift between the two gain sections. 1x4 and 1x2 MMI array lasers were fabricated. In the case of 1x4 MMI array laser, different MMI coupler lengths were fabricated. The MMI lengths were between 617 µm and 709 µm. The devices were tested electrically using 10 µs pulses and a 1 KHz repetition rate. They were tested to a

current level of  $22xI_{th}$ . The power achieved was  $> 440$  mW in pulsed mode from the single output facet. This power was equivalent to an optical intensity of  $17.6$  MW/cm<sup>2</sup>. The threshold current measured for the device was  $145$  mA. The external quantum efficiency ( $\eta_{ext}$ ) was  $32.1$  %. The MMI array laser device design with an MMI width of  $24$   $\mu$ m, length of  $617$   $\mu$ m and gain section spacing of  $3.5$   $\mu$ m had a strong phase locking up to an applied current of  $5.2xI_{th}$ . The far-field pattern width of the central lobe of the phase locked  $1x4$  MMI array laser was  $2.1$  ° measured from the array facets side. This value is comparable to the diffraction limited value of  $1.96$  ° calculated simply from  $(\lambda/N.p)$ . The quality factor ( $M^2_{emitter}$ ) for the  $2.5$   $\mu$ m wide single ridge emitter was estimated to be close to  $1$ . The beam quality factor of the  $1x4$  MMI array bar ( $M^2_{bar}$ ) was estimated to be  $1.07$ . The visibility ( $V$ ) of the pattern was very close to  $1$ . The phase locked power ( $P$ ) was  $152.0$  mW per facet for an operating current of  $5.2xI_{th}$  ( $I_{th}=145$  mA). The corresponding brightness was  $19.6$  MW/cm<sup>2</sup>.sr. The operating wavelength for a  $1x4$  MMI laser diode array was a  $0.822$   $\mu$ m. The single emission wavelength was measured from the four array side with a narrow spectral width ( $\Delta\lambda$ ) of  $0.22$  nm at the FWHM for an operating current of  $5.2xI_{th}$ . The narrow spectral width of  $0.22$  nm for the array was a much smaller than that for a ridge waveguide laser. The ridge waveguide laser had a spectral width of a  $0.65$  nm at FWHM. This spectral width was measured for a current of  $200$  mA in pulsed mode with a  $5$   $\mu$ s pulse width. The lasing spectra of the array showed four individual peaks, when the current was increased to  $6.2xI_{th}$ . At this point, the array is no longer phase locked. The wavelength peaks were as follows:  $\lambda_1=821.35$  nm,  $\lambda_2=821.59$  nm,  $\lambda_3=821.83$  nm and  $\lambda_4=822.08$  nm, respectively. The spectral width ( $\Delta\lambda$ ) was around  $0.22$  nm at FWHM for the each of the individual peaks. The  $1x2$  MMI array devices were pulsed to a current level of  $30xI_{th}$ . The output power was around  $332$  mW from the single output facet. The threshold current was  $85$  mA. The largest optical output power was realised for the device with an MMI length of  $480$   $\mu$ m. The external quantum efficiency was around  $33\%$ . The phase relationship between the gain sections for the  $1x2$  MMI array laser is an identical one (i.e.  $\Phi_1=\Phi_2$ ). The phase locking was achieved in the  $1x2$  MMI array laser. However, the phase locking was only evident up to  $3xI_{th}$  ( $I_{th}=85$  mA) CW. The width of the central lobe of the far-field pattern was  $4.49$  ° (equivalent to  $1.33x$  the diffraction limit). There was also a reasonable correlation between the far-field pattern from the measurement and the far-field pattern from the simulation. The quality

factor for the emitter ( $M^2_{\text{emitter}}$ ) was 1, while the beam quality factor ( $M^2_{\text{bar}}$ ) of the 1x2 MMI array (bar) was estimated to be 1.33. The visibility (V) of the pattern was estimated to be around 0.5. The lasing spectra showed a single wavelength emission with a peak of 823.55 nm and a very narrow spectral width of 0.3 nm at the FWHM. The optical power at an injection current of  $3.2I_{\text{th}}$  was a mere 60mW CW per facet, which corresponded to a brightness of 5.02 ( $\text{MW}/\text{cm}^2 \cdot \text{sr}$ ). The results for a 1x2 MMI laser array indicated that the length of the MMI section promoted the phase locking. An accurately designed MMI length resulted in a narrow spectral width of 0.3 nm at FWHM for an MMI length of 480  $\mu\text{m}$ . The spectral width increased with a reduction of the MMI length. The spectral width was 0.86 nm at FWHM for an MMI length of 465  $\mu\text{m}$ , whereas it increased to 3.1 nm at the FWHM for an MMI length of 444  $\mu\text{m}$ . Therefore, the phase locking and the bandwidth of the 1xN MMI array laser is a self imaging and MMI cavity length dependent.

# Acknowledgements

Foremost, I would like to thank my supervisor Prof. Catrina Bryce. She has provided me with invaluable encouragement and many useful suggestions for my research. Special thanks to my supervisor for her patience and continuous advice. My thanks goes to Prof. John Marsh for the useful discussions and support.

Next, I would like to thank my wife Nuha Ibrahim for all the support she gave me all those years. I thank as well all my children Mark, Marleen and Cezar for their patience and understanding. I thank as well all my family members my father Kheder Murad and my brother Saad for their continuous support and encouragement.

During these years, I was fortunate to get to know so many nice people, knowledgeable and helpful people: Barry was always ready to listen to any question that I had which I got the answer for. My thanks go to Dr. Marc Sorel for all his help and guidance. Also I thank my colleague Steve McMaster for the work collaboration with whom I shared ideas and overcame difficulties especially on the QWI work. Special thanks to the colleagues in Intense especially Dr. Valentin Loyo, Dr. Bocang Qui and Dr. Stewart MacDougall for their collaboration and practical help with some of the testing by getting access to Intense Ltd. test equipment.

I would like to thank the technical staff and colleagues at James Watt Nanofabrication Centre (JWNC) for their continuous help with dry etching namely Mark Dragsnes, Ronnie Roger and Douglas Lang in the dry etch department. My thanks go to Thomas Reilly for the help with sputter deposition processes.

My thanks go to all the technical staff in JWNC: David Gourlay, Robert H Harkins, Lesley Donaldson, Helen McLelland, Linda Pollock, Donald Nicolson and Eve Aitkenhead.

I would like also to thank all the colleagues in the optoelectronics group specially Gabor, Michael, Giuseppe, Piotr, Chidi, Yasir and Osman. Finally, I would like to acknowledge EPSRC for financial support.

# Publications

## Conference

- M. K. Murad, V. Loyo-Maldonado and A.C. Bryce “ High brightness array laser diode”, IEEE Laser and Electro-Optics Society (LOES) Conference, 177-178, Antalya, Turkey October 2009.
- A.C. Bryce, M. K. Murad, V. Loyo-Maldonado “Multimode interference coupled array laser”, High Power Diode Lasers and Systems Conference, Coventry, UK. 2009.

## Other Publications

- S. P. Najda, G. Bacchin, S. McKechnie, M. K. Murad, E. Goutain, X. Liu, C. J. Hamilton, and J. H. Marsh, “Optical system integration and reliability of very large arrays of individually addressable high-power single mode lasers” Proc. Of SPIE, Vol. 6133, Novel In-Plane Semiconductor Lasers V, 61330C, 2006.
- M. K. Murad and A.C. Bryce “Quantum well intermixing for high brightness MMI array laser diode”, Postgraduate Conference, Glasgow University, 2007.

# Table of Contents

<b>Declaration of Authorship</b> .....	<b>i</b>
<b>Abstract</b> .....	<b>ii</b>
<b>Acknowledgements</b> .....	<b>v</b>
<b>Publications</b> .....	<b>vi</b>
<b>Table of Contents</b> .....	<b>vii</b>
<b>List of figures</b> .....	<b>xiii</b>
<b>Abbreviations</b> .....	<b>xxvii</b>
<b>Dedication</b> .....	<b>xxix</b>
<b>Chapter 1</b> .....	<b>1</b>
1.1 Introduction.....	1
1.2 The aims of the presented work .....	2
1.3 High brightness laser diode limitations.....	3
1.4 High power laser diode figures of merits.....	4
1.4.1 The beam quality factor $M^2$ and the beam parameter product BPP .....	4
1.4.2 Brightness.....	8
1.5 Applications of high brightness semiconductor laser diode .....	9
1.6 Thesis Outline .....	10
<b>Chapter 2 Background and Review of High Brightness Semiconductor Laser</b>	
<b>Diodes</b> .....	<b>12</b>
2.1 Introduction .....	12
2.2 Brief history .....	13
2.3 Factors restricting brightness and output power of diode lasers.....	16
2.3.1 Catastrophic Optical Mirror Damage.....	17
2.3.2 Spatial Mode Instability .....	18
2.3.3 Thermal stability .....	18

2.3.3.1 Effect of the leakage .....	19
2.3.3.2 Laser mounting and packaging .....	20
2.3.3.3 Characteristic temperature ( $T_0$ ).....	22
2.3.4 Degradation of the Laser Diode with Aging .....	22
2.4 High brightness semiconductor lasers array .....	23
2.4.1 Arrays Supermode theory .....	23
2.4.1.1 Diffraction model .....	23
2.4.1.2 Coupled mode theory approach .....	24
2.4.1.3 Importance of coherent laser diode arrays .....	26
2.4.1.4 Characterization criteria for coherence in the laser array .....	29
2.4.2 Coherent high brightness laser diode arrays .....	30
2.4.3 Phase locking of array laser diode using monolithic approach.....	31
2.4.3.1 Laterally coupled Index guided array laser diode.....	31
2.4.3.2 Anti-guided array laser diode concept .....	34
2.4.3.3 Y-coupled array laser diode .....	35
2.4.3.4 Multimode interference coupler array laser diode .....	37
2.4.3.5 Array laser diode incorporating diffractive section .....	38
2.5 Master Oscillator power amplifier .....	39
2.6 ALFA DFB Semiconductor laser.....	41
2.7 Epitaxial structures review for high brightness lasers .....	42
2.8 Table summary of the reported results for high brightness single emitter laser diode and phase locked semiconductor laser arrays .....	46
<b>Chapter 3 High brightness GaAs/AlGaAs material design and characterisation ....</b>	<b>50</b>
3.1 Introduction .....	50
3.2 Bonding and crystal structure of gallium arsenide and related materials .....	52
3.3 Material parameters for GaAs/AlGaAs semiconductors .....	53
3.3.1 Bandgap energy for GaAs/AlGaAs material.....	53
3.3.2 Effective Mass in ternary and quaternary Alloys .....	53

3.3.3 Refractive index of GaAs/AlGaAs .....	54
3.4 GaAs/AlGaAs quantum well material system .....	54
3.4.1 Application to compute the electronic levels in the double quantum well structure	56
3.5 GRINSCH quantum well structures for high brightness lasers .....	58
3.5.1 GRINSCH structure concept.....	58
3.5.2 High power GRINSCH structures with high COMD level and low beam divergence .....	59
3.5.3 GaAs/AlGaAs quantum well optical properties.....	62
3.5.3.1 Free carrier absorption, bandgap shrinkage and band filling.....	62
3.5.3.2 Refractive index change in high brightness quantum well laser diode structures ..	65
3.6 The chosen GaAs/AlGaAs quantum well material structure .....	66
3.6.1 Core waveguide layers heterostructure (SCH) layers .....	67
3.6.2 Lower cladding (Trap region) .....	68
3.7 Broad area laser characterisation .....	71
3.7.1 Theory.....	72
3.7.2 Experimental results for broad area lasers .....	74
3.7.2.1 Standard laser structure results .....	74
3.7.2.2 Laser structure results with far-field reduction layer .....	76
3.8 Ohmic contacts.....	80
3.8.1 Electrical characterisation .....	82
3.8.2 Measurement and results .....	83
<b>Chapter 4 Device Fabrication .....</b>	<b>87</b>
4.1 Introduction.....	87
4.2 E-Beam lithography .....	88
4.3 PMMA Resist .....	90
4.4 Markers .....	92
4.5 Reactive ion etching.....	96

4.5.1 Etching process development .....	97
4.5.1.1 Micro-masking problem .....	97
4.5.1.2 Etching process development on RIE plasma lab system etcher .....	100
4.5.1.3 Developed process parameters using RIE plasma lab system 100 etcher .....	104
4.6 Quantum well intermixing .....	106
4.6.1 Introduction.....	106
4.6.2 Effect of point defects in the GaAs/AlGaAs disordering mechanism .....	107
4.6.3 Discovery and history of quantum well intermixing .....	108
4.6.4 Quantum well intermixing techniques .....	109
4.6.4.1 Impurity induced layer disordering .....	110
4.6.4.2 Photo-absorption induced disordering (PAID) .....	110
4.6.4.3 Sputter induced disordering (SID) .....	111
4.6.5 Rapid thermal annealing processing .....	115
4.6.6 QWI assessment .....	116
4.6.7 QWI experiments .....	116
4.6.7.1 QWI experiments using single target sputtering system .....	117
4.6.7.2 QWI experiments using multi-target sputtering machine.....	120
4.6.8 Quantum well intermixing process repeatability and contamination issues .....	123
4.7 Fabry-Perot propagation loss measurement.....	126
4.8 Multimode interferometer array laser fabrication steps.....	130
4.9 Contact metallization .....	132
4.10 Summary and conclusions.....	134
<b>Chapter 5 Device modelling and design .....</b>	<b>136</b>
5.1 Introduction .....	136
5.2 Beam Propagation Method .....	137
5.3 Waveguide modelling and design .....	139
5.4 Single mode operation .....	140
5.5 Modelling of ridge waveguide laser diode .....	141

5.6 Theory of multimode interference couplers .....	142
5.6.1 MMI design rules in high power array lasers .....	150
5.6.1.1 4x1 MMI array laser design .....	151
5.7 Multimode interference Coupler modelling .....	152
5.7.1 Optical field phase simulation for Nx1 MMI array laser .....	159
5.7.2 Simulation of 3x1 MMI array laser .....	163
5.7.3 Simulation of 2x1 MMI array laser .....	164
5.7.4 Modelling of 1xN tapered MMI array laser .....	165
5.7.5 MMI Modelling parameter scan for the MMI width, length and gain section spacing for 1x4 case .....	170
5.8 Far field modelling for 1xN MMI laser .....	174
<b>Chapter 6 MMI Array Laser Device Results and Discussion.....</b>	<b>178</b>
6.1 Introduction .....	178
6.2 1x4 MMI array laser device .....	179
6.2.1 1x4 MMI array laser device fabrication summary.....	183
6.2.2 1x4 MMI array laser device testing.....	185
6.2.3 Single lateral mode operation of the 1x4 MMI array laser .....	192
6.2.4 Far-field measurement and analysis of array side facets for 1x4 MMI array lasers .....	196
6.2.5 Far-field measurement and analysis of array side facets for 1x4 MMI array lasers with non-optimised MMI lengths .....	204
6.3 Further discussion and analysis .....	208
6.4 1x2 MMI array laser device.....	212
6.4.1 Light current characteristics of 1x2 MMI array laser devices.....	214
6.4.2 Far-field analysis of array facets side for the 1x2 MMI array laser .....	219
6.4.3 MMI operation effect on the phase locking and correlation with optical spectra ..	223
<b>Chapter 7 .....</b>	<b>226</b>
7.1 Future work.....	230

<b>Bibliography .....</b>	<b>231</b>
<b>Appendix .....</b>	<b>252</b>

# List of Figures

Figure (1.1)	Schematic of the proposed multimode integrated array laser diode which is comprised of NAMs (non-absorbing mirrors), gain section, MMI and single mode output waveguide.	3
Figure (1.2)	A schematic for Gaussian beam propagation.	5
Figure (1.3)	(a) BPM simulated near field profile for a 2.5 $\mu\text{m}$ a ridge waveguide laser for a wavelength of 830 nm (b) The corresponding far-field profile.	6
Figure (1.4)	Schematic diagram of a laser array module imaging a CtP plate. (Courtesy of Marsh ref 3).	9
Figure (2.1)	The evolution of threshold current density of semiconductor laser. (Courtesy from reference 21).	14
Figure (2.2)	Confinement of electrons and photons in a double heterostructure (23).	15
Figure (2.3)	schematic shows the difference of the gain in bulk DH semiconductor material (top) and in 2D QW material. (Ref 21)	16
Figure (2.4)	(a) LI curve for ideal laser. (b) LI curve for a laser post COMD.	17
Figure (2.5)	thermal rollover of laser diode.	20
Figure (2.6)	scheme for N coupled array emitters that are integrated with NAMs and MMI cavity and output waveguide. The emitters have a pitch p, the transverse mode profile is characterised by full width at $1/e^2$ of $2w$ .	25
Figure (2.7)	BPM simulation of lateral far-field pattern for 1x6 MMI array with dimensions of: $p= 6 \mu\text{m}$ , $N= 6$ , $2w= 2.5 \mu\text{m}$ , $\lambda= 0.83 \mu\text{m}$ , MMI width = $30 \mu\text{m}$ and MMI length of $979 \mu\text{m}$ . The fill factor (f) in this example is 41.6 %.	27
Figure (2.8)	BPM simulation of a lateral far-field pattern for 1x4 MMI with dimensions of: $p= 12.46 \mu\text{m}$ (measured from the centre to centre), $N= 4$ , $2w= 2.5 \mu\text{m}$ , $\lambda=0.83 \mu\text{m}$ , MMI width = $50 \mu\text{m}$ and an MMI length of $2770 \mu\text{m}$ . The fill factor (f) in this example is 20 %.	28
Figure (2.9)	Definition of parameters characterizing the far field for a phase locked 1x2 MM laser array.	30
Figure (2.10)	Schematic representation of the index guided channel substrate planar array. (Courtesy of D. Botez 60).	32
Figure (2.11)	schematic representation of the coupled ridge waveguide laser array. (Courtesy of Y. Twu 57).	32
Figure (2.12)	schematic representation of the non-uniformly pumped ridge waveguide laser array. (Courtesy of E. Kapon 73).	33
Figure (2.13)	Schematic representation of the ridge waveguide laser arrays with loss regions at one of ends of the laser. (Courtesy of T. Tsang 74).	33
Figure (2.14)	Anti-guided array laser fabricated using quantum well intermixing (Ref. 81).	35
Figure (2.15)	a) A Schematic of a Y-coupled index guided laser array. The coupling region is highlighted and the concept explained on the right hand side of the schematic. b) Epitaxial layer structure. (Courtesy of Welch 82).	36

Figure (2.16)	Far field measurement Y-coupled index guided laser array, which was taken from the AR side. The pattern shows a central peak of $1.5^\circ$ and two satellite peaks at $10^\circ$ . (Courtesy of Welch 82).	36
Figure (2.17)	(a) Schematic diagram of a diffraction coupled array GaAs/AlGaAs array laser (Ref 85) (b) Phase locked far-field of the array laser.	39
Figure (2.18)	Schematic diagram of monolithic master oscillator power amplifier with separate contacts for both the oscillator and the amplifier (courtesy of ref. 91).	40
Figure (2.19)	Schematic of broad area $\alpha$ -DFB laser (Courtesy from 94)	42
Figure (2.20)	Broad waveguide high brightness design (Courtesy of A. Al-muhanna ref. 96)	43
Figure (2.21)	Sab coupled ridge waveguide laser structure courtesy of Huang (Ref 98).	44
Figure (2.22)	Slab coupled ridge waveguide laser structure courtesy of Wenzel (Ref 100).	44
Figure (2.23)	PBC laser design, refractive index profile (bottom) and the calculated profile of the electric field (top). (Courtesy of ref 104).	45
Figure (3.1)	Face centred cubic structure (fcc) for GaAs crystal lattice.	52
Figure (3.2)	Schematic of GaAs/AlGaAs band structure with GaAs quantum well.	55
Figure (3.3)	Calculated wavelength as a function of the quantum well width. For a well width of 4.4 nm, the wavelength is 826 nm. Emission wavelength can be determined by measuring the wavelength at onset of lasing at the threshold using spectral measurements.	58
Figure (3.4)	(a) Bandgap profile for a GRINSCH structure. (b) Band gap profile for a SCH structure.	59
Figure (3.5)	Calculated facet temperature as a function of surface recombination velocity for quantum well AlGaAs/GaAs laser diode array. (Ref 141).	60
Figure (3.6)	Inter-valence band absorption is depicted, where three transitions are observed : the light-heavy-hole band transition (A), the split-off-light-hole band transition (B) and transition (C) which is between split-off hole band and heavy hole band.	63
Figure (3.7)	Free carrier absorption cross section for 808 nm structure as a function of the fraction of AlAs in AlGaAs. (Courtesy from ref 154).	64
Figure (3.8)	Standard grown structures (Separate confinement hetrostructure)	68
Figure (3.9)	Intense designed structures (GRINSCH) with a trap (far-field reduction layer).	68
Figure (3.10)	(a) Fimmwave simulation of the vertical far-field for a GRINSCH structure with far-field reduction layer. (b) Fimmwave simulation of the vertical far-field for a conventional structure.	69
Figure (3.11)	Vertical far-field plotted vs. the FRL (trap) thickness and optical overlap factor. Reference (148).	70
Figure (3.12)	separation between GRINCH and and FRL (trap) nm. Reference (148).	70
Figure (3.13)	Horizontal and vertical far-field plots for 830 nm high Intense epitaxial higher power design with V profile. (ref. 165).	71
Figure (3.14)	Typical oxide stripe (broad area) laser (Courtesy of reference 147)	71

Figure (3.15)	The inverse of external quantum efficiency with respect to cavity length for conventional broad area oxide lasers . The test was performed using a 400 ns pulse width, a 1 KHz repetition rate and an operating temperature of 25 °C. The standard error was ( $\pm 16.5\%$ ) and ( $\pm 17.15\%$ ) for internal quantum efficiency and the material loss, respectively.	75
Figure (3.16)	Logarithmic plot of threshold current density versus the inverse of cavity length for conventional broad area oxide lasers. Error bars are shown with a percentage error of 2.5 % in the data points. From the fitted logarithmic curve, the error in $J_{th(\infty)}$ is $\pm 10\%$ . The test was performed using 400 ns pulse width, 1 KHz repetition and operating temperature of 25°C.	76
Figure (3.17)	Inverse of external quantum efficiency with respect to cavity length for a broad area oxide laser made using high power laser design. The test was performed using a 400 ns pulse width, a 1 KHz repetition rate and an operating temperature of 25°C.	77
Figure (3.18)	Logarithmic plot of threshold current density versus the inverse of cavity length for broad area oxide laser made using high power laser design. The test was performed using a 400 ns pulse width, a 1 KHz repetition rate and an operating temperature of 25°C.	77
Figure (3.19)	LI curves for broad area lasers measured using pulsed measurements (400 ns pulse width and 1 KHz repetition rate). Roll over effects can be seen due to heating.	78
Figure (3.20)	LI curves for broad area lasers using pulsed measurements with a 5 $\mu$ s pulse duration at 1KHz repetition rate and an operating temperature of 25 °C. An optimised Intense Ltd laser test system was used to perform the measurements.	79
Figure (3.21)	Horizontal and vertical far-field patterns for a 1200 $\mu$ m broad area laser measured at the 200 mA CW at 25°C operating temperature.	79
Figure (3.22)	Emission spectra measured for a 1200 $\mu$ m broad area laser for an injection current of 200 mA CW and an operating temperature of 25° C. The central peak wavelength is 823.9 nm.	80
Figure (3.23)	band energy diagram for n-GaAs.	81
Figure (3.24)	Energy band diagram for a metal semiconductor interface where the semiconductor is highly doped.	81
Figure (3.25)	Schematic for four point probe measurement for metal pads with different spacing. Gaps (L) between metal pads were taken to be (40, 60, 80 and 100 $\mu$ m). Width (W) and length of the TLM pads were 776 $\mu$ m x 776 $\mu$ m.	82
Figure (3.26)	TLM were fabricated on each chip for contact resistance measurement. TLM 776 $\mu$ m x 776 $\mu$ m are shown in the optical microscope image. These were cleaved and tested prior to contact annealing.	82
Figure (3.27)	Resistance with respect to the TLM gap widths for different annealing temperature.	84
Figure (3.28)	(a) Resistance with respect to the TLM gap width for optimum annealing temperature of 380 C with linear fit. (b) Resistance with respect to the TLM gap width for an annealing temperature of 360 C	85

	with linear fit. (c) Resistance with respect to the TLM gap width for an annealing temperature of 390 C with linear fit.	
Figure (3.29)	Specific contact resistance ( $r_c$ ) with respect to annealing temperature. Inspection of the graph (3.28a) shows that the lowest specific contact resistance for the device is achieved at an annealing temperature of 380 °C.	86
Figure (4.1)	Monte Carlo simulation of 20 KV electrons striking a PMMA layer on silicon. (Courtesy of Macintyre 2006).	89
Figure (4.2)	Figure (a) shows a pattern with proximity correction. The areas exposed are white coloured. The Ridge type structure is exposed equally, which is visible by the straight lines. (b) The figure (b) shows an exposed pattern without a proximity correction, the areas exposed are not straight lines, so the designed shapes are different because of this effect. Figure (a) shows a properly exposed structure using the e-beam process with the error proximity correction.	90
Figure (4.3)	a) The microscope image shows a dose of 350 $\mu\text{C}/\text{cm}^2$ . The correct dose is verified through the simple measurement tool of the designed dimension. b) The optical microscope image shows a dose of 425 $\mu\text{C}/\text{cm}^2$ . The measurement showed that the pattern dimensions are less than the design parameters, therefore in this example dose (a) was selected when performing the exposure.	91
Figure (4.4)	(a) SEM image for etched markers two groups of nine etched markers are visible. Distance between markers is 200 $\mu\text{m}$ from centre to centre. Cross markers are also visible. (b) SEM image shows the marker with series of MMI array lasers.	93
Figure (4.5)	SEM image for etched cross, which is used for pattern alignment purposes on the wafer.	93
Figure (4.6)	Figure: (4.6) Four markers system for layer to layer alignment (registration) using e-beam lithography.	94
Figure (4.7)	Mask design using L-Edit mask design. (a) Full devices layout with markers used are shown. (b) The figure is a magnified version of (a) above which clearly shows the series of marker and crosses for good alignment. The device layout is shown as well. Red stripes are the ridge waveguides.	95
Figure (4.8)	Schematic of parallel plate reactive ion etching system	96
Figure (4.9)	Surface reaction sequence for the reactive ion etching process on top of a substrate.	97
Figure (4.10)	SEM images for GaAs/AlGaAs MMI waveguide etch using reactive ion etching with $\text{SiCl}_4$ . The wide pillars shown in the figure are the unetched areas of GaAs/AlGaAs due to formation of polymer on the surface, which acts as micro-mask.	99
Figure (4.11)	Etch for 1x4 MMI array laser, the interface between the intermixed and intermixed areas is clearly visible. Intermixed area is covered by grainy contaminants after post waveguide etch.	100
Figure (4.12)	The process used to etch (sample ID: F8) this profile was using $\text{SiCl}_4$ with gas flowrate of 10 sccm, 4 mTorr pressure and power of 120 W. Side wall angle measure to be around 87 ° with normal, other observation was the bowing (non flat surface).	102

Figure (4.13)	The process used to etch this profile was SiCl <sub>4</sub> with gas flowrate of 10 sccm, 7 mTorr pressure and power of 100 W.	102
Figure (4.14)	(a) The process used to etch this profile was: SiCl <sub>4</sub> with gas flowrate of 11 sccm, 6 mTorr pressure and power of 70 W. (b) Magnification of (a) which shows a slight slope for the etched profile.	103
Figure (4.15)	Figure 4.(a) The process used to etch this profile was using SiCl <sub>4</sub> with gas flowrate of 13 sccm, 9 mTorr pressure and power of 80 W. Side wall angle measure to be > 89 ° with the normal. This was the best results. (b) Different structure used the same recipe in (a). (c) The same recipe from (a) is used to etch 1x4 MMI array laser with remarkable results as seen in figure (c) above. Very smooth side walls and good interface seen between the MMI and ridge waveguide, which is proof of the good process recipe that has been developed.	104
Figure (4.16)	A scanning electron microscopy image for an etch whose process parameters were as follows: SiCl <sub>4</sub> gas flow rate was 18 sccm, the pressure was 11 mtorr and the RF power was 100 W, as indicated in table (4.3). The etch profile is undercut, which not was suitable for fabricating MMI array laser.	106
Figure (4.17)	Quantum well intermixing using sputtered silica concept.	112
Figure (4.18)	1x2 MMI array laser diode post QWI post annealing at 810° C. The sample in this example was capped with 200 nm sputtered silica followed by 200 nm PECVD. Interface between the intermixed and non-intermixed areas is clearly visible.	113
Figure (4.19)	Fabrication steps of quantum well intermixing process using SiO <sub>2</sub> sputtering.	114
Figure (4.20)	RTA temperature cycle for annealing GaAs for 90 seconds.	115
Figure (4.21)	Photoluminescence system used for PL characterisation with 532 nm green laser source.	116
Figure (4.22)	PL measurement in liquid N <sub>2</sub> 77 K for Intense material using different annealing temperature. As grown material has a wavelength of 775 nm at 77 K.	118
Figure (4.23)	Cu evaporation process for quantum well intermixing.	119
Figure (4.24)	Intermixing results for different SiO <sub>2</sub> cap for 60 s anneal. PL shift vs. annealing temperature for different silica caps where red triangle points represent 50 nm sputtered silica capped with 200 nm PECVD, circles represent 50 nm sputtered silica with no cap and the green triangles points represent Cu evaporation-e-beam silica process, while 200 nm PECVD is represented by squares.	120
Figure (4.25)	PL shift for Cu impurity in QWI using sputtered silica process. The 2x2 mm GaAs/AlGaAs samples were annealed for 60 seconds. The only variable is sputtering time for Cu. The time was varied from 5 seconds to 36 seconds.	122
Figure (4.26)	Intermixing results for three different RTA annealing times (30s, 60s, and 90 s) shown for 200 nm sputtered silica capped with 200 nm PECVD. A 200 nm PECVD anneal is also shown, which is used for suppressing intermixing. The annealing temperature used here was 825° C.	123

Figure (4.27)	(a) Figure above (a) shows etched MMI device post intermixing. The source of the spots on the MMI is contamination on the QWI sputtering stage. These spots and contamination were transferred onto the sample after etching causing pillars or micro-masking. (b) Figure (b) shows severe contamination of the deposited layer on the MMI after intermixing and annealing, which is followed by etching.	125
Figure (4.28)	Loss measurement setup for GaAs/AlGaAs waveguide	128
Figure (4.29)	Optical transmission through passive waveguide using temperature tuning. Losses can be measured using maxima and minima points.	129
Figure (4.30)	CW light/current characteristics of 830nm un-coated ridge waveguide lasers with (a) no-NAM/NIM (i.e. a conventional laser), (b) NIM only, (c) a NAM/NIM with a 45 nm bandgap shift, and (d) a NAM/NIM with a 65nm shift. (Courtesy of J. Marsh) (Reference 165). In fact, as can be seen in figure (32d), COD was not observed for the lasers with a shift of 65 nm. The rollover in power is due to heating of the diode.	129
Figure (4.31)	Fabrication steps for 1xN MMI array laser diode.	130
Figure (4.32)	P-metallization for a chip, which six devices can be seen and a scribing mark is observed on the right.	133
Figure (4.33)	Fabricated devices suffered from metal shorting for the reason of metal pads proximity for individually addressable array laser.	133
Figure (5.1)	Schematic diagram of a ridge waveguide to provide 2 dimensional channel guiding. Controlled etched depth ensures single spatial mode.	139
Figure (5.2)	(a) Fimmwave simulation showing the fundamental mode contour profile for a ridge depth of 1.84 $\mu\text{m}$ and ridge width of (2.5 $\mu\text{m}$ ). The wavelength used is 0.83 $\mu\text{m}$ . (b) Contour profile for 1 <sup>st</sup> order mode for a ridge depth of 1.84 $\mu\text{m}$ and ridge width of (2.5 $\mu\text{m}$ ). This mode is not supported as it is evident.	141
Figure (5.3)	Multimode waveguide which shows the cross section with refractive indices for the MMI and the cladding respectively denoted by $n_r$ and $n_c$ . On the right, representation is given of the modes propagating in the waveguide. The number of the waveguide modes is a function of the waveguide dimension and the field launch position. The diagram is an adaptation of figures by Soldano (196).	143
Figure (5.4)	3D-Schematic of the multimode interferometer array laser diode comprising four active gain section and passive MMI with single spatial mode waveguide.	145
Figure (5.5)	Schematic diagram for a 1x2 MMI symmetrical interference splitter/combiner. The device has gain sections, which are the lasers with NAMs (with dimensions of 50-150 $\mu\text{m}$ ), MMI section and output waveguide.	148
Figure (5.6)	schematic of 4x1 MMI array laser device.	151
Figure (5.7)	1x4 MMI simulated imaging length with respect to core layer refractive index for GaAs/AlGaAs material.	153
Figure (5.8)	1x4 MMI computed fundamental mode is launched at path1, so the input signal will go through the MMI guide, multiple images are formed. Naming the path in the software makes it easier to monitor	154

	each path during simulation.	
Figure (5.9)	Highest order mode for 24 $\mu\text{m}$ wide multimode Interference (MMI) section.	155
Figure (5.10)	Computed fundamental mode profile obtained using BPM for 2.5 $\mu\text{m}$ waveguide.	155
Figure (5.11)	Simulation for a 1x4 MMI for 700 $\mu\text{m}$ length using BPM mode solver.	156
Figure (5.12)	Simulation for a 1x4 MMI coupler, it can be seen that at distance 625 $\mu\text{m}$ the power is equal for the four waveguides. The waveguide width is 2.5 $\mu\text{m}$ and the MMI width is 24 $\mu\text{m}$ .	157
Figure (5.13)	Monitored optical power value for a 1x4 MMI GaAs/AGaAs array laser diode. The four image location is marked, as in the graph. Inspection of the graph shows that the monitored value is 0.25.	157
Figure (5.14)	Simulation of a 4x1 MM array laser diode using Rsoft BPM software. Equal power is verified as MMI length of 625 $\mu\text{m}$ .	158
Figure (5.15)	Cross sectional view of the simulated 4x1 MMI array laser illustrating the optical mode profile in each gain section at MMI length (L=617 $\mu\text{m}$ ).	158
Figure (5.16)	Phase relationship for symmetrical 1x4 MMI array laser. The spacing between the emitters is the same. The emitters have the same length. BPM calculations show that arms one and four have the same phase and arms two and three have the same phase. The relative phase difference between these two groups is $\pi/2$ .	159
Figure (5.17)	BPM phase Modelling for the optical field for 1x4 MMI laser.	160
Figure (5.18)	Magnified version of graph (5.17), which shows the relative phase difference between two adjacent gain sections.	161
Figure (5.19)	Phase simulation for a 1x4 MMI array laser versus the gain section number. There is a relative phase difference equal to ( $\pi/2$ ) between gain sections (1) and (2) and (3) and (4). Gain section (1) and gain section (4) have equal phases and similarly (2) and (3) have equal phases.	161
Figure (5.20)	Schematic diagram of a 1x3 MMI array laser. The phase relations are shown for a symmetrical 1x3 MMI. The phases of the two outer arms are equal, but the middle arm has a relative phase shift of $\pi/3$ .	162
Figure (5.21)	Phase simulation for a 1x3 MMI array laser versus the gain section number. There is a relative phase difference equal to ( $\pi/3$ ) between gain section (2) and each of gain sections (1) and (3). Gain section (1) and gain section (3) have equal phases.	162
Figure (5.22)	BPM simulation showing the fundamental mode for a 3 $\mu\text{m}$ waveguide, which is launched at the centre of a 1x3 MMI array laser.	163
Figure (5.23)	1x3 MMI simulation using the BPM method. By Inspection of the figure above, 3 images are seen at a Z distance of 566 $\mu\text{m}$ . The corresponding monitor values are 0.333. This means an equal power splitting ratio. The MMI width in this simulation was 19.5 $\mu\text{m}$ . The waveguide spacing is 3.5 $\mu\text{m}$ .	163
Figure (5.24)	Figure (5.24): Cross sectional view of the simulated 3x1 MMI array laser illustrating the optical mode profile in each gain section at an	164

- MMI length ( $L=566 \mu\text{m}$ ).
- Figure (5.25) 1x2 MMI simulation using BPM method. By Inspection of the figure above, 2 images are seen at a Z distance of  $465 \mu\text{m}$ . The corresponding monitor values are 0.5. This means an equal power splitting ratio. The MMI width in this simulation was  $15 \mu\text{m}$ . The waveguide spacing was  $3.5 \mu\text{m}$ . 164
- Figure (5.26) Figure (5.26): Cross sectional view of the simulated 2x1 MMI array laser illustrating the optical mode profile in each gain section at MMI length ( $L=465 \mu\text{m}$ ). 165
- Figure (5.27) A schematic of 1x4 tapered MMI array laser. 1x4 tapered MMI array laser with parameters as follows: taper length ( $L_{\text{taper}}$ ) was  $28.8 \mu\text{m}$  for  $\theta = 20^\circ$ , MMI spacing was  $3 \mu\text{m}$  (centre to centre  $=5.5 \mu\text{m}$ ), the optimum MMI length was  $520 \mu\text{m}$ , the waveguide width was  $2.5 \mu\text{m}$  and the MMI was  $22 \mu\text{m}$  wide. 166
- Figure (5.28) Simulation of 1x4 tapered MMI array laser with parameters as follows: taper length ( $L_{\text{taper}}$ ) was  $28.8 \mu\text{m}$  for angle  $\theta$  of  $20^\circ$ , MMI spacing of  $3 \mu\text{m}$  (equivalent to a centre to centre pitch of  $5.5 \mu\text{m}$ ), the optimum MMI was  $520 \mu\text{m}$  in length, the waveguide width was  $2.5 \mu\text{m}$  and the MMI was  $22 \mu\text{m}$  wide. This figure shows the monitored power in each guide. 167
- Figure (5.29) Simulation of the far-field pattern for the 1x4 tapered MMI array laser parameters were as follows: the taper length ( $L_{\text{taper}}$ ) was  $28.8 \mu\text{m}$  for an angle  $\theta$  of  $20^\circ$ , the MMI spacing was  $3 \mu\text{m}$  (equivalent to a centre to centre pitch of  $5.5 \mu\text{m}$ ), optimum MMI length was  $520 \mu\text{m}$ , the waveguide width was  $2.5 \mu\text{m}$  and the MMI width was  $22 \mu\text{m}$ . The angular separation between individual peaks is ( $\lambda/\text{spacing}$ ), which is  $8.6^\circ$ , the central lobe width at FWHM equals ( $\lambda/N*\text{spacing}$ ), which is  $2.16^\circ$ . These values are for a laser that is phase locked. 167
- Figure (5.30) Simulation of a far-field pattern of the 1x4 tapered MMI array laser with following parameters: the taper length ( $L_{\text{taper}}$ ) was  $200 \mu\text{m}$  for an angle  $\theta$  of  $3^\circ$ , the MMI spacing was a  $3 \mu\text{m}$  (equivalent to a centre to centre pitch of  $5.5 \mu\text{m}$ ), the optimum MMI length was a  $520 \mu\text{m}$ , the waveguide width was  $2.5 \mu\text{m}$  and the MMI was  $22 \mu\text{m}$  wide. The individual peaks in this simulation disappear due to non optimised taper. 168
- Figure (5.31) Simulation of 1x4 tapered MMI array laser with parameters as follows: taper length ( $L_{\text{taper}}$ )  $=200 \mu\text{m}$  for  $\theta = 3^\circ$ , MMI spacing of  $3 \mu\text{m}$  (centre to centre  $=5.5 \mu\text{m}$ ), MMI length of  $1000\mu\text{m}$ , waveguide with  $2.5 \mu\text{m}$ , MMI width  $=22 \mu\text{m}$ . This figure shows the monitored power in each waveguide. 168
- Figure (5.32) Simulation of the monitored power for different 1x4 MMI lengths. The parameters for the 1x4 tapered MM are: Tapered MMI length was varied within a range of  $460 \mu\text{m}$  to  $560 \mu\text{m}$  (red curve), The MMI width was  $22 \mu\text{m}$ , the spacing was a  $3 \mu\text{m}$  (equivalent to a centre to centre pitch of  $5.5 \mu\text{m}$ ) and the length of the taper was  $28.8 \mu\text{m}$  for an angle of  $20^\circ$ . The 1x4 not tapered MMI have parameters, which are: MMI length was varied within a range of  $560 \mu\text{m}$  to  $680$  169

	$\mu\text{m}$ . 617 $\mu\text{m}$ , MMI width of 24 $\mu\text{m}$ , the spacing was a 3.5 $\mu\text{m}$ (equivalent to a centre to centre pitch of 5.5 $\mu\text{m}$ ) and the MMI width was 24 $\mu\text{m}$ .	
Figure (5.33)	Represent 1x4 multimode interference coupler. Design parameters to be optimised are input waveguide spacing (d), the width of the MMI ( $W_e$ ) and the length of the MMI section (L).	171
Figure (5.34)	Optimisation data for a 1x4 MMI simulation using BPM. Percentage of transmitted power in TE mode plotted for different input waveguide spacing versus MMI width/ length.	172
Figure (5.35)	Optimisation data for 1x4 MMI simulation using BPM method. Percentage of transmitted power in TE mode plotted for different input waveguide spacings versus MMI width/ length.	173
Figure (5.36)	Horizontal far-field simulation for a 1x4 MMI array laser from the array side. The dimensions of the MMI laser array are as follows: the MMI length is 617 $\mu\text{m}$ , the inter-element spacing is 3.5 $\mu\text{m}$ (equivalent to a pitch p of 6 $\mu\text{m}$ that is measured from the centre of one emitter to the next one) and the MMI width is 24 $\mu\text{m}$ . This same device has been fabricated and the results will be discussed in Chapter 6. The fill factor (f) in this example is (41.6 %). The width of the central peak is $(\lambda/N.p)$ and the width at $1/e^2$ is comparable to envelope of individual emitter. The angular separation of individual peaks is equivalent to $(\lambda/p)$ .	175
Figure (5.37)	Horizontal far-field simulation for a 1x3 MMI array laser for the array side. The dimensions of the MMI laser array are as follows: MMI length (566 $\mu\text{m}$ ), inter-element spacing (3.5 $\mu\text{m}$ ), MMI width of (19.5 $\mu\text{m}$ ) and gain sections widths of (3.0 $\mu\text{m}$ ). The fill factor (f) in this example is (41.6 %).	176
Figure (5.38)	Horizontal far-field simulation for a 1X2 MMI array laser from the array side. The dimension of the MMI laser array is as follows: The MMI length is (465 $\mu\text{m}$ ), the inter-element spacing is (3.5 $\mu\text{m}$ ), the MMI width is (15 $\mu\text{m}$ ), the gain sections width is (3.0 $\mu\text{m}$ ) and the fill factor (f) in this example is (46 %).	176
Figure (6.1)	Concept for a 1x4 MMI array laser diode, which is comprised of NAMs, gain sections, MMI coupler and single mode output waveguide.	178
Figure (6.2)	a) Schematic diagram of the 1x4 MMI coupler array laser. The devices were etched up to 300 nm above the quantum well. The MMI section is etched again through the waveguide core. The gain sections are electrically connected with a single contact. b) Image taken of the array laser by optical microscope, showing the four sections of the integrated device.	181
Figure (6.3)	Photo-luminescence spectra from the as-grown, suppressed and intermixed device. A wavelength shift of 58 nm is observed. The non-intermixed areas are suppressed by using a layer of protective silica.	183
Figure (6.4)	(a) This SEM image shows a 1x4 etched waveguide with well defined waveguides. (b) This SEM image is a magnified image of (a), which shows a well etched waveguide with a good interface	184

	between the MMI and gain sections. (c) The SEM image shows the deeper etch used for the MMI section.	
Figure (6.5)	This SEM image (left) shows a bar of 1x4 MMI array devices mounted on a brass sub-mounts. The magnified image (right) shows the cleaved facets. The p-metallisation which covers all the four gain sections is well defined. The non-coated area represents the NAM area.	185
Figure (6.6)	Complete bar of 1x4 MMI laser arrays, which is mounted on a brass sub-mount, where six devices are visible.	185
Figure (6.7a)	Front facet (power per facet) light current/voltage (LIV) test results for a 1x4 MMI array laser. The devices were tested pulsed up to ( $20xI_{th}$ ). The MMI length was ( $617 \mu\text{m}$ ), the gain section length was ( $975 \mu\text{m}$ ), the NAM length was ( $100 \mu\text{m}$ ) and output waveguide length was $325 \mu\text{m}$ . The MMI length is very close to the simulated MMI length of $617 \mu\text{m}$ . The operating wavelength was $824 \text{ nm}$ , as shown in the inset.	187
Figure (6.7b)	LI curve for $2.5 \mu\text{m}$ single ridge waveguide performance. The length of the device was $1.5 \text{ mm}$ . There was no facet coating and no NAM which was fabricated using the same Intense Ltd material. The device suffered COMD at $98 \text{ mW}$ at this particular example.	187
Figure (6.8)	a) Maximum power values measured at $3.0 \text{ A}$ current for devices with different MMI length. The optimum MMI length from the simulations was $615 \mu\text{m}$ . The device with highest power has an MMI length of $617 \mu\text{m}$ . b) BPM Simulation resulted for the monitored power of a 1x4 MM array laser. The array laser dimensions are as follows: the MMI width was $24 \mu\text{m}$ , the ridge waveguide width was $2.5 \mu\text{m}$ and the emitter separation distance was $3.5 \mu\text{m}$ (equivalent to a centre to centre spacing of $6 \mu\text{m}$ ). The MMI length was varied for optimisation. MMI window for a monitored power of $0.95 \text{ (a.u.)}$ is in the range of ( $607\mu\text{m} - 630 \mu\text{m}$ ).	188
Figure (6.9)	Wall plug efficiency (WPE) and output power vs. drive current for an uncoated 1x4 MMI array laser with MMI length of $617\mu\text{m}$ . The power was measured from the single output waveguide side.	190
Figure (6.10)	Front facet light current/voltage (LIV) test results for a 1x4 MMI array laser. The devices were tested pulsed up to ( $20xI_{th}$ ). The MMI length was ( $642 \mu\text{m}$ ), the gain section length was ( $975 \mu\text{m}$ ), the NAM length was ( $100 \mu\text{m}$ ) and output waveguide length was $325 \mu\text{m}$ . The MMI length is longer than the simulated MMI length by $25 \mu\text{m}$ .	191
Figure (6.11)	Front facet light current/voltage (LIV) test results for a 1x4 MMI array laser. The devices were tested pulsed up to ( $20xI_{th}$ ). The MMI length was ( $665 \mu\text{m}$ ), the gain section length was ( $975 \mu\text{m}$ ), the NAM length was ( $100 \mu\text{m}$ ) and output waveguide length was $325 \mu\text{m}$ . The MMI length is longer than the simulated MMI length by $48 \mu\text{m}$ .	191
Figure (6.12)	a) Vertical and far field for 1x4 MMI array laser from single output facet side. b) Horizontal far field. The far field was measured from ( $1.24I_{th}$ ) mA up to ( $13I_{th}$ ) mA, which corresponds to $180 \text{ mA}$ up to	192

- 1900 mA.
- Figure (6.13) a) Horizontal far-field BPM simulation for the 1x4 MMI single output side. Ridge depth of a  $1.84 \mu\text{m}$  and waveguide width of a  $2.5 \mu\text{m}$  is used. The FWHM is  $9.3^\circ$  at  $3I_{\text{th}}$ . The far-field was measured at  $3I_{\text{th}}$ , which was  $9.4^\circ$  at FWHM. The far-field at  $1/e^2$  is  $23.2^\circ$  when measured at  $13I_{\text{th}}$ . The value of the far-field from the simulation above is  $21^\circ$ . b) The BPM simulation of the vertical far-field for a 1x4 MMI single output side shows a FWHM of  $22^\circ$ . The vertical far-field increases to  $23^\circ$  FWHM at  $3 I_{\text{th}}$ . A ridge depth of  $1.84 \mu\text{m}$  and waveguide width of  $2.5 \mu\text{m}$  are used. 193
- Figure (6.14) Back facet (array side) light current/voltage (LIV) test results for a 1x4 MMI array laser. The devices were tested pulsed up to  $(20xI_{\text{th}})$ . The MMI length was ( $617 \mu\text{m}$ ), the gain section length was ( $975 \mu\text{m}$ ), the NAM length was ( $100 \mu\text{m}$ ) and output waveguide length was  $325 \mu\text{m}$ . The MMI length is very close the simulated MMI length of  $617 \mu\text{m}$ . 195
- Figure (6.15) Output power of 1x4 MMI array lasers with different MMI lengths for 3 A pulsed current measured from the gain section side. From the simulation, the designed length of  $617 \mu\text{m}$  was in the range of optimum MMI lengths. The effect of mode mismatch and phase difference increased, as the MMI length deviation from optimum range increased. 196
- Figure (6.16) Horizontal far-field pattern for a 1x4 MMI array laser from the array side. The horizontal far-field pattern has been measured for  $2I_{\text{th}}$  up to  $7 I_{\text{th}}$ . The far-field pattern is a phase locked, which is very close to a diffraction limit of  $(\lambda/N.p)$  at the centre. The angular separation matches the pattern from a phase locked pattern. This angular separation equals to  $\lambda/p$ . In this example,  $N=4$ ,  $p= 6\mu\text{m}$ , the width of individual emitter is ( $2w = 2.5 \mu\text{m}$ ) and operating wavelength of  $0.822 \mu\text{m}$ . 197
- Figure (6.17) (a) The measured spectra from the back facet of a 1x4 MMI array laser show a single wavelength emission for an applied current of  $2xI_{\text{th}}$ . The peak wavelength is  $822.0 \text{ nm}$  and the spectral width ( $\Delta\lambda$ ) is  $0.13\text{nm}$  at the FWHM. (b) The measured spectra from the back facet of a 1x4 MMI array laser show a single wavelength emission for an applied current of  $4xI_{\text{th}}$ . The peak wavelength is  $822.04 \text{ nm}$  and the spectral width ( $\Delta\lambda$ ) is  $0.18\text{nm}$  at the FWHM. Figure (c) shows the measured spectra from the back facet of a 1x4 MMI array laser, whereby single wavelength emission is visible for a  $5.2xI_{\text{th}}$ . The peak wavelength is  $822.09 \text{ nm}$  and the spectral width ( $\Delta\lambda$ ) is  $0.22\text{nm}$  at FWHM for an applied current of  $5.2xI_{\text{th}}$ . The power at  $5.2xI_{\text{th}}$  is  $152 \text{ mW}$  per facet. 198
- Figure (6.18) Simulation of the horizontal far-field from the array facet side of a 1x4 MMI laser diode. A very similar pattern can be seen from the measurement in figure (6.15), which was measured from the array facet side. The far-field FWHM in this simulation is  $2.5$  degrees, which is very close to the measured value of  $2.1$  degrees. Overall, there is a good agreement between experiment and the simulation. 200

- Figure (6.19) (a) The measured spectrum from the back facet of 1x4 MMI array laser shows multiple wavelength emission for  $6.2 \times I_{th}$ . At this current, the phase locking is lost. An evidence of that is the four wavelength peaks, which are visible as follows:  $\lambda_1=821.35$  nm,  $\lambda_2=821.59$  nm,  $\lambda_3=821.83$  nm and  $\lambda_4=822.08$  nm, respectively. The  $\Delta\lambda$  width at FWHM is around 0.22 nm for the each of the individual peaks. (b) The spectrum in red colour represents the emission spectra for 2.5  $\mu\text{m}$  wide and 1000  $\mu\text{m}$  uncoated ridge waveguide laser. It was measured at 200 mA in pulsed mode of 5  $\mu\text{s}$  and a repetition rate of 1 KHz. The spectral width at FWHM is around 0.65 nm. 202
- Figure (6.20) The measured spectrum from the back facet of 1x4 MMI array laser shows lasing spectra at  $9 \times I_{th}$  ( $I_{th}=145$  mA). More array modes are visible with different wavelength separation between array modes. The phase locking is lost at this current level, whereby each mode consists of clusters of resonances. 203
- Figure (6.21) Measurement of the horizontal far-field from the array facets side of a 1x4 MMI laser diode for the optimum device with an MMI length of 617  $\mu\text{m}$ . 204
- Figure (6.22) Measurement from the horizontal far-field array facets side for a 1x4 MMI laser diode with an MMI length of 665  $\mu\text{m}$ . The 180° out of phase is visible, which is the reason for the double lobed far-field. It is a typical example of an array laser where the elements operate in anti-phase. 205
- Figure (6.23) Measurement from the horizontal far-field array facets side for a 1x4 MMI laser diode with an MMI length of 644  $\mu\text{m}$ . The fully unresolved side lobes are in agreement with angular side lobes separation of  $(\lambda/p)$ . 206
- Figure (6.24) (a)-(d) Evolution of the optical spectra with an increasing drive current from  $1.4 \times I_{th}$  to  $4 \times I_{th}$  for a 1x4 MMI array laser. The MMI length is 644  $\mu\text{m}$ . (a) The measured spectrum from the back facet of a 1x4 MMI array laser shows a multi-wavelength emission for a  $1.4 \times I_{th}$ . Four wavelength peaks are visible, which correspond to the four emitters as follows:  $\lambda_1=820.5$  nm,  $\lambda_2=820.8$  nm,  $\lambda_3=821.1$  nm and  $\lambda_4=821.31$  nm, respectively. In figures (b-d), the emission spectra broaden due to the spatial hole burning. The emission spectra were measured at in pulsed mode of 5  $\mu\text{s}$  width and a repetition rate of 1 KHz. 207
- Figure (6.25) a) Optical microscope image for a 1x4 tapered array MMI, which shows two complete devices comprising the NAM, gain section, tapered MMI and output waveguide. b) SEM images for the interfaces between the gain section and the MMI and the MMI with the output waveguide. The MMI is deeply etched although it is not shown in this particular SEM image. 209
- Figure (6.26) Light current characteristic for 1x4 tapered array MMI laser. NAM length 75  $\mu\text{m}$ , 975  $\mu\text{m}$  gain section, MMI length 440  $\mu\text{m}$ , width 22  $\mu\text{m}$ , the separation distance between gain sections is 3  $\mu\text{m}$  and output waveguide is 325  $\mu\text{m}$ . The angle of the taper was set at 31°, which was designed wider than the divergence angle of the laser to reduce 210

	any possibility of reflections.	
Figure (6.27)	(a) Schematic for a 1x2 MMI array laser design. The MMI comprises of NAMs, gain section, MMI, and output waveguide. (b) Example of an etched 1x2 MMI array laser, which shows the ridge waveguides and the MMI.	213
Figure (6.28)	Front facet light current/voltage (LIV) test results for the 1x2 MMI array laser. Devices tested pulsed up to $(30 \times I_{th})$ . The MMI length was $(480 \mu\text{m})$ , the gain section length was $(975 \mu\text{m})$ , the NAM length was $(75 \mu\text{m})$ and output waveguide length $(325 \mu\text{m})$ .	215
Figure (6.29)	Wall plug efficiency (WPE) and output power vs. drive current for a 1x2 MMI array laser with MMI length of $480 \mu\text{m}$ . The power was measured from the single output waveguide side.	215
Figure (6.30)	Maximum power values measured at 2.0 A current for devices with different MMI length. The devices with highest power had an MMI length of $480 \mu\text{m}$ .	216
Figure (6.31)	BPM simulation for 1x2 MMI array laser where an MMI length scan was performed using the following parameters: MMI length was $15 \mu\text{m}$ , ridge waveguide width was $2.5 \mu\text{m}$ the pitch was $3.5 \mu\text{m}$ and the length of the MMI was varied. The range of the optimum lengths is between $(456-482 \mu\text{m})$ . This is based on an optimum power value of $(0.9 \text{ a.u.})$ .	216
Figure (6.32)	Front facet light current/voltage (LIV) test results for a 1x2 MMI array laser. Devices tested pulsed up to $(30 \times I_{th})$ . The MMI length was $(420 \mu\text{m})$ , gain section length was $(975 \mu\text{m})$ , the NAM length was $(75 \mu\text{m})$ and output waveguide length was $325 \mu\text{m}$ .	217
Figure (6.33)	Horizontal far-field pattern from a 1x2 MMI array laser measured from the array side (back) facets.	219
Figure (6.34)	Horizontal far-field pattern for a 1x2 MMI array laser measured from the array side (back) facets. The MMI length for this device was $480 \mu\text{m}$ . The far-field pattern was measured for a current injection of $3.2 \times I_{th}$ to $21.0 \times I_{th}$ in CW mode. The threshold current ( $I_{th}$ ) for 1x2 MMI array laser was $85 \text{ mA}$ .	220
Figure (6.35)	Dotted graph in red shows the horizontal far-field pattern for a 1x2 MMI array laser measured from the array side (back) facets for an injection current of $3.2 \times I_{th}$ CW. The far-field pattern in blue colour show the simulation results for the 1x2 MMI array taken from Chapter 5. The MMI length for this device was $480 \mu\text{m}$ . The $I_{th}$ for this 1x2 MMI array laser was $85 \text{ mA}$ .	221
Figure (6.36)	Measured optical spectra in CW mode from the single facet side for a 1x2 MMI array laser diode. The figure shows a very narrow spectrum of $0.3 \text{ nm}$ at FWHM for an applied current of $3.2 \times I_{th}$ . The spectrum broadens to several nanometres at $6.3 \times I_{th}$ .	222
Figure (6.37)	Optical spectra measured from the single facet side for a 1x2 MMI array laser diode. The length of the MMI was $480 \mu\text{m}$ . The figure illustrates a very narrow spectral width ( $\Delta\lambda$ ) of $0.3 \text{ nm}$ at the FWHM for an applied current of $3.2 \times I_{th}$ ( $I_{th} = 85 \text{ mA}$ ). The power at $3.2 \times I_{th}$ was around $60 \text{ mW}$ per facet.	222
Figure (6.38)	A schematic for 1x2 MMI array laser, which shows the phase	223

- matching region.
- Figure (6.39) (a) Spectra of a 1x2 MMI array laser measured at 3.2xI<sub>th</sub> in CW mode. The device length was 465 μm. Two modes are oscillating one at 824.08 nm and the other mode at 823.22 nm with a spectral width ( $\Delta\lambda$ ) of 0.86 nm at FWHM. (b) Spectra of a 1x2 MMI array laser measured at 3.2xI<sub>th</sub> CW. Device length was 444 μm. It is clearly two modes are oscillating one at 823.76 nm and the other mode at 821.48 nm with spectral width ( $\Delta\lambda$ ) of 3.1 nm at the FWHM. There are cluster of resonances for each oscillating mode. In these two examples, there is no phase locking. 224
- Figure (6.40) The spectral bandwidth versus MMI cavity length for a 1x2 MMI array laser devices. Phase locking was achieved for the device with optimum self imaging with the accurate phase matching region, which was the device with a 480 μm. 225

# Abbreviations

MOPA	master oscillator power amplifier
M-MOPA	monolithic master oscillator power amplifier
PA	power amplifier
MO	master oscillator
DFB	distributed feedback
QWI	quantum well intermixing
GaAs	gallium arsenide
AlGaAs	aluminium gallium arsenide
COMD	catastrophic optical mirror damage
NAM	non-absorbing mirrors
MMI	multimode interference
BPP	beam parameter product
CtP	computer to plate
AR	anti-reflection
BA	broad area
CW	continuous wave
DBR	distributed Bragg reflector
MOCVD	metal organic chemical vapour deposition
MBE	molecular beam epitaxy
SCOWL	slab coupled optical waveguide laser
GRINSCH	graded index separate confinement heterostructure
SQW	single quantum well
MQW	multi-quantum well
SR	surface recombination
IVA	intervalence band absorption
FRL	far-field reduction layer
EBL	e-beam lithography
PMMA	polymethyl methacrylate

MIBK	methyl isobutyl ketone
IPA	isopropyl alcohol
PECVD	chemical enhanced vapour deposition process
RF	radio frequency
SL	superlattice
IILD	impurity induced layer disordering
IID	impurity induced disordering
PAID	photo-absorption induced disordering
SID	sputter induced disordering
RTA	rapid thermal annealing
TLM	transmission line method
PL	photoluminescence
RIE	reactive ion etching
SEM	scanning electron microscope
V-I	voltage-current
LI	light-current
BPM	beam propagation method
TE	transverse-electric
TM	transverse-magnetic
ECDL	external cavity diode laser
FPI	Fabry-Perot interferometer
FSR	free spectral range
FWHM	full width half maximum
GaAs	gallium arsenide
HR	highly reflecting
HT	highly transmissive
InGaAs	indium gallium arsenide

*To My Family*

# Chapter 1

## 1.1 Introduction

Low cost high brightness semiconductor lasers operating in a single spatial mode play a key role in an increasing number of applications, particularly applications that require good beam quality (coherent emission). Examples of such applications are storage systems, free space communication, printing applications, marking industry and medical applications. Major advances in increasing the brightness of the semiconductor laser have been made. Improving reliability and broadening the range of wavelengths available has allowed these types of devices to replace bulkier lasers in various applications, because they are very compact, easy to cool and achieve good efficiency when compared to other types of lasers.

Although excellent progress has been made toward the development of high brightness diode lasers in the output power range up to one watt operating continuous wave in a single transverse mode, there is still a great interest in developing high brightness laser diodes operating at even higher power levels in single transverse mode. High brightness semiconductor lasers operating at more than one watt CW are widespread through the use of broad area laser diodes. Additional examples include different types of laser diode arrays and

tapered laser diodes. However, most of these types of devices involve complex processing, beam correction optics which lead to increased costs. Furthermore, some types of these devices could suffer from a multi-lobed far-field operation, this is particularly valid when the output from these devices becomes difficult to focus the light into a small spot. A lot of work has been done in order to develop high brightness lasers operating in a single spatial mode. Examples of this type of device are the (Master oscillator power amplifier) MOPA, the ALFA DFB lasers and the anti-guided array laser diode.

## **1.2 The aims of the presented work**

The work described in this thesis investigated the performance of high brightness laser diode arrays incorporating a multimode interference coupler (MMI) and a single output waveguide using the GaAs/AlGaAs material system for an emission wavelength of 830 nm. The target of this work was to improve the brightness with preserving a good beam quality factor ( $M^2$ ) of the semiconductor laser diode beyond what is achieved using single ridge waveguide laser diode. Looking at the data sheet for different manufacturers of ridge waveguide laser, we notice that Intense Ltd (1) offers 200 mW device with a beam quality ( $M^2 = 1$ ) at a wavelength of 830 nm. Others manufacturer like Eagleyard Photonics Ltd just recently produced 808 nm ridge waveguide laser with an output power of 800 mW (2) with an  $M^2$  of 1.2. So, higher powers are achieved depending on the laser beam quality factor ( $M^2$ ), operating wavelength and the technology used.

Since the high-output power is partly limited by catastrophic optical mirror damage (COMD), non-absorbing mirrors (NAM) were fabricated using quantum well intermixing technology. This is a core technology developed by the University of Glasgow over the past two decades.

The integrated multimode interference array laser diode has been studied in the past by a number of researchers (3, 4), but the devices developed had flaws in their design. In this thesis, the research will focus on the development of an integrated MMI high brightness array laser that operates at a wavelength of 830 nm with good beam quality factor ( $M^2$ ) for use in printing applications.

The idea of using an integrated multimode interference coupler is to improve the phase locking between the laser gain sections, so that they will operate in a phase locked supermode and thus achieve high power with a diffraction

limited beam. A schematic of the proposed device can be seen in figure (1.1). In this particular schematic, four gain sections are integrated with a NAM, MMI and single mode output waveguide. The number of gain sections can be varied from one up to four. The proposed device has a low loss passive multimode interference coupler and a passive single-mode output guide, which are fabricated using the quantum well intermixing technology. The significance of using such a design is that coupling two or more ridge waveguides (gain sections) into a multimode interference coupler, then the output waveguide will contain a high brightness, high power beam if the correct phase relationship of the adjacent gain sections is maintained.

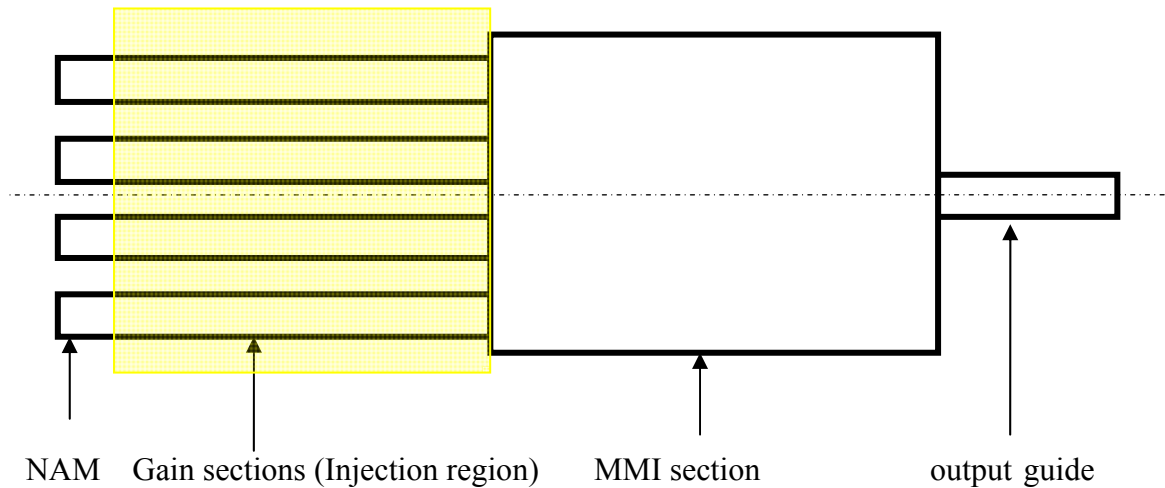


Figure (1.1) Schematic of the proposed multimode integrated array laser diode which is comprised of NAMs (non-absorbing mirrors), gain section, MMI and single mode output waveguide.

The benefit of using low power adjacent ridge waveguides (gain sections) will inhibit COMD, as this occurs at high output powers.

### 1.3 High brightness laser diode limitations

There are four main limitations of high brightness laser diodes operating in a single spatial mode. Each one of these limitations will be discussed and the solution developed in this work will be presented. These limitations are as follows:

1. Catastrophic optical mirror damage
2. Spatial mode instability

3. Thermal issues
4. Long term aging

Catastrophic optical mirror damage is one of the limitations of high brightness lasers, whereby the semiconductor laser facets suffer irreversible damage due to thermal runaway at the facet. This phenomenon is accompanied by a sudden drop in optical power which is irreversible, unlike the thermal rollover. The introduction of the band gap widened sections at the facets for the semiconductor devices and the implementation of non absorbing mirrors using quantum well intermixing, made it possible almost to eliminate the problem of a COMD. The other significant limitation for high brightness laser operating in a single lateral spatial mode is multimode operation, where the fundamental mode discrimination can be difficult to sustain due to the excitation of the second lateral order mode as a result of a temperature rise. The heating effect is an important limitation, which needs to be taken into account when designing high brightness lasers and using a good heat sinking. The heating instigates what is called thermal rollover limiting the power achieved by the laser. The last effect accelerates long term aging, which is related to the long-term reliability of the laser.

### **1.4 High power laser diode figures of merits**

There are a number of ways of characterizing a laser output beam, commonly, the laser radiation pattern (far-field), the power and the spectrum. These measures define in a qualitative way the usefulness of the laser for a particular application. The quantitative measures of the laser beam quality are the,  $M^2$  beam quality factor, brightness and beam parameter product (BPP), which are important. These are discussed below as follows:

#### **1.4.1 The beam quality factor $M^2$ and the beam parameter product BPP**

The quality of the laser beam is measured by the  $M^2$  factor. To specify the meaning of  $M^2$  for a real laser beam, let us first consider a Gaussian beam as depicted in figure (1.2). The Gaussian beam is characterized by the beam waist radius  $w_0$ , the half far-field angle  $\theta_0$  and the wavelength  $\lambda$ .

If we assume Gaussian beam propagation along the z –axis, one can obtain the beam waist radius at any z- position using the following relation (5, 6, 14):

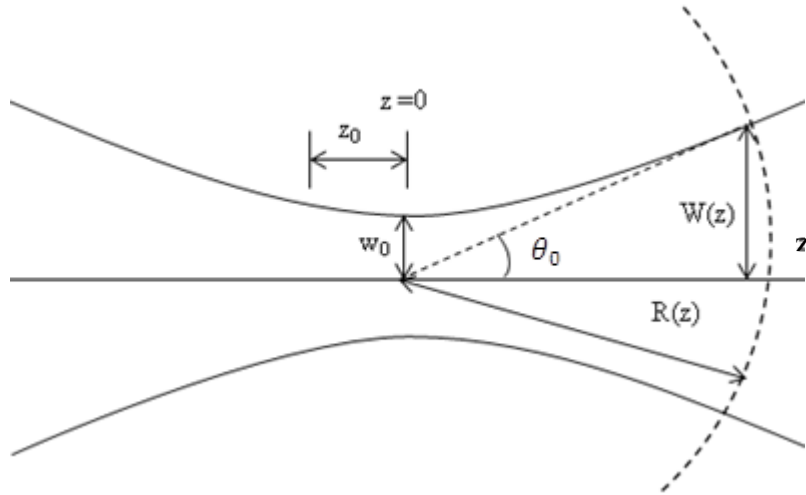


Figure (1.2): A schematic for Gaussian beam propagation

$$w^2(z) = w_0^2 \cdot \left[ 1 + \left( \frac{z}{z_0} \right)^2 \right] \quad (1.1)$$

Where:  $2w_0$  is the beam spot size at  $z=0$ . The width of the near field for a Gaussian beam is simply the width at the  $1/e^2$ . The width of the beam has a real physical meaning, which is actually the width of the beam.

$w(z)$  is distance propagated from the plane of the beam waist, and  $z_0$  is the Rayleigh range.  $z_0$  is expressed by using equation (1.2) below:

$$z_0 = \frac{\pi w_0^2}{\lambda} \quad (1.2)$$

The Rayleigh range  $z_0$  denotes the distance from the origin (location of the beam waist  $w_0$ ) to the point where the beam radius has increased by a factor of  $\sqrt{2}$ .

$$w(z_0) = \sqrt{2} \cdot w_0 \quad (1.3)$$

At distances of  $(z)$  much greater than the Rayleigh range, the Gaussian beam exhibits the behaviour of a spherical wave. The divergence half-angle in the far-field can be calculated for  $z \gg z_0$  as:

$$\theta_0 = \lim_{z \rightarrow \infty} \frac{w(z)}{z} = \frac{w_0}{z_0} = \frac{\lambda}{\pi w_0} \quad (1.4)$$

The full beam divergence for a Gaussian beam is:

$$2\theta_0 = \frac{2\lambda}{\pi w_0} \quad (1.5)$$

We see from the relationship of full beam divergence that the smaller the near field ( $2w_0$ ), the larger the far-field divergence angle.

In the paraxial approximation, the relationship between near field and far-field can be explained, directly from the Fourier optics Goodman (15) as follows:

$$E_{ff}(\theta_x, \theta_y, z) = \frac{i}{\lambda z} e^{-ikz} \iint E_{nf}(x, y) e^{-ik \sin(\theta_x)x} e^{-ik \sin(\theta_y)y} dx dy \quad (1.6)$$

We  $E_{ff}$  and  $E_{nf}$  are the far-field and near-field patterns, respectively, and  $\lambda$  is the wavelength. The far-field is directly proportional to the Fourier transform of the near-field.

The following two simulations represent the near field and the corresponding far-field for the fundamental mode of a waveguide with a width of ( $2w = 2.5 \mu\text{m}$ ).

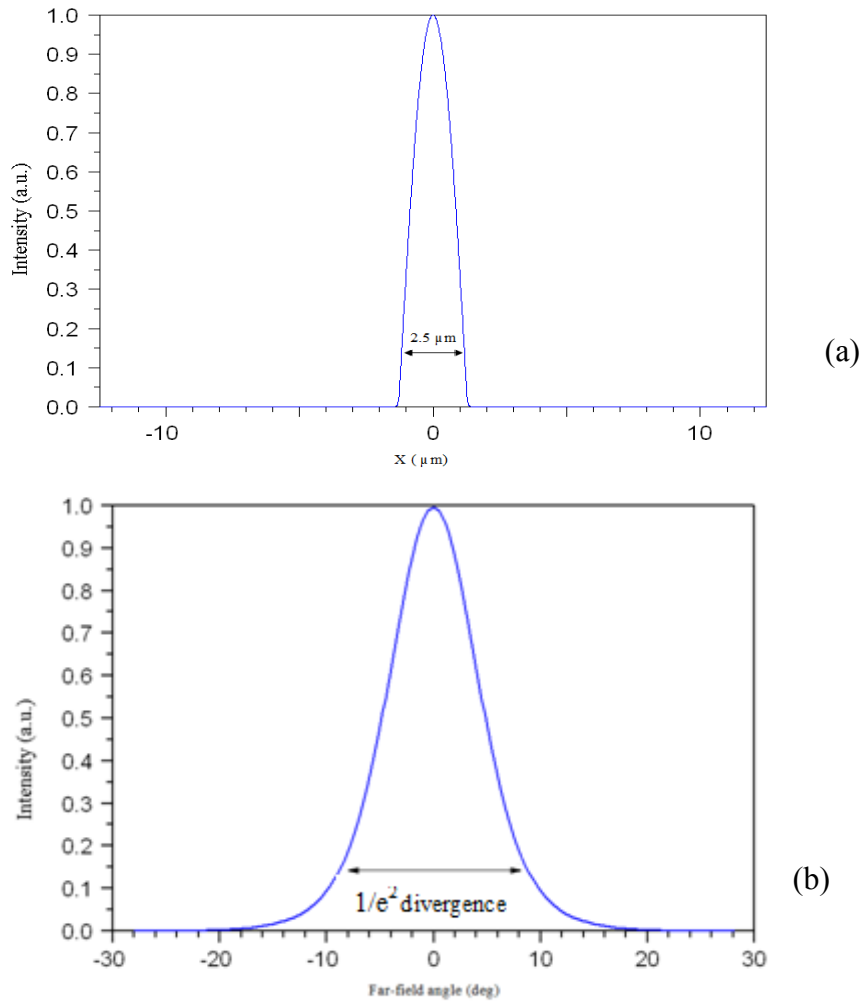


Figure (1.3) (a) BPM simulated near field profile for a  $2.5 \mu\text{m}$  wide ridge waveguide laser for a wavelength of  $830 \text{ nm}$  (b) The corresponding far-field profile.

The beam parameter product (BPP) of an ideal Gaussian beam is the product of the half opening of the angle of the beam  $\theta_0$  and the beam radius  $w_0$ :

$$BPP = \theta_0 w_0 = \frac{\pi}{\lambda} \quad (1.7)$$

In the equation (1.7) above, a cylindrically symmetric (non-astigmatic) beam is assumed. The beam product parameter remains constant when a laser beam propagates in free space and through the media without phase distortion. So, for a Gaussian shaped beam, the minimum focus is physically limited by wavelength. Gaussian beam is also a diffraction limited beam.

A non-diffraction limited laser beam has a factor which is  $M^2$ . This term is used to measure the imperfection in the laser beam, as compared to a diffraction limited beam. The  $M^2$  theoretical value for Gaussian laser beam is 1. The  $M^2$  value for actual laser beam is  $>1$ .

The BPP relationship for real beam in semiconductor laser diode incorporates the  $M^2$  as follows (6, 7, 14):

$$\theta \cdot w_{0r} = \theta_0 w_0 \cdot M^2 \quad (1.8)$$

Using equation (1.4) and (1.7), we can write,

$$\theta = \frac{\lambda}{\pi w_{0r}} \cdot M^2 \quad (1.9)$$

Equation (1.8) is expressed by:

$$M^2 = \frac{\pi w_{0r} \theta}{\lambda} \quad (1.10)$$

Where:  $\theta$  is the divergence angle of a real beam,  $w_{0r}$  is the beam diameter at the waist for the real beam and  $\lambda$  is the wavelength. This  $M^2$  factor specifies how much the beam divergence angle exceeds that of a Gaussian beam. Thus, the  $M^2$  is sometimes called the times-diffraction-limit-factor. There are different methods to measure the beam divergence and the beam width at the beam waist (5, 6, 9). One method utilizes the angle and position, where the intensities of the far-field and the beam waist drop to  $(1/e^2)$  of their maximum value. The full width at half maximum (FWHM) values for far-field and beam waist are sometimes used, but the value of the beam quality factor is optimistic. Another method which is widely accepted for measuring the  $M^2$ , the second moment method (13) is used to measure the beam waist  $w_0$  and the divergence in the far-field. However, this method works only for a good signal to noise ratio. This method was not used in this work.

### 1.4.2 Brightness

The brightness of a light source is defined as the power  $P$  emitted per unit solid angle per unit area (8, 9). The brighter the light source, the more intense the spot to which it can be focused and the further the distance it can be propagated. The brightness of a laser source can be expressed by the total power divided by the product of the mode area at the focus and the solid angle in the far-field. The brightness can be expressed using the following relation:

$$B = \frac{P}{S\Omega} \quad (1.11)$$

Where:  $B$  is the brightness,  $P$  is the optical power in W,  $S$  is the source area in  $\text{cm}^2$  and  $\Omega$  is the unit solid angle in sr.

The brightness ( $B_{DL}$ ) of a Gaussian beam is diffraction limited. It can be expressed by the following relation (9):

$$B_{DL} = \frac{P}{\lambda^2} \quad (1.12)$$

For non diffraction limited beams, the brightness ( $B_{NDL}$ ) is directly related to the beam parameter product ( $M_x^2 \cdot M_y^2$ ). The brightness of the non diffraction limited (7) reads:

$$B_{NDL} = \frac{P}{M_x^2 \cdot M_y^2 \cdot \lambda^2} \quad (1.13)$$

Where:  $M_x^2 \cdot M_y^2$  are the beam quality factors in the x, y directions respectively. Higher brightness is important for many coherent laser applications. The maximum brightness can be achieved, when the radiation pattern is diffraction limited, implying minimum distortion in the amplitude and phase of the laser beam. This distortion is very difficult to avoid at high output powers. Since maximum brightness is attained when the laser beam is diffraction limited, a laser source with this quality can be propagated over a long distance with maximum intensity. The diffraction limit source is easily focused to a small spot with maximum intensity. This feature is particularly important for fibre

coupling, printing, frequency doubling, optical recording, and other application including laser tweezers and scissors.

### **1.5 Applications of high brightness semiconductor laser diode**

830 nm lasers are used for printing applications. For example when an array of many lasers is used for printing specifically in the computer to plate (CtP) printing application. The CtP application uses high power diode lasers, which generate the image by scanning laterally while the plate drum rotates (10, 11). The layout of the thermal plate can be seen in figure (1.4). The laser is focused to a spot using a micro-optics system. Other printing applications include digital presses and labelling.

Laser printers are now widespread. These normally use a single laser or several smaller individually packaged lasers in a large expensive print head. The lasers are fibre coupled inside the print head. This type of print head is no longer cost effective, so monolithic laser arrays are replacing the individual laser inside the laser print head. Because these arrays are monolithic, good alignment is guaranteed (11). Moreover, with good beam quality, there is no need for these laser arrays to be fibre coupled. Instead, using micro-optics features, the laser is focused to directly image the print.

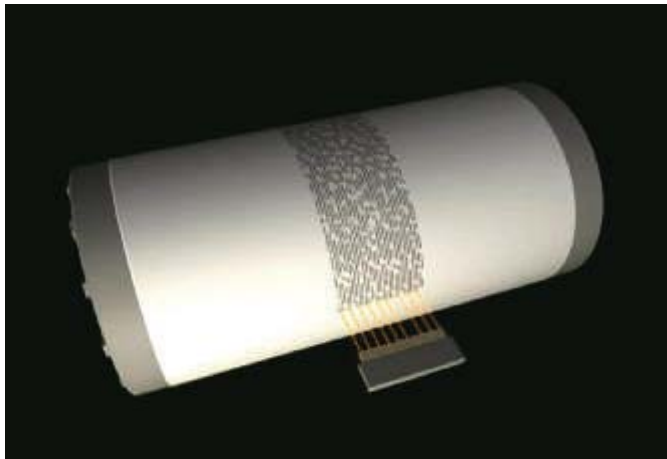


Figure: (1.4) schematic diagram of a laser array module imaging (CtP plate). (Courtesy of Marsh ref. 10)

The other most common applications for high power lasers is as pump sources for solid-state lasers. Other applications that will benefit from high brightness and the diffraction limited beam are in optical storage.

The diffraction limited beam is very important so the beam has smaller divergence, which makes it possible to couple the light into fibres or a waveguides. The additional crucial benefit is that, when the light is coupled into an optical system, it reduces the complexity and the cost of the system. More applications for high power laser diodes include analytical instruments (12) in spectroscopy and interferometry as well as sensor applications.

## 1.6 Thesis Outline

The thesis chapters are organised as follows:

### **Chapter 2: Background and Review of High Brightness Semiconductor Laser Diodes**

In this chapter, high brightness laser diodes are discussed in the context of diffraction limited output, focusing on different types of array laser diode devices with phase locked characteristics. The relationship between the near-field and far-field is discussed, along with the criteria of phase locking for the laser array. This Chapter also includes a brief review of the epitaxial structures used in array laser diodes. The literature on multimode interference array laser diodes is reviewed, with the main focus on high brightness laser operating with a single spatial mode with a single lobed far-field pattern. A survey of single ridge waveguides lasers is provided. This focuses on the beam quality factor  $M^2$ , operating power and the brightness of ridge waveguide lasers.

This chapter also includes a survey of laser diode arrays reported and the different techniques used. The operating characteristics of these arrays are assessed, in terms of the method of phase locking used, the beam quality and the brightness.

### **Chapter 3: High brightness GaAs/AlGaAs material design and characterisation.**

The properties of GaAs/AlGaAs quantum well materials are studied and the issues related to the COMD phenomenon in high power lasers are discussed. This chapter also includes a discussion of the optical properties of such materials with an emphasis on the effects of high power laser operation. Furthermore, the characterization of a broad area laser is included,

demonstrating the material quality and suitability for use in the design of MMI high brightness lasers.

#### **Chapter 4: Device Fabrication and Process Development**

In chapter 4, the device fabrication and process development are presented. This includes the quantum well intermixing technique (QWI), which is also discussed for the experiments carried out. The benefit of the process in the fabrication of integrated high brightness lasers is also discussed. The chapter also includes the assessment of QWI using photoluminescence measurement techniques and the optical loss characterisation of the passive waveguides.

#### **Chapter 5: Device Modelling and Design**

In Chapter 5, the theory of the multimode interference (MMI) coupler is presented. Complete device modelling is given using the beam propagation method. The phase relationship in a  $1 \times N$  MMI array laser is discussed and additional examples of different types of  $1 \times N$  MMI array laser are detailed. Optimisation of the final design parameters will be discussed along with the modelling of the final device parameters.

#### **Chapter 6: Device Results, Characterisation and Discussion**

Chapter 6 documents the results of the characterisation and testing of various designs of multimode array laser diode. This includes a demonstration of a phase locked single spatial mode array laser diode using quantum well intermixing. The phase locking of the array was studied using horizontal and vertical far-field measurements and the operating spectra. The coherence of the laser array was also assessed by measuring the visibility component. Discussion and analysis of the results are also given.

#### **Chapter 7: Conclusion and Further Work**

In Chapter 7, the conclusions and recommend actions for further work are summarised.

# Chapter 2

## Background and Review of High Brightness Semiconductor Laser Diodes

### 2.1 Introduction

Low-cost high-brightness semiconductor lasers play a key role in many applications. This is especially valid for applications that require good beam quality, including free space communications, printing, marking, industrial and medical applications. Improving reliability and broadening the range of wavelengths is crucial for the use of these types of high brightness laser diodes. These devices are ideal for replacing bulkier lasers in various applications because they are very compact, lower cost, easy to cool and achieve a good efficiency.

The current chapter will review the literature for different types of high brightness lasers operating mainly in a single transverse mode. This detailed review provides insight into various designs, and evaluates different approaches in terms of the high brightness laser designs, which should reduce the inherent limitations with these types of devices. The goal is to increase the brightness, and to extend the power achieved from a single ridge waveguide laser without paying a penalty in the quality of the output beam. The output beam quality is of a particular importance, such that the far-field is small enough for effective light coupling. A small far-field results in efficient coupling of light into a fibre, optical system and into another waveguide.

To increase the brightness of the laser diode, a number of limitations have to be overcome. Firstly, the effect of the temperature on the performance of the

high power laser must be reduced. Secondly, facet damage due to the increased intensity at the laser facet must be suppressed. Thirdly, the effect of filamentation must be avoided. In order to overcome these issues, different approaches have been pursued in the past thirty years. The subject of this thesis is a high brightness array laser diode interferometer. The main focus will be on this approach, giving only a general review for the other types of high brightness laser diode operating in a single transverse mode.

## **2.2 Brief History**

The semiconductor laser diode was invented in 1962, and was demonstrated by three groups, almost simultaneously: R. N. Hall 1962 (16), M. I. Nathan (1962) (17) and T. M. Quist (18) using a gallium arsenide pn junction. These first laser diodes were cooled with liquid nitrogen and operated in the pulsed regime. It was not until 1970, that the first hetero-structure laser operating in continuous wave (CW) was demonstrated at room temperature (19). The realization of the high brightness laser was many years away. Advances in a wide range of different technologies were required before it became possible to achieve continuous wave high power operation. For example, these include advances in crystal growth technology (D.F. Welch) (19), quantum well lasers, material passivation technologies and heat-sinking. Laser design improvements such as the single mode laser, tapered lasers and laser arrays contributed to the development of high brightness lasers.

The improvement in crystal growth technology and specifically the development of metal organic chemical vapour deposition (MOCVD) and molecular beam epitaxy (MBE) technologies gave the ability to control uniform material growth on the atomic scale. Thus, very thin layers (quantum wells) could be grown. Utilisation of these technologies resulted in a reduction in the threshold current and achieving higher power. Reduction in the threshold current is very significant, because it means a reduction in the spontaneous emission, non radiative recombination, leakage current. As a result, less heat is generated and an increase in the laser diode efficiency is achieved. The quantum well laser has many advantages over the simpler double hetero-structure laser. One of the important parameters is a threshold current density reduction. Inspection of figure (2.1) shows that the threshold

current density was as high as  $10^5$  A/cm<sup>2</sup> for first homojunction laser in 1962, while as low as 50 A/cm<sup>2</sup> (21, 22) has been reported for a GaInAs/GaAlAs strained quantum well laser. Furthermore, a reduction in the free carrier loss, lower temperature sensitivity with increased current injection, and improved overall efficiency of the laser diode is achieved by using a quantum well structure (20). The use of a QW also reduces the impact of carrier-induced changes due to the reduced optical confinement factor (39).

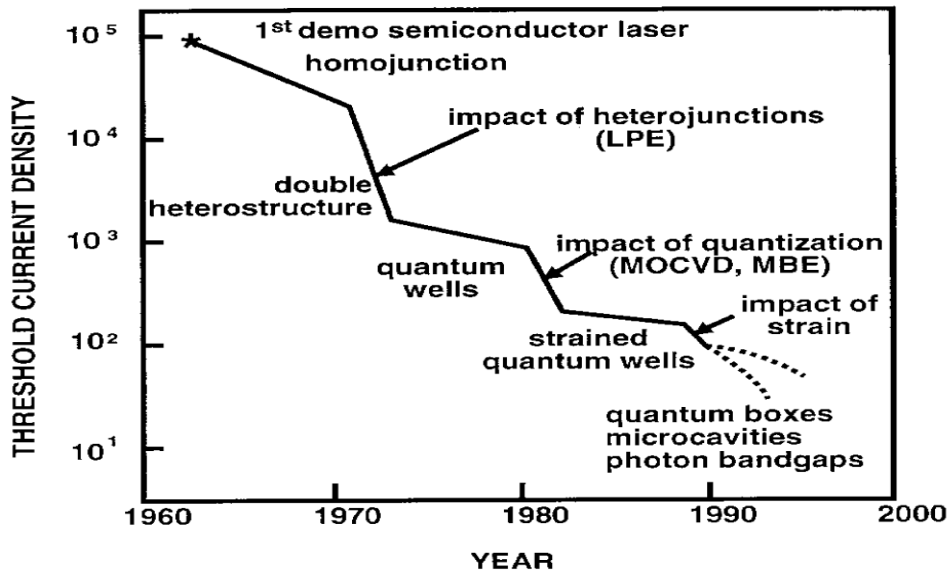


Figure (2.1) The evolution of threshold current density of semiconductor laser. (Courtesy from reference 21)

The laser threshold current for homojunction lasers was as high as  $10^5$  A/cm<sup>2</sup>, because of the simplicity of the GaAs p-n junction used in those days. As a result of poor carrier and photon confinement in such junctions, the waveguiding is not very efficient, and only allows laser action at the expense of vigorous pumping of current (23). Furthermore, the carriers leak away causing very high loss. To circumvent this problem, a double hetero-structure is used. It allows a reduction of the threshold current density through improved carrier and photon confinement. The double heterostructure was used in the form of a layer of GaAs sandwiched between two layers of the ternary compound Al<sub>x</sub>Ga<sub>1-x</sub>As. The two layers have wider energy bandgaps that create potential barriers in both conduction and valence bands. The barriers prevent electrons and holes injected into the GaAs layer from diffusing away. These same layers have a lower refractive index than the GaAs layer, because of their higher band gap energy. The two layers provide vertical confinement both for the electrons injected in the active region and for the photons generated in it.

The concept of carrier and photon confinement for double heterostructure laser is illustrated in figure (2.2) above from (23). Because of this carrier and photon confinement in the double heterostructure laser, the lasing action is confined effectively to the active region (GaAs layer). As a consequence, the

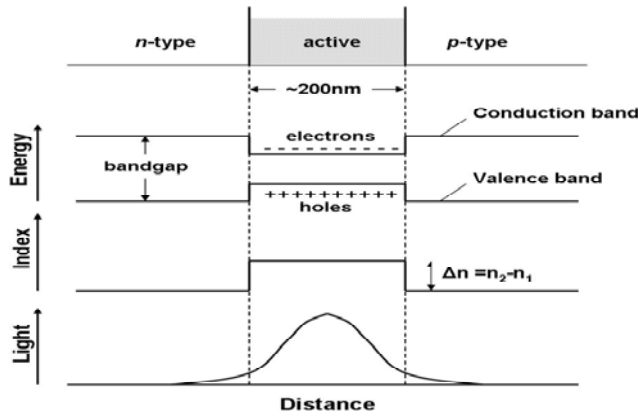


Figure 2.2: Confinement of electrons and photons in a double heterostructure (23)

losses are considerably lower than that for the homojunction structure allowing a threshold current density in the  $\text{KA/cm}^2$  range to be achieved (22). The use of the bulk materials for the active region of heterostructure lasers blocked further improvement in the threshold current. Further reduction in the threshold current density was achieved through the use of quantum wells. The main mechanism by which the use of a QW active region reduces the lasing threshold is simply a reduction in the volume of the gain material (38, 39).

It has been predicted since 1970s that reducing the dimensionality of the active region can enhance the laser performance (25). Restriction of the carrier motion in the direction perpendicular to the QW plane produces a stair-like density of states. This leads to more efficient devices operation at lower threshold currents compared to bulk active-region. The schematic in figure (2.3) illustrates (ref 21) the difference between the gain formation in 3D bulk DH active material (top of the figure 2.3) and in 2D QW material. The transparency current is diminished due to firstly, the use of a QW and double heterostructure, which allowed separate confinement of the electrons and photons, so that the electronically pumped gain region could be reduced further (21) and secondly the smaller density of states in 2D. As a result of the square density of the states, a given number of injected carriers are more efficient to create gain in 2D QW. This corresponds into a steeper gain current curve.

It was not possible to deposit thin films of good quality until the crystal growth techniques (MOCVD, MBE) were developed well enough even-though

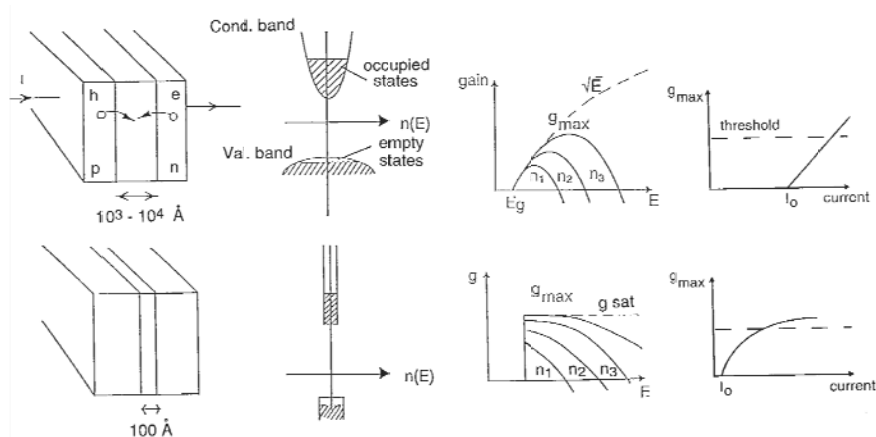


Figure (2.3) schematic shows the difference of the gain in bulk DH semiconductor material (top) and in 2D QW material. (Ref 21)

QW lasers were demonstrated earlier in 1975 and 1977 (27, 28), respectively. The superior quality thin films allowed the full potential of QW lasers to be realized. Further improvements in the quantum well design were achieved. These include reducing the doping of the layers around the active region and using a graded index separate confinement hetero-structure (GRINSCH). Such improvements made it possible for Tsang to produce a laser with  $J_{th}$  as low as  $160 \text{ A/cm}^2$  (28). This value of  $J_{th}$  is lower than that of bulk heterostructure lasers with a typical ( $J_{th} > 500 \text{ A/cm}^2$ ) (29–31). A very low value of  $J_{th}$  of  $50 \text{ A/cm}^2$  was achieved (22) through the use of strained QWs.

Nowadays, it is possible to develop efficient semiconductor laser devices that can be fabricated to be several millimeters in length. However, the output power and efficiency can only be increased if the internal loss  $\alpha_i$  is remained small enough, normally  $< 2 \text{ cm}^{-1}$ . Longer devices are also essential for reducing the heat dissipation of the laser diode, and thus achieving high power operational before thermal roll over.

### 2.3 Factors Restricting Brightness and Output Power of Diode Lasers

There are four main limitations for high brightness laser diodes operating in a single spatial mode. These limitations are as follows:

1. Catastrophic optical mirror damage.
2. Spatial mode instability.
3. Thermal issues.

#### 4. Long term aging.

In the next sections, we briefly talk about these effects in the context of a high power single spatial mode laser.

### 2.3.1 Catastrophic Optical Mirror Damage.

Catastrophic optical mirror damage (COMD) is one of the limitations of high brightness lasers, whereby the semiconductor laser facet suffers irreversible damage due to thermal run away at the facet. The increase in the facet temperature with respect to the bulk semiconductor leads to a decrease of the local band gap energy and an increase in the optical absorption at the facet (32). Recent studies (33) have indicated that the COMD occurs due to thermal flash or thermal runaway, which was detected by thermal imaging. Furthermore, the temperature measurement during the COMD was equivalent to 627 ° C. This phenomenon is accompanied by a sudden drop in the optical power, which is irreversible unlike thermal roll over. Figure (2.4a) illustrates the LI curves for an ideal laser, where the power increases linearly with current.

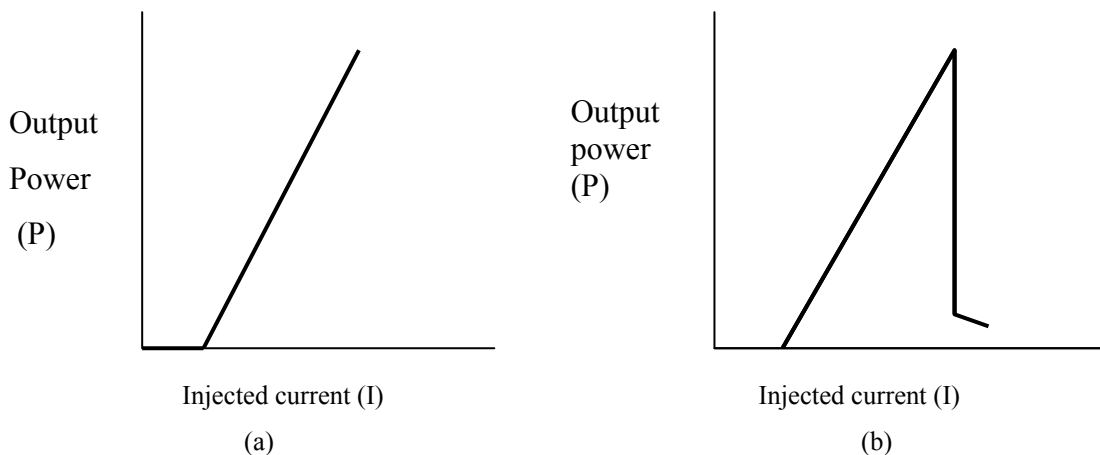


Figure (2.4) (a) LI curve for ideal laser. (b) LI curve for a laser post COMD

Figure 2.4b shows the LI curve for a semiconductor laser undergoing COMD, where the laser suffers an abrupt loss of power, which is irreversible and the facet is damaged. Advances in facet coating processes, laser waveguide design and the introduction of band gap widening at the facets for the semiconductor devices for the implementation of non-absorbing mirrors (34) have made it possible to almost eliminate the problem of COMD. A study by M. Silver (2005) (35) confirmed that using non-absorbing mirrors not only increased the COMD level, but could actually eliminate it. He also reported that the magnitude of the wavelength shift due to intermixing affects the COMD power level.

### **2.3.2 Spatial Mode Instability**

The spatial mode instability is very important issue for high brightness lasers. The evidence for this instability is a kink in the light current output characteristic for the semiconductor laser. There can be additional kinks appearing in the LI curves, which are attributed to the lasing of higher order modes (36). The lateral mode instability is more prominent in broad area lasers, where there is strong interaction between different parameters like the optical field, carrier density profile, gain/loss, temperature profile and the refractive index. All these parameters are interlinked.

Ridge waveguide lasers which are index guided, demonstrate better mode stability and the kinks appear at much higher drive currents than for broad area lasers. In ridge waveguide laser devices, the built-in refractive index compensates for the index change due carrier density changes. Therefore, ridge waveguide lasers are much more stable than broad area lasers. The stability of the transverse mode can be enhanced if a buried heterostructure is used. This stability is attained through the design of the active region, which is completely buried within a higher-bandgap lower-index semiconductor material. This arrangement produces an optical waveguide geometry (index-guided lasers) that has excellent simultaneous current, carrier and optical confinement (37, 38). It must be indicated that the buried layer, can be also be a lower-bandgap higher-index material, that utilises the anti-guiding effect. This results in a stable single lateral mode. Furthermore, a good thermal conductivity of the buried layer can improve the dissipation of heat that is produced during semiconductor laser device operation. The buried layer is realized through semi-insulating re-growth of a material that is lattice matched to the laser structure around the etched laser mesas.

### **2.3.3 Thermal stability**

The thermal issues associated with high power operation of a single stripe laser and an array laser diode are very important factor that must be taken into account in the design. The heat generated by non-radiative recombination of the carriers in the active layer of the semiconductor laser is one of the sources for the laser heating (39, 50). Additional sources of generating heat in the semiconductor laser are the electrical resistance of the epitaxial layers, the metal contacts and absorption of the spontaneous emission in the cladding

layers. The effect of the temperature on the laser diode characteristics is quite substantial. It manifests itself as a decrease of the band gap energy and an increase in the non-radiative recombination rate. These effects result in a rise in the threshold current density and a reduction in both the gain and internal quantum efficiency.

In GaAs/AlGaAs quantum well lasers, the rise in the threshold current can be due to the inefficient electron capture process. This QW electron capture process is LO-phonon induced and carrier-carrier scattering induced (40, 41). It was also revealed by P. Blom *et. al.*, (40, 41) that the predicted QW structure parameters for optimum capture efficiency are equivalent to these scattering processes. Furthermore, the capture processes enhance the cooling of the carriers after injection, leading to a reduction of the carrier temperature, and thus a low threshold current is achieved (40,41).

### 2.3.3.1 Effect of the leakage

During the thermal rollover, when the injection current is increased beyond a certain level, the charge carriers spillage out of the active region into the cladding layers start to increase. As a consequence, they cannot contribute to simulated radiative recombination. This increased leakage of carriers leads to a reduced optical output accompanied by a rise of the active region temperature. The leakage current is calculated using the following relation taken from (42,43,129):

$$J_{leakage} = \frac{eD_n n^+}{I_n \tanh\left(\frac{S}{L_n}\right)} \quad (2.1)$$

where  $J_{leakage}$  is the leakage current density in the P-region.  $L_n$  and  $D_n$  are the electron electron diffusion length and the electron diffusion coefficient, respectively.  $D_n$  is calculated using the Einstein relation ( $D_n = \frac{\mu_n kT}{e}$ ).  $\mu_n$  is the electron mobility.  $K$  is the temperature,  $e$  is the electron charge,  $n^+$  is the excess electron concentration at the edge of the p-cladding and depends on the electron density injected in the active layer.  $I_n$  is the electron diffusion current and  $S$  is the distance from the edge of the p-cladding to the p-GaAs contact layer. The leakage current leads to an increment in the current required to reach to the threshold. Furthermore, the whole process of the leakage current

leads to a thermal rollover phenomenon, that is illustrated in the figure (2.5) below.

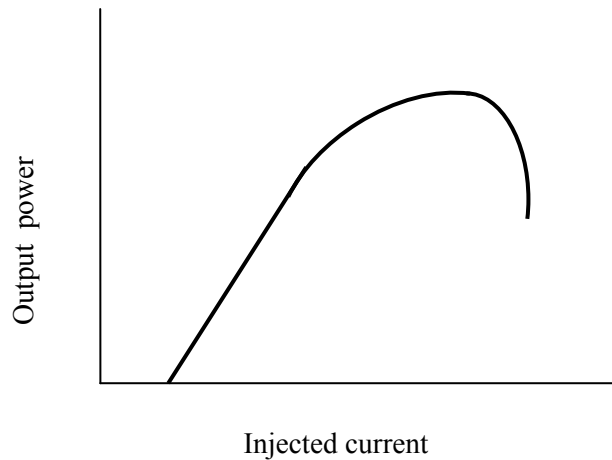


Figure (2.5) thermal rollover of laser diode.

The equation (2.1) describes a simplified leakage model. Precise estimation of the leakage current density in a semiconductor laser must include the amount of leakage for both holes and electrons.

### 2.3.3.2 Laser mounting and packaging

In a high brightness laser, the amount of heat generated in the device depends on the thermal resistance  $R_{th}$ , which can be expressed by equation (2.2):

$$R_{thermal} = \frac{\Delta T}{P_{elec} - P_{optical}} \quad (2.2)$$

where  $P_{elec}$  is the electrical input power,  $P_{optical}$  is the optical output power and  $\Delta T$  is the active region change in temperature due to radiative and non radiative processes in the laser device.

The thermal resistance can be influenced by the geometry of the laser device, and on the individual epitaxial layers. It is also dependent on mounting and the packaging, which are crucial for high brightness lasers. Certain criteria must be followed during mounting and packaging of the laser device. These criteria include (45):

- [1] The laser diode must be attached to a heat sink or heat spreader. The chip must be attached optimally for efficient heat transfer through the thermal interface. Furthermore, a thin void-free bonding interface is required to create an effective heat dissipation channel through the die attachment.
- [2] Heat dissipation is directly influenced by thermal resistance, which should be calculated to evaluate the thermal design. To improve the thermal design of the laser diode package, the thermal resistance must be minimized through: attachment of the heat source to the heat sink as intimately as possible, making the interface as thin as possible and increasing the thermal conductivity of the material.
- [3] There are two main bonding configurations epi-side up and epi-side down. The epi-side down configuration is recommended (46, 47), because of the proximity of the active region to the top of the heat sink. As a result, efficient heat transfer occurs. The thermal resistance of the laser diode is inversely proportional to the ridge width for epi-side bonded approach (48). It has been also reported that the thermal resistance of the epi-side down configuration is 30% lower than the epi-side up approach (49). There are on the other hand constraints with epi-side down approach, namely, the stress that causes physical distortion to the device due to the mismatch in the coefficient of thermal expansion. Efficient heat dissipation results in increased laser optical output power and improved spectral and spatial characteristics. Heat accumulation in the active region of laser diode causes longitudinal mode broadening (50).
- [4] Selection of the heat sink material is very important in a diode laser package. Material like copper is a common heat sink material that has good thermal conductivity which should be used. Heat sink by means of conduction alone is insufficient to remove all the heat flux generated to keep the operating temperature of the laser device package as low as possible. In high brightness, laser where the thermal power density is high, the heat sink material temperature can be further decreased with state of the art micro-channel heat sink cooling (51,52).
- The solder material selection is also quite important, It must have properties that include; low electrical resistivity to reduce the Joule heating at high current injection, exhibit low deformation during long term

operation, and provide an efficient heat dissipation channel to the heat sink. Its should also reduce thermally induced stresses arise from a CTE mismatch between the laser diode and the heat sink.

### 2.3.3.3 Characteristic temperature ( $T_0$ )

The temperature dependence of the threshold current is characterised by the characteristic temperature ( $T_0$ ) which is defined by equation (2.3) from Ref (42).

$$I_{th}(T + \Delta T) = I_{th}(T)e^{\left(\frac{\Delta T}{T_0}\right)} \quad (2.3)$$

Where,  $I_{th}(T)$  is the threshold current at temperature  $T$ ;  $I_{th}(T + \Delta T)$  is the threshold current at temperature  $(T + \Delta T)$ ; and  $T_0$  is the characteristic temperature of the laser.

$T_0$  is related to carrier leakage across the hetero-junction barrier in a semiconductor laser diode and to the thermal loss due to Auger recombination.  $T_0$  is influenced by many other factors depending on the actual configuration of the active region and the cavity length. The value of  $T_0$  for a single quantum well laser (SQW) is lower than that for a multi-quantum well laser (42), but the value of  $T_0$  is higher for longer laser devices than for shorter ones (42,43). The reason for that is the influence of increased leakage in SQW and shorter devices (42), whereby shorter devices require higher gain, which means higher carrier density. Thus, they are pumped harder to reach threshold. Furthermore,  $T_0$  depends on the potential barrier height. This barrier potential itself influences the leakage rates (44). The well width and the emission wavelength are the other important factors that affect  $T_0$  (43).

The higher the value of  $T_0$ , the less sensitive the device is to temperature increases. Thus,  $T_0$  is the key to measure of the temperature stability of the device. To conclude, the characteristic temperature ( $T_0$ ) is a strong function of the semiconductor laser active region and the design of the epitaxial structure.

### 2.3.4 Degradation of the Laser Diode with Aging

The aging of a semiconductor laser is a very important issue for both single stripe and array laser diodes. The long term reliability has to be tested for any laser diode product. GaAs /AlGaAs laser diodes have a few dominant failure modes causing power degradation with time. Therefore, many laser diode

manufacturers put a limit on the percentage of the reduction in optical power when performing reliability testing. GaAs/AlGaAs laser diodes do suffer from failure due to defect propagation inside the active region (105). In recent years, GaAs/AlGaAs type devices use with an InGaAs quantum well active regions. Active regions containing Indium are known to be robust against failure due to defect propagation in the active region (19, 105). Other failure modes include degradation of the COMD power level with time. Other important factors influencing the reliability are the epitaxial material defect density, the packaging and mounting technology. We have seen from the previous section, the importance of the packaging and mounting in reducing the thermal resistance of the material. This also decreases the operating temperature of the laser diode. Consequently, the reliability of the laser increases through the reduction of the thermal activation energy in the active region (105), thus, improving the operating life of the device. For more information on the laser device reliability, a book by Mitsuo Fukuda (1991) (105) is an excellent source of detailed information on the subject.

## 2.4 High brightness semiconductor lasers array

This section introduces the array supermode theory and reviews the literature on high brightness lasers. Different types and configurations of laser diode will be discussed in the context of high brightness lasers with a single lateral mode. We explore the array laser theory supermode concept as well as other designs that achieve high brightness, including their epitaxial design.

### 2.4.1 Arrays Supermode theory

#### 2.4.1.1 Diffraction model

The far-field intensity distribution  $I(\theta_x, \theta_y)$  can be derived using the Fresnel-Kirchhoff diffraction integral. In one dimension, the relation can be expressed by the following :

$$I(\theta_x) \propto \cos^2(\theta_x) \left| \int_{-\infty}^{\infty} E(x) \cdot \exp(ik_0 \sin\theta_x x) dx \right|^2 \quad (2.4)$$

$$I(\theta_y) \propto \cos^2(\theta_y) \left| \int_{-\infty}^{\infty} E(y) \cdot \exp(ik_0 \sin\theta_y y) dy \right|^2 \quad (2.5)$$

In a simple diffraction model , the emitters of an array can be approximated by a grating where N represents the number of emitters of the array. The far-field

distribution  $I(\theta_x)$  of the array, which is derived from the equation, can be written as follows (56):

$$I(\theta_x) = |E(\theta_x)|^2 \cdot A(\theta_x) \quad (2.6)$$

The far-field amplitude for one of the emitters is  $E(\theta_x)$ , and the function  $A(\theta_x)$  represents the array and the interference of the coupled emitters of the array. In the case of simple diffraction, this reads (56):

$$A(\theta_x) = A(u) = \frac{\sin^2\left(\frac{N \cdot u}{2}\right)}{\sin^2\left(\frac{u}{2}\right)} \quad (2.7)$$

where  $u = k_0 \cdot p \cdot \sin\theta$ ,  $k_0 = 2\pi/\lambda$ , where  $\lambda$  is the free space wavelength and  $p$  is the pitch between the emitters. This represents diffraction through a grating with  $N$  emitters, which is actually a sinc function.

Depending on the phase relationship between the emitters, constructive or destructive interference at certain far-field angles will be present. This can be expressed by introducing a phase shift term  $\Delta\phi$ , so the equation (2.7) adjusts to (55):

$$A(\theta_x) = A(u) = \frac{\sin^2\left[\frac{N}{2}(u + \Delta\phi)\right]}{\sin^2\left[\frac{u + \Delta\phi}{2}\right]} \quad (2.8)$$

If out-of-phase or an in-phase oscillation between neighboring emitters is assumed, the phase difference between adjacent emitters is  $m\pi$ . Here,  $m$  is the diffraction order giving in-phase oscillation for even numbers and out-of-phase oscillation for odd numbers.

### 2.4.1.2 Coupled mode theory approach

In coherent beam combining, semiconductor laser arrays are usually designed such that the coupling between the emitters results in global coupling of all the emitters. The array should operate in this case, in one supermode that characterises the emission of all the coupled emitters.

The coupled mode formalism is adopted for the optical field profile for  $N$  transverse modes. In the previous section, a simple diffraction theory model was discussed for the analysis of  $N$  coupled emitters. However, in this section we concentrate on coupled mode theory.

In the case of a coupled array of emitters that consists of  $N$  coupled single-mode laser diodes, as in the figure below (2.6),  $N$  number of modes oscillate corresponding to  $N$  intensity profiles and different phases. The emitters are equally spaced along the  $x$ -axis with a pitch of  $p$ . The Gaussian mode profile of each emitter is characterised by full width at  $1/e^2$  of  $2w$ .

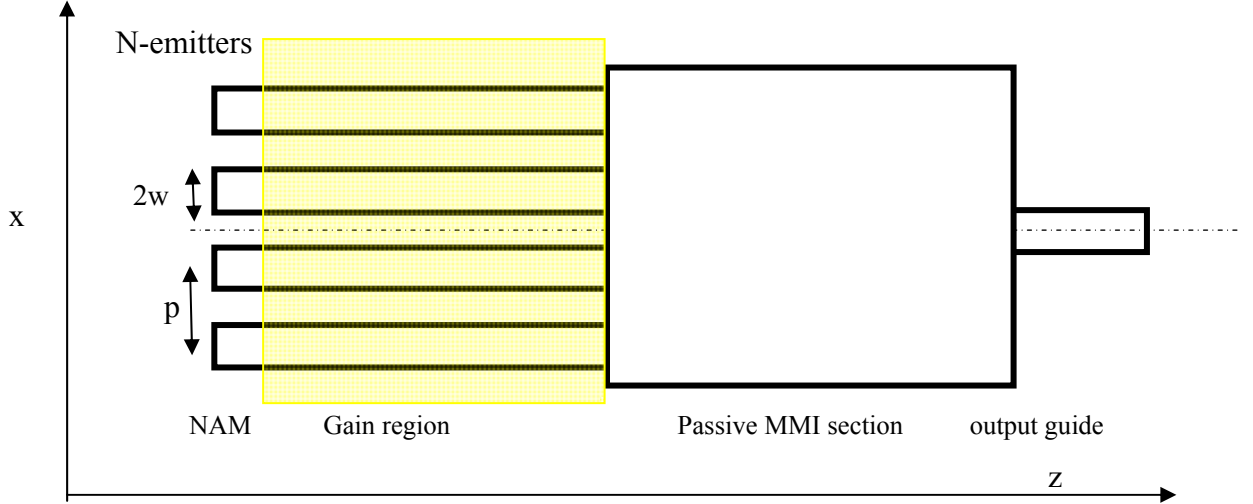


Figure (2.6) scheme for  $N$  coupled array emitters that are integrated with NAMs and MMI cavity and output waveguide. The emitters have a pitch  $p$ , the transverse mode profile is characterised by full width at  $1/e^2$  of  $2w$ .

The profile of these supermodes depends on the type of coupling between the transmitters. In the case, where the coupling is a nearest neighbour coupling type, the optical near field profile  $L_{th}$  mode of the  $N$  eigenmodes of  $N$  Gaussian emitters can be expressed using the following equation (55, 56, 68):

$$E_L(x, z = 0) = \sum_{n=1}^N \sin\left(\frac{L\pi}{N+1}n\right) * \exp\left(\frac{-(x + \frac{(N+1-n)p}{2})^2}{w^2}\right), \quad 1 \leq L \leq N$$

We assume that transmitters have a Gaussian profile of full width at  $1/e^2$  of  $2w$ , and that they are separated by a pitch  $p$ . The origin,  $x = 0$ , is located in the center.

The supermode with  $n=1$  is called the in phase mode, the supermode with  $n=N$  which is the highest order mode, is the out of phase mode. The highest order mode has a  $\pi$  phase shift between adjacent emitters. The intensity distribution of the far-field for array modes can be expressed by (55, 56, 68) the following relation:

$$I_L(\theta) \propto e^{-\frac{2\pi^2 w^2 (\sin(\theta))^2}{\lambda^2}} \left[ \frac{\sin\left(\frac{N}{2} \left(\frac{2\pi p}{\lambda} \sin(\theta) + \frac{L\pi}{N+1}\right)\right)}{\sin\left(\frac{1}{2} \left(\frac{2\pi p}{\lambda} \sin(\theta) + \frac{L\pi}{N+1}\right)\right)} - (-1)^L \frac{\sin\left(\frac{N}{2} \left(\frac{2\pi p}{\lambda} \sin(\theta) - \frac{L\pi}{N+1}\right)\right)}{\sin\left(\frac{1}{2} \left(\frac{2\pi p}{\lambda} \sin(\theta) - \frac{L\pi}{N+1}\right)\right)} \right]^2$$

The far-field profiles consist of narrow peaks spaced by  $\frac{\lambda}{p}$ , with a full width half maximum (FWHM) width  $\frac{\lambda}{N.p}$  within the envelope of the far-field pattern of the individual emitters. The number of the peaks depends on the filling factor of  $2w/p$  of the array laser.

### 2.4.1.3 Importance of coherent laser diode arrays

There are different techniques which have been used to improve the brightness of semiconductor lasers. In order to achieve high brightness for the whole array laser bar, coherent operation is required. The far-field distribution of a fully coherent semiconductor laser array should show a dominant single lobed output beam in the lateral direction along with secondary lobes. The number of the lobes depends on the number of coupled emitters and the separation distance between the emitters. The dominant single lobe for a coherent array laser has a far-field divergence, which is equivalent to the diffraction limited divergence that can be measured using the following relation (68):

$$\theta = \frac{\lambda}{N.p}$$

where,  $\theta$  is the far-field diversion angle at FWHM,  $p$  is the separation distance between the emitters ( $p$  is measured from the centre to centre),  $N$  is the number of the coupled emitters and  $\lambda$  is the operating wavelength. The angular separation between adjacent lobes in the far-field of the coherent array is equal to  $\left(\frac{\lambda}{p}\right)$ . The beam quality parameter  $M^2$  of a coherent array should be close to 1.

In case of an incoherent array, the far-field is as wide as the far-field of single emitter. Furthermore, the emitters of the free running array are not optically coupled with each other. As a result, the beam quality parameter  $M^2$  is at least equal to  $N$  times the single emitter value.

To illustrate the concept, we use figure (2.7) below, which shows a BPM simulation of a 1x6 MMI with emitter pitch  $p=6\ \mu\text{m}$ ,  $N=6$ ,  $2w=2.5\ \mu\text{m}$ , MMI width  $=30\ \mu\text{m}$  and a length of  $979\ \mu\text{m}$ .

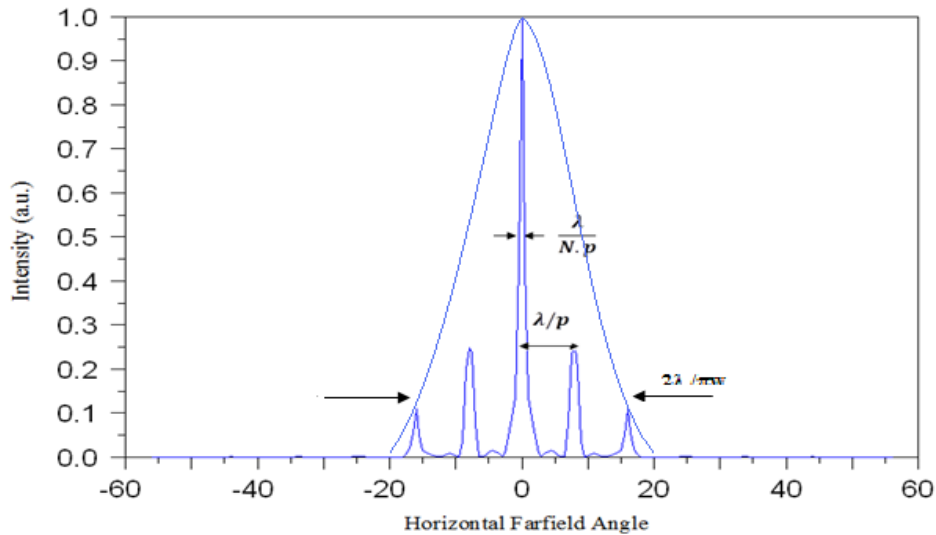


Figure (2.7) BPM simulation of lateral far-field pattern for 1x6 MMI array with dimensions of:  $p=6\ \mu\text{m}$ ,  $N=6$ ,  $2w=2.5\ \mu\text{m}$ ,  $\lambda=0.83\ \mu\text{m}$ , MMI width  $=30\ \mu\text{m}$  and MMI length of  $979\ \mu\text{m}$ . The fill factor ( $f$ ) in this example is 41.6 %.

The simulation (2.7) illustrates the phase locked lateral far-field profile of a 1x6 MMI array structure, with the following features:

1) The FWHM of the central peak is :

$$\theta = \frac{\lambda}{N \cdot p}$$

$=0.83/6 \cdot 6 = 23.05$  milli-radians  $= 1.32^\circ$ , which is the diffraction limited beam ( for the example above, as simulated by BPM).

2) The separation of the peaks of the peaks is  $\frac{\lambda}{p} = 0.83/6 = 7.92^\circ$ .

3) We also notice that the  $1/e^2$  value of  $(2\lambda/\pi w)$  is equivalent to the divergence of single emitter with a Gaussian profile.

4) The number of peaks depends on the fill factor between the emitters. The fill factor for figure (2.7) above is:

$$f = \frac{\text{width of single emitter}}{\text{emitter separation}} = 2.5 / 6 = 0.41 \text{ which is } (41.6 \%).$$

If the parameters of the array are changed, a different far-field pattern is acquired. To explain what happens, the simulation of a 1x4 MMI array

structure is performed for a very large MMI width of 50  $\mu\text{m}$ , centre to centre spacing ( $p$ ) of 12.46  $\mu\text{m}$  and  $N=4$ , as in figure (2.8).

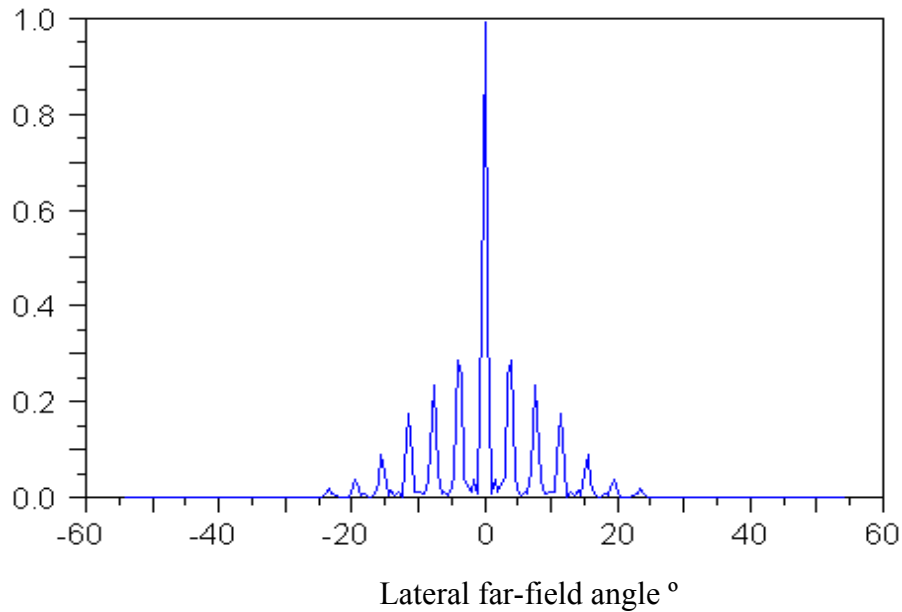


Figure (2.8) BPM simulation of a lateral far-field pattern for 1x4 MMI with dimensions of:  $p=12.46 \mu\text{m}$  ( measured from the centre to centre ),  $N=4$ ,  $2w=2.5 \mu\text{m}$ ,  $\lambda=0.83 \mu\text{m}$ , MMI width = 50  $\mu\text{m}$  and an MMI length of 2770  $\mu\text{m}$ . The fill factor ( $f$ ) in this example is 20 %.

Figure (2.8) illustrates the phase locked lateral far-field profile of a 1x4 MMI array structure for a very large MMI width of 50  $\mu\text{m}$ . The 50  $\mu\text{m}$  wide MMI is a direct consequence of using a larger pitch of 12.46  $\mu\text{m}$ . In the previous example, the pitch was 6  $\mu\text{m}$ . The correct MMI length for 1x4 MMI coupler is 2770  $\mu\text{m}$ . If we examine the characteristics for a phase locked 1x4 MMI array, we notice that:

- 1) The FWHM of the central peak is:  $\theta = \frac{\lambda}{N.p} = 0.83/4*12.46 = 16.65$  milliradians, which is a  $0.95^\circ$  for a diffraction limited beam.
- 2) The separation of the peaks is  $\frac{\lambda}{p} = 0.83/12.46 = 3.81^\circ$ , we notice that increasing the pitch (centre to centre) reduces the angular peak separation to less than half.
- 3) We also notice that the  $1/e^2$  value of  $(2\lambda/\pi w)$  is equivalent to the divergence of single emitter with a Gaussian profile.
- 4) The number of peaks depends on the fill factor between the emitters. The fill factor for figure (2.8) above is:

$$\text{Fill factor (f)} = \frac{\text{width of single emitter}}{\text{emitter separation}} = 2.5 / 12.46 = 0.2 \text{ (20 \%)}.$$

5) The visibility term which is the measure of the coherence of the beam can be estimated from the far-field pattern. The maxima and minima around the central peak are used. From far-field pattern in figure (2.8):

$$V = \frac{I_{max} - I_{min}}{I_{max} + I_{min}},$$

We approximately estimated the visibility pattern to be:

$V = (0.98 - 0.03) / (0.98 + 0.03) = 0.94$  so the visibility is 0.94. This must be measured from the far-field pattern for a 1x4 MMI real laser.

#### **2.4.1.4 Characterization criteria for coherence in the laser array**

The far-field of the laser diode array depends on the geometry of emitters. The number of interfering peaks depend on the filling factor. The filling factor as indicated in the previous section is:

$$f = \frac{\text{width of single emitter}}{\text{emitter separation}}$$

In order to characterize the results from different devices, one must quantify the criteria for phase locked operation of the laser array that results in a narrow single lobe, which contains the majority of the power. In this case, the divergence of the laser array is greatly reduced. In practice, several contributions can degrade the far-field profile, whereby the laser power could be distributed to several peaks. The characterization criteria for phase locked operation are illustrated in figure (2.9) (67,68,71). (The figure represents a simulation of a 1x2 MMI array laser, that is taken from chapter 5 of this thesis). To quantify the phase locking in an array of lasers, one should take into consideration the following:

1. The quality factor of the single emitter is  $M^2 = \Delta\theta \frac{\pi w}{\lambda}$ , which characterizes the envelope width with respect to the theoretical one,  $\Delta\theta$  is the half width of the far-field envelope at  $1/e^2$ ,  $w$  is the half width of the emitter and  $\lambda$  is the operating wavelength.
2. The quality factor of the bar is  $M^2 = 2\delta\theta \frac{Np}{\lambda}$ , where  $2\delta\theta$  is the total width of the central peak, this quantity can be considered as a quality factor for the bar. The width of the central peak is compared with the diffraction limit for the bar and the number of the emitters is also included.

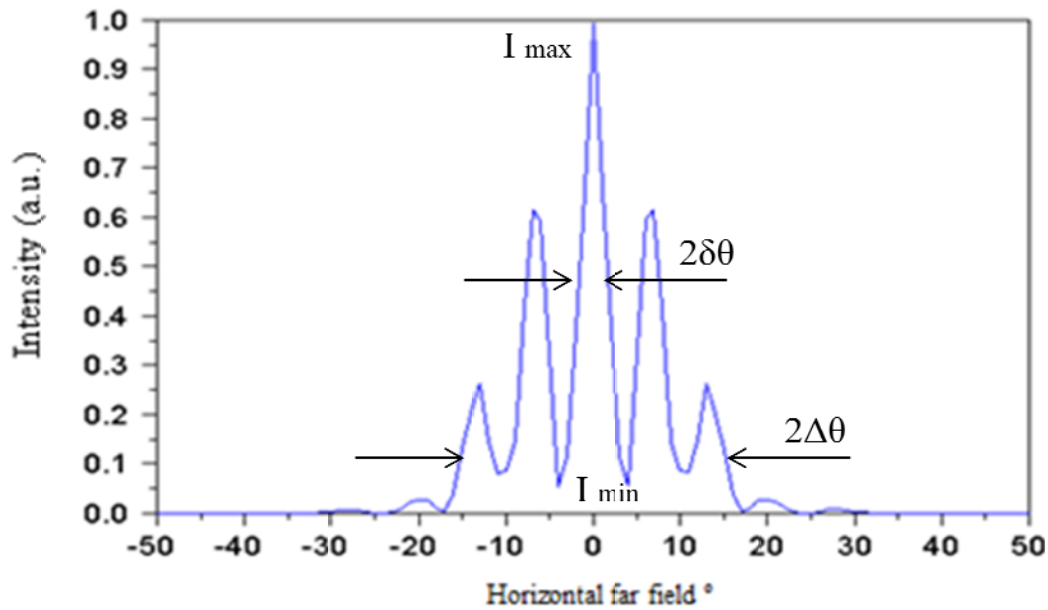


Figure (2.9) Definition of parameters characterizing the far-field for a phase locked 1x2 MM laser array.

3. The third criterion to assess the coherent array is by practical measurement of the degree of coherence. The visibility ( $V$ ), which quantifies the coherence of the beam is calculated using the following relation;

$$V = \frac{I_{max} - I_{min}}{I_{max} + I_{min}}$$

where,  $I_{max}$  and  $I_{min}$  are the maximum and the minimum intensities of the interference around the central peak.

4. The spectrum of the coherent beam results in a very narrow spectral linewidth  $\ll 1\text{nm}$ . All the emitters of a coherent beam should oscillate at the same wavelength.

### 2.4.2 Coherent high brightness laser diode arrays

There has been a desire for high output power diode lasers since the beginning of the 1970s. The need to overcome the limitation of catastrophic optical mirror damage led researchers to develop other ideas for achieving the required power. The idea developed to use laser arrays to increase the output power of the laser diode to overcome the COMD limitation of a single emitter. Placing several lasers in parallel with each other seemed a good idea, so the effort was made to obtain phase locked semiconductor laser arrays operating in a stable single spatial mode. The task of obtaining a coherent semiconductor

laser array has been proven to be very challenging. A number of different designs have been pursued in order to obtain phase locked operation and improve the brightness of the laser beam. There are different designs that have been reported including: coherent monolithic laser arrays (edge emitting devices) and non-monolithic laser array that incorporate an external cavity. The monolithic laser arrays use different coupling techniques that include: evanescent lateral coupling (57,60,83), beam splitting coupled arrays (58), diffraction coupled semiconductor laser arrays (59,85,99) and anti-guide coupling (79). Non-monolithic semiconductor laser arrays utilise an external cavity for phase locking that result in the highest brightness laser with high beam quality (near diffraction limited beam). Different external cavity approaches have been reported. These include: Talbot cavity (62,63,64), self-Fourier cavity (62), external cavity with phase grating (66, 67) and filtering angle in the Fourier plane (69,70). In the forthcoming section, a review of the different types of monolithic array laser diode will be discussed along with each of the lateral coupling mechanisms involved.

### **2.4.3 Phase locking of array laser diode using monolithic approach**

#### **2.4.3.1 Laterally coupled Index guided array laser diode**

The index guided semiconductor laser array employs, as the name suggests, an inbuilt index variation through the fabrication of the laser structure. When gain guided effects due to the injected carriers are dominated by the lateral index variation, optical coupling can be described by the evanescent fields of the guided mode of the individual waveguide elements.

Different laser arrays structures have been studied, such as the channel substrate planar array ((D. Botez) (60)), which was one of the first to be investigated. Botez developed a buried V shaped, 5  $\mu\text{m}$  period saw tooth grating etched into the substrate, for a nine element index guided array. The array was overgrown by liquid phase epitaxy, as illustrated in figure (2.10). The facets of the structure were coated to provide the highest power possible. The zero phase shift operation dominated up to 80 mW, but when the power was increased to 200 mw a mixture of  $0^\circ$  phase shift and  $180^\circ$  operation was obvious.

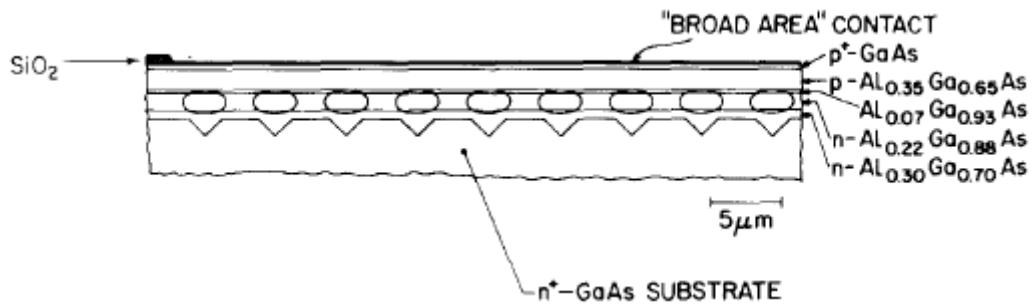


Figure (2.10) Schematic representation of the index guided channel substrate planar array. (Courtesy of D. Botez 60)

The  $180^\circ$  phase shift mode is normally dominant in index guided arrays. This makes achieving phase locked operation difficult and leads to the undesired double lobed far-field. This early design is difficult to implement due to the overgrowth that is involved. Furthermore, this type of structure suffers from low power operation and non-uniform current injection due the single broad area contact. The other approach is for index guided laser arrays, where the ridge waveguides are etched to just above the quantum wells. The separation between the ridge waveguides plays an important role in promoting a supermode. However, the out of phase mode dominates in this device type and there is a tendency for higher order modes to appear when high drive currents are injected. Thus, in order to discriminate efficiently against all the higher order lateral modes, different schemes have been proposed to achieve phase locking between the emitters. For example, a 10 element ridge waveguide structure was used by (Y. Twu) (57). A schematic of this device can be seen in figure (2.11). The ridge was  $4\ \mu\text{m}$  wide and the centre to centre the spacing from between the ridges was fixed to  $8\ \mu\text{m}$ .

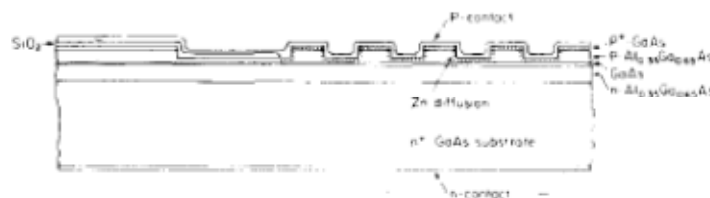


Figure (2.11): schematic representation of the coupled ridge waveguide laser array. (Courtesy of Y. Twu 57)

The device was tested under pulsed condition. The maximum output power reached was 250 mW, but the far-field was broad indicating multimode operation. The diffraction limit of the central peak of this array laser should

have been 1 degree, but the measured from the far-field pattern was 3 degrees. This indicates that the array far-field is three times the diffraction limit. It is not possible to decide if the device was phase locked, especially no spectrum or fringe visibility measurement was reported. In those days, the understanding of the whole issue of array laser phase locking was not complete. The same group of (Y. Twu) (57) and a group led by E. Kapon (73, 75) used the approach as illustrated in figure (2.12) to tailor the gain by

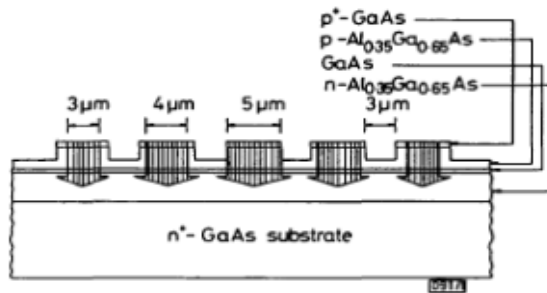


Figure (2.12): schematic representation of the non-uniformly pumped ridge waveguide laser array. (Courtesy of E. Kapon 73)

limiting the contact window opening while keeping the width and the inter-emitting spacing constant. The different schemes employed had limited success in achieving a single fundamental supermode for the array, limiting the optical power to about 100 mW. Moreover, when higher currents were injected, the phase locking would disappear resulting in an undesired double lobed far-field.

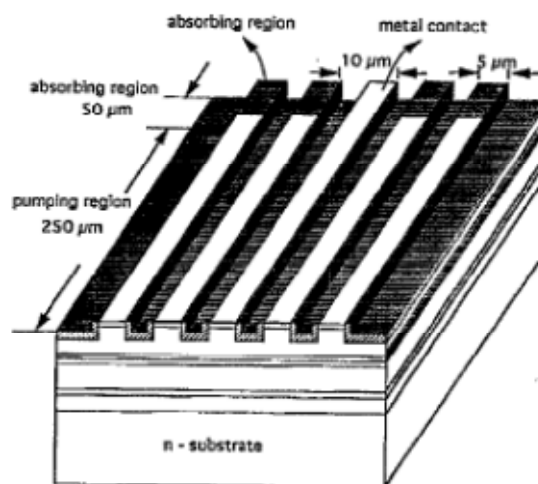


Figure (2.13): Schematic representation of the ridge waveguide laser arrays with loss regions at one of ends of the laser. (Courtesy of T. Tsang 74)

Other arrangements in the design of phase locked index guided laser arrays have been implemented, where Tsang (74) utilised 5 ridge waveguide laser

arrays. He introduced a loss region (with no metal) at one of the end facets, but the central element in the array was left without this loss region, as illustrated in figure (2.13). Phase locked operation was achieved up to a very modest power of 100 mW. In this type of edge emitting device, the lateral coupling occurs by the leakage of light of individual elements into each other. However, for closely spaced elements the dominant operation of the mode is out of phase, which leads to the far-field being double lobed which is highly undesirable. The other problem is that the inter-coupling coefficient is non-uniform across the array, which restricts the number of array elements that could be successfully utilized. If the number of the elements is increased, the elements at the edge of the array tend to drop out of lock. This means certain emitters in the array do not contribute to coherent operation. Instead, they operate in free running mode.

#### **2.4.3.2 Anti-guided array laser diode concept**

In the continued effort to develop a phase locked array laser diode, Dan Botez (79,113) developed the anti-guided laser array, which is more robust against the effects of the lateral coupling that favours the out of phase mode. The gain sections in this design have a lower refractive index than the inter-element regions, which are not pumped, while the inter-element regions has a higher refractive index. As the pump current increases, the carrier anti-guiding enhances the mode competition, which causes instabilities to arise. The increase in the free carriers and injected carrier can reduce the effective index to a level that disturbs the wave guiding. Therefore, the built in index ( $\Delta n$ ) is fabricated as high as possible, which is typically between (0.02-0.05). This makes the anti-guided array more stable against thermal and/or carrier-induced index variations (79,81). Therefore, they are almost prone to the effect of index variation with gain. In this type of array, the coupling occurs through the leaking optical mode from the gain stripe to higher index inter-element area, which results in the phase locking. The power achieved is 0.5 W CW for a GaAs/AlGaAs anti-guided array in a diffraction limited beam, which is much higher than achieved by the other types of coherent coupling described earlier. However, the problem with this type of phase locked array semiconductor laser is that it requires overgrowth, adding more complexity and cost. The anti-guided array semiconductor laser diode has been studied further by (J.

Marsh 1994) (80), where a different approach has been used to fabricate the anti-guided laser arrays without the need for overgrowth. Instead, quantum well intermixing was used successfully to create an effective refractive index step between the anti-guided core and the inter-element region. (Zinc disordering was used in this experiment). To achieve a large increase of the refractive index, a superlattice structure was used in the cladding layer producing an index step change of 6 % after intermixing. The power achieved was 400 mW per facet for the in-phase array mode with a  $3^\circ$  diffraction limited beam. Later experiments by J. Marsh and J.M. Gray (1998) (81) produced 1.5 watt per facet when tested in pulsed mode using a GaAs/AlGaAs superlattice structure operating at 860 nm, as illustrated in figure (2.14).

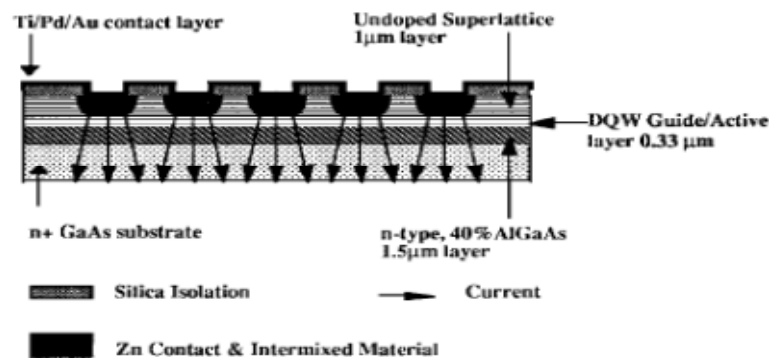


Figure (2.14): Anti-guided array laser fabricated using quantum well intermixing (Ref. 81)

The far-field demonstrated in the experiment was  $1.2 \times$  diffraction limit, which is considered very good. However, the difficulty, as J. Marsh explained, remains in the uncertainty of the profile of the intermixed material. This makes it difficult to produce the exact parameters (inter-element spacing and anti-guide dimension) required to achieve the anti-guiding mechanism responsible for the leaky modes that lead to a stable locking of the anti-guiding laser array. The other important limitation of using an anti-guided array laser even with novel quantum well intermixing is the relatively high threshold current density. It has a range of  $1.6\text{-}2 \text{ kA/cm}^2$ .

### 2.4.3.3 Y-coupled array laser diode

The Y-coupled array laser diode is another type of index guided array, which used a Y-shaped region to couple the mode into the single output waveguide as illustrated in the figure (2.15).

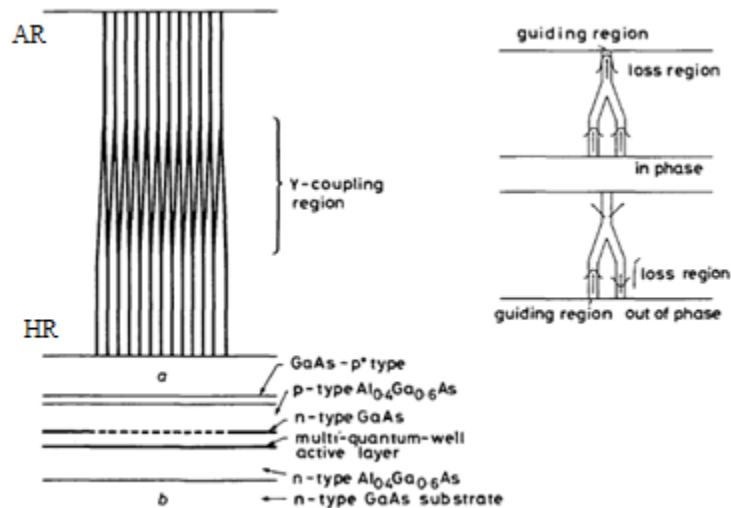


Figure (2.15): a) A Schematic of a Y-coupled index guided laser array. The coupling region is highlighted and the concept explained on the right hand side of the schematic. b) Epitaxial layer structure. (Courtesy of Welch 82).

To achieve phase locking of array modes, the modes in both arms must be in phase for the light to be coupled. If the arms are out of phase, then the light in the recombining arm suffers destructive interference, so that, no coupling occurs. Y-coupling is different from the evanescent wave coupling in traditional ridge guided laser arrays. Constructive interference occurs in the Y-coupling region, as described in figure (2.15) above. Y-coupled arrays were reported by D.F. Welch (58, 82). Although good quality power was produced, the far-field pattern revealed three main lobes, one located at  $0^\circ$  and two other lobes at  $10^\circ$ . This observation is in conformity with a phase locked far-field pattern. The far-field pattern of the array is shown below in figure (2.16) which, was measured from the AR side. The central lobe width is  $1.5^\circ$ .

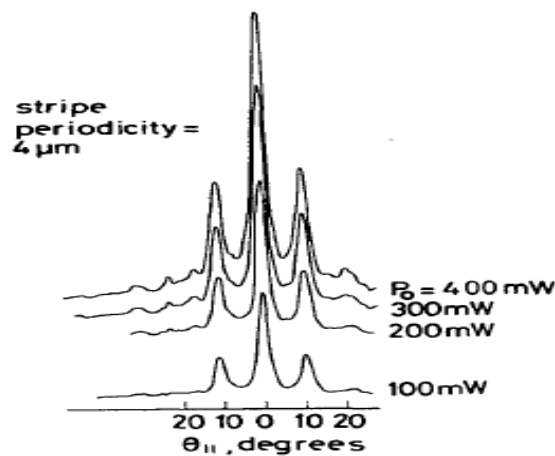


Figure (2.16): far-field measurement Y-coupled index guided laser array, which was taken from the AR side. The pattern shows a central peak of  $1.5^\circ$  and two satellite peaks at  $10^\circ$ . (Courtesy of Welch 82).

The HR side had a facet reflectivity of 95 %, but the reflectivity of the AR facet was not reported. The Y coupled arrays were difficult to implement, due to the overgrowth that is involved. Hence, they cannot be cost effective. Furthermore, they suffer from weak coupling and the inherent problems of spatial hole burning and thermal effects (83).

#### **2.4.3.4 Multimode interference coupler array laser diode**

Multimode interference (MMI) devices have been extensively studied and are of considerable interest as key optical components in photonic integrated circuits (PICs).

The principle of MMI devices is based on constructive and destructive interference occurring in the MMI area with a large number of modes. The low loss for such devices makes it possible to use them as the coupling region for laser gain sections. Camacho (3) reported a 4x1 array laser diode based on GaAs/AlGaAs, which consisted of four gain sections, an MMI coupler and an output waveguide. The MMI interferometer was used as a passive section to couple the light from the main four gain sections. The power achieved was about 180 mW. However, the device was inefficient, even though it had a single lobed far-field output. The far-field pattern measured from the 4 gain section side was stable with increasing drive current. This device proved very attractive to explore further particularly the single spatial mode that resulted from the use of a single output waveguide.

Active MMI laser diode devices have also been reported operating at 1.45  $\mu\text{m}$  by H. Hamamoto (76). Four active MMIs have been used in a series using five InGaAsP strained quantum wells on InP substrate, where the use of buried hetero-structures made it possible to obtain reasonably narrow far-field and maximum power of 290 mW. To increase the power further, Hamamoto (77) used eight MMI couplers in series to achieve a maximum power of 700 mW in a single spatial mode. The slope efficiency appears to be quite low (around 15 % per facet) in active MMI lasers. The output power was improved further to about 0.9 W by using a broadened waveguide structure and a longer active MMI (78). The far-field in this type of devices is large (in the region of 40 °) and the active MMI configuration is susceptible to carrier induced refractive index changes.

### 2.4.3.5 Array laser diode incorporating diffractive section

The phase locking of laser arrays can be implemented using a diffractive section. The diffractive section works as the mixing region, where the light that propagates from the laser elements is optically mixed. The mixed light is reflected back into the gain sections from the mirror. This reflection of light causes overall inter-element coupling in the diffraction section, which is stronger than the lateral inter-element coupling. This results in a phase locked laser array, which has the desired diffraction limited narrow single lobed far-field.

This coupling effect in the diffraction region can happen more effectively if the length of the diffraction section is equal to the Talbot distance, forming a Talbot cavity. The Talbot length is the length whereupon self imaging of a periodic source array occurs, as explained by J.Z. Wilcox (1989) (84). An array can be imaged into another array using this technique to maintain the overall inter-element coupling, which leads to coherent operation.

This technique has been used by a number of groups. For example, J. Katz *et al.* (1983) (85) used an array of uncoupled elements, as illustrated in Figure (2.17). The device has two diffraction sections which have their lengths optimized. The light is uncoupled as it propagates through the array. It diffracts in the diffraction section and is reflected back from the mirror, which ensures phase locked operation. The phase locking of the array has been achieved and a power of 1.1 W was obtained in the pulsed regime with a narrow far-field of 3 ° at  $2.1 \times I_{th}$ . No information of the spectra was reported to verify the phase locked operation.

The diffraction coupled devices that utilise the self-imaging properties of Talbot cavities do operate in diffraction limited single lobed far-field pattern, but these early devices were phase locked for low current ranges  $(2-3) I_{th}$ . If the current is increased further, the devices lost their coherence. The far-field is normally multi-lobed (Jenson 1989) (114) from the diffraction section side, reducing the power available in the central lobe.

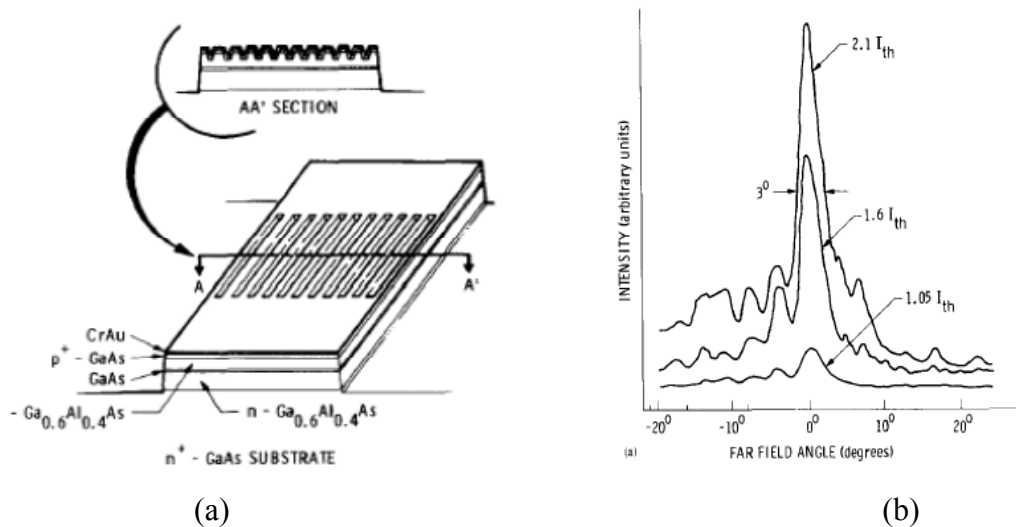


Figure (2.17) (a) Schematic diagram of a diffraction coupled array GaAs/AlGaAs array laser (Ref 85) (b) Phase locked far-field of the array laser.

A recent study by D. Yanson *et. al.*, (2008) (87) indicated that the phase locking does occur in a diffraction coupled array, which uses a Talbot cavity. However, in this particular work, the power achieved in the diffraction limited beam was low. A much more successful approach was demonstrated by using external Talbot cavities, which resulted in much higher power in a diffraction limited beam.

## 2.5 Master Oscillator power amplifier

The master oscillator power amplifier (MOPA) is another type of high power laser that has been investigated in order to extend the power achieved from semiconductor laser diode beyond 200 mW in a single frequency and a single spatial mode. The MOPA consists of an oscillator section with a low power. This can be a DBR laser, which determines the wavelength and the spectrum. As well as the oscillator, it has a power amplifier that amplifies the laser light and determines the output power level. The output characteristics are determined by both. For more recent devices, the gain and amplifier are on the same chip. In this case, the MOPA is called a monolithic MOPA (M-MOPA). One of the main challenges in the design of the MOPA is that two growth steps that are required, which adds an increased complexity in this type of devices.

The first MOPA configuration was proposed by Kosonocky and Comely in 1968 (89) and their devices lased at 77 K. The oscillator and the amplifier were two separate chips. The amplifiers were made by lapping one end at an

angle of 10 to 15 degrees to reduce back reflections. There are two main MOPA configurations, which have been actively researched. The first is the edge emitting MOPA and the second is the grating coupled surface-emitting MOPA. The first monolithic MOPA was realized by Koshino *et. al.* (1978) (90).

The device provided 130 mW of power when tested under low duty cycle short pulse conditions. There was no major breakthrough in MOPA design until the early 1990s, when Ross Parke *et. al.* (91) reported a 2 Watt diffraction limited M-MOPA with a stable far-field with current. The design comprised of a DBR oscillator, pre-amplifier and flared amplifier using GaAs/AlGaAs material system, with each of the sections having a separate contact as illustrated in figure (2.18) from (91). In this design, the output of the DBR laser was injected into the output power amplifier with a 4 micron input aperture and an index guided region. The DBR output was diffracted along the 2 mm amplifier length with a wide aperture of 250  $\mu\text{m}$ . The output aperture was coated with an anti-reflection coating with a reflectivity of 0.1 %. The output beam had a single spatial mode with a lateral beam divergence of 0.21° at FWHM. The power achieved was 2 W CW for a driving current of 3.5A injected to the amplifier with a differential efficiency of 50 %.

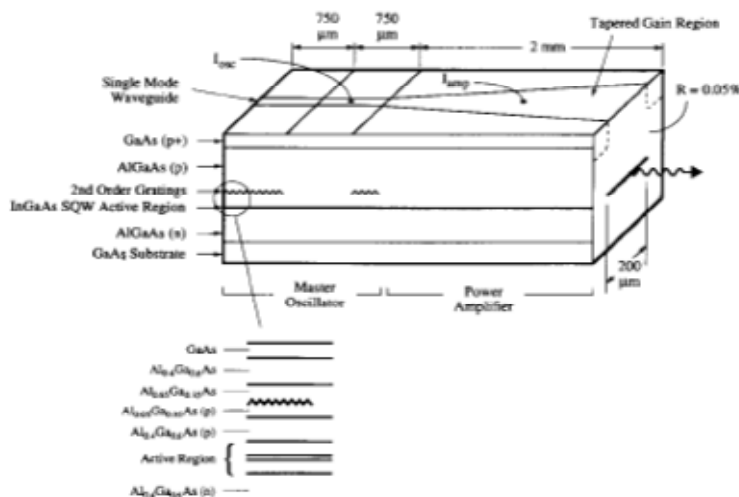


Figure (2.18) Schematic diagram of monolithic master oscillator power amplifier with separate contacts for both the oscillator and the amplifier (courtesy of ref. 91)

As this was an edge emitting MOPA, it was susceptible to catastrophic optical mirror damage. Therefore, other groups for example, R.M. Lammert (1999) (92) integrated a DFB-MOPA with non-absorbing mirrors to reduce the

possibility of COMD and minimise the absorption at the facet. The diffraction limited power reported was 1.5 W at 980 nm wavelength for an amplifier current of 2.6 A in a diffraction limited beam. A differential efficiency of 0.67 W/A was attained at an amplifier current of 1.0 A. Recently a 10 W CW MOPA was reported by H. Wenzel *et. al.*, (2007) (93). This device was 8 mm in length. The master oscillator was 4 mm in length and consisted of a three section DBR laser. The first section was 500  $\mu\text{m}$  long DBR section, the second operates an active gain section and a passive 65  $\mu\text{m}$ , which fed into a 4 mm power amplifier. Separate contacts for both the MO and PA enabled controlled current injection to both the MO and the PA.

Having described the previous work on MOPAs, problems remain to be solved with this kind of device. The first problem is the design of the power amplifier section, for which a wide taper ( $>100 \mu\text{m}$ ) is common in most of the designs. Such designs suffer from filamentation at high output powers, accompanied by refractive index changes. The coupling from the master oscillator has to be unidirectional. Any light injected back from the amplifier into the oscillator can disrupt the whole MOPA operation, leading to device instability. Moreover, the antireflection coating required is in the region of 0.01, which is very challenging to achieve.

## **2.6 ALFA DFB Semiconductor laser**

DFB lasers have been around for some time. The one difficulty with angled DFB lasers is the two step epitaxy process, which is considered to be high cost with added complexity. However, DFB/DBR lasers have a narrow spatial beam quality, which make them attractive for exploitation. The gratings are mainly used to stabilise the wavelength. However, the power they provide is far below the 100 mW mark. A new type of DFB laser has been investigated by different groups, which is called the angled DFB ( $\alpha$ -DFB) laser. The device supports broad area laser ring modes emitting in a diffraction limited beam with a good side mode suppression ratio. The device is described in the schematic from R.J. Lang *et. al.*, (1998) (94) in Figure (2.19). The device uses angled DBR grating to create ring modes. The active region has a broad area design with DFB gratings embedded laterally between the DBR gratings. The

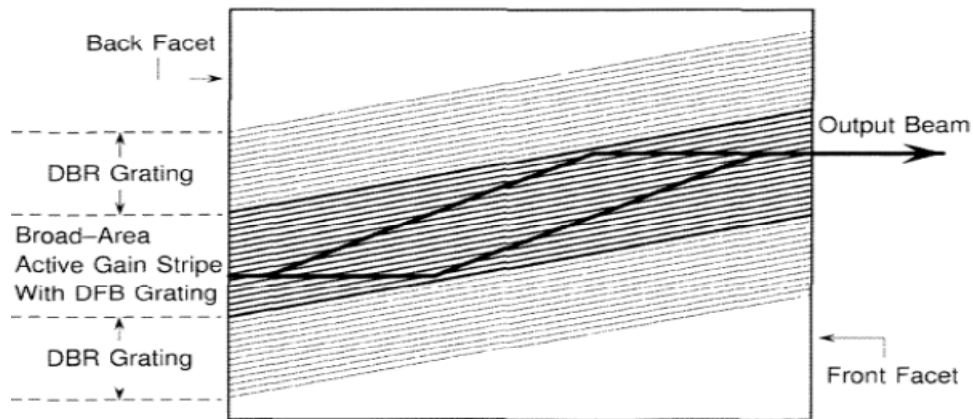


Figure (2.19) Schematic of broad area  $\alpha$ -DFB laser (Courtesy from 94)

angled gratings act as spatial filters that promote single mode operation and single longitudinal mode oscillation. The device is a very attractive alternative to the phase locked, MOPA, and tapered lasers because of their superior lateral beam divergence, which allows better coupling to external optics. Studies by K. Paschke *et. al.* ( 2003) (95) on the angled grating DFB laser resulted in  $> 1$  watt CW power in a diffraction limited beam from an optimised 4 mm long cavity.

## 2.7 Epitaxial structures review for high brightness lasers

This section is dedicated to a review of different epitaxial structures that have been employed in high brightness semiconductor lasers. The vertical (transverse) design of the epitaxial material is very important, as it defines the shape of the single mode in the vertical direction.

In high brightness lasers, the designs for increasing the optical power prior to COMD and the control of the higher order mode have been the most important motivations. The increase in the COMD power requires a large spot size of the optical mode. In addition, the far-field of such a laser structure is reduced significantly, which is a very desirable feature for coupling into an optical fibre or a waveguide. Enlarging the spot size increases the power achieved prior to COMD.

The Botez group (1998) (96, 97) used a broadened waveguide to increase the COMD power with reduced internal optical losses. The loss value reported was  $1 \text{ cm}^{-1}$ , which is quite low. The low loss value is attributed to optical confinement being limited to the undoped region of the waveguide core. The

material used was Al free, which consists of InGaAsP/InGaP/ GaAs separate confinement hetero-structure quantum-well diode laser structures operating at 970 nm wavelength. The epitaxial structure was widened by inserting a 1.3  $\mu\text{m}$  transverse waveguide, as shown in figure (2.20) from (96). Inspection of this figure shows that the upper and lower cladding regions are 1  $\mu\text{m}$  each. Such a small thickness of the cladding region is vital to reduce the thermal resistance. This improves the heat removal, thus achieving high output power prior to COMD effect. The limitation of such an epitaxial design structure is the single mode instability of the large waveguide core, which supports multiple modes. An additional limitation of enlarging the waveguide is the thermal resistance issue, which should be controlled.

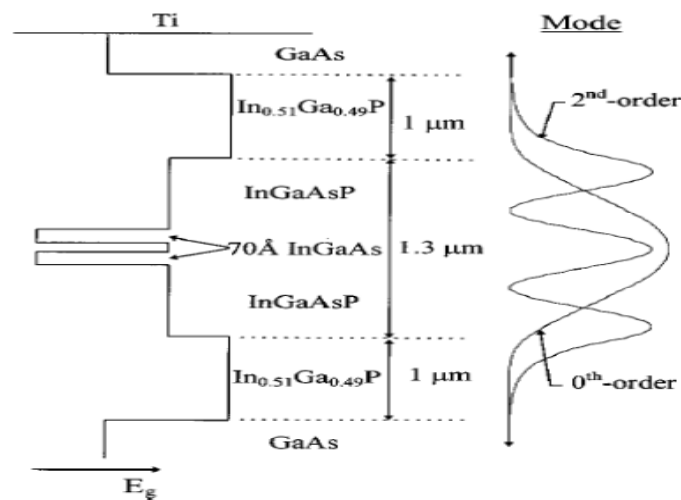


Figure: (2.20) Broad waveguide high brightness design (Courtesy of A. Al-muhanna ref. 96)

The slab coupled large optical waveguide laser (SCOWL) approach, illustrated in figure (2.21), has been demonstrated by Huang *et. al.* (98). The single spatial mode of the SCOWL laser had dimensions of (3.8 x 3.4  $\mu\text{m}$ ) at the  $(1/e^2)$ , which is nearly circular. The power achieved was 1 W in a nearly diffraction limited beam with a beam quality  $M^2$  of 1.1. At the highest output power levels, the spatial brightness is approximately 100  $\text{MW}/\text{cm}^2\text{-str}$ . If we compare this value with the ridge waveguide laser by Intense (1), we observe that the power of the ridge waveguide laser is 200 mW for an emitter area of  $1 \times 3 \mu\text{m}^2$ , the  $M^2 = 1$  and an operating wavelength of 830 nm. Therefore, the brightness was equivalent to 29  $\text{MW}/\text{cm}^2\text{-str}$ . The concept of the SCOWL laser is an important one. However, as the etching for the ridge can leave the quantum well exposed, this could be a serious reliability problem, but this has not been proven yet.

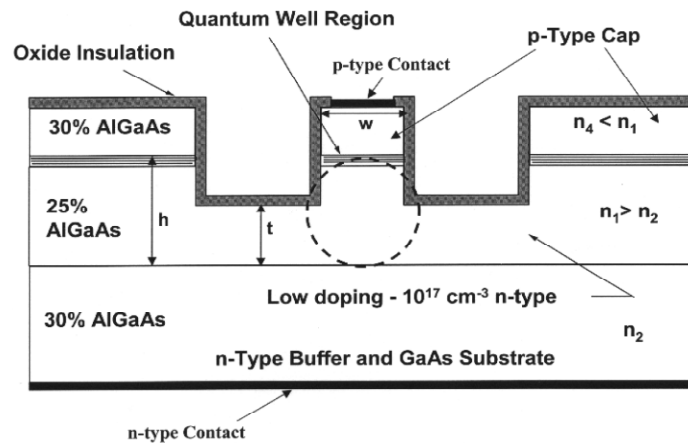


Figure (2.21) Sub coupled ridge waveguide laser structure courtesy of Huang (Ref 98).

Other researchers, like H. Wenzel (2008) (100) have used a leaky waveguide with trenches. This works as a loss element which increases the threshold of the higher order modes. The increased threshold of higher order modes results in a single mode waveguide even for waveguide widths was up to 5  $\mu\text{m}$ , as in this example. Figure (2.22) shows the structure used. The output power achieved was 2 W in a single spatial mode and an operating wavelength of 1064 nm.

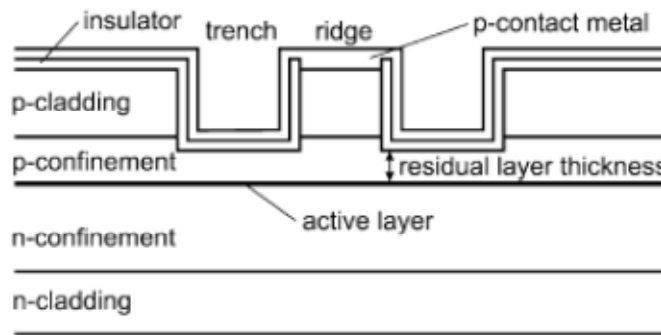


Figure (2.22) Slab coupled ridge waveguide laser structure courtesy of Wenzel (Ref 100).

A new concept  $d/\Gamma$  has been studied (101) 2002, and more recently developed further by a study conducted by I. B. Petrescu-Prahova (102) as part of the group led by J. Marsh. This approach uses an asymmetric epitaxial structure with an optical trap. This optical trap was positioned in the n-region, which allowed considerably higher power to be achieved. Furthermore, the study emphasised the optimisation of the  $d/\Gamma$  value for the structures used. The optimisation of this value allows very long devices to be fabricated without a

considerable increase in the attenuation coefficient. Enlarging the spot size increases the power achieved prior to COMD.

One of the more advanced structures that used the  $d/\Gamma$  concept was developed earlier by Bocang *et. al.* (103). The structure was comprised of an asymmetric waveguide structure with a far-field reduction layer (works as a secondary waveguide) inserted in the lower cladding to enlarge the mode and reduce the far-field to about  $17^\circ$ . This same structure has been used as the main epitaxial material throughout this work.

Other approaches for high brightness epitaxial design include the use of a photonic crystal band gap waveguide, which is reported by M. V. Maximov *et. al.* (Ref. 104) and illustrated in figure (2.23). The output power achieved was 2 W CW in a single spatial mode with a far-field of  $6^\circ$  FWHM. The epitaxial layers are very thick in this design and growing such waveguide is very complex.

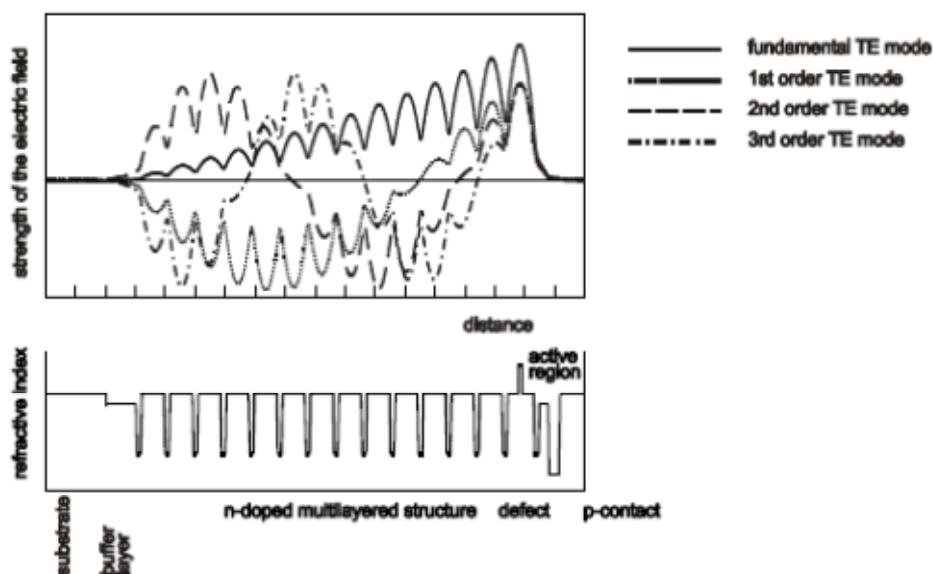


Figure (2.23): PBC laser design, refractive index profile (bottom) and the calculated profile of the electric field (top). (Courtesy of ref 104)

## **2.8 Table summary of the reported results for high brightness single emitter laser diode and phase locked semiconductor laser arrays**

Table (2.2) summarises some of the results for single emitter high power lasers with respect to power, emitter quality factor and brightness. The brightness is calculated according to the definition in Chapter One and the use of section 2.4.1.4 of the thesis. In the table, the state of the art for single tapered lasers is also included. Two configurations for tapered lasers exist, gain guiding and index guiding. However, the tapered structure leads to astigmatism effects, which means that the beam source is different for the slow-axis and fast-axis directions. This is an important limitation for the tapered laser emitter.

In Table (2.3), a survey of different techniques is described. The table refers to the state of the art of different diffraction limited phased locked laser arrays. Most of these techniques are passive, non-monolithic and depend on an external cavity configuration. Therefore, there is a loss of compactness, complexity and higher cost than the monolithic solutions. The beam quality factors for single emitters and bars (array of lasers) are denoted  $M^2_{\text{emitter}}$  and  $M^2_{\text{bar}}$ , respectively. These are calculated according to the definition in section (2.4.1.4). Visibility component is measured according to the definition in the same section (2.4.1.4) of the chapter. The use of any wavelength stabilisation mechanism is also recorded.

Device details	Power	Beam quality	Technology	Brightness (MW/cm <sup>2</sup> -str)	Year	Reference
Ridge waveguide $\lambda=0.83 \mu\text{m}$ , width= $2\mu\text{m}$	200 mW@ 250 mA	$M^2 = 1.0$	simple	29	Present	(1)
SCOWL laser $\lambda=0.83 \mu\text{m}$ , width= $3\mu\text{m}$	1 W	$M^2 = 1.1$	complex	100	2008	(100)
Ridge waveguide $\lambda=0.808 \mu\text{m}$ , ridge width = $4 \mu\text{m}$	0.8 W@ 1.3 A	$M^2=1.2$	complex	102	2011	(2)
Tapered waveguide width = $256 \mu\text{m}$ $\lambda=0.845\text{-}0.865 \mu\text{m}$	2W@ 3.25 A	$M^2=1.7$	complex	-----	present	(115)
Tapered waveguide width = $167 \mu\text{m}$ , ridge width = $3 \mu\text{m}$ , $\lambda=0.808$ $\mu\text{m}$	4.4W @4.6 A	$M^2=1.9$	Gain guiding	460	2006	(117)
Tapered waveguide width = $14 \mu\text{m}$ , ridge width = $3 \mu\text{m}$ , $\lambda=0.915$ $\mu\text{m}$	0.65 W	$M^2=1.3$	index guiding	46	2005	(119)
Tapered waveguide width = $20 \mu\text{m}$ , ridge width = $3 \mu\text{m}$ , $\lambda=0.975 \mu\text{m}$	1.3W@ 1.65A	$M^2=1.6$	index guiding (SLOC)	85	2008	(118)

Table (2.2) Ridge waveguide laser results in terms of power, beam quality and brightness. If the values of  $M^2$  beam quality and brightness were not reported in particular reference, they were estimated according to the definitions in Chapter One and Chapter two.

<b>Monolithic phase locked semiconductor laser arrays</b>								
<b>Configuration</b>	<b>Cavity</b>	<b>Device characteristics</b>	<b>Power</b>	<b>Beam quality</b>	<b>Visibility</b>	<b>Spectral stabilisation</b>	<b>Year</b>	<b>References</b>
Antiguinding arrays with Talbot filter	Resonant optical waveguides	N=20, p=1 $\mu$ m 2w= 5 $\mu$ m , $\lambda$ =0.980 $\mu$ m	0.5W@ 0.82A	M <sup>2</sup> bar = 1.35	-----	No stabilisation included	1993	(113)
Evanescent lateral coupling	Index guided parabolic Bow-Tie laser arrays	N=5, 2w= 20 $\mu$ m, $\lambda$ =0.980 $\mu$ m	2.5 W/facet @3.5 A	M <sup>2</sup> bar = 1.4	-----	No stabilisation included	2005	(61)
MMI combining	1x3 active MMI monolithic	N=3, 2w=2 $\mu$ m 1.3 $\mu$ m		M <sup>2</sup> bar = 3.6	V= 0.7	No stabilisation included	2009	(116)
<b>Non-monolithic phase locked semiconductor laser arrays ( External cavity designs)</b>								
<b>Configuration</b>	<b>Cavity</b>	<b>Device characteristics</b>	<b>Power</b>	<b>Beam quality</b>	<b>Visibility</b>	<b>Spectral stabilisation</b>	<b>Year</b>	<b>Reference</b>
Talbot	Tapered array	N=10, p=100 $\mu$ m $\lambda$ =976 nm	0.8W @2.5 A 1.7W@3.9 A	M <sup>2</sup> emitter = 3	0.8 0.7	Volume Bragg grating	2011	(68)
Angular filtering	Tapered array	N=6, p=30 $\mu$ m $\lambda$ =979 nm	0.7W@3A	M <sup>2</sup> bar= < 2	-----	Volume Bragg grating	2010	(112)
Talbot	Individually addressable SCOWL	N=10, p=100 $\mu$ m 2w= 6 $\mu$ m , $\lambda$ =760	4W@10.8A	M <sup>2</sup> emitter =1.1 M <sup>2</sup> bar= 2.4	<b>1</b>	none	2009	(108)

Spectral beam combining	SCOWL	N=100, p=100 $\mu\text{m}$ 2w= 5.7 $\mu\text{m}$ , $\lambda=970$	30W@90A	$M^2_{\text{bar}}= 2.0$	-----	stabilisation included	2007	(106)
Talbot	Tapered laser	N=10, p=100 $\mu\text{m}$ 2w= 25, $\lambda=980$ nm	1W@2A	$M^2_{\text{emitter}}=3.0$	-----	none	2007	(111)
Spectral beam combining	multimode broad area laser	N=1, p=100 $\mu\text{m}$ 2w= 400 $\mu\text{m}$ , $\lambda=980$ nm	5.7W @6 A	$M^2_{\text{emitter}}=35$	-----	diffraction gratings	2008	(109)
Talbot	multimode	N=49, p=200 2w= 100 $\mu\text{m}$ , $\lambda=765$	5.3W@30 A	$M^2_{\text{emitter}}= 7$ $M^2_{\text{bar}}= 16$	0.82	none	2008	(110)
Spectral beam combining	Tapered lasers	N=12 p=500 $\mu\text{m}$ , $\lambda=980\text{nm}$	9.3W@ 30A	$M^2_{\text{emitter}}=2.5-$ 4.6 $M^2_{\text{bar}}= 5.3$	-----	none	2010	(107)
External cavity using (GRIN) lens	gain guided (multimode) evanescent	N=10, p=10 $\mu\text{m}$ 2w= 6 $\mu\text{m}$ , $\lambda=840$	0.7W@ 1A	$M^2_{\text{bar}}= 1.4$	-----	No stabilisation included	1987	(70)

Table (2.3) Phase locked semiconductor laser results are recorded in terms of phase locking configuration, device characteristic, power with corresponding current, single emitter beam quality, bar quality and the method of wavelength stabilisation. The values for the beam quality denoted by  $M^2_{\text{emitter}}$ , bar quality denoted  $M^2_{\text{bar}}$  and visibility are calculated (or reported from the source) using the definition of these terms in section (2.4.1.4) of this chapter.

# Chapter 3

## High brightness GaAs/AlGaAs material design and characterisation

### 3.1 Introduction

The most common III-V semiconductor material system employed in the design and fabrication of high brightness semiconductor lasers for the 800-1000 nm wavelength range is GaAs/AlGaAs. The GaAs/AlGaAs system is very mature and is used for high performance devices. The very small lattice mismatch between GaAs and AlGaAs makes it possible to grow epitaxial structures in a wide range of AlGaAs compositions and thicknesses on a GaAs substrate without introducing dislocations or other defects, thereby producing very good quality devices. Although we are concerned with developing high brightness lasers working at 830 nm, it is possible to extend the operation to the wavelengths of GaAs/Al<sub>(x)</sub>Ga<sub>(1-x)</sub>As materials by varying the Al concentration according to (120, 123) the following formula:

$$E_g(x) = (1.42 + 1.087x + 0.438x^2)$$

For quantum well lasers, the wavelength is a function of the quantum well thickness, so there is more flexibility in the design of the emission wavelength. As is evident from the formula, the bandgap of AlGaAs varies quadratically with x. Therefore, it is possible to engineer the band gap from (1.42-1.97) eV,

which corresponds to emission wavelengths of 873 nm to 630 nm. The bandgap becomes indirect for  $x > 0.43$ , which is not desirable as there will be no lasing.

The AlGaAs/GaAs material system is also suitable for the operation of devices that cover the range of wavelength from 800 nm to 1100 nm. This wavelength range is achievable by using InGaAs quantum wells instead of GaAs. However, the InGaAs lattice parameter is higher than the lattice parameter for GaAs, so only thin InGaAs quantum wells with compressive strain can be grown before defects are created (123). In this thesis, the work involved operation at a wavelength of 830 nm, which is normally used for printing applications.

In this chapter, the properties of GaAs/AlGaAs are briefly reviewed. This is followed by a discussion of energy levels in a one dimensional quantum well. The aim of this chapter is to present both the design and the characterisation of the novel GaAs/AlGaAs material structure used in this project. This chapter will include the assessment of the semiconductor laser material through the fabrication of broad area lasers and single mode ridge waveguide lasers. The ohmic contact will be also characterised through the fabrication and testing of metal contact pads with different gaps and by using the transmission line method. Achieving a lower contact resistance is vital for the design of a high brightness array laser diode, whereby the conversion efficiency of the electric power to the optical output power increases. This can be observed through the following relation for the power conversion efficiency (124,125,126);

$$\eta_T = \frac{P_{out}}{IV(I)} = \frac{\eta_{ext} \left( \frac{E}{e} \right) (I - I_{th})}{I (V_0 + IR_S)},$$

where:  $\eta_T$  is the power conversion efficiency,  $P_{out}$  is the output power,  $I$  is the drive current,  $V(I)$  is the current voltage characteristics of the diode,  $\eta_{ext}$  is the external quantum efficiency,  $E$  is the photon energy,  $e$  is the electronic charge,  $I_{th}$  is the threshold current,  $V_0$  is the turn-on voltage of the diode and  $R_S$  is the series resistance.  $R_S$  is given by;

$$R_S = \frac{\rho_s}{wL}$$

where  $\rho_s$  is the sheet resistivity of the laser diode structure. This ( $\rho_s$ ) is due to both the material resistivity of the epi-layers and the resistivity of the metal contact.  $w$  is the width of the active region and  $L$  is the length of the laser

diode. The denominator of the conversion efficiency relation, which corresponds to the electrical input power, is comprised of the power associated with the voltage drop across the bandgap ( $IV_0$ ) and the power dissipated due to the ohmic heating ( $I^2R_s$ ).

Reducing the contact resistance means lowering the series resistance of the laser diode. This also means a reduction in the heat dissipated. Increasing the length of the device while maintaining low optical losses, reduces the series resistance. The reduction of the series resistance results in an increase of the power conversion efficiency. Other factors include: threshold current ( $I_{th}$ ) and  $V_0$ , both of which should be minimized. Moreover,  $\eta_{ext}$  should also be increased. High conversion efficiency results in a higher brightness laser.

### 3.2 Bonding and crystal structure of gallium arsenide and related materials

The gallium arsenide crystal has two sub-lattices. Each of the sub-lattices are face centred cubic, where each atom has four nearest neighbour atoms. This is called a zincblende lattice. In figure (3.1), the arrangement of Ga and As atoms is illustrated.

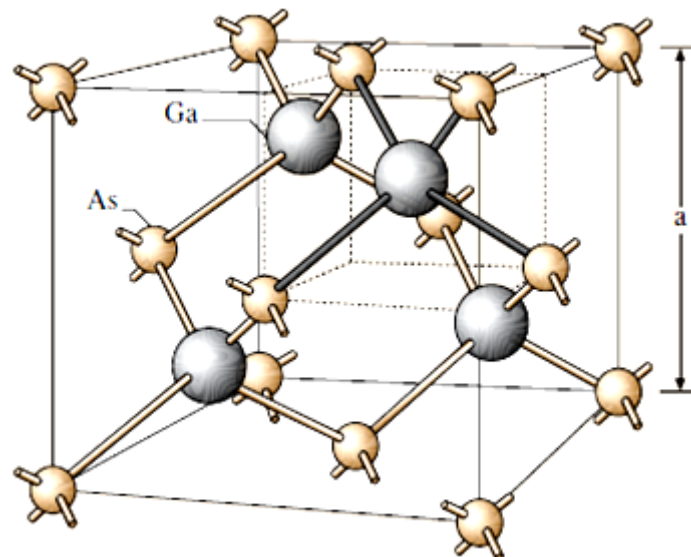


Figure (3.1): Face centred cubic structure (fcc) for GaAs crystal lattice.

A close examination of the lattice structure for GaAs/AlGaAs shows that there are crystallographic planes that can have one type of atom. Furthermore, different planes can have an entirely different lattice spacing. Therefore, the electrical properties can be very different for each crystallographic plane. The

device characteristic depends on the crystal orientation (121, 123). The crystal plane that is extensively used is the (100) plane (135). The fabrication and cleavage planes for such a wafer are the <110> planes.

### 3.3 Material parameters for GaAs/AlGaAs semiconductors

#### 3.3.1 Bandgap energy for GaAs/AlGaAs material

The energy levels for GaAs/AlGaAs structure can be calculated using the following two formulae (123, 133, 135):

$$E_g(x) = 1.424 + 1.247x \quad \text{for } (0 < x < 0.45) \quad (3.1)$$

$$E_g(x) = 1.424 + 1.247 + 1.147(x - 0.45)^2 \quad \text{for } (0.45 < x < 1) \quad (3.2)$$

where  $x$  is the aluminium mole fraction.

#### 3.3.2 Effective Mass in ternary and quaternary Alloys

The effective mass is a very important parameter in the design of a quantum well semiconductor laser. In GaAs/AlGaAs bands, the values of the effective masses for the electron, heavy hole and light hole can be found using the relations below (123, 128):

In GaAs, the effective masses are:

$$m_e = 0.067m_0$$

$$m_{hh} = 0.38 m_0$$

$$m_{lh} = 0.09 m_0$$

where  $m_0$  is the free electron rest mass.

In AlGaAs, the effective masses are:

$$m_{hh}^* = (0.5 + 0.29x)m_0 \quad \text{for } (0 < x < 0.45)$$

$$m_{lh}^* = (0.087 + 0.063x)m_0 \quad \text{for } (0 < x < 0.45)$$

$$m_e(x) = (0.0665 + 0.83x)m_0 \quad \text{for } (0 < x < 0.45)$$

### 3.3.3 Refractive index of GaAs/AlGaAs

The refractive index of the material is very important when designing the semiconductor laser waveguide. There are many models for refractive index, but the model from (129) shows the expression for the composition dependent refractive index, as observed in the equation below:

$$n(x) = 3.590 - 0.710x + 0.091x^2$$

The equation above confers approximately the refractive index with respect to the aluminium mole fraction. However, in this work the refractive indices were calculated using ref (127). The refractive index is calculated using Sellmeier equation, which is expressed by the following general relation form:

$$n(\lambda) = 1 + \sum_i \frac{\lambda^2 B_i}{\lambda^2 - C_i}$$

The wavelength has been taken into account when calculating the refractive indices.

### 3.4 GaAs/AlGaAs quantum well material system

In the GaAs/AlGaAs material system, a quantum well is formed when a very thin GaAs layer (the well) is sandwiched between two thick AlGaAs layers which are the barriers. In the design of the quantum well width, a few features need to be taken into consideration. Firstly, the quantum well thickness determines the emission wavelength and must be comparable to the de-Broglie wavelength. Secondly, the design of semiconductor laser depends on the quantum well thickness. Typically, the well thickness should be at least  $> 2.5$  nm. As the electrons and holes are confined in such a small dimension, they display quantum size effects, with free motion occurring in two dimensions perpendicular to the growth direction.

A sufficiently deep quantum well can be approximated, as an infinite quantum well. However, a finite well design is much more realistic, as illustrated in figure (3.2).

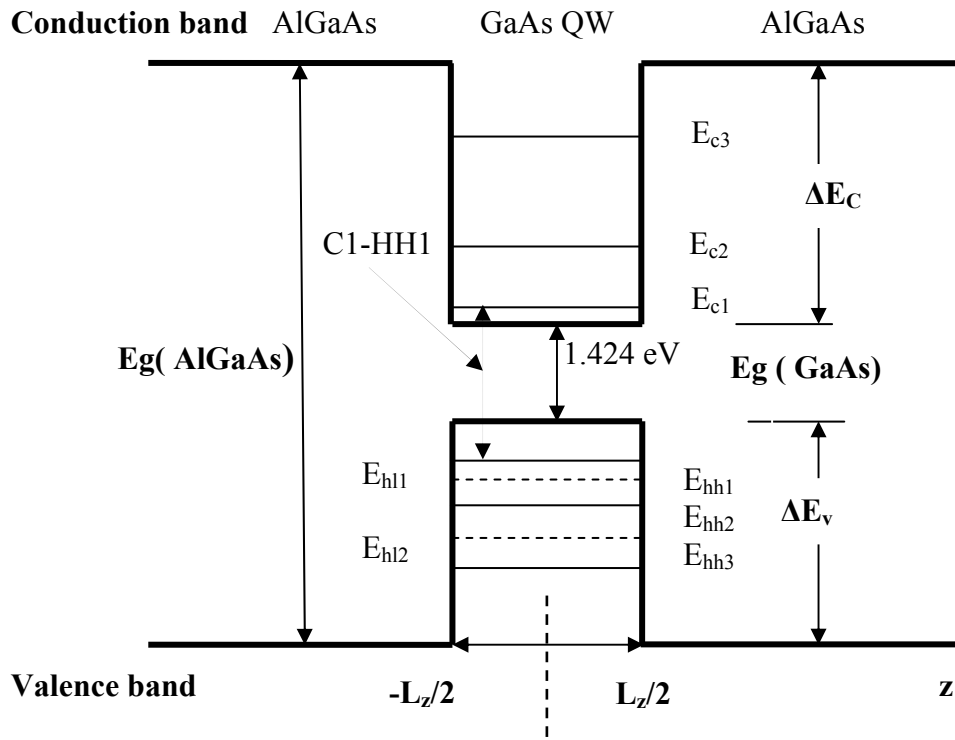


Figure (3.2) Schematic of GaAs/AlGaAs band structure with GaAs quantum well

The energy levels in the conduction band and the valence band can be found by solving the Schrödinger equation using suitable boundary conditions.

The time independent Schrödinger equation can be expressed as:

$$-\frac{\hbar^2}{2m} \frac{d^2}{dz^2} \psi(z) = E \psi(z) \quad \text{for} \quad (0 \leq z \leq Lz) \quad (3.03)$$

$$-\frac{\hbar^2}{2m} \frac{d^2}{dz^2} \psi(z) + V(z) \psi(z) = E \psi(z) \quad (z \geq Lz; z \leq 0), \quad (3.04)$$

where  $\psi$  is the Schrödinger wave function and  $V$  is the depth of the potential well.

The solutions of the wave function for an infinite quantum well are expressed by equations (3.05 and 3.06) below. In this case,  $V_0$  is infinitely high and the wave function goes to zero at the boundaries (130,131).

$$\psi(z) = \sqrt{\frac{2}{Lz}} \sin\left(\frac{n\pi}{Lz} z\right) \quad \text{where } n = (2, 4, 6, \dots) \quad (3.05)$$

$$\psi(z) = \sqrt{\frac{2}{Lz}} \cos\left(\frac{n\pi}{Lz} z\right) \quad \text{where } n = (1, 3, 5, \dots) \quad (3.06)$$

The corresponding energies are:

$$E(n) = \frac{\hbar^2}{2m} \left( \frac{n\pi}{L_z} \right)^2 \quad (\text{Infinite well}) \quad (3.07)$$

When investigating equation (3.06), it is found that, if  $L_z$  is increased significantly, then the system does not exhibit quantisation.

The infinite quantum well model is not an accurate model. In GaAs/AlGaAs epitaxial structure that is used in this project, a more accurate model is the finite quantum well model, as in equation (3.03).

The possible solutions of equation (3.03) are:

$$\psi(z) = C \begin{cases} \sin kz \\ \cos kz \end{cases} \quad (3.08)$$

where  $k = \sqrt{\frac{2mE_n}{\hbar^2}}$ .

The solutions for equation (3.04) for  $E < V_0$  are:

$$\psi(z) = D \exp(\pm \kappa z) \quad (3.09)$$

with

$$\frac{\hbar^2 \kappa^2}{2m} = V_0 - E_n \quad (3.10)$$

where  $\kappa$

$$\kappa = \sqrt{\frac{2m(V_0 - E_n)}{\hbar^2}} \quad (3.11)$$

Equations (3.08) and (3.09) can be solved graphically (130) by plotting the values for  $k$  and  $\kappa$ . The intersection points are the solutions for the wave equations.

### 3.4.1 Application to compute the electronic levels in the double quantum well structure

We are concerned with a GaAs/AlGaAs structure, with the band diagram described in figure (3.2). The corresponding epitaxial structure can be found in section (3.6) in table (3.2). In order to calculate the wave functions in the

valence band, the effective masses of both the light and heavy holes must be taken into account. The effective masses of electrons, heavy holes and light holes in GaAs and AlGaAs have been calculated using the relations in section 3.3.2. The aluminium mole fraction of the first barrier is 0.24. For the second barrier, it is 0.23. Therefore, using equation (3.1), the band gap energies at room temperature are 1.748eV and 1.711eV, respectively.

Well Width (Å)	Ec1 (meV)	Ec2 (meV)	Ehh1 (meV)
30	15.832	63.326	142.484
40	8.905	35.621	80.147
44	7.39	29.439	69.58
50	5.699	22.797	51.294
60	3.958	15.832	35.621
100	1.425	5.699	12.824

Table (3.1) Calculated results for the GaAs/AlGaAs structure that is described in section 3.6 as in table (3.2)

Table (3.1) shows the QW energy levels for different QW thicknesses using the procedure in the previous section. (See the material structure as in table 3.2 in section 3.6). The band offset values for  $\Delta E_c$  and  $\Delta E_v$ , were taken from (130) as:

$$\frac{\Delta E_c}{\Delta E} = 0.67$$

$$\frac{\Delta E_v}{\Delta E} = 0.33$$

We can calculate the initial wavelength from the results in table (3.1) using equation (3.12):

$$E = E_g + E_{c1} + E_{hh1} \quad (3.12)$$

Therefore, we get the initial wavelength for the material as being 826 nm. Figure (3.3) confirms the variation of the initial approximate wavelength with respect to the various well widths.

The initial wavelength estimation differs from the actual threshold lasing wavelength, which is obtained at the onset of lasing. Furthermore, the wavelength is gain dependent. The lasing wavelength at the threshold is determined

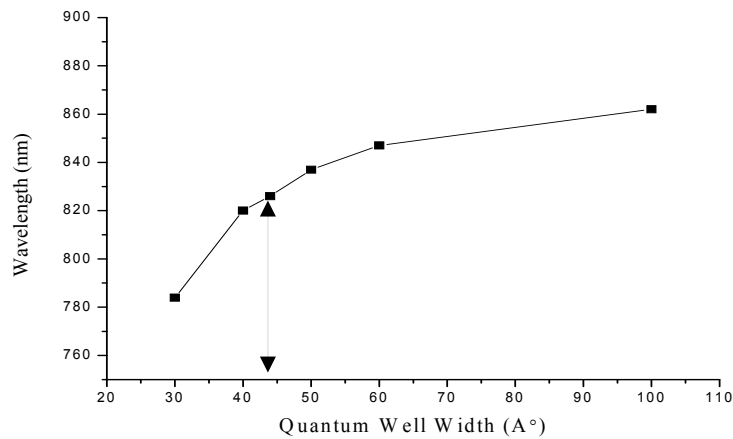


Figure (3.3): Calculated wavelength as a function of the quantum well width. For a well width of 4.4 nm, the wavelength is 826 nm. Emission wavelength can be determined by measuring the wavelength at onset of lasing at the threshold using spectral measurements.

at the point, whereby the gain matches the losses in the laser cavity at the onset of lasing. However, the emission wavelength, depends strongly on the carrier density at the peak gain and the temperature. In practice, it is important to include many body effects when determining the optical transitions of the material. These many body effects include: lineshape broadening, exciton states and bandgap shrinkage (170).

In conclusion, the actual emission wavelength can only be accurately determined using spectral measurements. The gain, the carrier density and the operating temperature should be taken into consideration.

### 3.5 GRINSCH quantum well structures for high brightness lasers

#### 3.5.1 GRINSCH structure concept

The GaAs/AlGaAs Graded refractive index separate confinement heterostructure (GRINSCH) comprises a gradual variation in the Al composition, which acts as a waveguide for the optical field. It is a refinement of the separate confinement heterostructure, which is a rectangular waveguide with no variation in the Al composition. Examples of GRINSCH and SCH structures are shown in figure (3.4a, b).

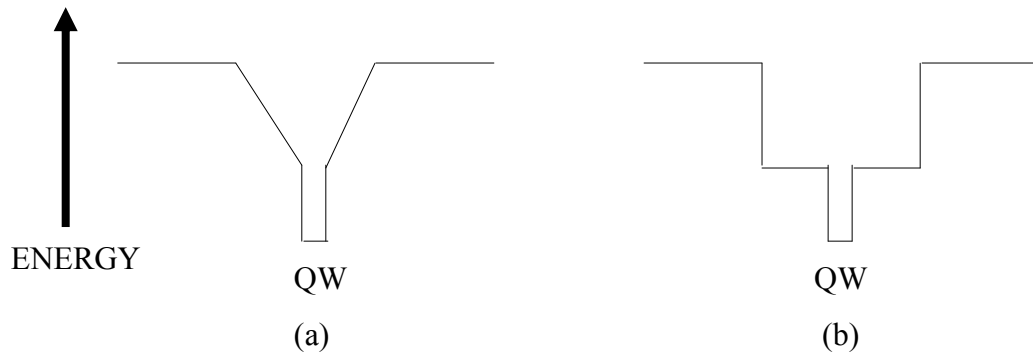


Figure: (3.4): (a) Bandgap profile for a GRINSCH structure. (b) Bandgap profile for a SCH structure.

The high brightness lasers (few hundreds mW range) utilize the graded refractive index separate confinement heterostructure GRINSCH. This is particularly valid, if a far-field reduction layer (FRL) design is included (148, 149, 150). Furthermore, once the FRL is introduced, the optical mode size is increased and the facet load is reduced. This design leads to an increase in  $d/\Gamma$  value, which is discussed in the next section. A proper GRINSCH structure is designed with low internal loss. This enables the design of longer cavities to be realized and hence, a high brightness is achieved. A GRINSCH structure with a FRL provides adequate parameters, specifically for high brightness lasers, particularly, if a smaller beam divergence is required (e.g. when the laser is used in printing application). These parameters include: Firstly, the threshold current, which is much lower than double heterostructures laser (DH) and separate confine heterostructures (SCH). Secondly, it has a higher external quantum efficiency. Thirdly, the characteristic temperature ( $T_0$ ) is larger, which is an important factor for high brightness laser (42, 128). The advantage of the GRINSCH structure over the DH and SCH structure is the superior suppression of the loss of carriers, due the internal electric field in the sloped GRINSCH. This loss is the leakage of carriers when the laser is injected with current to areas outside the quantum well region. This is applicable to a typical p-i-n laser structure.

### 3.5.2 High power GRINSCH structures with high COMD level and low beam divergence.

The applications of high brightness lasers require high power with low beam divergence. This ensures a lower design tolerance for the optics. In the case of fibre coupling, this means a higher coupling efficiency. As shown previously, the high brightness design requires the suppression of catastrophic optical

mirror damage (COMD) by means of non-absorbing mirrors (35, 138, 139). However, high performance requires an appropriate design of the epitaxial semiconductor structure. By carefully designing the vertical epitaxial structure, it is possible to reduce the far-field of the laser light and simultaneously increase the near field spot size. This results in a higher COMD power, which is an essential design goal for a high brightness laser. The highest power achieved prior to the COMD can be expressed with the following equation (144, 145, 146):

$$P = \frac{p \cdot w \cdot d}{\Gamma}, \quad (3.13)$$

where P is the maximum power achieved prior to COMD;

p is the characteristic COMD power related to the material which is actually the power density measured in (MW/cm<sup>2</sup>);

w is the strip width for the laser device;

d is the quantum well width of the material, and;

Γ is the optical confinement factor.

The values for characteristic power density P<sub>COMD</sub> can be found in (144). The value for a GaAs active region has been given to be 10-12 MW/cm<sup>2</sup>.

The COMD mechanism is directly interrelated with the existence of large amounts of nonradiative recombination centres, due to oxides and segregated atoms on the surface (140). The local heating process starts due to the nonradiative recombination of carriers simultaneously with increased current. A measure of the density of the nonradiative recombination centres at the surface is surface recombination velocity. The increase of surface recombination

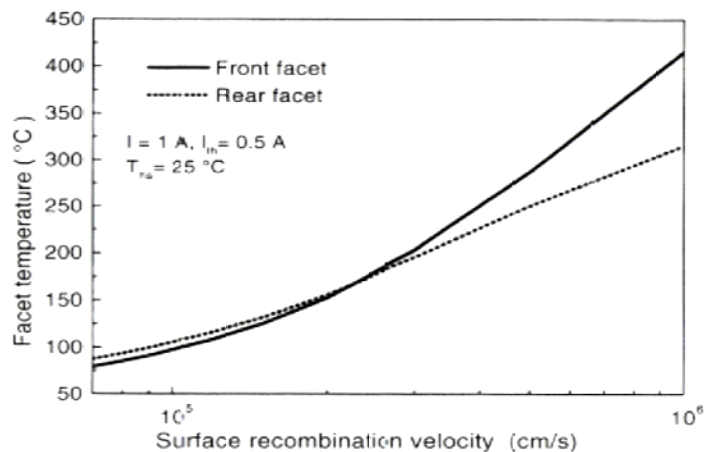


Figure: (3.5): Calculated facet temperature as a function of surface recombination velocity for quantum well AlGaAs/GaAs laser diode array. (Ref 141)

velocity results in the heating of both rear and front facets of laser diode. This is illustrated in figure (3.5) taken from (141). In the figure, the temperature of the rear facet is higher than that for the front facet for values of SR velocity lower than  $2 \times 10^5$  cm/s. However, at SR velocity  $\geq 2 \times 10^5$  cm/s, the temperature of the front facet exceeds the rear facet temperature.

Since the surface recombination velocity is the characteristic of surface recombination rate, it is a source of the heating that initiates COMD. One of the ways of circumventing the possibility of COMD occurrence is the reduction of the SR velocity. This can be decreased by cleaving the wafer in ultrahigh vacuum and coating the facets with passivation layers (142). Moreover, additional method includes surface treatment with sulphuric reagents to replace the non-stable oxide. The sulphur treatment results in a reduction of nonradiative surface recombination velocity and an increase in the COMD level (134).

The equation (3.13) has been reported to have another form as in equation (3.14) from (145);

$$P_{max,CW} = \left(\frac{d}{\Gamma}\right) W \left(\frac{1-R}{1+R}\right) \bar{P}_{COMD} \quad (3.14)$$

Inspection of both equations (3.13) and (3.14) reveals that the concept and the ideas are the same. The term  $p = \bar{P}_{COMD}$ , the only difference is in the reflectivity term that was added, where R is the front facet reflectivity.

The design of the high power laser structure should be focused on maximising the power before the onset of COMD. The design of the epitaxial structure plays an important role in achieving a high brightness laser. There are many high power laser epitaxial structures reported in the literature. Garbuzov *et. al.* (1996) (155) used a broad waveguide structure in order to increase the optical power. Although, an improvement in COMD power is achieved, the width of the far-field was slightly high, with value of about  $40^\circ$ . Such a laser with a broad waveguide is susceptible to instabilities and lasing in higher order modes. Therefore, careful design of the cladding is essential in order to suppress the high order modes and reduce the propagation losses. The other epitaxial structure type is the asymmetric large optical cavity used by Buda (146). In this structure, the quantum well is positioned far from the maximum optical field distribution. One of the problems with this structure is that it

supports higher order modes. The concept of high  $d/\Gamma$  has been utilised by I.B.Petrescu-Prahova 2009 (102), namely by asymmetric structure that has a waveguide with quantum well and an optical trap located in the n-region. The benefit of the optical trap is that it shifts the optical distribution towards the n-region near the trap, which reduces the free carrier absorption as well as the confinement factor. The benefit of a higher value of  $(d/\Gamma)$  is that a high  $P_{\max}$  can be achieved before COMD occurs. If this is combined with designing an optical trap in the n-region to enlarge the mode, a smaller far-field can also be attained. The other advantage of having a large spot size is that the beam will be closer to a truly circular beam, which is ideal for coupling into a fibre and simplifies the optical system during packaging. Furthermore, other problems associated with high power lasers may be minimised, such as spatial hole burning and self focusing. There are, however, some limitations. Firstly, decreasing the confinement factor could make it difficult to obtain sufficient gain. Secondly, Longer devices with low internal loss would be required. In this work, a structure with a secondary waveguide in the n-cladding was used, which is a far-field reduction layer (FRL). The detail and analysis of the structure are presented in section 3.6.

### **3.5.3 GaAs/AlGaAs quantum well optical properties**

#### **3.5.3.1 Free carrier absorption, bandgap shrinkage and band filling**

The carriers effect on the optical properties of the GaAs/AlGaAs quantum wells can be expressed in terms of three main effects, free carrier absorption, bandgap shrinkage and band filling. In this section, these effects are briefly discussed. Firstly, in the free carrier absorption effect, the free carriers in a given band have the possibility of absorbing a photon and moving to a higher energy level within the band. This is called free carrier absorption. (135, 136). Free carrier absorption has to be taken into account in the epitaxial design of a high power semiconductor laser. Specifically, the optical field interaction with the p-doped cladding region of the semiconductor laser has to be minimised. One of the reasons is that the light hole has a low effective mass. Therefore, the ability to scatter light is greater in the p-region. Furthermore, the free carrier loss results in a negative index change. These effects can be seen through the Drude model (136), whereby the index change due to free carrier

loss is proportional to the concentration of carriers and the wavelength squared. The free carrier loss is higher in the p-doped cladding than that in the n-cladding regions. This makes the modifications for the epitaxial design improvement purposes of n-cladding layers possible. Such improvements may include: adding blocking layers for reducing the leakage current and inserting far-field reduction layers in a semiconductor laser diode.

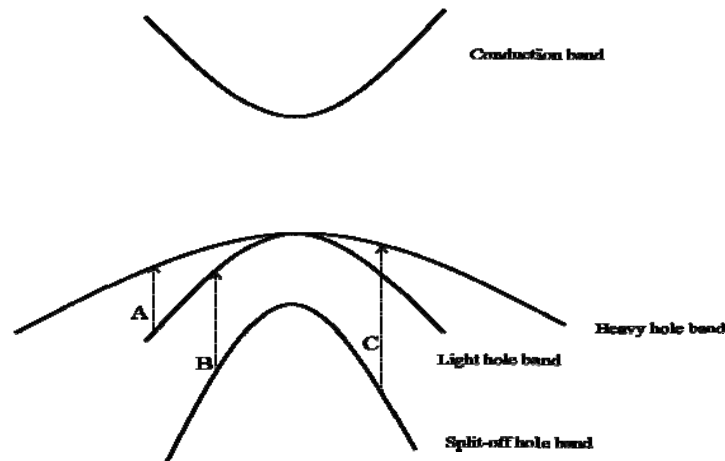


Figure (3.6) Intervalence band absorption is depicted, where three transitions are observed : the light-heavy-hole band transition (A), the split-off-light-hole band transition (B) and transition (C) which is between split-off hole band and heavy hole band.

The free carrier absorption in the valence band, which is known as intervalence band absorption (IVA) is an important contributor to the carrier absorption losses in the p-doped region. This loss is the main reason for higher losses in the p-region than that in the n-region.

The IVA occurs via direct optical absorption, as illustrated in figure (3.6) above. The IVA is very important, which must be considered in any semiconductor laser design. There are three possible types of vertical transitions (151, 152): the light-heavy-hole band transition (A) is not considered to be important. The reason for this, is that the transition energies are small for all heavy-hole states with a high probability of hole occupancy. Next in the energy, is the split-off-light-hole band transition (B), which is neglected on the basis of a low density of states in the light-hole band. Moreover, there is a very low hole occupancy of final states for transitions at the band-gap energy. The absorption at high energies leads to cavity loss in lasers, which is attributed to the transition (C). This transition occurs between split-off hole band and heavy hole band. The IVB

absorption contribution to total loss must be taken into account in quantum well laser design. The loss due to the free carrier absorption is substantial in GaAs/AlGaAs lasers (153). Therefore, it must be considered. The inter-valence band absorption (p-doped region loss) is higher than inter-conduction (n-doped region loss) due to the larger hole absorption cross section. This is described in figure (3.7) taken from (154).

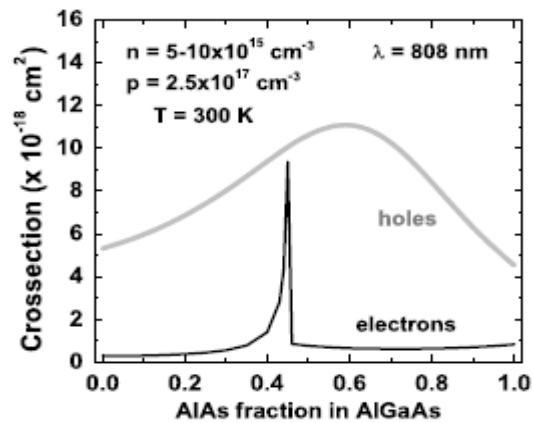


Figure (3.7) Free carrier absorption cross section for 808 nm structure as a function of the fraction of AlAs in AlGaAs. (Courtesy from ref 154)

Secondly, the band shrinkage effect occurs when a high concentration of injected electrons occupies the states at the bottom of the conduction band causing their wave functions to overlap. This overlapping of the electron wave functions forms a gas of interacting particles that repels one another by Coulomb forces. These effects result in the lowering of energy of the conduction band edge. At the same time, similar effects for the hole increase the energy of the valence band edge. The sum of the effects on the conduction band electrons and valence band holes is the bandgap shrinkage effect. The estimated bandgap shrinkage effect (136) is proportional to the cubic root of the carrier concentration. Furthermore, this effect is negligible for low carrier concentrations due to the lack of particle interactions inside the quantum well sub-bands.

The third effect is the band filling effect that occurs when the material is doped. This causes reduction in the absorption for photon energies above the bandgap. As the states of conduction band electrons and valence band holes become occupied, the energy required for an electron to be excited from the valence band to the conduction band will be greater than the bandgap. This effect manifests itself as a change in the refractive index for photon energies near the bandgap.

### 3.5.3.2 Refractive index change in high brightness quantum well laser diode structures

In this section, the carrier induced refractive index change will be addressed due to its effects on the operation of high power lasers. The factors that most affect the refractive index variation in a semiconductor laser can be expressed by the following equation;

$$\Delta n_{(total)} = \Gamma \Delta n_1 + \Gamma \Delta n_2 + \Delta n_3 + \Delta n_4, \quad (3.15)$$

where  $\Gamma \Delta n_1$  is the variation due to free carriers in the active region;  $\Gamma \Delta n_2$  is the variation due to injected carriers in the active region;  $\Delta n_3$  is the index variation due to temperature change and  $\Delta n_4$  is the ridge waveguide step change. The first two terms include the variation due to free carriers and injected carriers, which can be expressed by equation (3.16a) (167):

$$\Delta n_{(carriers)} = -\frac{N\lambda^2 e^2}{8\pi^2 c^2 m \xi n}, \quad (3.16a)$$

where  $N$  is the free carrier concentration,  $e$  is the electron charge,  $m$  is the electron hole effective mass,  $n$  is the refractive index,  $\lambda$  is the wavelength of light,  $c$  is the speed of light, and  $\xi$  is the dielectric constant.

Regarding the free carriers effect (i.e.  $\Delta n_1$ ) such as free carrier absorption, the effect on the refractive index can be obtained, directly from Drude model (136). It results in a negative index change. The term  $\Delta n_2$  in equation (3.15) can be due to band filling effect. In a system, when the carrier injection is increased the quasi-Fermi level will deepen into the conduction and valence bands. The corresponding absorption constant change  $\Delta \alpha(E)$  is given by (136):

$$\Delta \alpha(E) = \alpha_0(E)[f_v(E) - f_c(E) - 1], \quad (3.16b)$$

where  $f_v(E)$  and  $f_c(E)$  are the Fermi-Dirac distribution functions in the valence and conduction bands respectively and  $\alpha_0(E)$  is the unperturbed absorption spectrum. Equation (3.16b) above can be substituted into the Kramers-Kronig Relationship, the change in the refractive index ( $\Delta n_2$ ) from the band filling effect can be obtained.

The third term in equation (3.15) is the index variation due to temperature change, which can be expressed by:

$$\Delta n_{(Temp)} = 0.0004 \Delta T, \quad (3.17)$$

where  $\Delta T$  is the temperature variation.

For a GaAs laser diode, the lasing threshold carrier density is  $1.02 \times 10^{18} \text{ cm}^{-3}$  (15) at room temperature. If the wavelength is  $0.83 \text{ }\mu\text{m}$  and assuming  $n= 3.41$  and a free carrier concentration of  $3 \times 10^{18} \text{ cm}^{-3}$ , then  $(\Delta n_{(carriers)}) = - 0.00848$ .

The lasing regime can change from index guiding to a gain guiding regime, if there was an index change of  $1 \times 10^{-3}$  (164). Thus, if the operating current is increased beyond certain limits the combined effects on the index change will have a profound effect on the lasing condition of a laser diode. Furthermore, the index change due to free and injected carriers becomes a limiting factor at high injection currents for the single spatial mode operation of semiconductor lasers.

### 3.6 The chosen GaAs/AlGaAs quantum well material structure

The semiconductor material design that is used in this project is based on the GaAs/AlGaAs system and was supplied by Intense Ltd. The high power laser structure used is shown in the table (3.2). The novel epitaxy design layer that is being used in the project is the graded index separate confinement heterostructure (GRINSCH) type design with a far-field reduction layer (optical trap).

Specification						
Layer No.	Material	Composition	Thickness (um)	C-V Doping Level (cm <sup>-3</sup> )	Type	Dopant
17	GaAs	x	0.100	$1\text{E}+19 > 1\text{E}+20$	p	Zn
16	$\text{Al}_x\text{Ga}_{1-x}\text{As}$	$0.32 > 0.05$	0.120	$1\text{E}+18 > 5\text{E}+18$	p	Zn
15	$\text{Al}_x\text{Ga}_{1-x}\text{As}$	0.32	1.700	1E18	p	Zn
14	$\text{Al}_x\text{Ga}_{1-x}\text{As}$	0.32	0.200	$5\text{E}+17 > 1\text{E}+18$	p	Zn
13	$\text{Al}_x\text{Ga}_{1-x}\text{As}$	$0.20 > 0.32$	0.1200			U/D
12	GaAs		0.0044			U/D
11	$\text{Al}_x\text{Ga}_{1-x}\text{As}$	0.20	0.0090			U/D
10	GaAs		0.0044			U/D
9	$\text{Al}_x\text{Ga}_{1-x}\text{As}$	$0.27 > 0.20$	0.070			U/D
8	$\text{Al}_x\text{Ga}_{1-x}\text{As}$	$0.30 > 0.27$	0.030	1E17	n	Si
7	$\text{Al}_x\text{Ga}_{1-x}\text{As}$	$0.32 > 0.30$	0.020	$5\text{E}+17 > 1\text{E}+17$	n	Si
6	$\text{Al}_x\text{Ga}_{1-x}\text{As}$	0.32	0.750	$5.00\text{E}+17$	n	Si
5	$\text{Al}_x\text{Ga}_{1-x}\text{As}$	$0.29 > 0.32$	0.350	$5.00\text{E}+17$	n	Si
4	$\text{Al}_x\text{Ga}_{1-x}\text{As}$	$0.32 > 0.29$	0.350	$5.00\text{E}+17$	n	Si
3	$\text{Al}_x\text{Ga}_{1-x}\text{As}$	0.32	1.600	$7.00\text{E}+17$	n	Si
2	$\text{Al}_x\text{Ga}_{1-x}\text{As}$	$0.05 > 0.32$	0.200	$2\text{E}+18 > 7\text{E}+17$	n	Si
1	GaAs		0.500	$2.00\text{E}+18$	n	Si

Table (3.2) GaAs/AlGaAs epitaxial layer structure used in the project for high power MMI array laser.

This epitaxial structure was designed by Dr. Bocang Qui (103, 148) from Intense. The structure was grown by metal organic chemical vapour deposition (MOCVD). The upper 100 nm GaAs cap layer is heavily p-doped with an average Zn doping of  $5 \times 10^{19} \text{ cm}^{-3}$ , followed by a graded  $\text{Al}_{(0.32-0.05)}\text{Ga}_{(0.68-0.95)}\text{As}$  layer of thickness of 120 nm p-doped with  $[\text{Zn}] = 3 \times 10^{18} \text{ cm}^{-3}$ . This layer is followed by a 1700 nm  $\text{Al}_{0.32}\text{Ga}_{0.68}\text{As}$  layer, p-doped with  $[\text{Zn}] = 3 \times 10^{18} \text{ cm}^{-3}$ . The cladding layer is finished with a third layer of 200 nm thick  $\text{Al}_{0.32}\text{Ga}_{0.68}\text{As}$ , which is p-doped with  $[\text{Zn}] = 3 \times 10^{18} \text{ cm}^{-3}$ .

### 3.6.1 Core waveguide layers heterostructure (SCH) layers

High brightness laser diodes make use of a graded index separate confinement heterostructure with a far-field reduction layer, which effectively provides the optical guiding layer as well as ensuring carrier confinement by using quantum wells. The upper and lower claddings have lower refractive indices to ensure core waveguiding.

The waveguide core layer consists of an undoped upper  $\text{Al}_{(0.20-0.32)}\text{Ga}_{(0.80-0.68)}\text{As}$  barrier layer with a thickness of 120 nm. The structure has two 4.4 nm thick GaAs quantum wells separated by a 9 nm  $\text{Al}_{0.20}\text{Ga}_{0.8}\text{As}$  barrier.

For a high brightness structure, the maximum power (P) must be maximised before COMD occurs. For example, if we are to calculate the maximum P achieved for this structure:

$$P = \frac{p \cdot w \cdot d}{\Gamma}, \quad p_{\text{comd}} = 24 \text{ MW/cm}^2, \quad w = 100 \text{ } \mu\text{m} \text{ broad area laser width, } \Gamma = 0.011, \quad d = 4.4 \text{ nm}$$

The  $\Gamma$  value has been calculated for the structure using a commercial package from Photon Design which is called Fimmwave.

$$P = \frac{p \cdot w \cdot d}{\Gamma} = \frac{24 \cdot 100 \cdot 10^{-4} \cdot 0.0044 \cdot 10^{-4}}{0.011}, \quad \text{then } P = 9.6 \text{ W.}$$

This is a very good power compared to what is reported in the literature even-though the ratio ( $d/\Gamma$ ) is around  $0.4 \text{ } \mu\text{m}$  for the structure used. The equation above shows that increasing  $d/\Gamma$  will result in increased  $P_{\text{max}}$ , which is the maximum power achieved prior to COMD. Recently, the  $P_{\text{max}}$  value was significantly increased to about 26.1 W for a  $90 \text{ } \mu\text{m}$  wide broad area laser (102) by using the GRINSCH structure with an optical trap that has high  $d/\Gamma$  value of  $1.19 \text{ } \mu\text{m}$ .

### 3.6.2 Lower cladding (Trap region)

The lower cladding, which is the n-type region, contains the far-field reduction (trap) layer as, illustrated in figure (3.9). This has been positioned in the n-region for two reasons. Firstly, the free carrier absorption loss in this region is much lower than in the p-region. Secondly, this layer (as the name suggests) reduces the vertical far-field by trapping part of the optical field, while keeping the optical losses low. A standard separate confinement heterostructure usually does not have the far-field reduction layer, as illustrated in figure (3.8).

The far-field reduction layer (or trap region) not only reduces the far-field, but also increases the mode spot size. Hence, this reduces the power density at the facet. This is a feature that is very influential in increasing the maximum P before COMD happens. This layer inserted in the lower cladding does not have an impact on the optical overlap. The other benefits of this design are the suppression of higher mode lasing, and a better coupling efficiency. The large kink power relates to the enlarged optical mode due to the far-field reduction layer.

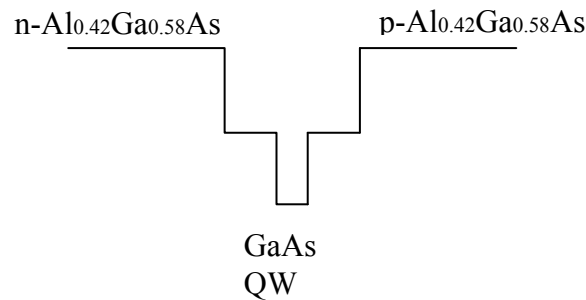


Figure (3.8) Standard grown structures (Separate confinement heterostructure)

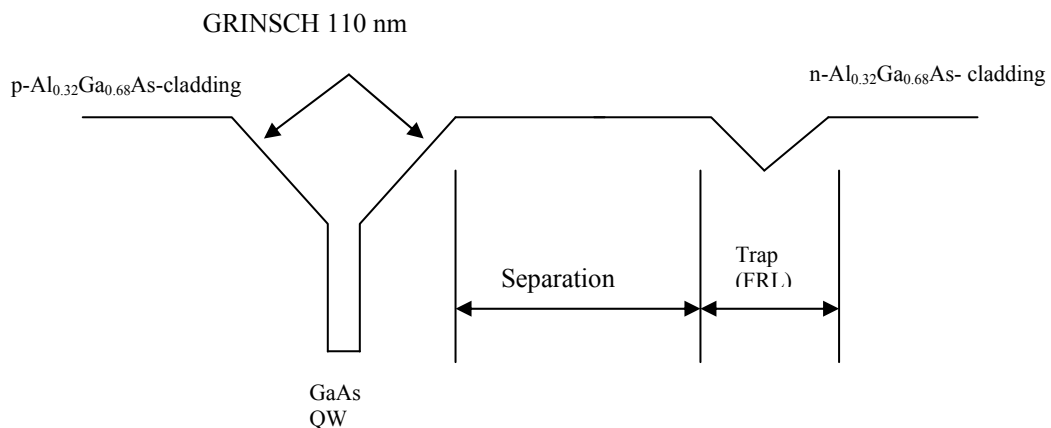


Figure (3.9) Intense designed structures (GRIN SCH) with a trap (far-field reduction layer)

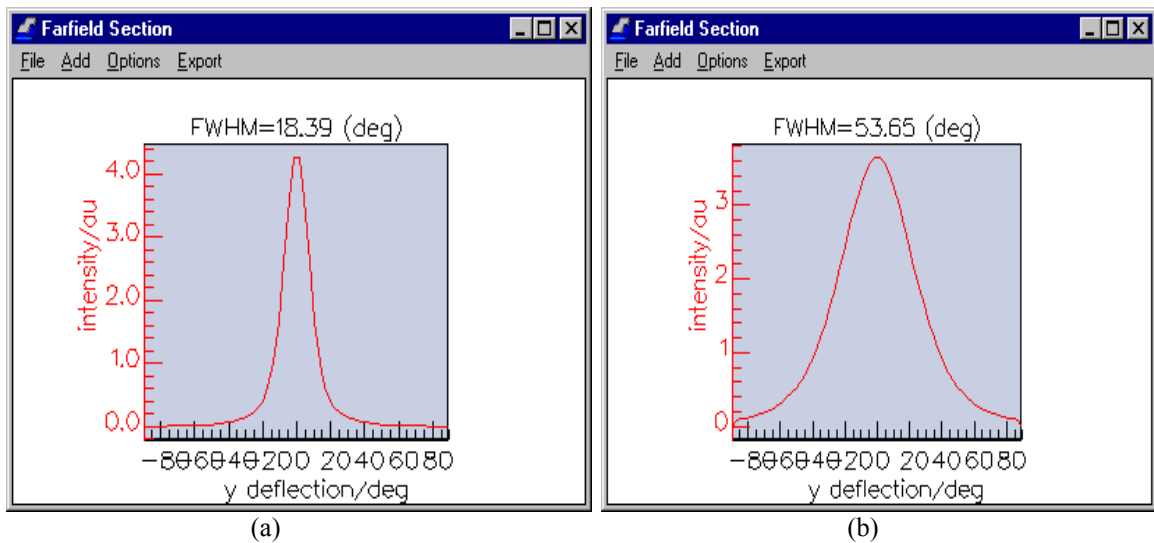


Figure (3.10): (a) Fimmwave simulation of the vertical far-field for a GRINSCH structure with far-field reduction layer. (b) Fimmwave simulation of the vertical far-field for a conventional structure.

To calculate the far-field, FIMMWAVE from Photon Design, a commercial simulation package, was used. Both the horizontal and vertical far-fields were calculated for a single mode ridge waveguide structure. The simulation was carried out for both structures-the optical trap structure (FRL) and the standard structure. The simulations indicate that the former structure has a much smaller vertical FWHM far-field divergence of about  $18.39^\circ$  than that for the standard design, which is about  $53.65^\circ$ . This can be found clearly in figures (3.10a) and figure (3.10b). The very low vertical far-field value is due to the existence of the optical trap (far-field reduction layer) in the Intense design.

The results of the simulation for the Intense designed structure can be seen in figure (3.10a). The far-field reduction layer has resulted in the reduction of the far-field from  $26^\circ$  to around  $18^\circ$  (Fimmwave shows that this value is about  $18.39^\circ$ ).

The parameters that were taken into account in the design of this structure were (148): the thickness of the trap layer, the separation between the GRINSCH and the trap layer and the material composition at the middle point of the trap layer. In this section, they are mentioned briefly. The vertical far field is plotted versus the thickness of the trap layer (FRL) and the confinement factor, as shown in figure (3.11). From the graph, it is evident that the lowest vertical far-field can be as low as  $17^\circ$ , reduced from  $26^\circ$ .

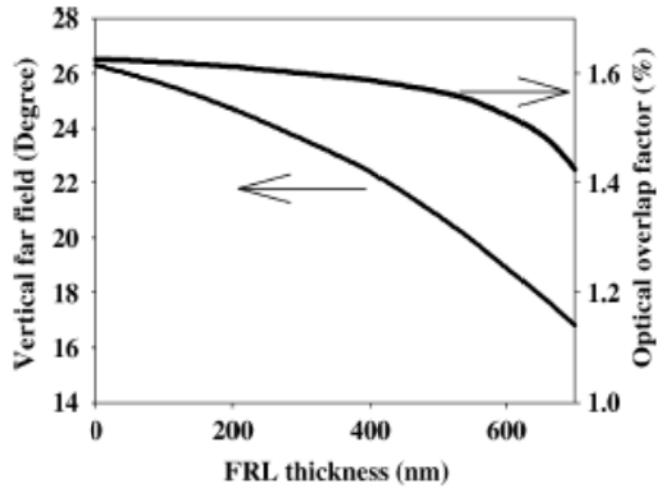


Figure (3.11): Vertical far-field plotted vs. the FRL (trap) thickness and optical overlap factor. Reference (148)

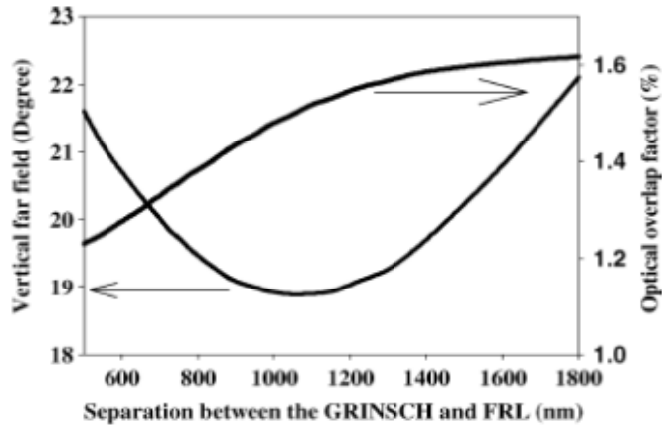


Figure (3.12): separation between GRINCH and and FRL (trap) nm. Reference (148).

Figure (3.12) shows the plot of the vertical far-field and the optical overlap factor versus the trap layer distance from the GRINCH. For a minimum vertical far-field, the separation between the GRINCH needs to be around 1100 nm. The other reason that the V-profile is superior to the conventional epitaxial design is that the suppression of the lasing of higher order modes causes the kink power to increase.

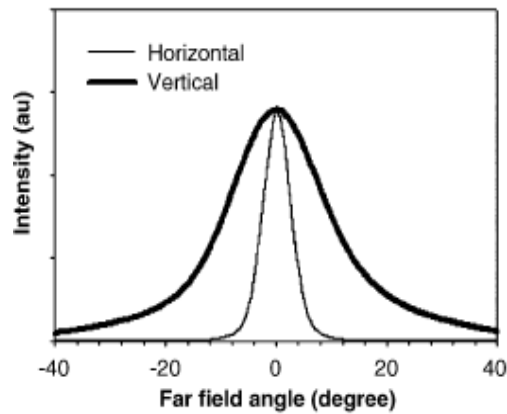


Figure (3.13): Horizontal and vertical far-field plots for 830 nm high Intense epitaxial higher power design with V profile. (ref. 165)

Intense Ltd has designed and tested a ridge waveguide laser. Figure (3.13) shows the far-field characteristic of the 830 nm ridge waveguide laser, which has the reduction layer (J.H Marsh ) 2006 (165).

### 3.7 Broad area laser characterisation

In order to evaluate the quality of the EPI layer struture that will be used in the design and fabrication of the high brightness MMI laser, broad area laser diodes have been fabricated. Oxide stripe lasers with a 75  $\mu\text{m}$  stripe width have been fabricated. Broad area laser fabrication is an essential part of the evaluation of the epitaxial design. Two laser structures have been used. The first one is a standard laser with no optical trap or far-field reduction layer. The second structure includes an optical trap or far-field reduction layer. Figure (3.14) shows a schematic diagram of the GaAs/AlGaAs broad area laser.

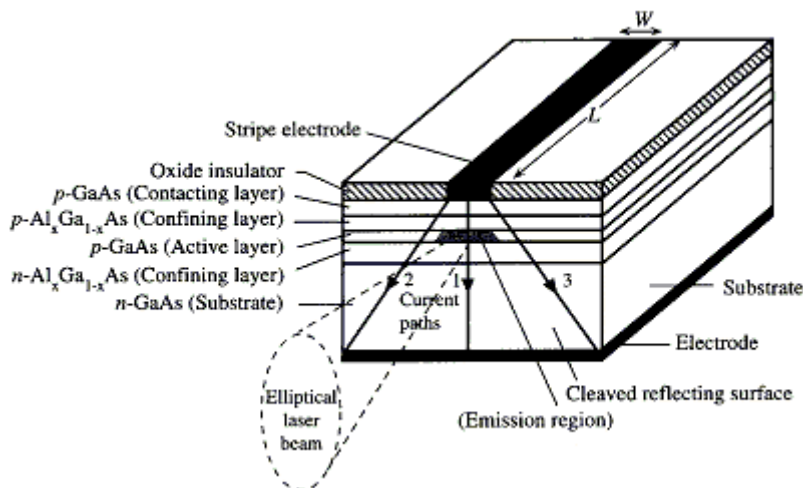


Figure (3.14) Typical oxide stripe (broad area) laser (Courtesy of reference 147)

The laser fabrication is very simple and uses just one lithographic stage. It is a useful and quick test of the semiconductor laser material, from which the threshold current density, internal losses and internal quantum efficiency can be extracted.

To effectively measure the parameters mentioned earlier, the testing is performed in a pulsed mode to avoid the heating effects which occur in continuous wave operation.

### 3.7.1 Theory

The theory and the methodology used to analyse the broad area laser structures will be summarised in this section.

For laser oscillation to occur, the gain must be equal to the loss at threshold. Thus, for a double quantum well semiconductor laser, the gain at threshold can be expressed by (156):

$$n\Gamma_w g_{th} = \alpha + \frac{1}{2L} \ln \frac{1}{R_1 R_2} \quad , \quad (3.18)$$

where  $g_{th}$  is the gain at threshold for a single quantum well,  $n$  is the number of the quantum wells,  $\Gamma_w$  is the optical confinement factor for a single quantum well,  $L$  is the cavity length and  $R_1$ ,  $R_2$  are the reflectivities for the front and back facets.

$\alpha$  is the total internal loss in the laser cavity. This loss can be due to several factors: free carrier absorption in the active region and the cladding layer, intervalence band absorption in the p-doped region (152, 153, 158). The other factor that can affect the internal loss is the scattering at rough surfaces and the imperfection of the waveguide (159).

The external quantum efficiency is an important parameter that can be extracted experimentally from LI curves. The external quantum efficiency can be calculated using the equations:

$$\eta_{ext} = \eta_{int} \frac{\text{mirror loss}}{\text{total loss}}$$

$$\eta_{ext} = \eta_{int} \frac{\frac{1}{2L} \ln \frac{1}{R_1 R_2}}{\alpha + \frac{1}{2L} \ln \frac{1}{R_1 R_2}}$$

By simplifying we get,

$$\frac{1}{\eta_{ext}} = \frac{1}{\eta_{int}} + \frac{2\alpha}{\eta_{int} \ln \frac{1}{R_1 R_2}} L, \quad (3.19)$$

where  $\eta_{int}$  is the external quantum efficiency (the fraction of injected electrons converted to optical power).

Equation (3.19) indicates that by plotting  $\frac{1}{\eta_{ext}}$  against device length (different cleaved laser length)  $L$ , which results in a straight line where the y-intercept is  $\frac{1}{\eta_{int}}$  and the gradient of the line is  $\frac{2\alpha}{\eta_{int} \ln \frac{1}{R_1 R_2}}$ .

From the y-intercept and the gradient, values for the internal quantum efficiency and internal loss coefficient can be estimated for the material.

The external quantum efficiency can be calculated from the slope of the measured LI curve above threshold (156, 159) using:

$$\eta_{ext} = 2 * \frac{q}{hf} \left( \frac{dp}{dI} \right)_{I > I_{th}}, \quad (3.20)$$

where  $hf$  and  $p$  are the photon energy and optical output power, respectively.

The threshold gain is related to the current density as shown by McElroy (156) and Kurobe (159), who found that the gain can be approximated by the following relationship:

$$\frac{g_{th}}{g_0} = \ln \left( \frac{J_{th} \eta_{int}}{J_{tr} n} \right), \quad (3.21)$$

where  $g_0$  is constant,  $J_{th}$  is the threshold current density and  $J_{tr}$  is the transparency current density. Substituting equation (3.18) into (3.21) yields:

$$\ln(J_{th}) = \left[ \frac{\alpha}{n \Gamma_w g_0} + \ln \left( \frac{J_{tr} n}{\eta_{int}} \right) \right] + \left[ \frac{1}{2Ln \Gamma_w g_0} \ln \frac{1}{R_1 R_2} \right] \quad (3.22)$$

At infinite length ( $L$ ), equation (3.22) can be rewritten in terms of  $J$ :

$$\ln(J_{\infty}) = \frac{\alpha}{n \Gamma_w g_0} + \ln \left( \frac{n J_{tr}}{\eta_{int}} \right) \quad (3.23)$$

Therefore  $\ln(J_{th})$  in equation (3.22) can be expressed by;

$$\ln(J_{th}) = \ln(J_{\infty}) + \left[ \frac{1}{2Ln \Gamma_w g_0} \ln \frac{1}{R_1 R_2} \right] \quad (3.24)$$

Through the fabrication of broad area lasers, all of the parameters can be estimated. For example, the internal loss coefficients, internal quantum efficiency, and the threshold current density for infinite length.  $J_{th(\infty)}$  is important in assessing material quality as it is free from the effects of the facet reflectivity.

### 3.7.2 Experimental results for broad area lasers

Although the standard laser design is not used in this project, the results for this structure are presented here for comparison. The first set of results for broad area standard lasers was obtained using laser test pulse set up in the department. The high power design (epitaxy as in table 3.2) presented in this chapter was tested using Intense's test rig. Therefore, the results for this design are more accurate due to the quality of the test rig used at Intense Ltd. This is why the proposed final device design fabricated was tested using Intense's test rig.

#### 3.7.2.1 Standard laser structure results

Table (3.3) shows the parameters for the standard laser design with no optical trap. The important parameter is the threshold current density at infinite length  $J_{th(\infty)}$ , which is 209 (A/cm<sup>2</sup>). The test results here especially the internal quantum efficiency and the optical loss parameter, are affected by the accuracy of collecting all the light from the facets of the laser. This makes the calculated parameter less reliable. This is particularly true for the internal quantum efficiency and the material loss, which are extracted from the plots of  $1/\eta_{ext}$  as function of L. The measurement of  $J_{th}$  is more reliable than the internal loss ( $\alpha$ ) and  $\eta_{int}$ . The reason for that is the reliability of  $J_{th}$  measurement, which does not suffer from the experimental errors associated with material loss and  $\eta_{int}$  measurement. However, there is a statistical spread in the measured  $J_{th}$  values. This spread may be attributed to non-uniform current injection along the device due to the localised imperfection in the device contacts, and to the imperfection of the cleaved facets (171). We notice from the figure (3.16), that the error in the data points is ( $\pm 2.5\%$ ). From the logarithmic fitting to these data points, the estimated standard error is ( $\pm 10\%$ ) in the value of  $J_{th(\infty)}$ , and the standard error was ( $\pm 16.5\%$ ) and ( $\pm 17.15\%$ ) for internal quantum efficiency and the material loss, respectively.

The internal quantum efficiency was 19 % , which is on the low side. The material loss calculated was  $18 \text{ cm}^{-1}$ . The plots for inverse external quantum efficiency versus cavity length and threshold current density versus the inverse of cavity length can be found in figures 3.15 and 3.16, respectively.

Slope efficiency (dp/dl) W/A	Internal quantum efficiency	Confinement factor ( $\Gamma$ )	$\alpha \text{ (cm}^{-1}\text{)}$	$J_{tr} \text{ (A/cm}^2\text{)}$	$J_{th(\infty)} \text{ (A/cm}^2\text{)}$
0.09	19 %	0.06	18	14	209

Table (3.3): Laser parameters measured from the testing of broad area oxide lasers.

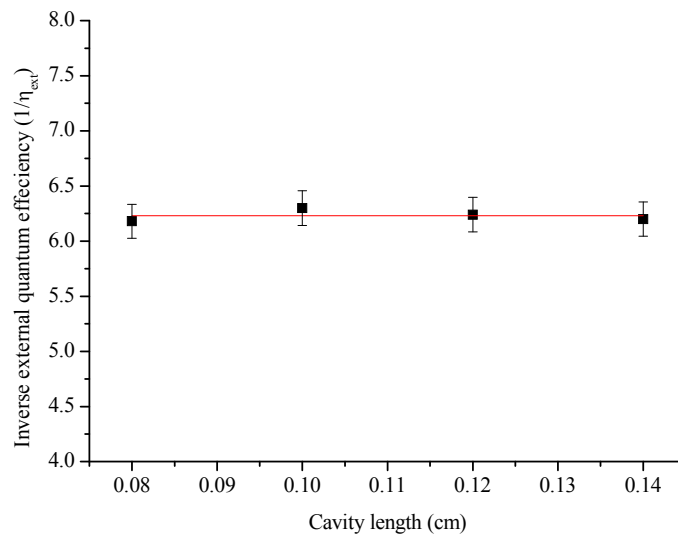


Figure (3.15): The inverse of external quantum efficiency with respect to cavity length for conventional broad area oxide lasers . The test was performed using a 400 ns pulse width, a 1 KHz repetition rate and an operating temperature of  $25^\circ\text{C}$ . The standard error was ( $\pm 16.5\%$ ) and ( $\pm 17.15\%$ ) for internal quantum efficiency and the material loss, respectively.

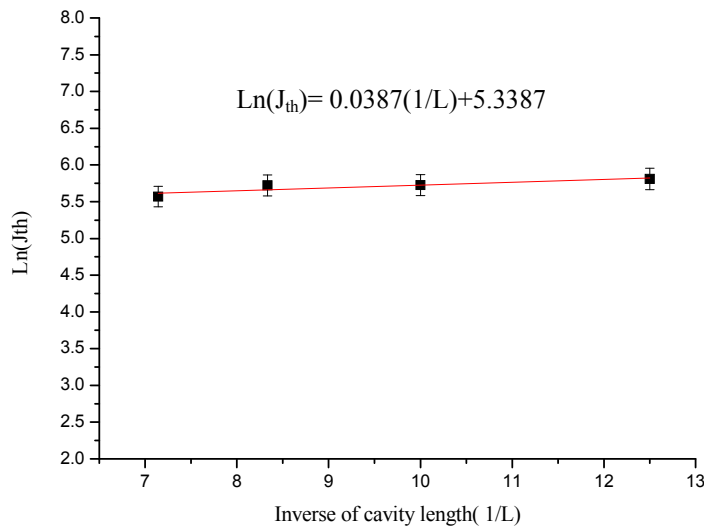


Figure (3.16): Logarithmic plot of threshold current density versus the inverse of cavity length for conventional broad area oxide lasers. Error bars are shown with a percentage error of 2.5 % in the data points. From the fitted logarithmic curve, the error in  $J_{th(\infty)}$  is  $\pm 10$  %. The test was performed using 400 ns pulse width, 1 KHz repetition and operating temperature of 25°C.

### 3.7.2.2 Laser structure results with far-field reduction layer

Table (3.4) represents the parameters for the laser design with an optical trap (d/Γ structure). From the data, we could conclude that this structure is much better, with a threshold current density for infinite length of 175 A/cm<sup>2</sup> and the internal quantum efficiency of 71 %.

Slope efficiency (dp/dI)	Internal quantum efficiency	Confinement factor (Γ)	$\alpha$ (cm <sup>-1</sup> )	$J_{tr}$ (A/cm <sup>2</sup> )	$J_{th(\infty)}$ (A/cm <sup>2</sup> )
50%	71%	0.011	1.59	22	175

Table (3.4): Laser parameters measured from the testing of broad area oxide lasers made using the high power laser design.

The other important parameter is the optical loss, which is 1.59 /cm which is quite low for the GRINSCH laser structure used. However, recent designs based on large optical cavity (LOC) and super large optical cavity (SLOC) have internal losses that are typically around 0.4 cm<sup>-1</sup> (118). Plots of  $1/\eta_{ext}$  versus cavity length and threshold current density versus inverse of the cavity length are presented in figures 3.17 and 3.18, respectively.

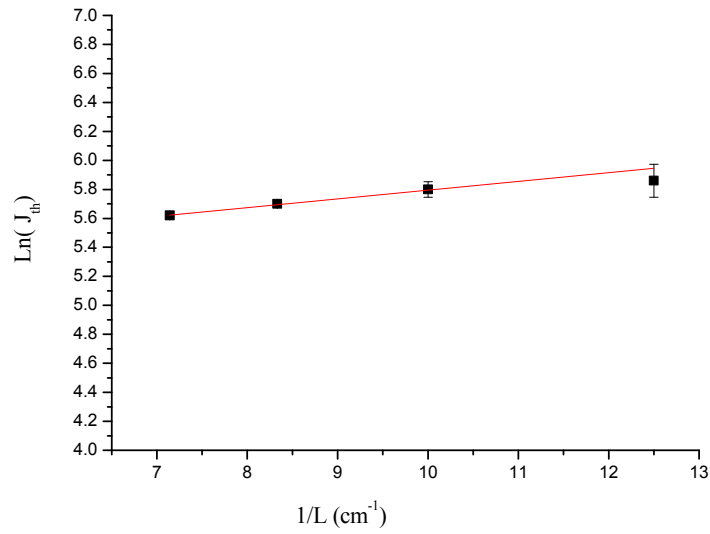


Figure (3.17): Inverse of external quantum efficiency with respect to cavity length for a broad area oxide laser made using high power laser design. The test was performed using a 400 ns pulse width, a 1 KHz repetition rate and an operating temperature of 25°C.

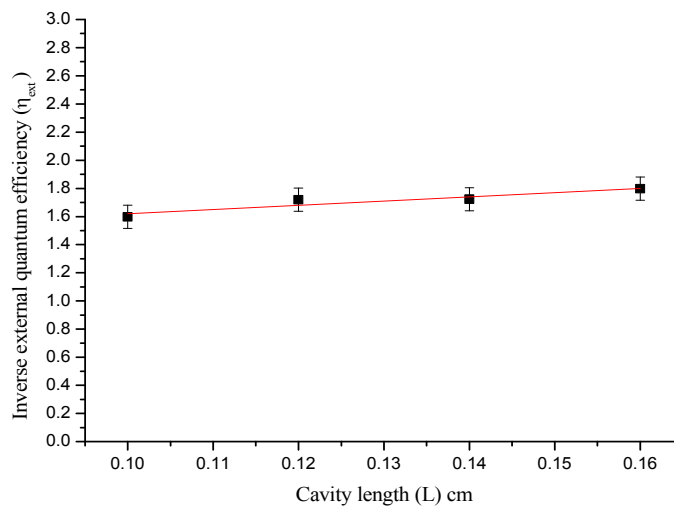


Figure (3.18): Logarithmic plot of threshold current density versus the inverse of cavity length for broad area oxide laser made using high power laser design. The test was performed using a 400 ns pulse width, a 1 KHz repetition rate and an operating temperature of 25°C.

In Figures 3.17 and 3.18 above, when a larger number of the tested devices is included in the analysis, this resulted in a reduction of the error and the uncertainty. Furthermore, the deviation in the parameters can be analysed accurately. In figure (3.17), the error bars are for the standard error. The standard error for the main data points was 2.35 %. However, in the figure the standard error for each data point is illustrated.

Since the internal quantum efficiency is measured from the intercept, which includes a standard error, the ( $\eta_{\text{int}}$ ) incorporates an error of ( $\pm 7.6\%$ ). The material loss, which depends on the gradient of the line, consists of a standard error of ( $\pm 24.6$ ). This value is considered on the high side.

In Figure (3.18) the error bars are plotted. The figure shows that the errors are minute for two of the data points. The standard error of the main data points was 0.83 %.

Since the threshold current density values depend on the accuracy of measuring the material loss ( $\alpha$ ) and the internal quantum efficiency, there will be an accumulated error. The threshold current density depends on the accuracy of the measurement of the transparency current density ( $J_{\text{tr}}$ ). As indicated, there is an inherent standard error for both intercept and the slope of the curve, which affects the accuracy of the threshold current density estimation. The threshold current density for infinite length ( $J_{\infty}$ ) had an error of ( $\pm 5.34\%$ ), where the value measured was ( $179.4 \text{ A/cm}^2$ )  $\pm$  ( $5.34\%$ ). From all this, we conclude that the measured values have a reasonable standard error associated with them. This confirms the validity of the results attained even with associated statistical standard errors, which is the case with any measurement/testing method.

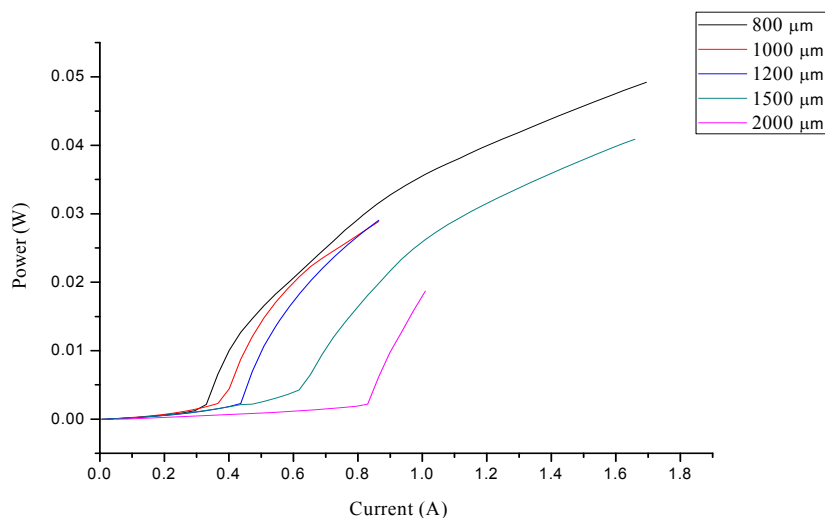


Figure (3.19): LI curves for broad area lasers measured using pulsed measurements (400 ns pulse width and 1 KHz repetition rate). Roll over effects can be seen due to heating.

Figure (3.19) shows the light -vs- current characteristics measured with an in-house laser test system using pulsed measurements for different cavity lengths.

Heating effects can be observed as rollover in the LI curves. These LI curves were not used for laser diode evaluation purposes. It is worth indicating that that the observed rollover at very low current of  $1.5 I_{th}$ , was due to problems with device heating due non-optimum device mounting, or severe leakage of the device.

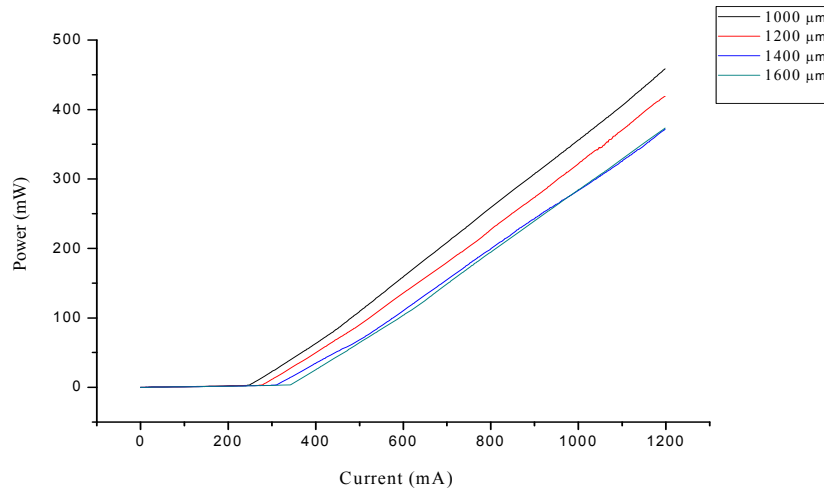


Figure (3.20): LI curves for broad area lasers using pulsed measurements with a  $5\mu s$  pulse duration at 1KHz repetition rate and an operating temperature of  $25^\circ C$ . An optimised Intense Ltd laser test system was used to perform the measurements.

The LI curves showed the effect of heating. Therefore, for proper evaluation a test rig with temperature control has been used at Intense Ltd. Sample of the data obtained for an optimised and calibrated system is illustrated in figure (3.20). The LI curves seem to curve upward due to the existence of many oscillating modes observed as mini kinks. Such kinks are characteristic of multimode behaviour for a broad area laser. Spatial hole burning is another possible reason for this behaviour.

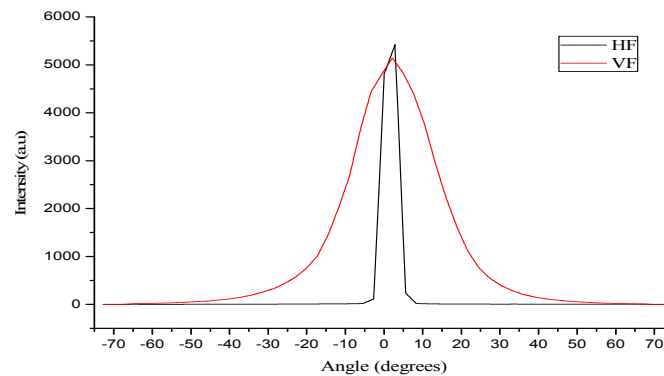


Figure (3.21): Horizontal and vertical far-field patterns for a  $1200\mu m$  broad area laser measured at the 200 mA CW at  $25^\circ C$  operating temperature.

Figure (3.21) shows the horizontal and vertical far-field patterns for a 1200  $\mu\text{m}$  broad area laser using the material with a far-field reduction layer. Figure (3.22) represents the spectral measurement for the BAL with 1mm cavity length. It shows a central peak of 823.9 nm.

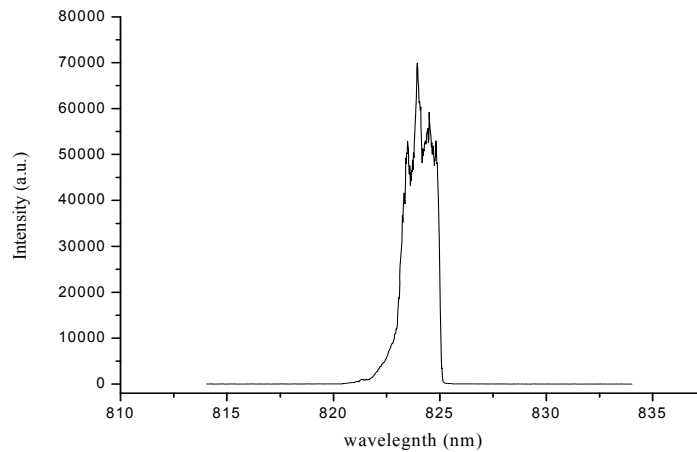


Figure (3.22): Emission spectra measured for a 1200  $\mu\text{m}$  broad area laser for an injection current of 200 mA CW and an operating temperature of 25 °C. The central peak wavelength is 823.9 nm.

### 3.8 Ohmic contacts

Ohmic contacts on a semiconductor are used to allow the flow of electrical current into and out of the semiconductor device. A linear I-V characteristic is expected from an ohmic contact. Any deviation from this linearity would render the contact to behave similar to a rectifying (Schottky) contact, which has a high barrier potential. This affects the flow of current from the metal to the semiconductor and results in a non-linear I-V relationship. When a metal is placed in intimate contact with a III-V semiconductor such as GaAs, the valence and conduction bands of the semiconductor bend to make the Fermi level in the metal and the semiconductor equal at thermal equilibrium. The potential barrier that is generated from the contact depends on the work function of the metal ( $\phi_m$ ) and the semiconductor work function ( $\phi_s$ ). Figure (3.23) shows the band energy diagram for n-GaAs.

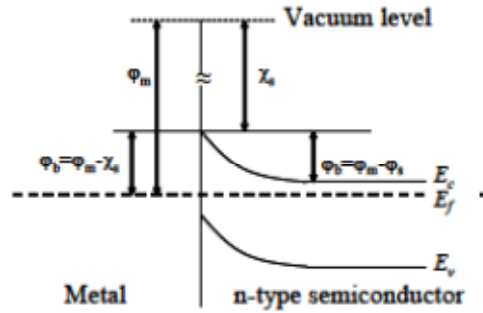


Figure (3.23): band energy diagram for n-GaAs.

The ohmic contact should be designed to have sufficiently low barriers (160), which enable the flow of current through the metal-semiconductor interface by means of quantum tunnelling transport (161). This is a characteristic of present day ohmic contacts. Quantum tunnelling transport can be achieved in an ohmic contact if the semiconductor is highly doped above  $1 \times 10^{19} \text{ cm}^{-3}$ . The reason for that is the narrowing of the depletion region (120, 121). An example of this effect can be seen in Figure (3.24), which shows the energy band diagram for a barrier with high doping, where the field emission (quantum tunnelling) is dominant. The depletion layer in this case is only a few nanometers wide. In fact, the tunneling current increases as the square root of the doping concentration, because the depletion layer width decreases as the square root of the doping concentration.

In this work, a 100 nm GaAs layer is doped with  $[\text{Zn}] = 1 \times 10^{20} \text{ cm}^{-3}$  for the p-contact. The reported specific p-contact resistance  $R_c$  values for this concentration were on order of  $10^{-5} (\Omega \cdot \text{cm}^2)$  (162). The N-type contact for the material used is Si doped ( $[\text{Si}] = 1 \times 10^{18} \text{ cm}^{-3}$ ), which is found in table (3.2).

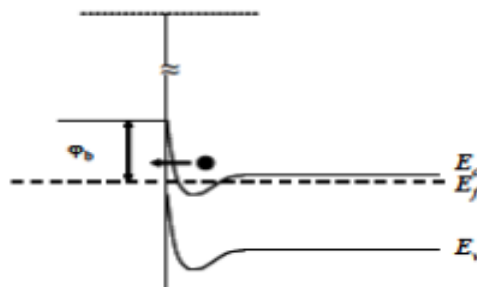


Figure (3.24): Energy band diagram for a metal semiconductor interface where the semiconductor is highly doped

### 3.8.1 Electrical characterisation

The electrical characteristics of a laser diode have a substantial effect on its optical performance. This is particularly true for high brightness lasers, where high currents are injected into the device. These effects can be due to heat and even to electrical breakdown.

Two important parameters are usually used to evaluate semiconductor diodes electrically; the sheet resistance and the metal contact resistivity.

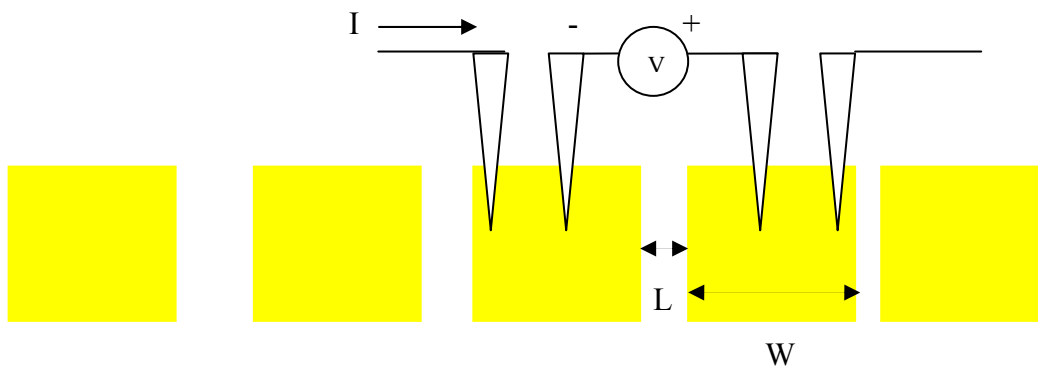


Figure (3.25) Schematic for four point probe measurement for metal pads with different spacing. Gaps ( $L$ ) between metal pads were taken to be (40, 60, 80 and 100  $\mu\text{m}$ ). Width ( $W$ ) and length of the TLM pads were 776  $\mu\text{m}$  x 776  $\mu\text{m}$ .

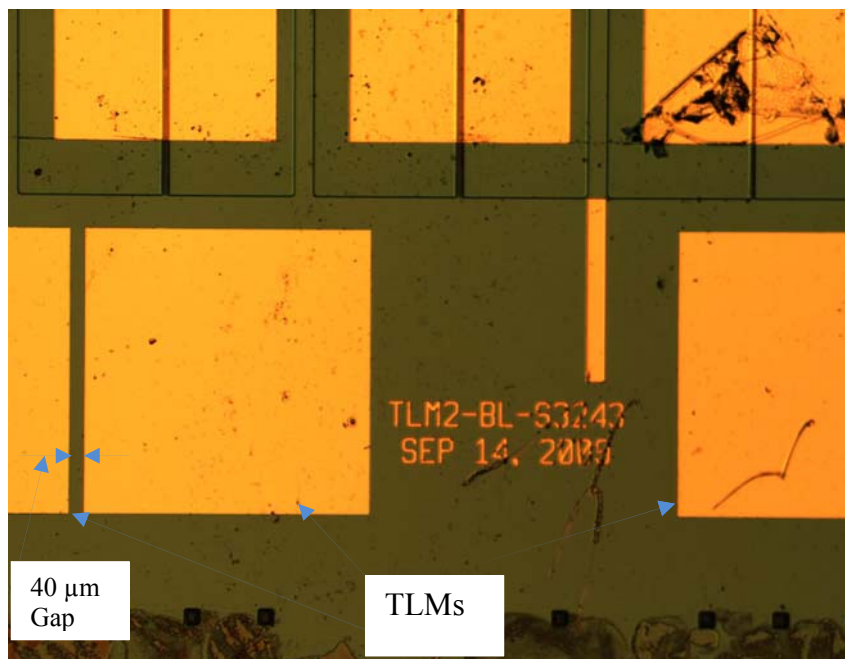


Figure (3.26) TLM were fabricated on each chip for contact resistance measurement. TLM 776  $\mu\text{m}$  x 776  $\mu\text{m}$  are shown in the optical microscope image. These were cleaved and tested prior to contact annealing.

The sheet resistance is important for the uniform distribution of the injected current to the active layer, while the contact resistance should have ohmic characteristics (i.e. linear). In order to measure the sheet resistance and the contact resistance accurately, transmission line measurements are used widely in the characterisation of planar semiconductor devices (120, 162).

To perform transmission line measurements of the contact resistance, metal pads, which are separated by different gaps of 40, 60, 80 and 100  $\mu\text{m}$  are deposited onto the de-oxidised semiconductor, as illustrated in figures (3.25) and (3.26).

The total resistance ( $R_T$ ) across the gaps between all the adjacent metal pads is measured using a 4- probe I-V measurement, as illustrated in the schematic in figure (3.25). The measurement is evaluated using equation (3.25).

$$R_T = \frac{R_{SH}}{W} L + 2 R_C , \quad (3.25)$$

where  $R_{SH}$  is the semiconductor sheet resistance and  $W$  is the width of metal contact pads (776  $\mu\text{m}$ ). To design a measurable contact pad which reflects the contact resistance of the device, it is the normal to place several pads on the same device. Prior to the final device contact resistance anneal, these pads are cleaved off the device then annealed at different temperatures and tested using a 4- probe IV measurement.

### 3.8.2 Measurement and results

For each device fabricated, a few TLM pads are fabricated and these TLM structures are cleaved to be measured, as mentioned in the previous section.

To optimise the temperature for the metal contact annealing process, three to four temperatures points are used say from (360 – 400 ° C) range. The resistance is measured for all TLM structures annealed at the different temperatures. The optimum value will be the lowest contact resistance achieved for one of the annealing temperatures used. Figure (3.27) shows all the results for the different annealing temperatures used. From this graph, an annealing temperature is deduced which offers lowest contact resistance. This happens to be 380 ° C.

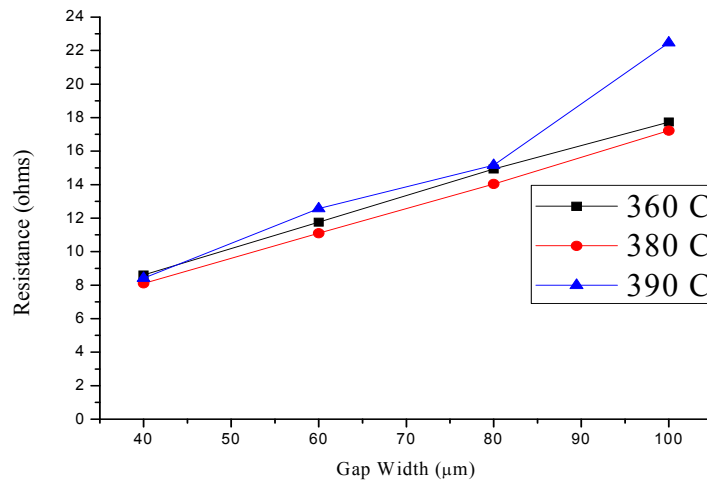
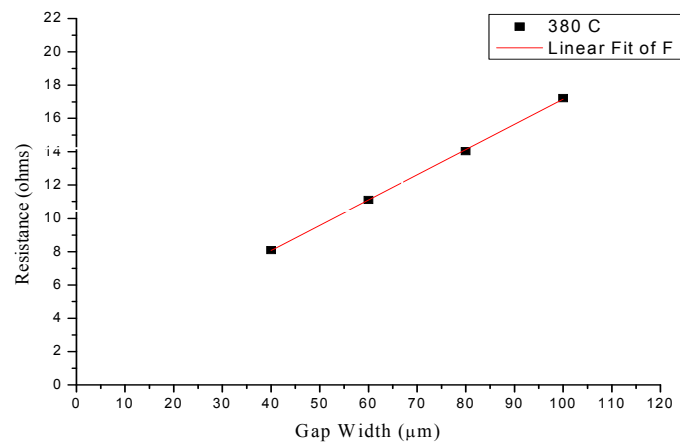
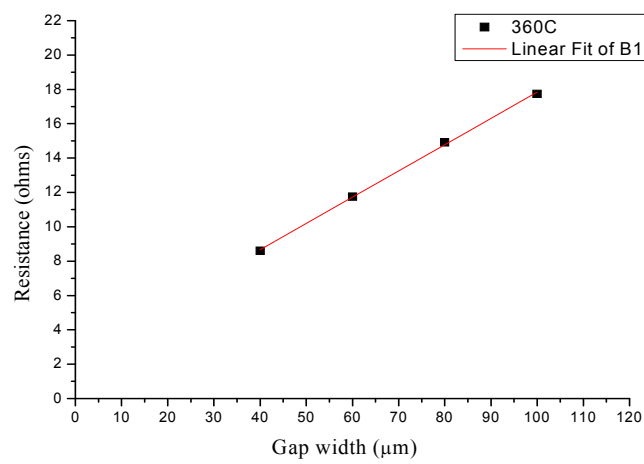


Figure (3.27) Resistance with respect to the TLM gap widths for different annealing temperature.

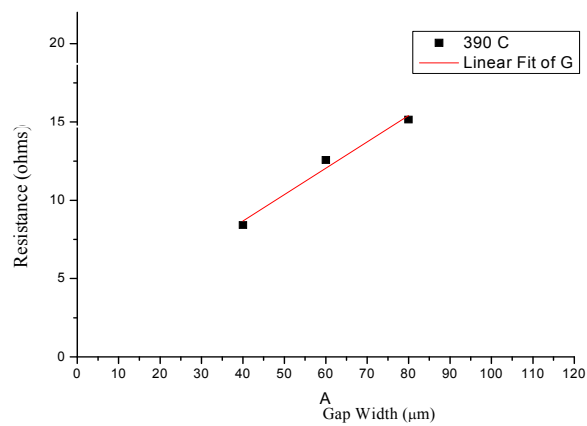
The sample is then annealed at an optimized temperature, which is 380 ° C. The details of the acquired contact resistance can be seen in Figures (3.28) and (3.29).



(a)



(b)



(c)

Figure (3.28) (a) Resistance with respect to the TLM gap width for optimum annealing temperature of 380 C with linear fit. (b) Resistance with respect to the TLM gap width for an annealing temperature of 360 C with linear fit. (c) Resistance with respect to the TLM gap width for an annealing temperature of 390 C with linear fit.

From the graph (3.28b) for 380 ° C, R is plotted as a function of L. One can then infer the value of the contact resistance ( $R_c$ ) by linearly extrapolating the data to the intercept with the R axis. The slope of the line is equal to  $R_{sh}/W$ . Therefore, one may also determine the sheet resistivity. Another important quantity, related to the lateral distance necessary for the flow of current into and out of the device, is the transfer length  $L_t$ . This is equal to  $\sqrt{r_c/R_{SH}}$ , (135) where  $r_c$  is an important parameter known as the specific contact resistance. The sheet resistivity  $R_{SH}$  is found to be 117.57 ohm/□. Thus, the contact resistance of the metal semiconductor contact is  $R_c= 1.005$  ohms, this value is smaller than what is measured for the same material as reported by (168) which was  $R_c= 1.4$  ohms. The specific contact ( $r_c$ ) resistance is  $4.493 \times 10^{-5} \Omega\text{-cm}^2$ . If we consider a ridge waveguide laser of 1mm in length and 2.5  $\mu\text{m}$  ridge, so the resistance is equivalent to about 1.8  $\Omega$ . This value is considered acceptable, where ( $r_c$ ) can vary from 0.8 to  $0.4 \times 10^{-6} \Omega\text{-cm}^2$ . The value of ( $R_c$ ) measured here for GaAs/AlGaAs lasers is higher than high power laser with no aluminum content by a factor of 3-4 (169). This could be due to a thicker p-cladding structure used in this work. Finally, if we plot the  $r_c$  with respect to the annealing temperature, we get a figure (3.29).

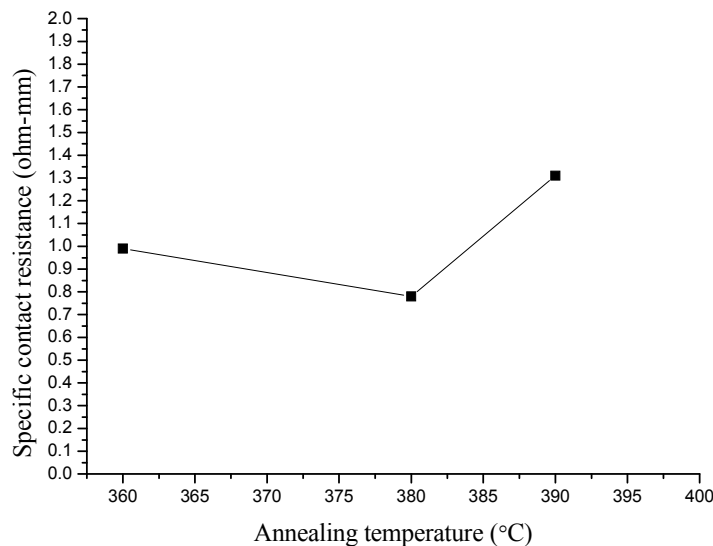


Figure (3.29) Specific contact resistance ( $r_c$ ) with respect to annealing temperature. Inspection of the graph (3.28a) shows that the lowest specific contact resistance for the device is achieved at an annealing temperature of 380 °C.

# Chapter 4

## Device Fabrication

### 4.1 Introduction

This chapter begins by introducing the methods that have been used in device fabrication. The technologies that have been used and the development of each specific process will be outlined. All of the fabrication was carried out in the James Watt Nano-Fabrication Center (JWNC) clean room and the clean room at level six of the Rankin building at the University of Glasgow. This chapter includes a summary of the electron beam (e-beam) lithography technology that was used throughout this work. The types of the e-beam markers that were used and the benefits of using such markers in the e-beam lithography process will be detailed. The reactive ion etching development process is detailed alongside the problems that was encountered and solved during this research. The quantum well intermixing (QWI) development will be detailed along with the challenging aspects of using this process. The QWI assessment methods and the measurement results obtained from QWI will be reported. Furthermore, a passive waveguide loss measurement technique will be presented along with the measurement results. The rest of the chapter will deal with the contact metallisation and the general fabrication process for the array laser diode. Finally, the conclusions of the chapter will be presented.

## 4.2 E-Beam Lithography

Electron beam lithography (EBL) can be used for patterning the photo-masks used in optical lithography, as well as for the direct writing of the patterns on the semiconductor wafers. The importance of using e-beam lithography lies in the improved resolution when compared with optical lithography. Therefore, the main devices produced during this research were fabricated using e-beam lithography. Optical lithography was used to fabricate the oxide stripe lasers with a width of 75  $\mu\text{m}$ , where high resolution was not required. The other benefits of e-beam lithography include, easy pattern modification, the absence of mask defects and excellent layer to layer alignment tolerance i.e. registration. E-beam lithography has good resolution because it has a small beam spot size. As the e-beam is a direct writing process on the wafers, photo-masks are not needed. Any defects with photo-masks are avoided.

The EBL tool used in this work is the state of the art Vistec VB6 UHR EWF (172) that offers a very high resolution of less than 10 nm. In fact, the tool is capable of writing 3 nm spots with a 15 nm placing accuracy, with maximum field size of 1.2 x 1.2 mm. (173) (Macintyre 2006). The EBL technique is very expensive. Therefore, a minimum writing time on the e-beam machine is a preferred. This can be achieved by modifying the beam current, beam step size, spot size, pattern dose, resist sensitivity and the resolution. These parameters need to be taken into account when submitting a wafer for exposure in the e-beam lithography tool.

The EBL tool uses an e-beam with parameters (mentioned above) controlled to expose an electron sensitive layer, which is the polymethyl methacrylate (PMMA) resist. This exposure induces reactions, which leave the resist either less or more sensitive to the developer solution. The EBL process uses 100 KV electron beams with diameters from 3 nm to 400 nm, depending on the feature size required. For the process used in fabrication of the MMI array laser, a beam current of 32 nA was used. This is equivalent to a beam diameter of 24 nm, which is adequate for the minimum feature size of 1  $\mu\text{m}$  in our devices.

Figure (4.1) shows a Monte Carlo simulation of 20 KV electrons striking a PMMA layer on silicon (2). Inspection of the figure shows that there is backscattering of the electrons within the PMMA and the Si substrate. The

backscattering is responsible for the undercut, which is required for example, in the metallisation lift off process. As the Vistec VB6 UHR EWF EBL machine uses a 100 KV beam, the undercut should be minimal and the angle of the scattering can be decreased. The exposure dose is a very important parameter, which is defined as the required charge per unit area to expose the PMMA resist. The dose is measured in  $\mu\text{C}/\text{cm}^2$ . The values required for the EBL process are around  $500 \mu\text{C}/\text{cm}^2$ . A very accurate dose obtained through a dose test was found to be  $350 \mu\text{C}/\text{cm}^2$  for the EBL exposure process for PMMA.

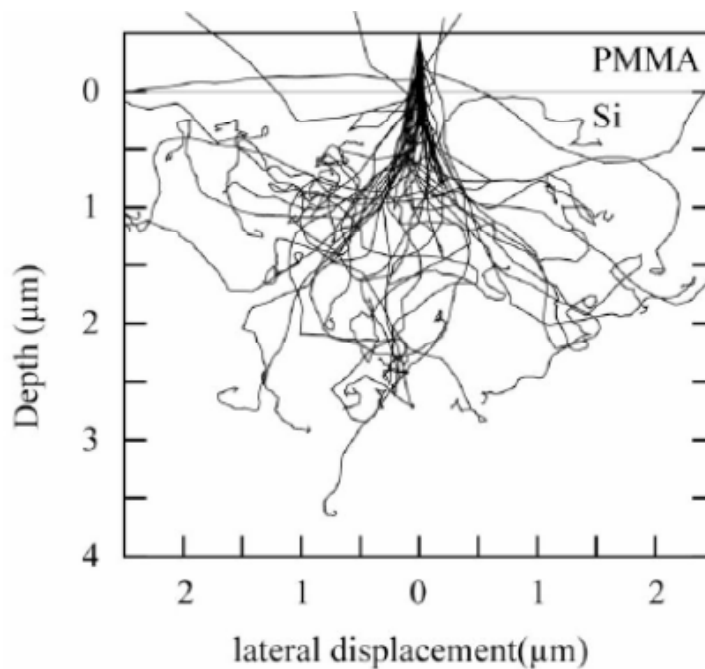


Figure (4.1) Monte Carlo simulation of 20 KV electrons striking a PMMA layer on silicon. (Courtesy of Macintyre 2006).

There is one more important limiting factor for e-beam lithography, which is known as the proximity error. This error occurs in corners or closely separated spaces, leading to overexposure. This happens due to the existence of secondary electrons alongside the backscattered electrons. These act as additional radiation, decreasing the contrast of the incident electron beam exposure. Inspection of figure (4.1) reveals that the exposure occurs at distances of up to  $3.5 \mu\text{m}$  for 20 KV. This exposure is likely to be much higher for an acceleration voltage of 100 KV, which is used in the EBL process. This causes an increased dose on the areas of the wafer due to this secondary exposure. This can be solved by using separate doses for various patterns. This is carried out by using the software interface for the e-beam machine, which

has a feature called proximity error correction. So, the open large areas on the pattern have correct doses which are not affected by close spaces, edges and corners effects of the pattern. The solution is to use very small areas and this is done by the software interface. Thus, those areas were exposed and the effects of the secondary electrons is circumvented. This effect can be seen in figure (4.2a) with proximity correction and the same pattern in figure (4.2b) without proximity correction (173). The effect on the device fabricated can be very influential, as the fabricated pattern dimensions will be different from what is designed. This can affect the device operation, particularly for ridge waveguide based laser devices.

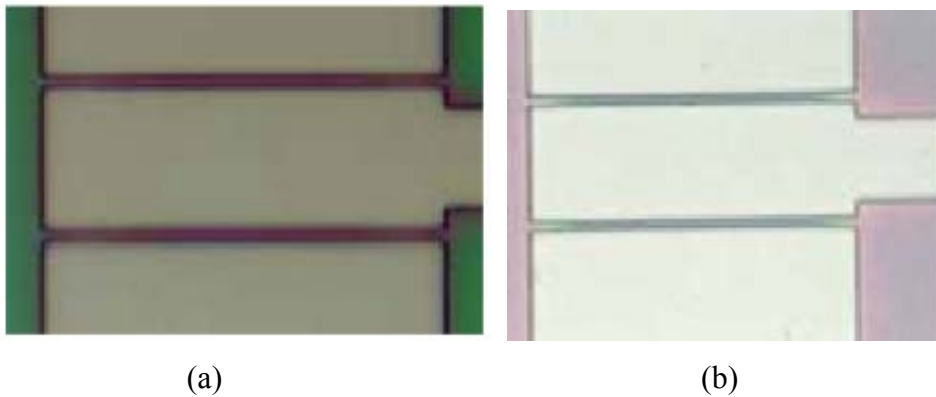


Figure (4.2): Figure (a) shows a pattern with proximity correction. The areas exposed are white coloured. The Ridge type structure is exposed equally, which is visible by the straight lines. (b) The figure (b) shows an exposed pattern without a proximity correction, the areas exposed are not straight lines, so the designed shapes are different because of this effect. Figure (a) shows a properly exposed structure using the e-beam process with the error proximity correction.

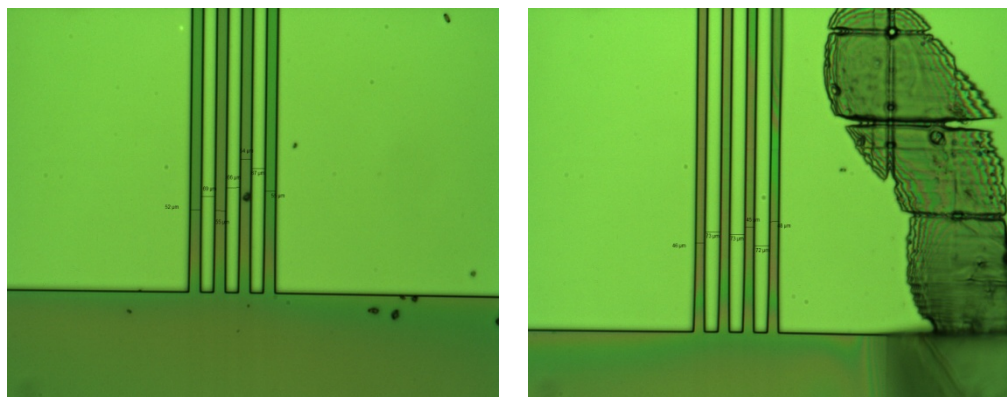
### 4.3 PMMA Resist

Polymethyl methacrylate (PMMA) resist is used for all the lithography steps and has very good resolution. Furthermore, it has a reasonable dry etching resistance. The PMMA resist and the developer solution are relatively low cost, which is vital for reducing the overall expenditure for any research environment.

The PMMA that is used in the e-beam lithography process is applied to the semiconductor wafer with spinning speeds of 5000 RPM in our work. The thickness of the (15%) 2010 PMMA is 1.1  $\mu\text{m}$ , which is an adequate mask for etching the PECVD  $\text{SiO}_2$ . The  $\text{SiO}_2$  is subsequently used as a mask to define the GaAs/AlGaAs waveguides. The PMMA must be hardened by baking it in

an oven at 180 °C for 120 minutes. This baking process for the PMMA resist removes any solvents from it. By now, the PMMA resist can go through e-beam electron exposure process, which is followed by sample development using a solution of methyl isobutyl ketone (MIBK) and isopropyl alcohol (IPA) with a ratio of 1:1. This is done at 23.5 ° C. After the pattern development, the pattern can be inspected using optical microscopy. The inspection of the developed pattern is very important to determine if the sample is developed properly. Sometimes incomplete development of the sample will require optimising the e-beam dose. Therefore, it is important to carry out a dose test regularly prior to the EBL process. The dose test improves the results of the lithography in two ways: ensuring clearing the PMMA properly using the development time with accurate features and the required dimensions of the design are fabricated. Figure (4.3) shows an optical microscope image for different dose tests. Good inspection and use of feature measurement on the optical microscope of the device ensures accurate ridge dimensions, which are very close to the designed dimensions in figure (4.3a) and smaller than the designed in figure (4.3b).

A bi-layer PMMA resist which is based on 1.1 μm and 0.1 μm thicknesses is used for metal lift process. The smaller thickness resist has a lower sensitivity, which forms an undercut during development. This undercut is important for neat lift off of the metal, which is located on top of the PMMA resist. This thick



(a)

(b)

Figure 4.3: a) The microscope image shows a dose of 350 μC/cm<sup>2</sup>. The correct dose is verified through the simple measurement tool of the designed dimension. b) The optical microscope image shows a dose of 425 μC/cm<sup>2</sup>. The measurement showed that the pattern dimensions are less than the design parameters, therefore in this example dose (a) was selected when performing the exposure.

resist is ideal for the opening of the contact window, which requires a thicker resist for good coverage of the etched waveguide.

#### **4.4 Markers**

The alignment markers used in the e-beam lithography can be very demanding in terms of the processing time. Generally, two different marker types are used. The fabrication process step route for each laser device dictates what type of marker can be used.

Gold markers and etched markers are used. The gold markers are usually 40x40  $\mu\text{m}$  rectangles, which are made by using 20 nm NiCr and 120 nm Au. The lift off process is used to define the markers by EBL. The problem with gold markers is that they cannot be used when the fabrication of a device requires quantum well intermixing. QWI is used to define the passive waveguides or, as is the case with the devices concerned here, when structures like NAMs and long passive waveguides need to be fabricated. The quantum well intermixing process involves a high temperature annealing process, which can be at temperatures up to 810 ° C in the case of GaAs/AlGaAs laser diode. This elevated temperature destroys the gold markers, so they cannot be used for alignment by EBL.

There are a couple of options for the etched markers, either wet etched markers or dry etched markers. Wet etched markers are not an option here, because of the e-beam edge location. Dry etched markers therefore have been used. Using deeply etched markers by reactive ion etching require more processing, but this is the most suitable choice when a QWI step is required. The etched markers are 40 x 40  $\mu\text{m}$  squares. The markers are etched to around 6  $\mu\text{m}$  depth. To make the markers, a 1.1  $\mu\text{m}$  thick silica oxide ( $\text{SiO}_2$ ) mask is deposited by chemical enhanced vapour deposition process (PECVD) to protect the AlGaAs/GaAs layers. Then, a bi-layer PMMA resist consisting of 15 % (2010) type and 4 % (2041) with a thickness of 1.2  $\mu\text{m}$  is used as a mask for the oxide layer. EBL is used to define the marker pattern. The markers are then etched using a reactive ion etcher tool for GaAs. Examples of the marker can be found in the SEM images in Figures (4.4a and 4.4b), which show series of markers that are used for e-beam alignment purposes on the top and bottom sides of the semiconductor laser chip. Figure (4.5) shows a cross type marker that is used for alignment as well.

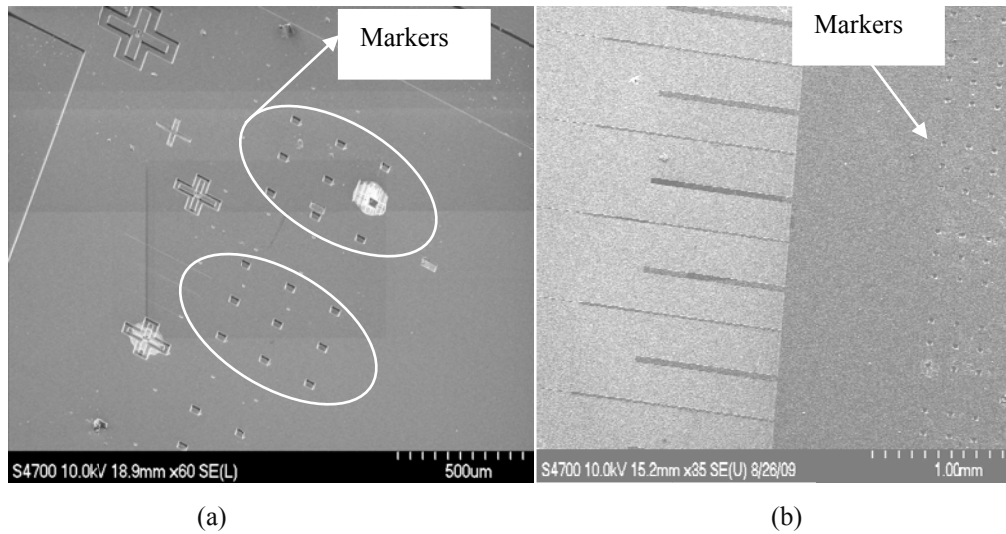


Figure 4.4: (a) SEM image for etched markers two groups of nine etched markers are visible. Distance between markers is 200  $\mu\text{m}$  from centre to centre. Cross markers are also visible. (b) SEM image shows the marker with series of MMI array lasers.

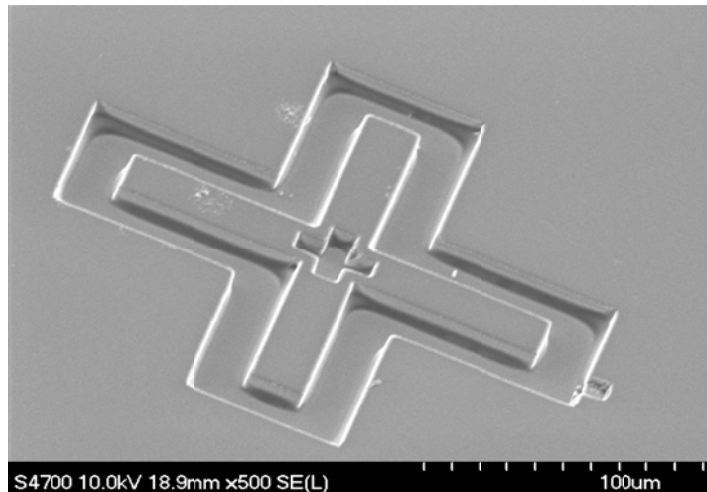


Figure (4.5): SEM image for etched cross, which is used for pattern alignment purposes on the wafer.

The location of markers on the semiconductor chip is used for registration purposes, i.e. layer to layer alignment. This location is in the four corner edges of the semiconductor sample. They should be at least 1mm from the edge of the sample for good fabrication results. The reason for leaving the 1 mm distance is that the thickness of the PMMA at the edge of the sample can be several microns, which cannot be used for patterning. Each position of the marker edge serves as an alignment purpose. The first edge marker is to provide offset error compensation and the four markers alignment arrangement offers ultimately the best alignment option. This is illustrated in figure (4.6),

which shows the offset, rotation, scale and keystone alignments. This ensures excellent layer to layer alignment, which can be as good as 20 nm. Therefore, care should be taken when designing the markers for e-beam lithography. Normally, sets of markers are used in each corner edge of the sample to compensate for marker damage during exposure and etching. The same markers can be used at least twice on condition they are not deformed or damaged during exposure.

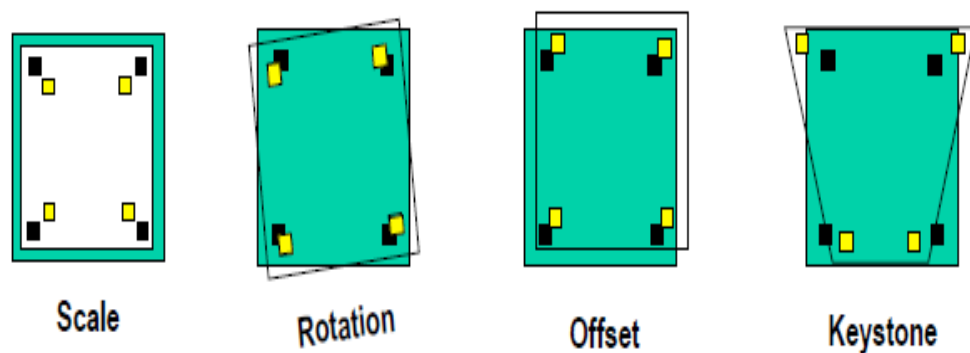
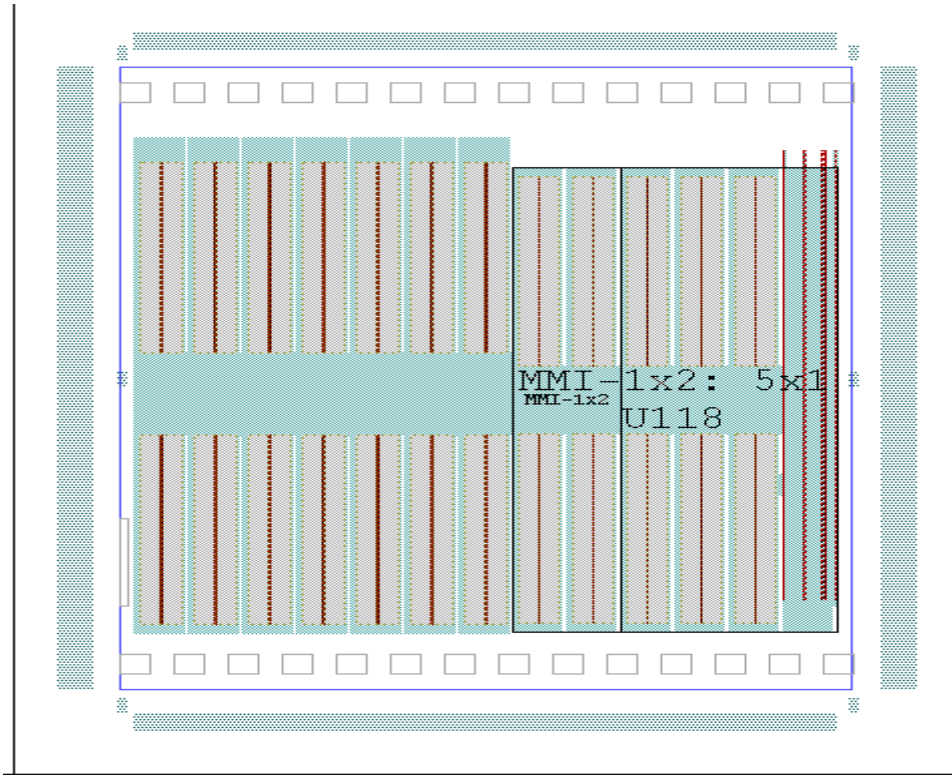
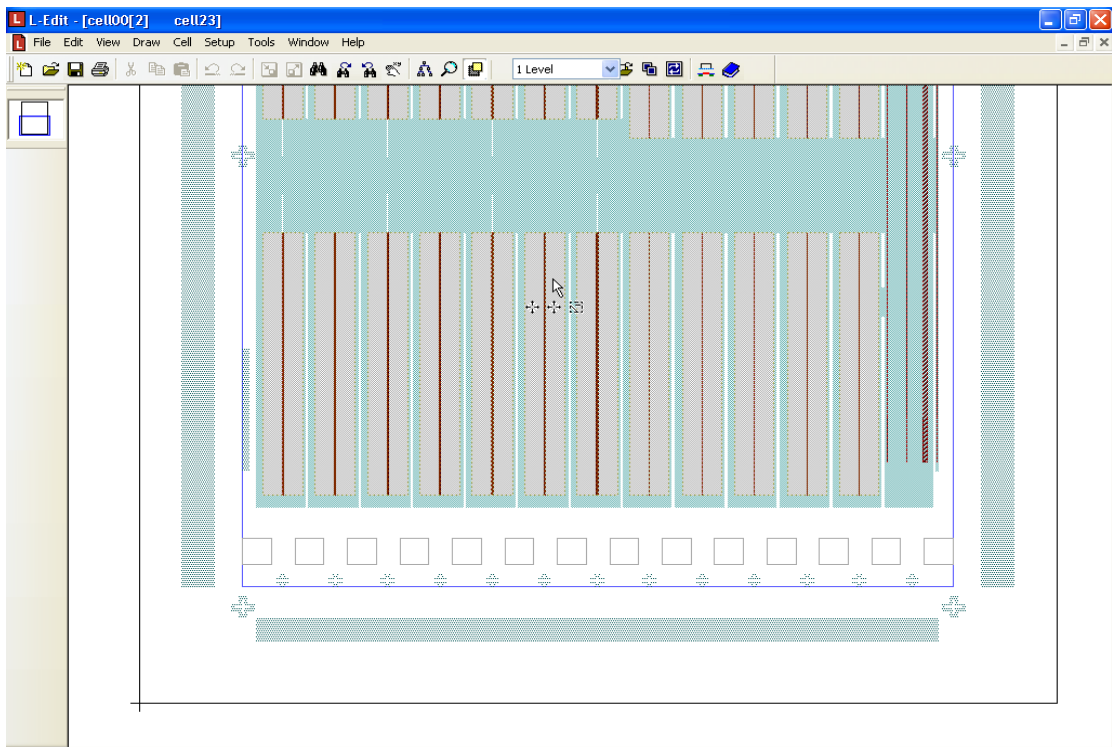


Figure: (4.6) Four markers system for layer to layer alignment (registration) using e-beam lithography.

Figures (4.7a) and (4.7b) represent the full mask for the array laser diode device, which show a series of markers on the upper side and the lower sides of the figure. Figure (4.7b) is a more highly magnified version of (4.7a), where the markers are visible at the bottom of the layout. Also shown is the device layout in the pattern, which includes two different types of MMI lasers in this case (1x2 and 1x4 MMI laser). In this example, there are 24 MMI devices as well as 4 ridge waveguides in the right hand side of the graphs. The above mask is an example of the fabrication of a variety of different devices on the same chip using EBL.



(a)



(b)

Figure: (4.7) Mask design using L-Edit mask design. (a) Full devices layout with markers used are shown. (b) The figure is a magnified version of (a) above which clearly shows the series of marker and crosses for good alignment. The device layout is shown as well. Red stripes are the ridge waveguides.

## 4.5 Reactive ion etching

The reactive ion etching mechanism is initiated when the reactive species in the plasma are combined with the surface that is to be etched. The chemical reaction is combined with ion bombardment effects, which causes the removal or etching of the material. The plasma reactive species are made of the ionised gas due an applied electric field and free electrons, which are released from negatively biased electrodes.

For semiconductor device processing, a low pressure plasma is used with a pressure range between 0.01 and 0.1 torr (120). The electron concentration in the plasma dry etching is in the range of  $10^9$  to  $10^{12}$  /  $\text{cm}^3$ . The gas molecule concentration is much higher than the electron concentration (121).

The reactive ion etching tool used in this work is an Oxford RIE System 100<sup>TM</sup> (S100), which has two electrodes. The electrode (cathode) that holds the wafer has a smaller area and is connected to the RF source. The second electrode (anode) is much larger in size and comprises the whole chamber. A schematic of parallel electrode chamber (174) can be seen in the schematic in figure (4.8) below.

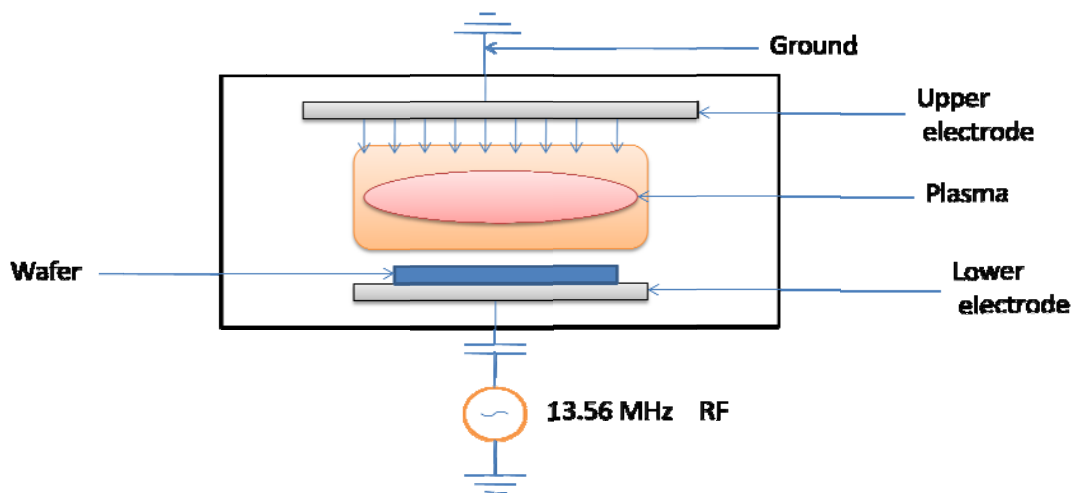


Figure (4.8): Schematic of parallel plate reactive ion etching system

The lower electrode, which holds the wafer that is to be etched, is the RF powered electrode. Most of the voltage drop appears across the plasma sheath at the lower electrode (cathode), which is due to the big difference in area between the two electrodes. The larger electrode (which is the chamber in most of the cases) is grounded. This voltage drop at the lower electrode enhances the ion energy, which in return increases the directionality of the

etching. The etching is also assisted by the chemical reaction at the surface of the wafer material. The reactive ion etching process can be summarised in the following steps and in figure (4.9) below:

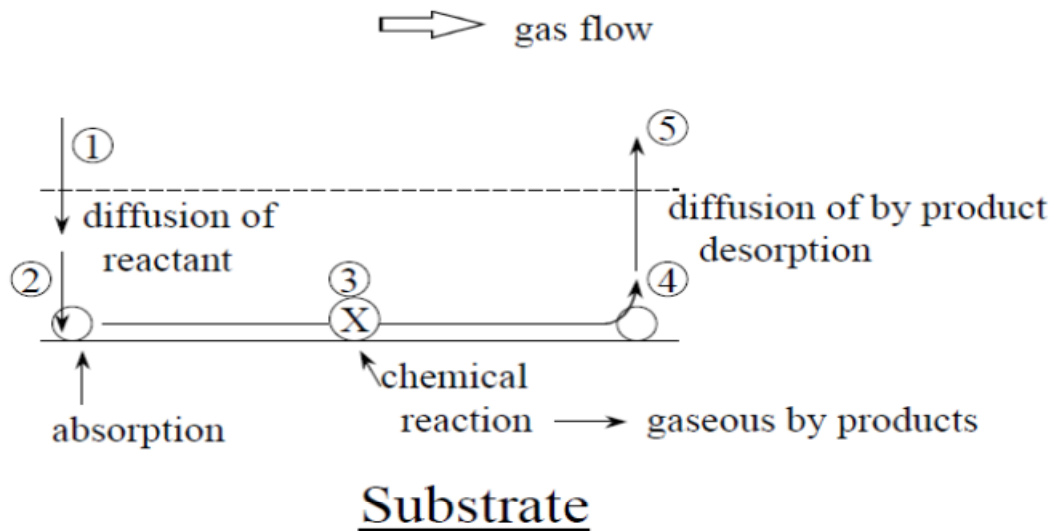


Figure (4.9) Surface reaction sequence for the reactive ion etching process on top of a substrate.

- 1) Generation of the plasma reactive species.
- 2) Diffusion of the reactant to the substrate.
- 3) Absorption of the reactants at the surface of the material.
- 4) The chemical reaction of the reactant and the substrate material to form volatile compounds, which are the by-products that are pumped away from the chamber.

## 4.5.1 Etching process development

### 4.5.1.1 Micro-masking problem

The reactive ion etching system used initially was an Oxford RIE System 100<sup>TM</sup> (S100), which consist of an integrated load lock. The main chamber is evacuated by a turbo pump to a typical base pressure of 10 mTorr. The chamber is similar to the schematic in figure (4.8). Using this particular system, it proved very difficult to get a proper etching process for the material

that was used in this work. The problem with the process in the Oxford RIE system 100 was the micro-masking issue, which is related to the contaminants on top of the wafer post silica oxide hard mask etching. The source of the contamination can be attributed to non volatile by-products, which come from the oxide hard mask pre-waveguide etch. CHF<sub>3</sub> reactive ion etching was used for silica etch. The non volatile compounds AlF and AlF<sub>3</sub> were formed during the etch, which cover the GaAs/AlGaAs surface. Another source is the formation of a fluorocarbon polymer, which is related to the increased density of CF<sub>x</sub> radicals during CHF<sub>3</sub> reactive ion etching. The polymer formation can be substantial during CHF<sub>3</sub> reactive ion etching (175).

The CHF<sub>3</sub> gas pressure used was 97 mTorr. The process that is used in this work uses the reactive ion etching machine plasma Oxford 80 plus. The process used is based on CHF<sub>3</sub> gas as follows:

<b><i>Gas used</i></b>	CHF <sub>3</sub>	Unit
<b><i>Gas flow rate</i></b>	20	sccm
<b><i>Pressure</i></b>	17	mTorr
<b><i>Power</i></b>	100	W
<b><i>Bias voltage</i></b>	-314	V
<b><i>Etch time with over etch of 500 nm oxide</i></b>	30	Min

Table (4.1) reactive ion etching conditions for 500 nm oxide mask

The process above is used to etch an oxide layer of 500 nm. The process for the recipe above has an etch rate of 20nm/min when etching the oxide with a PMMA etch mask with a thickness of 1.2 μm. Over-etch of SiO<sub>2</sub> by 50 % is employed in the process, so polymer formation and deposition can occur on top of the etched substrate. Returning to the discussion about the micro-masking, as the polymer is formed on top of the surface of the GaAs/AlGaAs wafer, this works as tiny masking particles, which are resistant to the reactive ion etching process of the GaAs/AlGaAs waveguide. Consequently, the etched GaAs/AlGaAs substrate contains dense pillars of un-etched GaAs/AlGaAs material, which cover all of the etched areas of the semiconductor. An example of this phenomenon can be seen in the scanning electron microscope images in Figure (4.10).

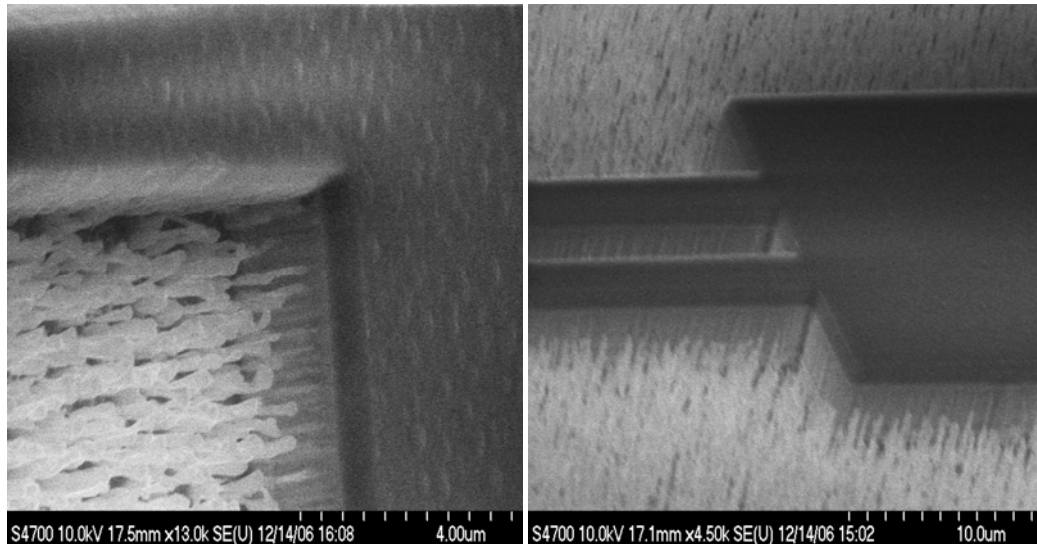


Figure (4.10) SEM images for GaAs/AlGaAs MMI waveguide etch using reactive ion etching with  $\text{SiCl}_4$ . The wide pillars shown in the figure are the unetched areas of GaAs/AlGaAs due to formation of polymer on the surface, which acts as micro-mask.

The micro-masking can be seen as pillars, which are equal in height with the etched waveguide. The micro-masking in the areas to be etched on the semiconductor wafer makes it difficult to use reflectometry assisted etching. This is a method for measuring the etch depth, which uses a laser situated on top of the chamber. The laser has a wavelength of 675 nm. The RIE system used initially is extensively used for etching different types of metals especially aluminium (Al) that covers the chamber side walls. The normal plasma cleaning process, which is a 30 minutes oxygen plasma followed by a 30 minutes hydrogen plasma, is not effective in cleaning the chamber. Therefore, only manual cleaning of the chamber is capable of chamber clean. This is impractical, so a second new version of the Oxford Plasmalab system 100 is used. The process development using this new system is explained in the next section.

Investigation into the micro-masking problem revealed that it is affected by the following factors:

1. Plasma cleaning processes for the etching chamber pre-dry etching.
2. The number of dry etching steps for GaAs/AlGaAs waveguides using  $\text{SiCl}_4$ .
3. The micro-masking can be more severe on an etch tool that uses different chemistries for etching a variety of metals and semiconductors.

4. The micro-masking increases with the inclusion of quantum well intermixing in the processing steps. One clear evidence of this is the increased micro-masking pillars in the intermixed areas of the semiconductor sample. The reason behind this phenomenon is that the QWI process involves using a silica sputtering process, which contains impurities such as Cu. Figure (4.11) below shows the etched 1x4 MMI array laser, where the intermixing interface can be seen clearly. The gain section, which is not intermixed, is free from surface roughness while the intermixed MMI section has a rough surface area.

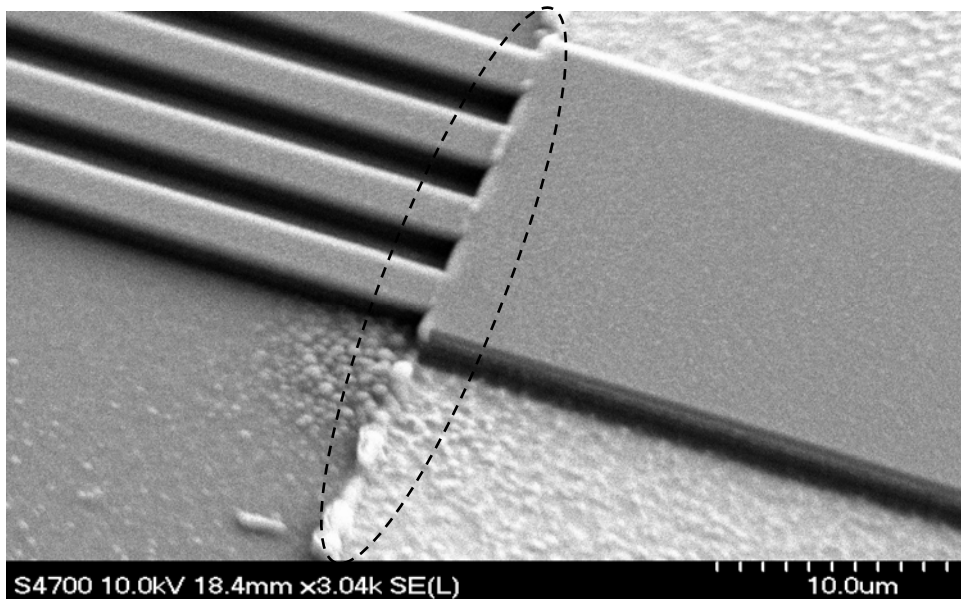


Figure (4.11) Etch for 1x4 MMI array laser, the interface between the intermixed and intermixed areas is clearly visible. Intermixed area is covered by grainy contaminants after post waveguide etch.

#### **4.5.1.2 Etching process development on RIE plasma lab system100 etcher**

The GaAs/AlGaAs etch process requires the resultant etch profile to be as close as possible to the vertical  $90^\circ$  i.e. with excellent anisotropy. Any deviation from this causes significant optical waveguide loss due to scattering, which could affect the laser device performance. Secondly, there must be a low dry etch damage, which results in smooth side walls for the etch profile. This is highly desired for efficient light guiding, this low damage is important in the surface as well. Thus, a good surface morphology with minimum roughness (i.e.) no micro-masking should be present, as was discussed in the

previous section. Lastly, high selectivity against the etching of the mask material is needed. Therefore, all of the criteria above must be satisfied to get a successful etch with good uniformity.

To develop the dry etch process, an RIE Plasmalab 100 system was used. Chlorine based gases are common for the etching GaAs/AlGaAs materials. Therefore, silicon tetrachloride ( $\text{SiCl}_4$ ) gas chemistry is used and the chemical reaction in the chamber given by (174) can be summarised as follows:



The chlorine in the reaction is the etchant for the GaAs/AlGaAs layers, which can be expressed by the following reactions:



Inspecting the reactions above, we notice that there are three volatile by-products, which are  $\text{AlCl}_3$ ,  $\text{AsCl}_3$  and  $\text{GaCl}_3$ . Alongside the chemical reactions, there must be a physical sputtering effect to achieve the required anisotropy. The physical sputtering is provided by RF power in the plasma.

To optimise the dry etching process, equal sizes of GaAs/AlGaAs material are used and patterned using EBL lithography.

In the design of the etching process parameters, the verticality of the etch profile is essential. Therefore, as explained at the start of this section, a balance between reactive ion etching and physical etch (sputtering) should exist to achieve a vertical profile. To optimise the etch process conditions, the etch profile has to be measured every time, which should be close to  $90^\circ$ . In the process development, a considerable number of runs have been carried out. We started with initial parameters for a  $\text{SiCl}_4$  gas flow rate of 10 sccm, a pressure of 4 mTorr and a power of 120 W. The results of the etch process can

be seen in figure (4.12) below. The etch profile verticality was measured through using SEM imaging. The profile showed a small angle with the normal.

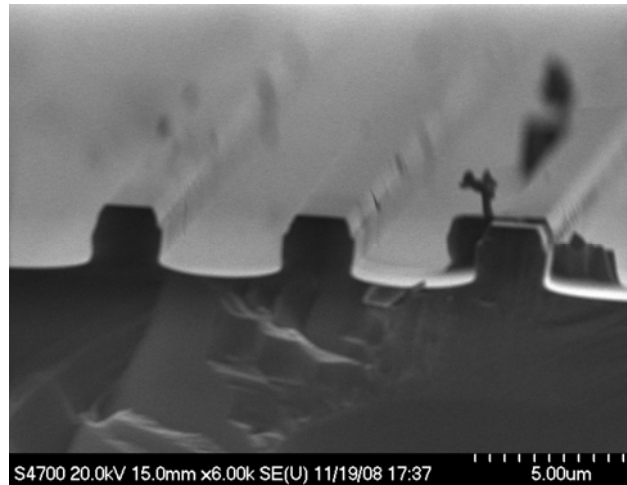


Figure 4.12: The process used to etch (sample ID: F8) this profile was using  $\text{SiCl}_4$  with gas flowrate of 10 sccm, 4 mTorr pressure and power of 120 W. Side wall angle measure to be around  $87^\circ$  with normal, other observation was the bowing (non flat surface).

To improve the etch profile further, the pressure was increased to 7 mTorr and the power was reduced to 100 W. The results of this etch can be seen in figure (4.13a, 4.13b). There was a slight improvement in the etch profile, but that was not good enough. The pressure was slightly reduced to 6 mTorr, the power was also reduced to 70 W while the gas flowrate was increased to 11 sccm. The results of these etch parameters can be seen in figure (4.14a, 4.14b). The etch profile showed still some sloping.

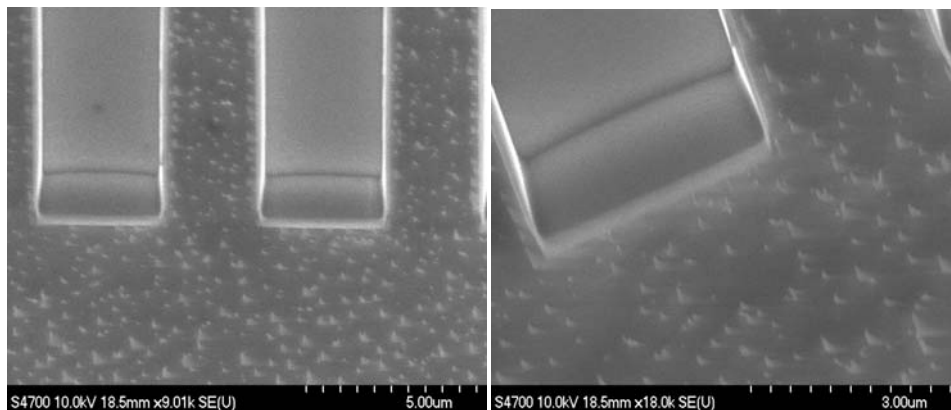
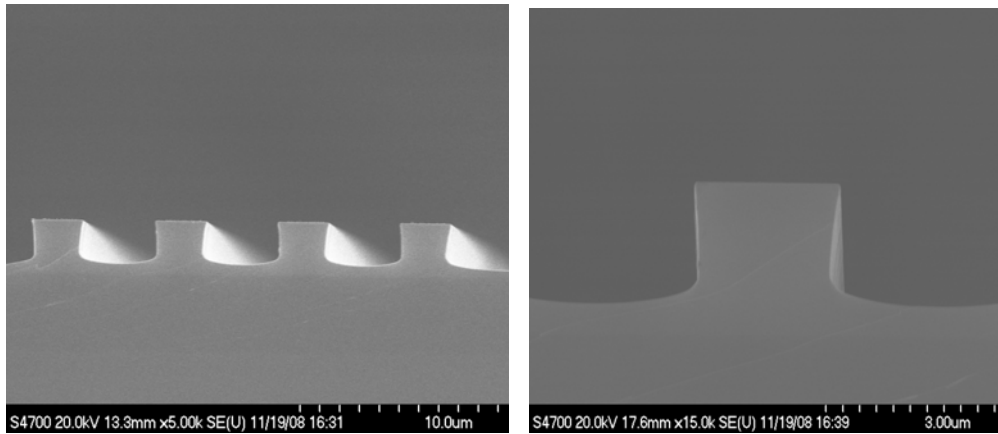


Figure (4.13a)

Figure (4.13b)

Figure 4.13: The process used to etch this profile was  $\text{SiCl}_4$  with gas flowrate of 10 sccm, 7 mTorr pressure and power of 100 W.



(a)

(b)

Figure 4.14: (a) The process used to etch this profile was:  $\text{SiCl}_4$  with gas flowrate of 11 sccm, 6 mTorr pressure and power of 70 W. (b) Magnification of (a) which shows a slight slope for the etched profile.

The process that achieved the best results was: the  $\text{SiCl}_4$  flowrate, 13 sccm; RF power, 80 W and the pressure used was 9 mTorr, which resulted in an etch profile  $> 89^\circ$ , which is acceptable. The results of this etching process can be seen in the figures: (4.15a, 4.15b), which show the etch profile for the ridge waveguide structure. The benefit is the good uniformity as can be seen clearly from Figure (4.15a). Figure (4.15c) shows the results obtained for the MMI laser device, which shows the etch profile obtained.

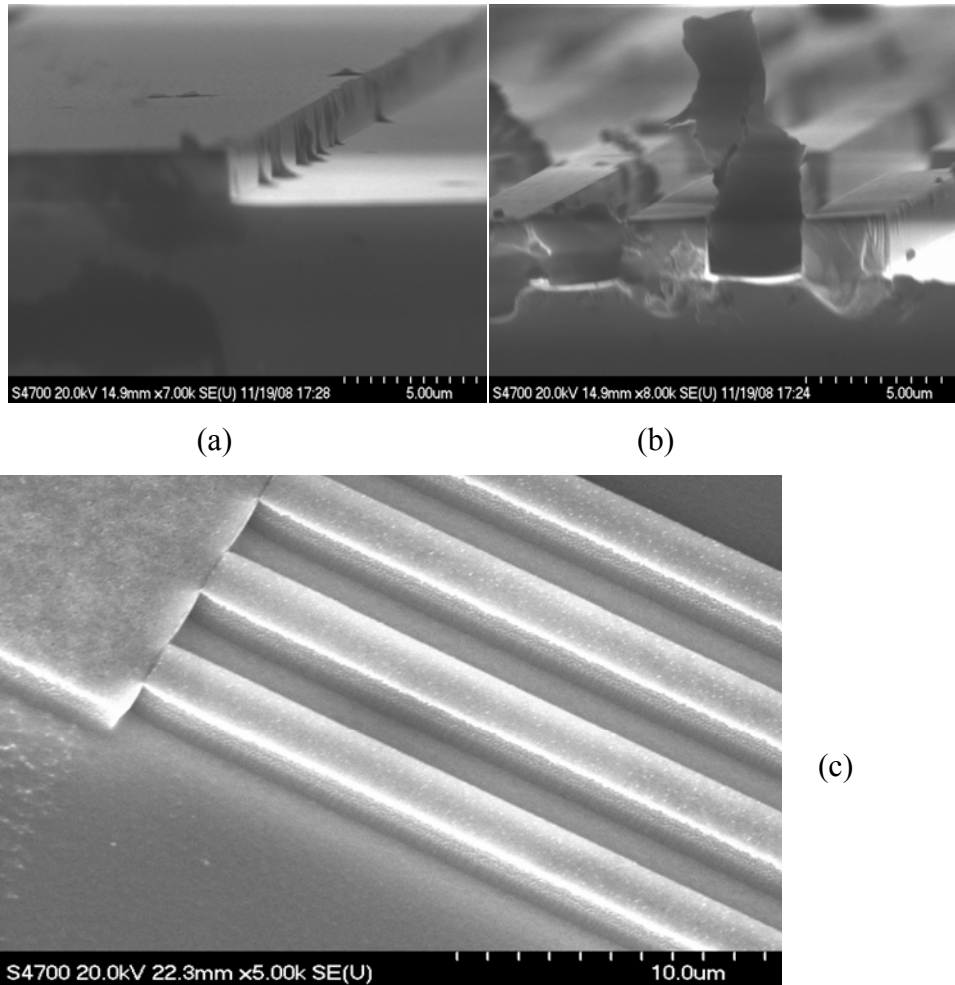


Figure 4.15: (a) The process used to etch this profile was using  $\text{SiCl}_4$  with gas flowrate of 13 sccm, 9 mTorr pressure and power of 80 W. Side wall angle measure to be  $> 89^\circ$  with the normal. This was the best results. (b) Different structure used the same recipe in (a). (c) The same recipe from (a) is used to etch 1x4 MMI array laser with remarkable results as seen in figure (c) above. Very smooth side walls and good interface seen between the MMI and ridge waveguide, which is proof of the good process recipe that has been developed.

#### 4.5.1.3 Dry etch parameters for the process development using RIE plasma lab system100 etcher

The process parameters, which were found to offer the best results are summarised in table (4.2). The original process parameters are summarised in table (4.3). The process migrated to a different RIE plasma lab 100 for the following reasons:

1. The old RIE plasma lab 100 system was heavily used for etching different types of materials, which contaminated the chamber.
2. The process was developed to reach an optimized process that resulted in a proper vertical etch profile-even to a relatively very deep etch of (4  $\mu\text{m}$ ) for the MMI. The smoothness of side walls reduces any possible losses inside the

MMI cavity. In figure (4.16), the etch profile obtained using the old RIE plasma lab machine is shown. The recipe used to obtain this etch profile is described in table (4.3).

3. The most important aspect of etching process development was to minimize the micro-masking. The micro-masking is an extremely relevant issue, when a QWI is used in the fabrication of the device. The effort focused on the reduction and elimination of the micro-masking the problem.

<b>Etching Process Development for GaAs/AlGaAs</b>			
<i>Gas used</i>	SiCl <sub>4</sub>	<b>Unit</b>	<b>Effects on the etch process</b>
<i>Gas flow rate</i>	13	sccm	Lower gas flow rate results in a reduction of the chemical etching.
<i>Pressure</i>	9	mtorr	
<i>Power</i>	80	W	Lower power results in a reduced etch rate, which results in achieving accurate etch depth.
<i>Etch rate</i>	95 – 120	nm/minute	Lower etch rate results in a controlled etch depth and decreases the number of etches to achieve the required etch depth.
<i>Number of etches</i>	1		Less processing
<i>Micromasking</i>	Minimum		Decreased micro-masking allows quality devices to be fabricated.
<b>Chamber parameters for pre-cleaning and conditioning before every etching run</b>			
<i>O<sub>2</sub> plasma clean</i>			
<b>Power</b>	200		W
<b>Time</b>	30		minutes
<i>H<sub>2</sub> plasma clean</i>			
<b>Power</b>	200		W
<b>Time</b>	30		minutes

Table (4.2) The table shows the process parameters for the dry etching process, which was developed during this research.

<b>Previous process for old RIE etching system</b>		
<i>Gas used</i>	SiCl <sub>4</sub>	Unit
<i>Gas flow rate</i>	18	sccm
<i>Pressure</i>	11	mtorr
<i>Power</i>	100	W
<i>Etch rate</i>	180 – 230	nm/min
<i>Number of etches</i>	Multiple	
<i>Micromasking</i>	Extremely heavy	
<i>Profile</i>	undercut	

Table (4.3) The table shows the process parameters for the dry etch process using the old RIE plasma lab 100 system. The etch process using this system was no capable of producing an acceptable etch profile for device fabrication.

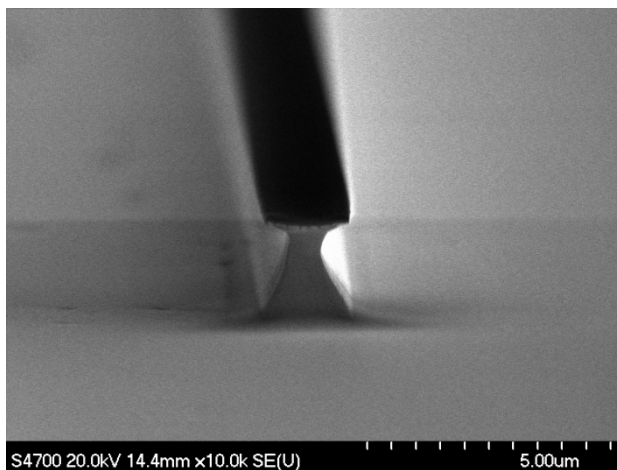


Figure (4.16): A scanning electron microscopy image for an etch whose process parameters were as follows : SiCl<sub>4</sub> gas flow rate was 18 sccm, the pressure was 11 mtorr and the RF power was 100 W, as indicated in table (4.3). The etch profile is undercut, which not was suitable for fabricating MMI array laser.

## 4.6 Quantum well intermixing

### 4.6.1 Introduction

Quantum well intermixing is a major technology for monolithic optoelectronic integration of semiconductor quantum well heterostructures by selectively modifying the bandgap energy of the semiconductor wafer. This technique allows the control of the absorption edge of quantum well structures. Many types of device have been fabricated using this technique, which include

integrated quantum well lasers, modulators, photo-detectors and low loss waveguides.

The need for low manufacturing cost and high reliability led many research centres to focus on integrating different functionalities on the same chip. This requires integrating many optoelectronic devices on the same chip i.e. making optoelectronic integrated circuits. Band modification by quantum well intermixing is a simple and powerful technique to monolithically integrate optoelectronic devices on a single wafer, with no deleterious effects on the optical, electrical or lifetime properties of the manufactured devices. This process can be applied to different quantum well material systems, including GaAs/AlGaAs, InGaAs/GaAs, InGaAs/InAlGaAs, GaInP/AlGaInP, InGaAs/InGaAsP, and InGaAsP/InP.

As this thesis is concerned with the fabrication of GaAs/AlGaAs high brightness multimode interferometer array laser diodes, the benefits of using quantum well intermixing specifically in producing high brightness lasers will be discussed in this chapter. The development of the device concerned in this thesis requires a passive MMI structure, a NAM structure and an output passive waveguide. All of these structures need to be integrated with low loss. Hence, quantum well intermixing is crucial and is a core process that has to be used to increase the brightness of the semiconductor laser diode. This rest of this chapter includes: an explanation of the point defects in GaAs/AlGaAs, the discovery of quantum well intermixing, an overview of the QWI methods and the details of the fabrication procedure used for QWI process. Furthermore, the chapter contains the details of the experimental work carried out to develop the process with the results acquired and a passive waveguide loss measurement. Finally, we end the chapter with a summary of the fabrication steps for multimode interference array laser diode and conclusions of the chapter.

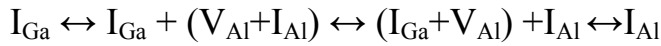
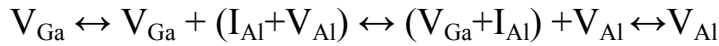
#### **4.6.2 Effect of point defects in the GaAs/AlGaAs disordering mechanism**

The point defects in AlGaAs play a major role in the quantum well intermixing process. These defects include column III and V vacancies, interstitials and antisites. These can be summarised, as in the table (4.4):

Point defect type	Column III	Column V
Interstitial	$I_{III}$ (Ga or Al)	$I_{As}$
Vacancy	$V_{III}$ ( $V_{Ga}$ vacancy or $V_{Al}$ vacancy)	$V_{As}$
Antisite	$III_{As}$	$As_{III}$

Table (4.4): Point defects in the GaAs/AlGaAs disordering mechanism.

Understanding the diffusion mechanism and the concentration of the point defects above, makes an analysis of the disordering mechanism possible. Deppe and Holonyak (177) (1988) presented a model for disordering of GaAs/AlGaAs using column III vacancies and interstitials. According to the model, two equations can be used to describe the Al-Ga inter-diffusion mechanism. The equations are as follows:



$(I_{Al} + V_{Al})$  is the Frenkel pair of Al lattice atoms. The equations above show how the Frenkel pair is replaced. The Ga-Al inter-diffusion is enhanced through the vacancy and interstitial medium.

This inter-diffusion (intermixing) is influenced by other variables as Deppe *et al.* (177) showed. He showed that this inter-diffusion is enhanced under high As vapour pressure for n-type crystals or under low As pressure for P-type crystals. The explanation for this behaviour is that, under high As pressure, the defects related with excess As increase. Therefore, inter-diffusion increases. In poor or low As pressure, the inter-diffusion is determined by  $I_{Al}$ ,  $I_{Ga}$ , group III antisite defects and  $V_{As}$ . The intermixing is also influenced by the depth of the quantum well.

### 4.6.3 Discovery and history of quantum well intermixing

The discovery of quantum well intermixing came as surprise discovery by Nick Holonyak's group in November 1980, while conducting experiments on

Zn diffusion into GaAs/AlGaAs heterostructures and superlattices (SL). The experiments conducted by Holonyak and Laidig (1976) were for the diffusion of Zn in an AlAs/GaAs superlattice at an annealing temperature of 575 ° for 4 hours in a closed ampoule with a ZnAs<sub>2</sub> source. They noticed after removing the GaAs substrate that the material samples were transparent and pale yellow. The photoluminescence output of the sample was reduced significantly due to the disordering. The material was different from the red, as-grown SL. The experiment was repeated with only excess As in a sealed ampoule with another as-grown SL. The crystal remained red, demonstrating that there was no disordering occurring due to As diffusion with no Zn present. Further Zn diffusion experiments followed, using ZnAs<sub>2</sub> at 575 ° for 10 minutes using the same AlAs/GaAs SL with Si<sub>3</sub>N<sub>4</sub> as a strip mask. The effect of Zn impurities was clear as the unmasked areas of material were compositionally disordered in less than 10 minutes. This demonstrated that Zn impurity diffusion caused the disordering. The areas masked with Si<sub>3</sub>N<sub>4</sub> did not disorder, as the Zn impurity was not able to penetrate the Si<sub>3</sub>N<sub>4</sub> mask.

They discovered that disordering with Zn diffusion occurred at an annealing temperature of 575 °C, which is far lower than the MOCVD growth temperature of 750 ° for the heterostructure and SLs used in their work (Laidig) 1981. Holonyak and Laidig indicated that Zn greatly enhanced the inter-diffusion of Ga and Al in the superlattice structure.

They concluded that this process can be applied selectively to intermix quantum well heterostructures and superlattices. This discovery is of great importance for optoelectronic integration. The process was called impurity induced layer disordering (IILD), also known as impurity induced disordering (IID).

#### **4.6.4 Quantum well intermixing techniques**

There are a number of techniques for quantum well intermixing. The purpose of this section is to provide an overview of the techniques that have been researched by various groups and specifically for the GaAs/AlGaAs system, which is the material system used in this research. In this section, the pros and cons of each method will be outlined. Thus, the selection of a suitable intermixing technique is imperative.

#### **4.6.4.1 Impurity induced layer disordering**

Impurity induced layer disordering makes use of different impurities. The process can be carried in a number of ways, by diffusion from the surface or by ion implantation. Several different impurities have been found to cause disordering upon diffusion followed by annealing, such as Si, Ge, S, Sn and Se which act as donors as well as Zn, Be and Mg as acceptors (177). All of these impurities are electrically active. The disordering by the IID process is induced by the impurities through the generation of free carriers, which increase the equilibrium number of vacancies at the annealing temperature.

The problem with active impurities like Zn (p-type) and silicon (n-type) is that the concentration of the impurities, which needs to be present is greater than  $10^{18} \text{ cm}^{-3}$  (Marsh (178)) to enhance the disordering of the lattice element. At this concentration of impurities, the absorption coefficient can be as high as 43 dB/cm as a consequence of free carrier absorption. This high absorption figure is not acceptable for most applications. Furthermore, the electrical isolation required between devices cannot be achieved by the IID intermixing method.

#### **4.6.4.2 Photo-absorption induced disordering (PAID)**

Impurity free photo-absorption induced disordering is another method reported by Mclean (179) that has been used. It uses a 1.064  $\mu\text{m}$  Nd: YAG laser with a relatively low power density of (1-20  $\text{Wmm}^{-2}$ ) when compared to other methods of laser induced disordering (which use a considerably high power density of  $10^5 \text{ W mm}^{-2}$ ). The laser is used in CW and multimode for time periods of 30 minutes including 2 minutes ramp up time to the maximum power level. During laser irradiation band to band and free carrier absorption of the incident photons takes place, where the semiconductor surface is subjected to the laser beam, coupled with non-radiative recombination. This leads to considerable heating of the semiconductor. This heating results in the inter-diffusion between the quantum wells and the barriers, which is effectively the intermixing. This process is particularly useful in GaInAs/GaInAsP and GaInAs/AlGaInAs systems, which are known to have limited thermal stability. This process, however, suffers from low spatial resolution, which is in the range of 100-200  $\mu\text{m}$ . The passive waveguides produced using this process has a loss of around  $16 \text{ cm}^{-1}$ , although a much

lower values of the passive waveguide loss have been reported to be around  $5 \text{ cm}^{-1}$  (180), which is a very useful value.

#### **4.6.4.3 Sputter induced disordering (SID)**

Sputter induced disordering is one of the techniques that has been developed by the Marsh group (178). Most of this section and the experimental work that has been carried out is based on the process using sputter induced disordering. In this process, the sputter induced disordering occurs in two fundamental steps. Firstly, ion bombardment during Cu sputtering generates point defects near the surface of the semiconductor, which diffuse during the annealing process. The energy required for releasing the Ga from the lattice is reduced, so the out-diffusion of Ga atoms into the PECVD silica cap is increased by the point defects near the semiconductor surface. These components lead to the subsequent inter-diffusion between the quantum wells and the barriers. As this process needs to be selectively controlled, PECVD silica caps are used to protect the sample surface during the high temperature anneal.

During high temperature annealing of the GaAs/AlGaAs system, the Ga out-diffusion results in the vacancies which diffuse into the active region. This is explained in the figure (4.17), which shows sputter induced intermixing process with a post high temperature anneal. The PECVD silica cap used not only protects the sample surface during high temperature anneal, but it enhances the intermixing.

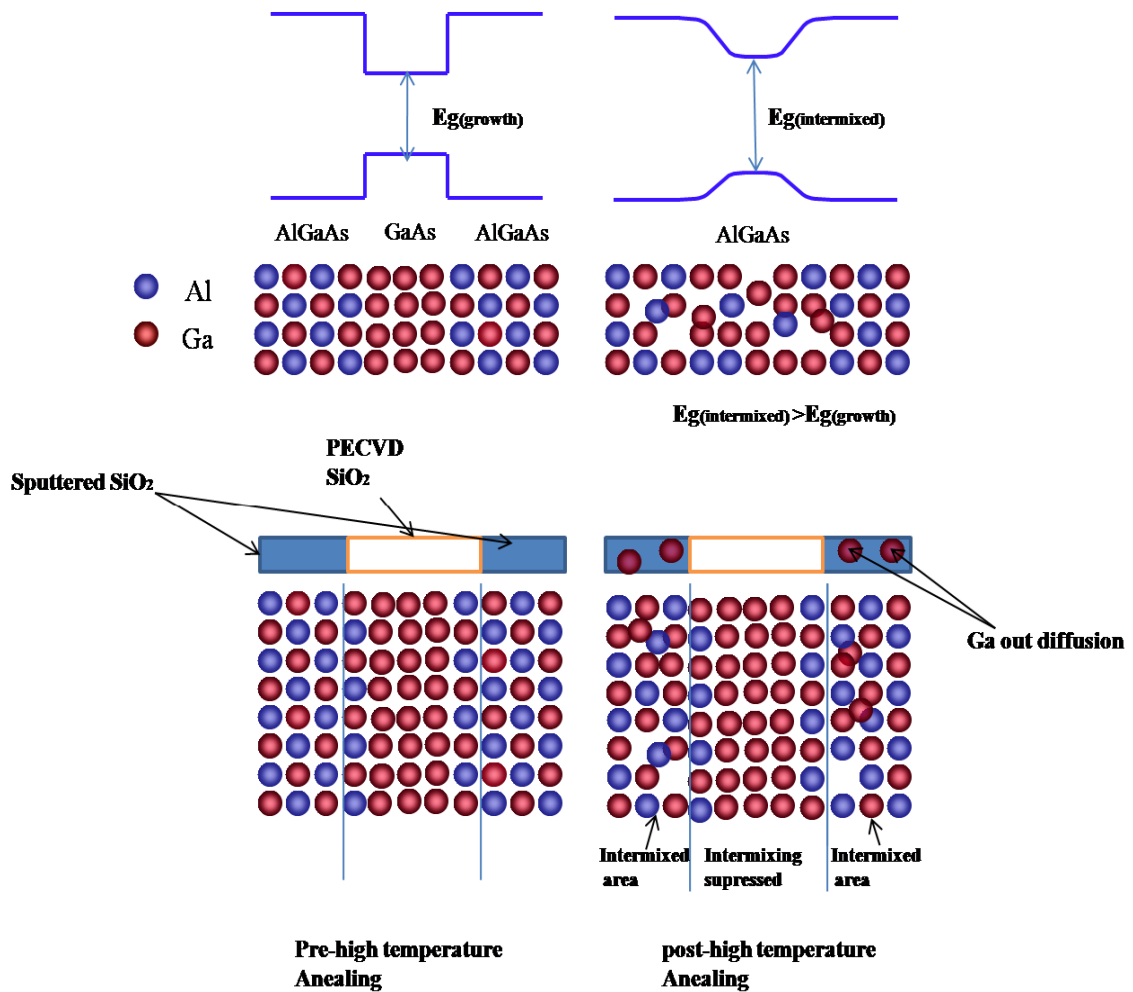


Figure 4.17: Quantum well intermixing using sputtered silica concept.

During the argon ion sputtering process, minute amounts of Cu are used which promote the intermixing. The concentration of Cu impurities in the sputtered silica film is much smaller than the impurity induced disordering (IID). Hence, the free carrier loss is substantially less than that for the IID process. Figure (4.18) shows a 1x2 MMI array laser device with a post quantum well intermixing process annealed at 810 ° C. The interface between the intermixed and non-intermixed areas is clearly visible.

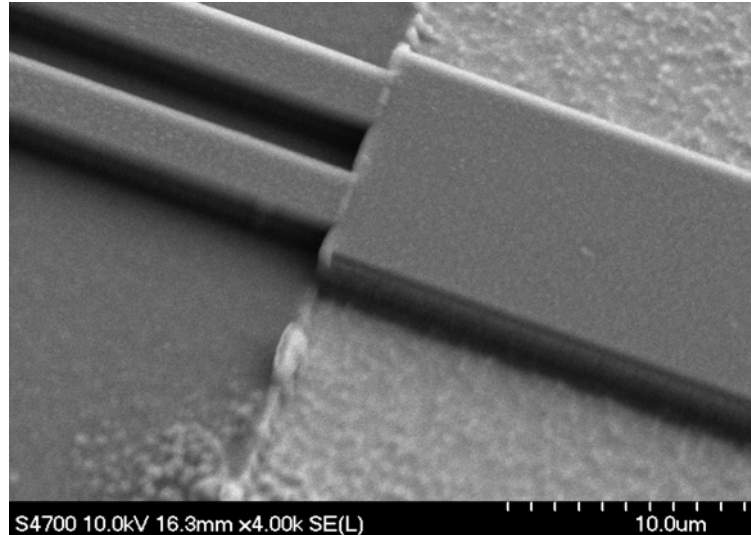


Figure: (4.18) 1x2 MMI array laser diode post QWI post annealing at 810° C. The sample in this example was capped with 200 nm sputtered silica followed by 200 nm PECVD. Interface between the intermixed and non-intermixed areas is clearly visible.

This process has been used commercially by Intense Ltd. The process of SiO<sub>2</sub>:Cu sputter film is patented by Intense and the University of Glasgow. A similar process which is called impurity free vacancy disordering, has the same processing steps. However, SiO<sub>2</sub> evaporation is used (178) instead of SiO<sub>2</sub> sputtering and a smaller shift is achieved with a commensurate increase of the annealing temperature. Further studies by Kowalski (181) indicated that the SiO<sub>2</sub> sputtering process results in damage near the semiconductor surface. The decrease in the photoluminescence intensity measured was attributed to the non-radiative recombination, which was increased by defects induced by the sputtering process.

The process has been used to develop a range of integrated devices, including wavelength tuned lasers, extended cavity lasers and most substantially integrated array laser diodes reported by MacDougall (182).

Furthermore, a large bandgap shift achieved of up to 68 nm was achieved in the GaAs/AlGaAs system, which is required for the fabrication of a high brightness array laser with non-absorbing mirrors.

The processing steps used in sputter induced intermixing, which was used throughout this research, can be summarised as follows:

1. Spin bi-layer PMMA resist of a thickness of 1.2 μm, which should be enough to suppress the sputtering.



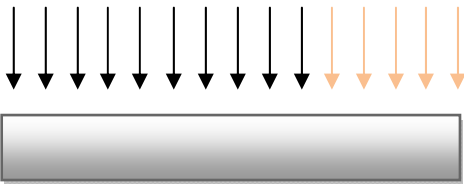
2. Pattern the wafer with the desired mask (e-beam writing process).



3. Sputter the sample using sputtering for a period of 25 seconds using Cu. 2-3 nm of Cu is deposited in the process. This is followed by sputtering 200 nm silica.



4. Hot acetone lift off  
Sputtering suppressed    Sputtered area



5. Deposit 200 nm PECVD silica



6. High temperature annealing at around 810 ° C.
7. At the end, remove the PECVD silica to leave a selectively intermixed sample with good surface morphology.

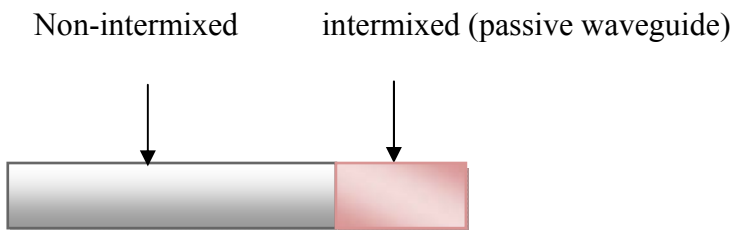


Figure (4.19) Fabrication steps of quantum well intermixing process using SiO<sub>2</sub> sputtering.

### 4.6.5 Rapid thermal annealing processing

Rapid thermal annealing is one of the vital steps to induce quantum well intermixing in GaAs/AlGaAs materials. The tool used in this work was a rapid thermal annealer, model JIPELEC FAV4. This machine is designed to produce temperatures up to 1250 °C using 12 tubular halogen lamps. The sample is normally placed face down on a piece of silicon and another piece of Si is placed on top of the GaAs piece.

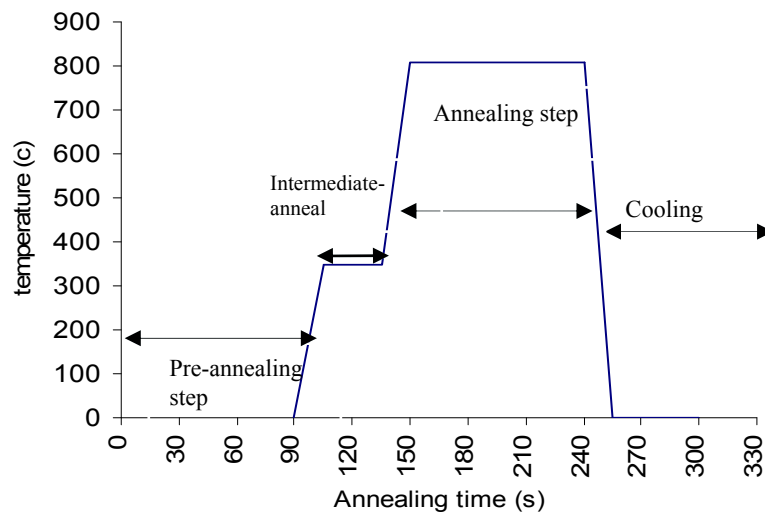


Figure (4.20) RTA temperature cycle for annealing GaAs for 90 seconds

The sample processing cycle can be seen in Figure (4.20) above. The RTA cycle for a sample starts with a 30 second initial low temperature anneal of 350 °C. The initial anneal reduces the probability of surface damage during the fast high temperature ramp up. The pre-heat is followed by a ramp up to 810 ° C for a high temperature anneal of 90 seconds (depending on the annealing time used). The high temperature anneal is followed by the ramp down and the machine cooling.

#### 4.6.6 QWI assessment

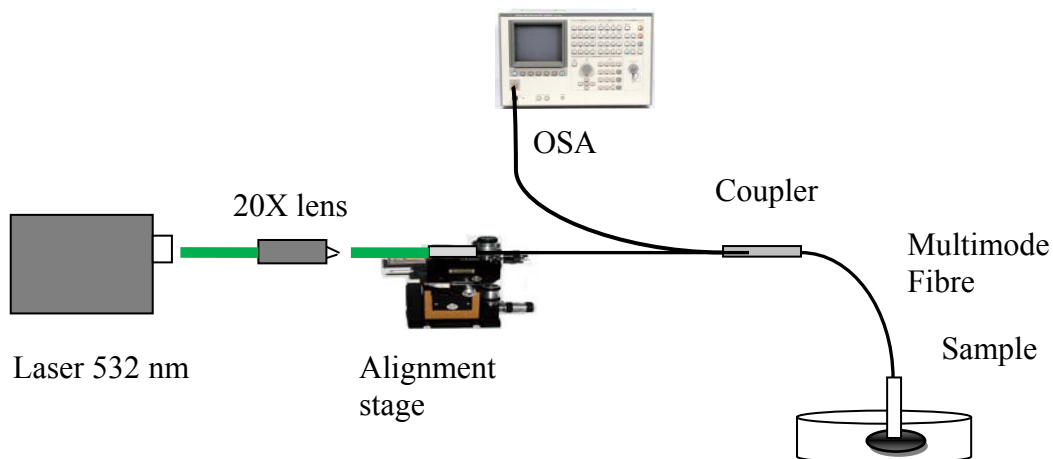


Figure (4.21) Photoluminescence system used for PL characterisation with 532 nm green laser source.

The quantum well intermixing process is evaluated by measuring the differential bandgap shift using a photoluminescence set up, as shown in figure (4.21). The set up consists of a 532 nm green laser running in free space continuous waves (CW) through a 20X objective lens, which is directed to a multimode fibre with a metal ferule at both ends. The multimode fibre is a 3 dB coupler that feeds the light to be injected onto the sample. The other fibre segment is connected to an optical spectrum analyzer for wavelength measurement, as shown in figure (4.21).

The photoluminescence measurement process is initiated by injecting the light into sample, which is immersed in liquid nitrogen at 77 K. Measuring the sample in liquid N<sub>2</sub> results in improved and clear spectra, because it lowers the rate of non-radiative recombination. The light injected into the sample (having a higher energy than the bandgap) will excite an electron to move up from the valence band into the conduction band by absorbing a photon. The excited electron leads to the generation of a hole in the valence band. The electron will relax to the bottom of the conduction band, followed by the recombination of electron-hole pairs with the emission of photons. The photon energy is equal to the bandgap energy of the material.

#### 4.6.7 QWI experiments

The quantum well intermixing experiments were conducted initially using a single target sputtering system. The process was later migrated to a new system due to the death of the old system.

#### 4.6.7.1 QWI experiments using Single target sputtering system

The initial quantum well intermixing development work was carried out using the available Nordiko single target sputtering machine. In this section, the experiments carried out will be detailed.

The sputtering is done in this system using a silica target assisted with minute amounts of Cu in the chamber. The presence of Cu is normally in a minute quantity. Hence, the contribution to the free carrier absorption will be much less than for the IID process. In the sputtering process, SiO<sub>2</sub> is deposited with the Nordiko RF machine, using an Ar: O<sub>2</sub> gas mixture at a pressure of  $5 \times 10^{-3}$  mbar, an RF power of 100 W, and a DC self bias of 1 kV. The SiO<sub>2</sub> film thickness used was 50 nm. Prior to the high temperature anneal, a PECVD cap of 200 nm is deposited on top of the sputtered silica to provide suppression of the intermixing. The sputtered SiO<sub>2</sub> with the Cu impurity enhances the generation of the point defects, which are the vacancies on the semiconductor surface. This process is accompanied by interstitial Cu diffusion into the semiconductor. The Cu impurity moves to (III<sub>Al</sub> and III<sub>Ga</sub>) lattice sites. However, as the Cu is an active impurity, it should be controlled in such a way that it should not degrade the material's electrical and optical properties. The Ga atoms diffuse out following the high temperature anneal and it is known that Ga has a high diffusion coefficient in SiO<sub>2</sub> at temperatures higher than 800 ° C (184, 185). The processes above create a concentration gradient assisted by high temperature annealing between the Ga in the quantum well and Al in the barriers. Thus, Al: Ga inter-diffusion occurs between the quantum well and the barriers. Subsequently, the QW bandgap shifts to a higher energy.

To study the intermixing and to optimise wavelength shift, GaAs/AlGaAs material (the structure is described in table 3.2 Chapter 3) with two quantum wells is used with three different sets of samples. For the first set of samples, a piece of wafer was cleaved, 50 nm of sputtered silica was deposited, then cleaved into 2 x 2 mm samples. This size is suitable for PL measurement. The first set of samples was annealed at different temperatures, starting from 775 ° C to 950 ° C in 25 ° C steps. The second set of samples was used with 50 nm sputtered silica deposited followed by a 200 nm PECVD cap.

The samples were annealed at temperatures from 500 °C to 850 °C to cover a wide range of temperatures. The third set of samples used was capped with 200 nm PECVD SiO<sub>2</sub>. They were annealed at temperatures from 625 to 850 °C. After the annealing, the samples were assessed using the PL set up. Figure (4.22) shows the photoluminescence spectra for different annealing temperatures for the first set of samples. The samples were cleaned after the sputtering without any damage to the topography of the GaAs wafer.

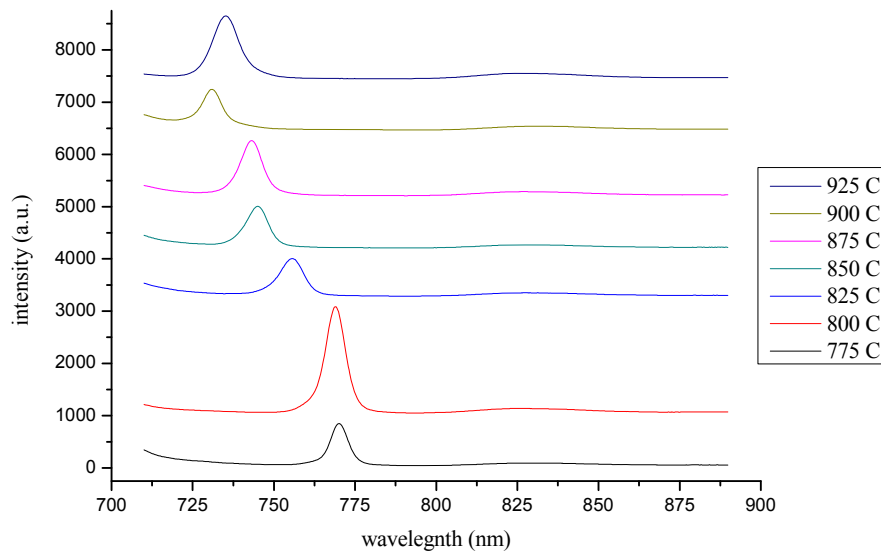


Figure: (4.22) PL measurement in liquid N<sub>2</sub> 77 K for Intense material using different annealing temperature. As grown material has a wavelength of 775 nm at 77 K

The maximum blue shift achieved was 42 nm at 925 ° C. At an annealing temperature > 925 ° C, the shift in wavelength did not increase. This means that the intermixing was saturated.

From all the above observations, the process with a 42 nm blue shift is adequate to reduce the passive waveguide losses for integration. The single target sputtering system was used for intermixing in the early devices. However, this machine being 30 years old, suddenly stopped working. Therefore, an alternative machine and the process was sought. The unavailability of Nordico single target sputter machine that is used for the silica sputter process led to the exploration of alternative quantum intermixing processes. An evaporator has been used, which can evaporate a very thin layer of copper (Cu) onto the GaAs/AlGaAs sample. This was followed by e-beam evaporated silica of 50 nm. The results of this experiment are plotted in figure

(4.23), which shows the PL shift versus the annealing temperature. The figure shows a clear increase in the blue shift of the wavelength with increasing the temperature, as expected.

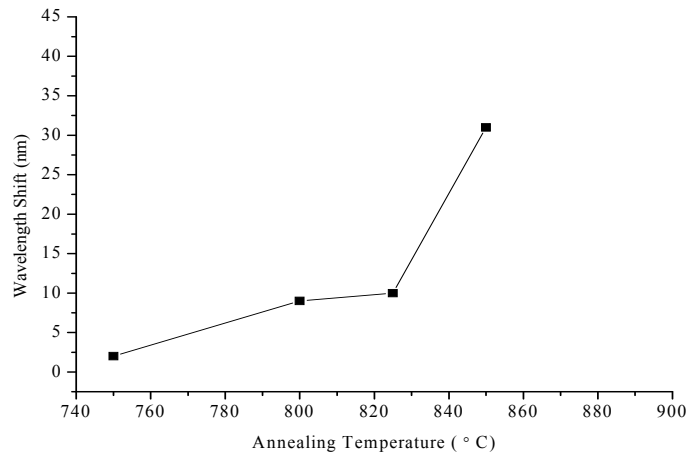


Figure: (4.23) Cu evaporation process for quantum well intermixing.

The results of the wavelength shift for the evaporation is comparable to the results of the sputtered silica process. The difference is that a lower blue shift is obtained for the same annealing temperature.

The sputtered silica process that comprised 50 nm and 200 nm of sputtered and PECVD silica respectively has the largest shift. The sputtered silica process with 50 nm sputtered silica without PECVD capping had a maximum shift of 41 nm. The latter two processes are effectively the same. However, the PECVD silica capping results in better surface morphology and improved PL intensity from the annealed sample.

Figure (4.24) summarises the results that have been achieved for four different caps, 50 nm sputter, 50 nm sputtered silica with 200 nm cap, 200 nm PECVD layer and Cu evaporation with E-beam silica cap.

From inspection of figure (4.24), it can be concluded that the 50 nm sputtered silica process capped with 200 nm PECVD was the most suitable process using the single target sputtering system.

The thickness of the sputtered silica was increased to 200 nm and it was capped with 200 nm PECVD. The best result of this process was a 43 nm blue shift at 850 °C.

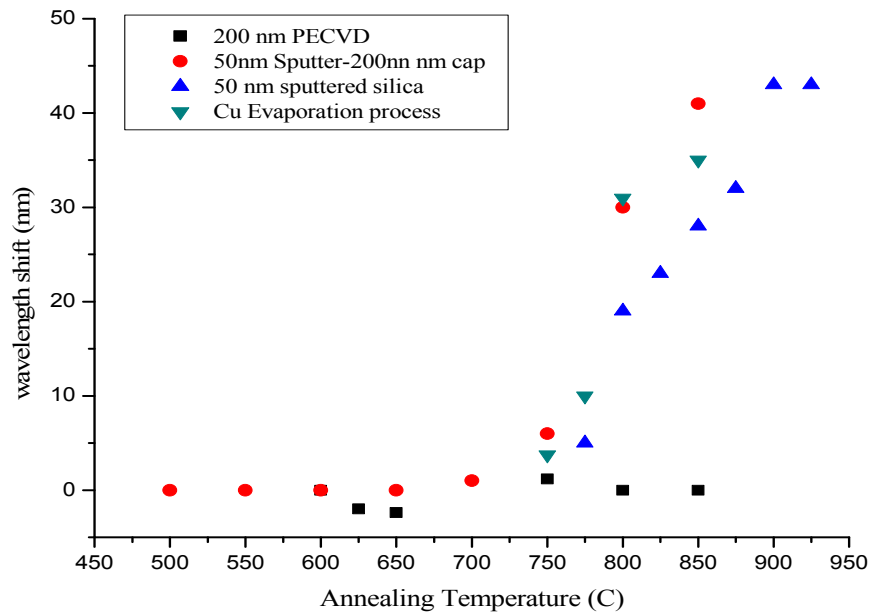


Figure (4.24) Intermixing results for different SiO<sub>2</sub> cap for 60 s anneal. PL shift vs. annealing temperature for different silica caps where red triangle points represent 50 nm sputtered silica capped with 200 nm PECVD, circles represent 50 nm sputtered silica with no cap and the green triangles points represent Cu evaporation-e-beam silica process, while 200 nm PECVD is represented by squares.

#### 4.6.7.2 Intermixing using multi-target sputtering machine

A multi-target sputtering system has been used following the loss of the tool discussed in the previous section. The process development of quantum well intermixing involved optimising the sputtered SiO<sub>2</sub> film thickness as well as controlling the Cu impurity that is used is for quantum well intermixing enhancement. Cu and silica targets have been used. Due to the design of this sputtering system, different runs were required in order to develop the intermixing. However, the initial process parameters used were suggested by Dr. Steven McMaster, a colleague in the Department (191).

The final process parameters used, are given in table (4.5).

Parameters	Process	Unit
Ar flow rate	35	sccm
Ar pressure	3	mTorr
Cu target clean	30	minutes
Cu deposition time	25	seconds
Cu deposition RF power	30	W
Cu deposition DC bias	200	V
SiO <sub>2</sub> target clean	30	minutes
SiO <sub>2</sub> deposition time	44	minutes
SiO <sub>2</sub> deposition RF power	200	W
SiO <sub>2</sub> deposition DC bias	0.18	V

Table: (4.5) Sputter deposition parameters used in the SID process in the multi-target sputtering system.

The amount of Cu impurity is very critical for quantum well intermixing. Therefore, optimisation of impurity sputtering is vital to obtain a good differential shift for bandgap widening. The deposition time for Cu was varied while maintaining the thickness of the sputtered silica at 200 nm, which was optimised as well. The thickness of sputtered silica was selected to be 200 nm and a time of 44 minutes was found to be the optimum deposition time. The deposition rate of silica was 4.54 nm/min. To execute a controlled experiment, 200 nm PECVD silica was used after silica sputtering.

Initially, 200 nm SiO<sub>2</sub> sputtered silica is deposited and capped with 200 nm PECVD. The Ga atoms diffuse through this cap, thereby increasing the number of vacancies and increasing the degree of intermixing.

In this experiment, the amount of Cu impurity was varied by varying the sputtering time for Cu from 5 seconds to 40 seconds. For this purpose, 2x2 mm GaAs/AlGaAs pieces were sputtered with Cu. The results from this experiment can be seen in figure (4.25). The maximum wavelength shift was achieved for a sputtering time of 25 seconds. Increasing the sputtering time further to 30 seconds did not increase the shift. This means that optimum intermixing has been achieved at a sputtering time of 25 seconds. A differential shift of 58 nm was achieved for a Cu sputtering time of 25 seconds, 44 minutes for the sputtered silica and 200 nm PECVD deposited silica cap. The experiments have been repeated a few times. The optimum conditions selected from the experiments were 200 V bias voltage, sputtering

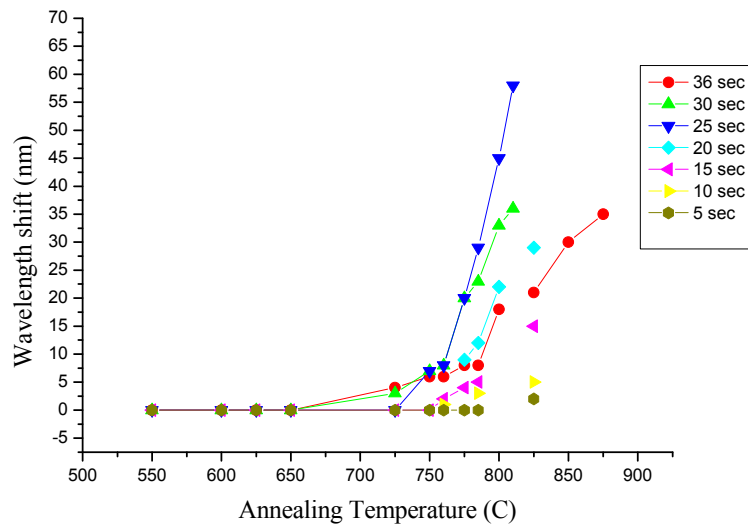


Figure (4.25) PL shift for Cu impurity in QWI using sputtered silica process. The 2x2 mm GaAs/AlGaAs samples were annealed for 60 seconds. The only variable is sputtering time for Cu. The time was varied from 5 seconds to 36 seconds.

time of 44 minutes for silica, 25 seconds for Cu deposition. The optimum process parameters can be seen in table (4.5).

From the basic diffusion definition, increasing the time or the diffusion coefficient can result in increased diffusion i.e. maximising the intermixing. The increased diffusion occurs by increasing the annealing temperature provided that the optical properties of the film are maintained.

Annealing time was the next parameter that has been optimised. In figure (4.26), the results of the intermixing for three different annealing times can be seen. Using the optimised parameters in table (4.5), the maximum shift achieved was about 68 nm for a 90 second RTA annealing time with a corresponding annealing temperature of 825 °C. However, this temperature is somewhat high for un-intermixed GaAs quantum wells. Therefore, an annealing temperature of 810 °C has been used in the majority of the intermixed devices. In section (4.7), a simple waveguide loss measurement was performed. For an intermixed waveguide with bandgap shift of 58 nm, the measured waveguide loss is around 4.48 db/cm, which is a very reasonable value. On the other hand, a bandgap shift of 58 nm is an excellent value for the intermixing, which ensures a low passive waveguide loss. A large wavelength shift is desired for the high power laser diodes we are dealing with in this research. The higher the bandgap shift, the higher COMD level achieved. Furthermore, materials exhibit absorption extending to energies below the nominal

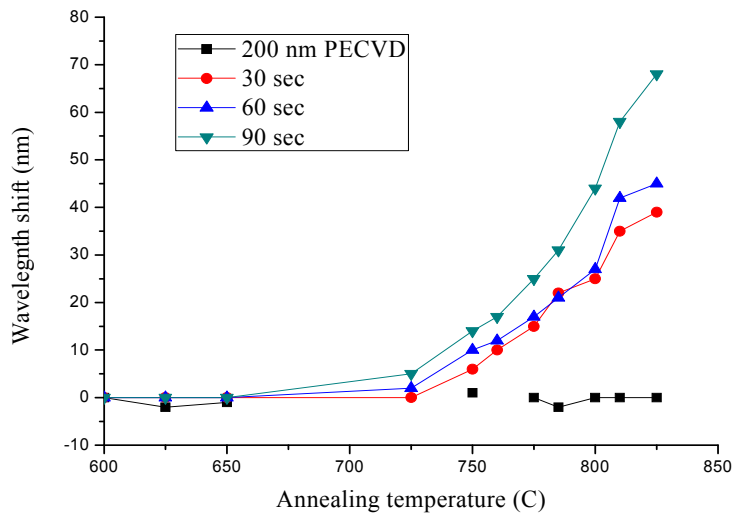


Figure (4.26) Intermixing results for three different RTA annealing times (30s, 60s, and 90 s) shown for 200 nm sputtered silica capped with 200 nm PECVD. A 200 nm PECVD anneal is also shown, which is used for suppressing intermixing. The annealing temperature used here was 825° C.

bandgap. This absorption tail, known as the Urbach edge, results from phonons, impurities, excitons, and internal electric fields (222). The presence of this tail could cause higher losses near the band-gap, and hence the need for higher band gap shift. The annealing temperature used was much lower than that for the previously used process on the single target sputtering system.

#### 4.6.8 Quantum well intermixing process repeatability and contamination issues.

In the course of the fabrication work carried out during this research, the QWI process required great effort in terms of reliability and repeatability, due to the several critical steps involved in it. These critical steps, which directly affect the repeatability of QWI process, are as follows:

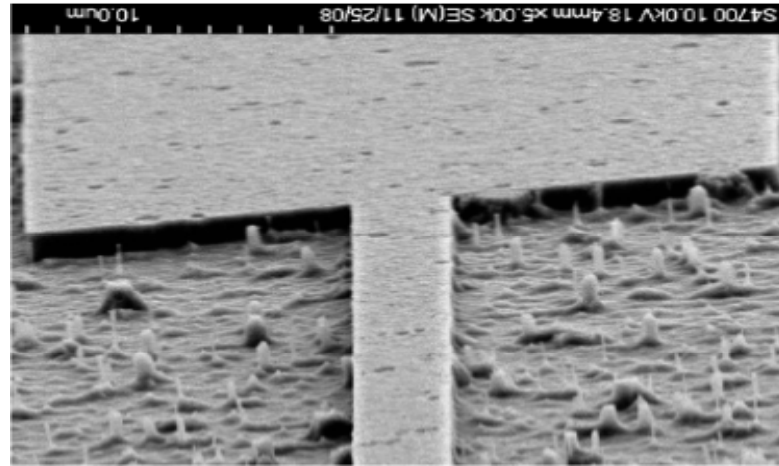
1. The first critical aspect is the sputtering process. After the failure of the single target sputtering system, a multi-target sputtering machine used in this work, which was still not completely reliable, as it was still an old machine. The multi-target sputtering machine is not computer controlled and had to be manually operated by its responsible technician, with unavoidable reduced accuracy in the control of the sputtering conditions and duration. This was particularly critical for the deposition of the 1-2 nm thick Cu layer.

2. Another aspect related to the type of sputtering machine under use is that this does not have a separate chamber for loading the sample into it. Instead, the load is done directly in the chamber where the targets are set and where the sputtering takes place. This causes repeated exposures of the chamber and of the targets to the atmosphere and thus to contamination.
3. One of the important issues with sputtering machine used for QWI is that it was used for the deposition of different materials like: Au, Cu, SiO<sub>2</sub>, Ti, Ni, Al, Pt and Ge. The machine itself was equipped with only two target holders. This causes the continuous need to replace the targets, to satisfy the needs of different users. Furthermore, the machine is not placed in a proper clean room environment, causing further contamination of the sample and of the chamber during the loading stage.

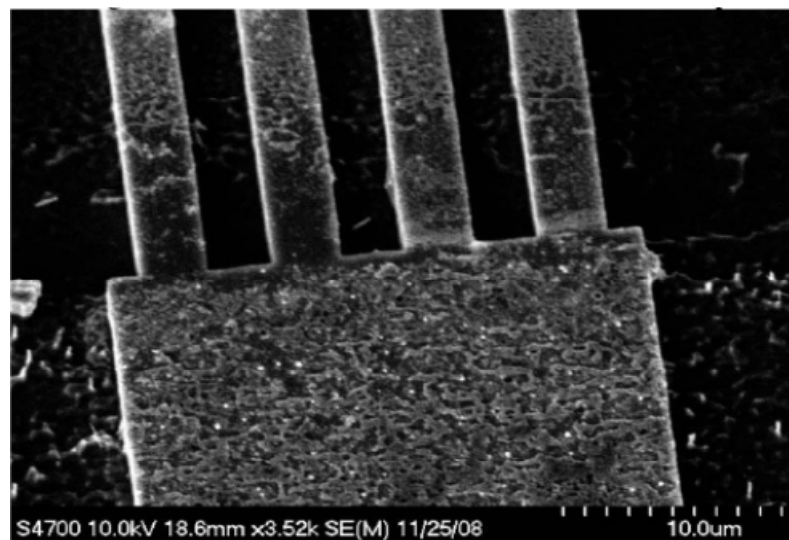
The cross contamination of the process samples with one of the different sources of contamination can affect the QWI process and device fabrication. In figure (4.27a and 4.27b), two SEM images are shown of an etched sample after the QWI intermixing stage. The spots on the MMI and the pillars on the surface were caused by the contamination in the sputtering stage. This contamination is extremely difficult to remove after high temperature anneal during QWI process. Thus, it is an avoidable that this contamination is transferred to the sample during further processing.

4. The control of the RTA step is also critical for the repeatability of the QWI process, because the bandgap shift induced in the material is strongly dependent on temperature and duration of the annealing. The fact that the RTA machine was used for several different processes and sample materials was found to be a further source of contamination. For this reason, in all the RTA runs made, the shared sample holder (silicon wafer) present in the machine was replaced by a fresh one (personal wafer), always pre-cleaned and only used for the QWI process. In addition to this, before every RTA run, the integrity and position of the thermocouples put in contact with the RTA sample holder were checked, in order to guarantee the same annealing conditions (as the RTA process was computer-controlled through the thermocouples). Moreover, the sample had to be placed on the sample holder always in the same position (on top of the

central thermocouple) and covered by the same piece of silicon wafer. The piece of silicon put on top of the sample is essential for avoiding the desorption of the As atoms.



(a)



(b)

Figure (4.27) (a) Figure above (a) shows etched MMI device post intermixing. The source of the spots on the MMI is contamination on the QWI sputtering stage. These spots and contamination were transferred onto the sample after etching causing pillars or micro-masking. (b) Figure (b) shows severe contamination of the deposited layer on the MMI after intermixing and annealing, which is followed by etching.

5. The definition of passive sections in the MMI array laser diode required a reliable intermixing process. An additional difficulty with QWI process lies in the usage of double PMMA film, which is required to lift off the sputtered film from the areas to be left un-intermixed. This lift off process not to be confused with lift off of the p-contact pads, because it is entirely different. Mostly, the lift off process used in the QWI process results in PMMA residues at the edges of the QWI window. These residues can be

extremely difficult to remove after the RTA stage, where high temperature is used.

Failure in the QWI process leads to a very high losses in the passive sections leading to COMD at very low power levels. Moreover, the material optical loss increases dramatically, which leads to an increase in the device threshold current. Hence, it would not be possible to fabricate devices with higher powers.

#### **4.7 Fabry-Perot propagation loss measurement**

The losses in a semiconductor optical waveguide can be generated from three sources, absorption, scattering and leakage (186). The absorption occurs due to free carriers and the presence of mid bandgap energy levels, which exist due to defects introduced during the crystal growth and the diffusion of impurities. Sidewall and epitaxial interface roughness are the largest sources of scattering. The third source of waveguide loss is the leakage, whereby radiation losses occur in the GaAs/AlGaAs material system due the large substrate refractive index, which in this case is GaAs. The leakage could occur as well to a heavily doped cap layer in passive waveguides.

The loss in the waveguide must be small. This is particularly important in the design of high brightness laser diodes and when longer passive waveguides are required within the device. Higher losses in the passive section reduce the round trip gain of the semiconductor laser, thus affecting the laser output power. One way to reduce the losses in passive optical waveguides is by employing the quantum well intermixing technique described in the previous section. The loss in the waveguide is reduced significantly by intermixing, which results in a blue wavelength shift i.e. enlarging the bandgap of the waveguide, making it transparent. The lower absorption at the facets increases the COD limit for high power lasers. To evaluate the losses in the GaAs/AlGaAs material, passive waveguides have been fabricated using the reactive ion etching process. The waveguide etch depth has been optimised to support only a single lateral mode.

A few methods for waveguide loss measurements (186,187) have been studied in the past with varying accuracy. For example, the cut back method has been used by (186). The problem with this method is that every time the waveguide

is aligned, the coupling will be different. Therefore, the results obtained using this method are likely to be not very accurate. The method that has been used in this research is the Fabry Perot method developed by Walker (187). The measurement is based on the resonance action in the semiconductor waveguide. The transmission of a Fabry Perot straight waveguide resonator with uniform propagation loss can be described by (186):

$$T(\varphi) = \frac{(1-R)^2 e^{-\alpha L}}{(1-r)^2 + 4r \sin^2(\varphi)} I_0, \quad (5)$$

where:

$I_0$  is the intensity of incident light, which includes the input and output intensity;

$\alpha$  is linear propagation loss coefficient ;

$R$  is the end facet reflectivity, and

$$r = R(e^{-\alpha L}) \quad (6)$$

$$\varphi = 2\pi n_{eff} \frac{L}{\lambda} \quad (7)$$

Equation (7) represents the single-pass phase shift, while  $n_{eff}$  is the effective mode index. As coherent monochromatic incident light is assumed, the transmission contrast is expressed by;

$$K = \frac{T_{max} - T_{min}}{T_{max} + T_{min}} = \frac{2r^2}{1+r^2} \quad (8)$$

This will lead to;

$$r = R(e^{-\alpha L}) = \frac{1 - \sqrt{1 - K^2}}{K} \quad (9)$$

The propagation loss is therefore given by:

$$\alpha = -\frac{1}{L} \ln \left[ \frac{1 - \sqrt{1 - K^2}}{RK} \right] \quad (10)$$

where  $K$  is the loss pass amplitude reduction factor and  $R$  is the average of the reflected power from the back and front waveguide facets.  $R$  can be computed from equation (11).

$$R = \left[ \frac{n_{eff}-1}{n_{eff}+1} \right]^2 \quad (11)$$

To calculate the optical passive waveguide losses, the setup has been used as in figure (4.28).

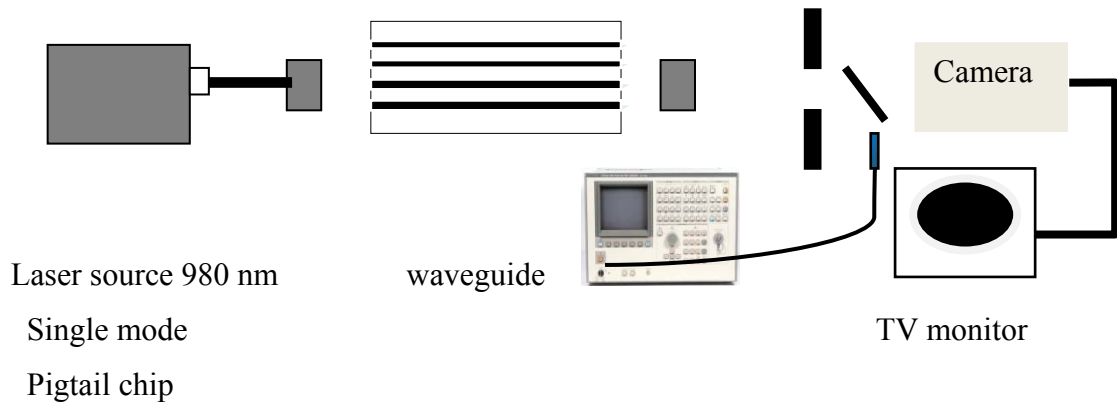


Figure (4.28): Loss measurement setup for GaAs/AlGaAs waveguide

The transmission through the waveguide is measured, while varying the waveguide temperature by using a cotton bud which immersed in liquid  $N_2$ .

The summary of the method used during this measurement is as follows:

1. Couple the light into the waveguide.
2. Use the optical spectrum analyser to find the peak wavelength.
3. Set the wavelength span to zero.
4. Prepare some liquid  $N_2$  in a small container.
5. Dip a cotton bud into the  $N_2$ .
6. Place the cotton bud as close as possible to the waveguide structure (without touching).
7. This will change the transmission of the waveguide in a periodic manner produce maxima and minima.
8. Use the equation (8), (10) and (11) to calculate the loss.

The transmission was measured using an optical spectrum analyser while varying the temperature. From figure (4.29),  $K$  is calculated to be 0.261. The waveguide used was 9.8 mm in length. Therefore, the losses calculated using this method were 4.48 dB/cm. This value is lower than the value found by measuring the broad area laser characterisation, which was found to be 6.9 dB/cm. The difference in the value could be attributed to the low loss through the use of the quantum well intermixing. The blue wavelength shift for the waveguide used was 58 nm, so lower losses have been achieved. These lower

losses are important for the design of an array laser diode. Firstly, they allow the fabrication of very long passive sections ( $\geq 1$  mm in length) and NAMs (30 – 200  $\mu\text{m}$  in length). Secondly, a large bandgap shift ( $> 40$  nm) increases the

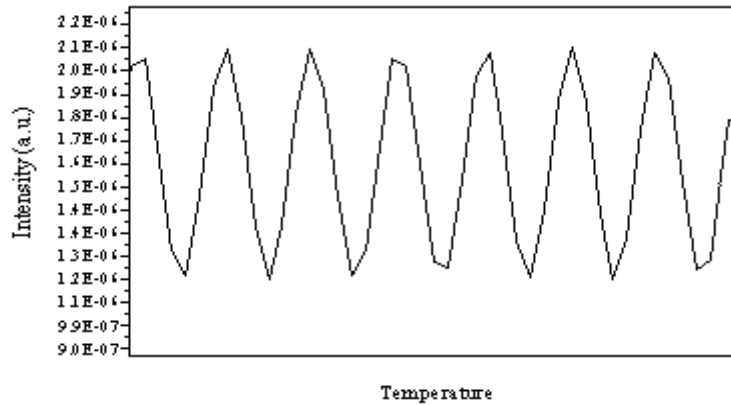


Figure: (4.29) Optical transmission through passive waveguide using temperature tuning. Losses can be measured using maxima and minima points.

catastrophic optical damage limit (35, 165) that can be achieved in a high brightness laser diode. This effect is evident in figure (4.30) from (165). Inspection of the figure shows that the highest power achieved was for a laser with NAM (non absorbing mirror) section that is blue shifted by 65 nm. This is the reason that this level of intermixing is important to increase the COD limit.

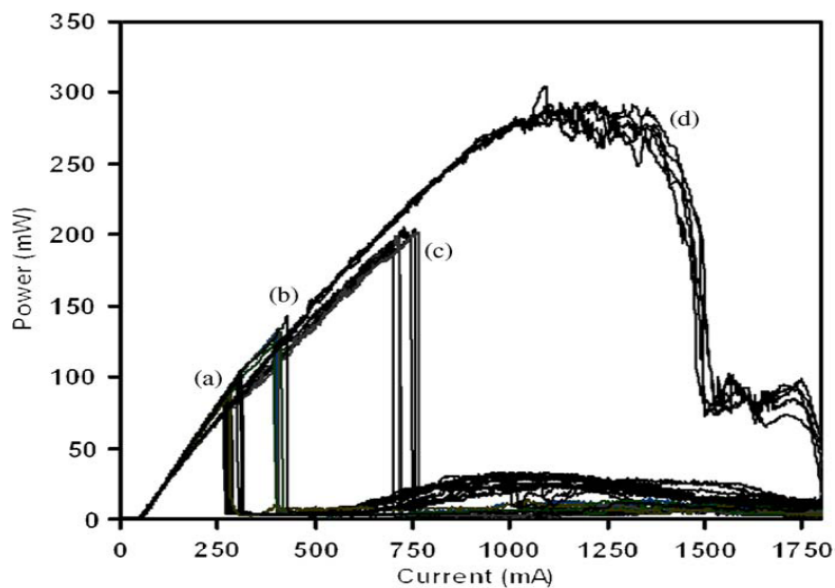
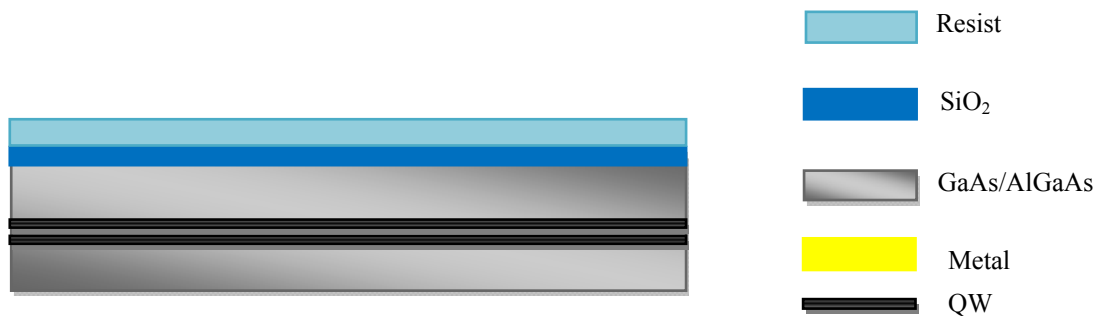


Figure (4.30): CW light/current characteristics of 830nm un-coated ridge waveguide lasers with (a) no-NAM/NIM (i.e. a conventional laser), (b) NIM only, (c) a NAM/NIM with a 45 nm bandgap shift, and (d) a NAM/NIM with a 65nm shift. (Courtesy of J. Marsh) (Reference 165). In fact, as can be seen in figure (32d), COD was not observed for the lasers with a shift of 65 nm. The rollover in power is due to heating of the diode.

## 4.8 Multimode interferometer array laser fabrication steps

The fabrication steps of the multimode interferometer array laser can be summarised as follows:

1. Sample clean: The sample is cleaned using 5 minutes in an ultrasonic methanol bath, which is followed by 5 minutes in an ultrasonic acetone bath and finally a dip in IPA and using a nitrogen gun to dry.
2. PECVD SiO<sub>2</sub> deposition.
3. Alignment markers e-beam lithography.
4. Alignment markers etch using GaAs/ AlGaAs etch using SiCl<sub>4</sub> reactive ion etching.
5. Deposit 700 nm PECVD SiO<sub>2</sub> layer and spin resist.



6. PMMA resist development.



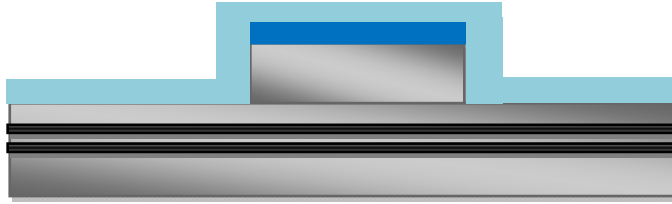
7. PECVD silica etch.



8. AlGaAs etch and resist removal. A second etch is used for two level AlGaAs etching to define a deeply etched MMI.



9. AlGaAs etch and resist removal. A second etch is used for two level AlGaAs etching to define deep etch MMI. AlGaAs etching to etch MMI.



10. Etching MMI area only through the core using  $\text{SiCl}_4$  etch. This etch is vital for the MMI. It is done after etching the ridge waveguide gain sections. The etch is made through the core only in the MMI region for reduced losses and optimum imaging.



11. Post AlGaAs waveguide etch, 300 nm PECVD is deposited to define the contact window through etching window in the PECVD mask. Contact window is opened on the gain sections only.



12. A p-metallisation is followed. The devices are thinned mechanically. Cleaning process follows to remove all the debris. n-metallisation is last fabrication process pre-contact anneal. After annealing, the devices are cleaved into individual bars, which are ready for testing at this stage.

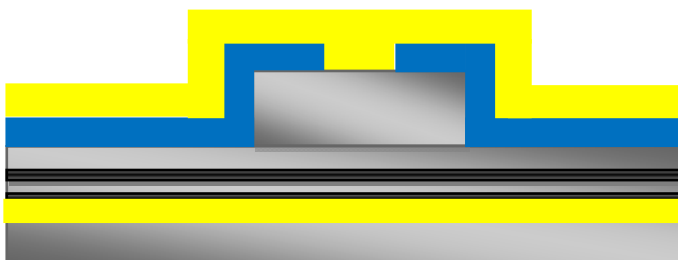


Figure (4.31) Fabrication steps for 1xN MMI array laser diode.

## 4.9 Contact metallization

Contact metallization is one of most important steps in laser diode fabrication, particularly for high brightness lasers, where high injection currents are used to obtain high brightness.

The metal electron beam evaporation process does not provide good step coverage. This becomes very important at the side edges of the ridges, where the metallization can be very thin and the side walls do not have good coverage. The directionality of the evaporation process is the main reason for this effect. Coverage of the side walls is vital for achieving a low sheet resistance, hence reducing the junction temperature for the high brightness lasers.

As good step coverage cannot be achieved using metal evaporation alone, therefore metallization using plasma sputtering is employed. Prior to any metallization step, the surface cleanliness of the semiconductor is of great importance for low ohmic contact resistance. As we are dealing with GaAs, an oxide layer in the region of 20 Å (189) can be formed at room temperature in one hour. Therefore, a clean step of the device involving a 30 seconds dip in HCl: H<sub>2</sub>O (1:40) is done to remove any oxide layer prior to any metallization step.

In the metallization step of the p-type contact, the process involves evaporation of Ti, Pt and Au layers. A 30 nm thickness of Ti layer used, which works as an adhesion layer to silica for isolation purposes. The Pt layer used was 60 nm. The third layer is Au and the thickness used is 240 nm. This metal evaporation process is followed by a metal sputtering process. A 300 nm Au layer has been used to improve the step coverage and side wall coverage. Moreover, this thick layer of Au is important for high current injection for the laser diode maintaining a low p-type contact resistance. During the chip fabrication, several contact pads are patterned on the semiconductor and the contact resistance is measured using the transmission line method (TLM). Figure (4.32) shows an example of contact pads that have been patterned for this purpose. After metal deposition, lift off is performed by placing the semiconductor wafer in warm acetone (50 °C) until all the extra metal is removed. For good metal lift off results, the sample should be left in the acetone for a few hours.

The n-type metallization used consists of five layers, which are Au/Ge/Au/Ni/Au with corresponding thickness of 14,14,14,11 and 240 nm, respectively. The n-type contact metallization is evaporated. The contact annealing follows the contact deposition. An example of the final device with



Figure: (4.32) P-metallization for a chip, which six devices can be seen and a scribing mark is observed on the right.

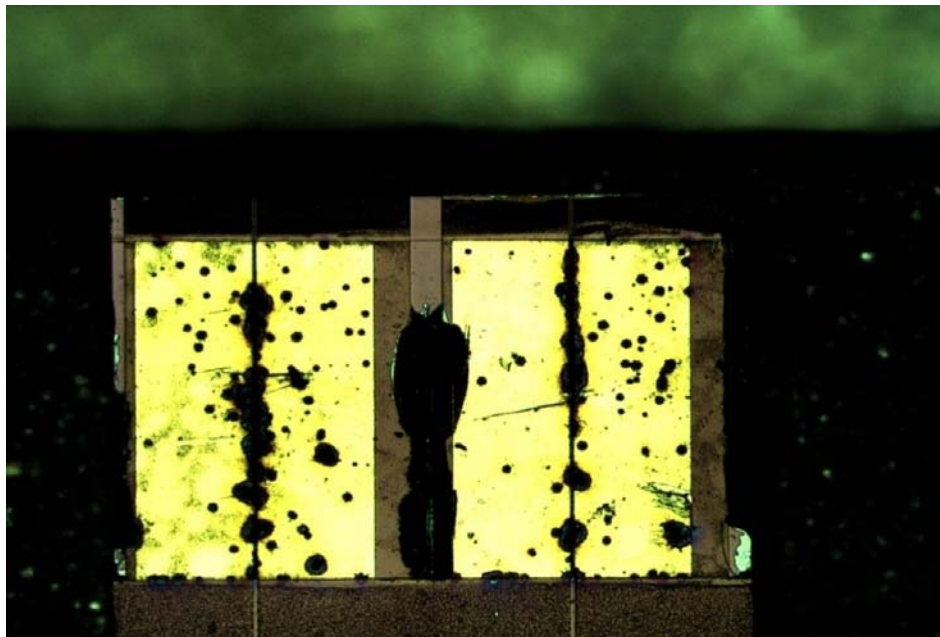


Figure (4.33) Fabricated devices suffered from metal shorting for the reason of metal pads proximity for individually addressable array laser.

the P-metallization can be seen in the optical microscope image in figure (4.32). The contact metallization of very small gaps of around 1-2  $\mu\text{m}$  proved

extremely difficult to achieve reliably, so the fabrication of a multi-contact individually addressable laser array laser was not sought, because of the short circuits between the gain sections for the devices (see figure (4.33)). This led to the fabrication of wide single contact for the array laser diode.

#### **4.10 Summary and conclusions**

The work that had been carried out in Chapter four was considerable. Most of the processes were developed in order to produce functioning devices. The important ones are:

1. Etch process development of GaAs/AlGaAs material.
2. The development of new quantum well intermixing process (QWI), which included technology development and transfer from Intense Ltd. This resulted in a considerable development work to be carried out. This includes: firstly, sourcing new targets for the Nordico Sputtering system. Secondly, optimisation of deposition of silica sputtering and Cu sputtering processes. Thirdly, the requirement of the development of rapid thermal annealing process to obtain the optimised annealing conditions. All the above, made it possible to arrive at the results for the quantum well intermixing. The results of the QWI differential blue shift were 68 nm and 58 nm for annealing temperatures of 825 ° C and 810 ° C, respectively. This QWI shift was adequate to obtain monolithically integrated MMI array laser devices with a low loss. These low losses of the passive sections of the device (NAMs, MMI section and output waveguides) enabled practically good devices to be fabricated. However, the development process for the QWI was not without difficulties. These difficulties lay in the process repeatability that is actually inherent to the Cu assisted QWI process. The repeatability problem of the QWI process was also due to the fact that the sputtering machine was in use for the deposition of many other materials. These materials included materials like Au, Cu, SiO<sub>2</sub>, Ti, Ni, Al, Pt and Ge. The consequence of multi-usage of the sputtering machine was the non repeatable process. Therefore, in many process runs the material electrical and optical properties were affected causing non functioning devices or premature COMD failure.
3. In every stage of the device fabrication, the processes have been developed. These processes include the following:

- i. Fabrication markers design along with the etching process for the markers.
  - ii. Resist spinning and baking. Optimization of the thickness of the PMMA resists used in the process.
  - iii. E-beam photolithography process. Correct parameters were required for the optimisation of the sample exposure in the e-beam lithography.
  - iv. Development process optimisation.
4. The development of the metallisation processes, especially the p-metal process. The optimization of the annealing processes was also required. This is followed by testing the TLMs, which were fabricated for every device. The development of the p- metallisation process resulted in devices with a minute resistance.
  5. The thinning processes were also developed. The thinning of the material to about 120  $\mu\text{m}$  was very challenging, which was absolutely vital to obtain a functioning device. Furthermore, The scribing and cleaving processes were also improved to produce laser array bars.
  6. Producing functional devices for every design almost requires the modelling work, the design of the devices, QWI intermixing processes, etch processes, wet etching processes, metallisation processes, thinning processes, device mounting and complete device fabrication to be absolutely perfect.

# Chapter 5

## Device modelling and design

### 5.1 Introduction

This chapter begins by introducing the beam propagation method (BPM), the commercial software package from Rsoft. The BPM was used here mainly in the simulation of ridge waveguide and integrated MMI array laser diodes. In this thesis, the main usage of the BPM was for passive device modelling only. Hence, no active laser modelling was carried out. The use of the BPM package was crucial for the simulation and the optimization of the integrated  $1 \times N$  MMI device. This allowed accurate device dimensions, far-field profile and all the other related device parameters to be calculated. This chapter provides the details of the simulation methodology adopted in this thesis.

The first part is related to the general optical waveguide theory, along with the simulation and design of a GaAs/AlGaAs optical waveguide in the context of a single spatial mode laser. The details of the structure used can be found in Chapter 3 in table (3.2) of the thesis.

The high brightness device that is being researched in this thesis uses a multimode interference coupler for coupling the light. The MMI array laser diode device comprises: a NAM, a ridge waveguide gain region, a MMI coupler, and an output waveguide. All of these sections are integrated by means of quantum well intermixing. The theory of multimode interference couplers is included in this chapter. Furthermore, a simulation of the different parameters of the MMI array laser device is also included in the modelling to investigate the effect of each parameter on the coupled optical power. The final section summarises the results of the modelling that are applied in the

final device design. Modelling and simulation of the far field pattern of the array laser will be performed, because of its importance for coupling the light in an optical system. The phase locking of the array laser is best verified by studying the far field profile from the array laser device.

## 5.2 Beam Propagation Method

The beam propagation method has been used for the analysis of the optical waveguide. The BPM method takes into account the guided modes as well as the radiation fields. The axial variations in the index are also included in the simulation.

The BPM is a very attractive method for the simulation of various optoelectronic devices. A commercial software BPM package from Rsoft has been used for the simulation of the MMI lasers throughout this thesis. The computational core of the Rsoft BPM package (202) is based on the Finite difference BPM, which solves the well-known parabolic or paraxial approximation of the Helmholtz equation. This can be expressed as follows:

$$\frac{\partial^2 \phi}{\partial x^2} + \frac{\partial^2 \phi}{\partial y^2} + \frac{\partial^2 \phi}{\partial z^2} + k(x, y, z)^2 \phi = 0 \quad (5.1)$$

The scalar electric field here is written as:

$$E(x, y, z, t) = \phi(x, y, z)e^{-i\omega t},$$

and the notation:  $k(x, y, z) = k_0 n(x, y, z)$  is introduced for the spatially dependent wave number, with  $k_0 = 2\pi/\lambda$ . The geometry of the problem is defined by the refractive index distribution  $n(x, y, z)$ .

Alongside the scalar assumption, the phase variation in the field  $\phi$  due propagation along the guiding axis is factored by slowly varying field  $u$ . So,

$$\phi(x, y, z) = u(x, y, z)e^{-i\bar{k}z}, \quad (5.2)$$

where  $\bar{k}$  represents a reference wave number, which is the average phase variation of the field  $\phi$ . The reference wave number is represented in terms of the reference refractive index  $\bar{n}$ , via  $\bar{k} = k_0 \bar{n}$ .

$$\frac{\partial^2 u}{\partial z^2} + 2i\bar{k} \frac{\partial u}{\partial z} + \frac{\partial^2 u}{\partial x^2} + \frac{\partial^2 u}{\partial y^2} + (k^2 - \bar{k}^2)u = 0 \quad (5.3)$$

The equation (5.3) is the same as the Helmholtz equation, but is expressed in terms of  $u$ . Equation (5.3) above reduces to the following:

$$\frac{\partial u}{\partial z} = \frac{i}{2\bar{k}} \left( \frac{\partial^2 u}{\partial x^2} + \frac{\partial^2 u}{\partial y^2} + (k^2 - \bar{k}^2)u \right), \quad (5.4)$$

Equation (5.4) above is the basic BPM equation in 3D.

The fundamental physical limitation of the above approach results from the parabolic approximation to the Helmholtz equation, which implies a paraxiality condition on the primary direction of propagation. BeamPROP has the option of removing the restrictions imposed by paraxiality through the use of what is called the wide-angle BPM formulation. The wide angle BPM scheme is employed via Pade approximants, which includes (1,0), (1,1), (2,2), (3,3), and (4,4).

The wide angle BPM formulation is important in the simulation work carried out, because it enables modelling of high index contrast structures (like the deeply etched MMI) with larger propagation angles and complex mode interference. Moreover, the simulation results are more accurate. The second limitation of a scalar BPM approach is that polarization effects cannot be considered. Therefore, the commercial BPM software used is a full vectorial BPM formulation, where the polarization effects are included. This is also important when high index contrast structures are used, which is the case here.

The only limitation of the BPM software used is that it does not account for the back reflections. Although the BPM software package in use has the bi-directional algorithm built in, it is only valid for the use in 2D and when there is a small index contrast waveguide. This makes the reflection modelling of the integrated 1xN MMI array inaccurate. However, the simulation data for modelling the integrated passive MMI remain valid. The main purpose of using the BPM software was to passively model the integrated MMI laser structure.

The physical propagation problem requires two key pieces of information:

- 1) The refractive index distribution,  $n(x, y, z)$ .
- 2) The input wave field,  $u(x, y, z=0)$ . From these, the physics dictates the wave field throughout the rest of the domain,  $u(x, y, z>0)$ . The solution

algorithm requires additional input in the form of numerical simulation parameters such as:

- A finite computational domain for  $x$  in range  $(x_{\min}, x_{\max})$ ,  $y$  in range  $(y_{\min}, y_{\max})$ , and  $z$  in range  $(z_{\min}, z_{\max})$ .
- The transverse grid sizes,  $\Delta x$  and  $\Delta y$ .
- The longitudinal step size,  $\Delta z$ .

As is the case with any simulation method, confidence in the accuracy of the numerical solution requires experimentation to determine the sensitivity to the numerical parameters. The commercial package used in this work is 3D software, which is ideal for passive modelling of the integrated MMI array laser used in this work. Since we have different etch depths, it is vital to have the 3D option which is more accurate than 2D. However it takes longer computation time.

### 5.3 Waveguide modelling and design

Two dimensional optical confinement is required in many optical devices. Examples of these are lasers, switches and other optoelectronic devices, which are based on ridge or buried ridge waveguide structures. Figure (5.1) shows a ridge waveguide that provides single spatial mode wave guiding. Single mode wave guiding in both the vertical direction and the lateral direction can be achieved by using a ridge structure with controlled dimensions. Single mode lasers require good confinement in order to obtain a low threshold current as well as single lateral mode operation.

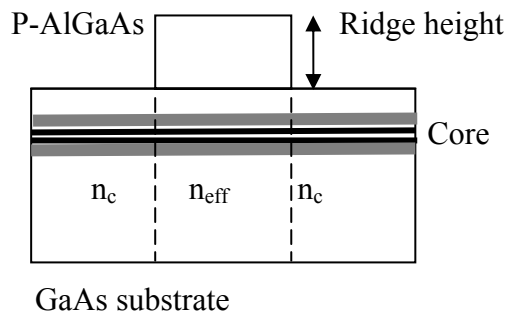


Figure (5.1): Schematic diagram of a ridge waveguide to provide 2 dimensional channel guiding. Controlled etched depth ensures single spatial mode.

To provide optical mode guiding in two directions, proper design of the ridge waveguide is of paramount importance, specifically the design of the ridge

dimensions. The single mode ridge waveguide can be formed by etching the semiconductor to an etch depth that ensures the guiding of only a single lateral mode. In order to compute the geometrical dimensions of the ridge waveguide, the commercial software, FIMMWAVE has been used. To find the best waveguide ridge depth and width, a number of iterations are used to find the optimum effective index contrast. A scan method can be used as well, which makes it much quicker to find the optimum ridge dimensions. The BPM package mentioned in the previous section has also been used. This method is used to model both the ridge waveguide and the multimode mode interference coupler, which are essential parts of the device design.

### 5.4 Single mode operation

To understand the single lateral mode operation, this section provides a useful method that can be used with simple design rules.

The single mode control is very important in both the lateral and transverse directions. Single vertical (transverse) mode operation can be achieved (192) only if:

$$d < d_{critical} = \frac{\lambda}{2} \frac{1}{\sqrt{(n_{core}^2 - n_{cladding}^2)}},$$

where  $d$  is the thickness of the active layer (core layer);

$n_{core}$  is the refractive index of the core layer and  $n_{cladding}$  is the cladding refractive index. The thickness of the core layer can be determined with a simple calculation. For example, if we take epitaxial structure used in table (3.2), the cladding thickness is 1.9  $\mu\text{m}$  and the core waveguide thickness is 2.0  $\mu\text{m}$ . Therefore,

$$d_{critical} = \frac{0.83}{2} \frac{1}{\sqrt{(3.67^2 - 3.47^2)}} \quad (5.5)$$

$$d = 347 \text{ nm.}$$

If we look at the core layer thickness (active layer), we see that it is 208.0 nm. This is much less than the critical thickness of 347 nm, so there is flexibility in the design.

Single lateral mode operation can be achieved according to equation (5.6):

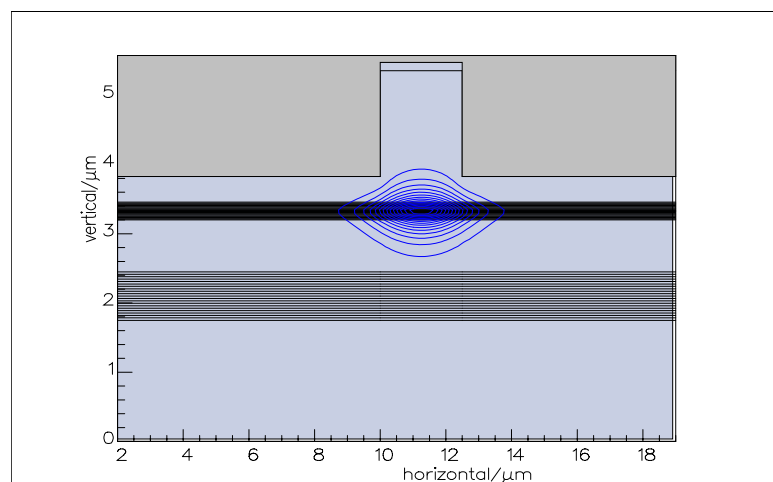
$$W < W_{critical} = \frac{\lambda}{\sqrt{8\Delta n n_{eff}}}, \quad (5.6)$$

where:  $W$  is width of the ridge waveguide;

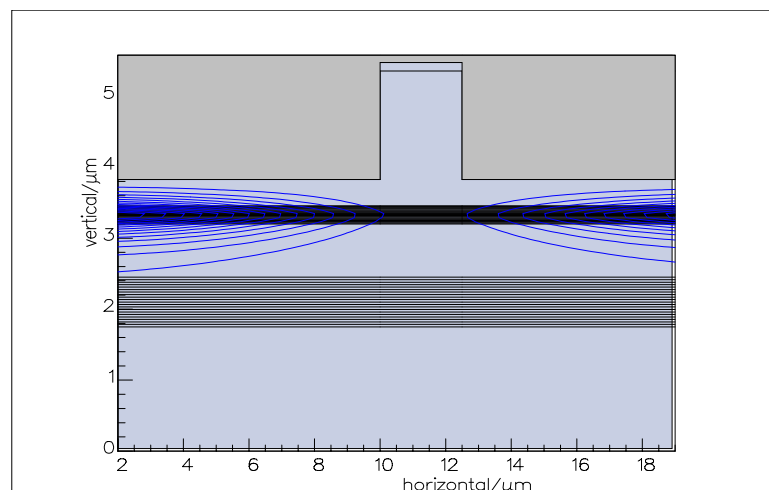
$n_{\text{eff}}$  is the effective index of the ridge waveguide; and  $\Delta n$  is the contrast between the etched and unetched regions. It is obvious from equation 5.6 that there is a critical ridge waveguide width, which ensures single lateral mode operation. Therefore, the ridge waveguide width must be controlled in order to achieve single mode operation.

### 5.5 Modelling of ridge waveguide laser diode.

As explained in the previous section, the ridge waveguide that supports single mode propagation was modelled using both FIMMWAVE and beam propagation method. The simulation of a ridge waveguide with a width of  $2.5 \mu\text{m}$



(a)



(b)

Figure (5.2): (a) Fimmwave simulation showing the fundamental mode contour profile for a ridge depth of  $1.84 \mu\text{m}$  and ridge width of  $(2.5 \mu\text{m})$ . The wavelength used is  $0.83 \mu\text{m}$ . (b) Contour profile for 1<sup>st</sup> order mode for a ridge depth of  $1.84 \mu\text{m}$  and ridge width of  $(2.5 \mu\text{m})$ . This mode is not supported as it is evident.

and an etch depth of 1.84  $\mu\text{m}$  supports a single lateral mode. This is illustrated in figure (5.2), which shows the contour profiles for the fundamental mode and first order mode. The effective index measured using this method is 3.408. The confinement factor for the guide is measured which was 0.01. To ensure that only the fundamental mode is supported, the first order mode profile has been calculated and plotted in figure (5.2b), which indicates clearly that the first order mode is not supported. Increasing the ridge width up to 3.3  $\mu\text{m}$ , while maintaining the etch depth at 1.84  $\mu\text{m}$  results in only the fundamental mode being supported. This gives the flexibility in the ridge waveguide design. A ridge dimension of a 2.5  $\mu\text{m}$  was used in the 1x4 MMI array laser. Since the simulation does not take into account the effects of high current injection and current spreading, the device could operate in multimode due to carrier induced index changes. Since a 3.0  $\mu\text{m}$  ridge waveguide still supports single spatial mode, it was used in the 1x2 MMI array laser.

## **5.6 Theory of multimode interference couplers**

Multimode interference (MMI) devices have been extensively studied and are of considerable interest as key optical components in photonic integrated circuits (PICs). The operation of MMI devices is based on constructive and destructive interferences occurring in the MMI area with a large number of modes. There are many potential applications of the MMI, such as combiners, splitters, mode converters, filters and routers.

The MMI structures have unique properties, such as good fabrication tolerances, low loss, compactness and polarisation insensitivity. These are the reasons why they are employed extensively in PICs.

The MMI is based on self imaging in a uniform index slab waveguide, which was first suggested by Bryngdahl (193) (1973) and explained in more detail by Ulrich (194) (1975). It was not until 1986, that Niemeier (195) developed the concept of the self-imaging further and produced a 4x4 directional coupler with a single mode fibre input. After this, many research groups realised the potential of multimode interference devices and their application in photonic integrated circuits. Soldano (1995) (1996) provided a comprehensive study of multimode interference devices and their applications. The principle of self-imaging is characteristic of multimode waveguides, by which an input field

profile can be produced in single or multiple images at periodic intervals along the propagation direction of the guide. In order to illustrate the concept of MMI self-imaging in a multi-mode waveguide, figure (5.3) shows a step index multimode waveguide with width  $W_m$ . The waveguide supports  $m$  lateral modes, usually  $m \geq 3$ . The representation of the first few modes is shown in Figure (5.3). This figure is a general case for multimode interference couplers. When the MMI laser structure is designed so that the optical mode is launched in the centre of the MMI, only the symmetrical even or odd modes are supported (195, 196). This is the basis of the MMI array laser that has been fabricated, which has the output waveguide positioned at the centre of the MMI. Hence, this ensures symmetric operation and only even or odd modes are

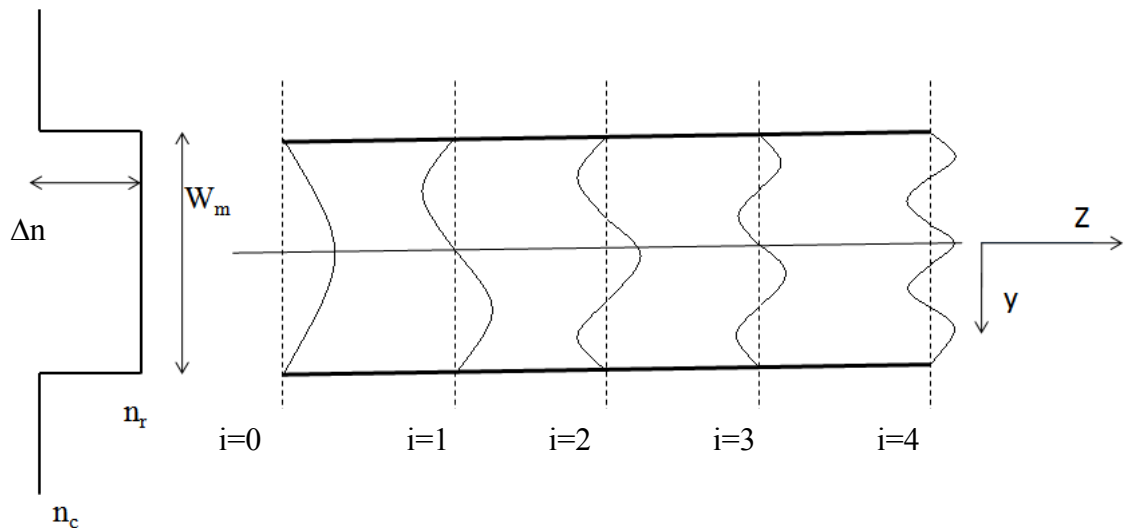


Figure (5.3): Multimode waveguide which shows the cross section with refractive indices for the MMI and the cladding respectively denoted by  $n_r$ , and  $n_c$ . On the right, representation is given of the modes propagating in the waveguide. The number of the waveguide modes is a function of the waveguide dimension and the field launch position. The diagram is an adaptation of figures by Soldano (196).

supported. From slab waveguide theory, either by using the optic ray model or the electromagnetic model, the propagation constant  $B_i$  is related to both the ridge effective index  $n_{eff}$  and wave number through equation (5.7) below:

$$n_{eff}^2 k_0^2 = k_{y_i}^2 + B_i^2 \quad (5.7)$$

where:

$$k_0 = \frac{2\pi}{\lambda_0} \quad (5.8)$$

The wave number  $k_{yi}$  is expressed by:

$$k_{yi} = \frac{(i+1)\pi}{W_{eff}} \quad (5.9)$$

where  $W_{eff}$  is the effective width. This width takes into account the lateral penetration depth of each mode field, which is related to the Goos-Hähnchen shift. This shift is not very critical in high contrast waveguides, which are deeply etched, as is the case in our device concept. Thus, in the case of the deeply etched MMI,  $W_{eff}$  is equal to the actual MMI width ( $W_m$ ), as shown in figure (5.3).

The effective width is larger in low contrast waveguides due to the Goos-Hähnchen shift, which occurs because of the lateral penetration of the each mode field into the regions adjacent to the MMI. The effective width can be measured using equation (5.10). We notice that the effective index is used in this equation.

$$W_{eff} = W_M + \left(\frac{\lambda_0}{\pi}\right) \left(\frac{n_c}{n_{eff}}\right)^{2\sigma} (n_{eff}^2 - n_c^2)^{-\frac{1}{2}}, \quad (5.10)$$

where  $\sigma=0$  for TE and  $\sigma=1$  for TM.

As the squared value of the wave number ( $k_{yi}^2$ ) is very small compared to the value of ( $n_{eff}^2 k_0^2$ ), (see equations (5.7) and (5.9)), the mode propagation constant can be expressed by equation (5.11) below:

$$B_i \cong n_{eff} k_0 - \frac{(i+1)^2 \pi \lambda_0}{4 n_{eff} W_{eff}^2} \quad (5.11)$$

$L_\pi$  in equation (5.12) is the beat length of the two lowest order modes:

$$L_\pi \cong \frac{\pi}{B_0 - B_1} \cong \frac{4 n_{eff} W_{eff}^2}{3 \lambda_0} \quad (5.12)$$

The propagation constant spacing becomes:

$$(B_0 - B_i) \cong \frac{i(i+2)\pi}{3L_\pi} \quad (5.13)$$

Since the aim is to use the MMI coupler as a combiner to couple the mode from N number of gain sections, the MMI we are dealing with is a 1xN structure. The MMI must be symmetric to get efficient coupling into the MMI region.

The device concept for this work is in the form shown in figure (5.4). This particular design is a 1x4 MMI array laser. The value of N studied here varied from two gain sections to four gain sections. Increasing the number of gain sections (emitters) will increase the device complexity. This complexity arises from the fact that the gain sections are index guided array lasers that use optical coupling to form a supermode. The array should lock in phase, but this has been proven to be extremely difficult due to the inherent problems

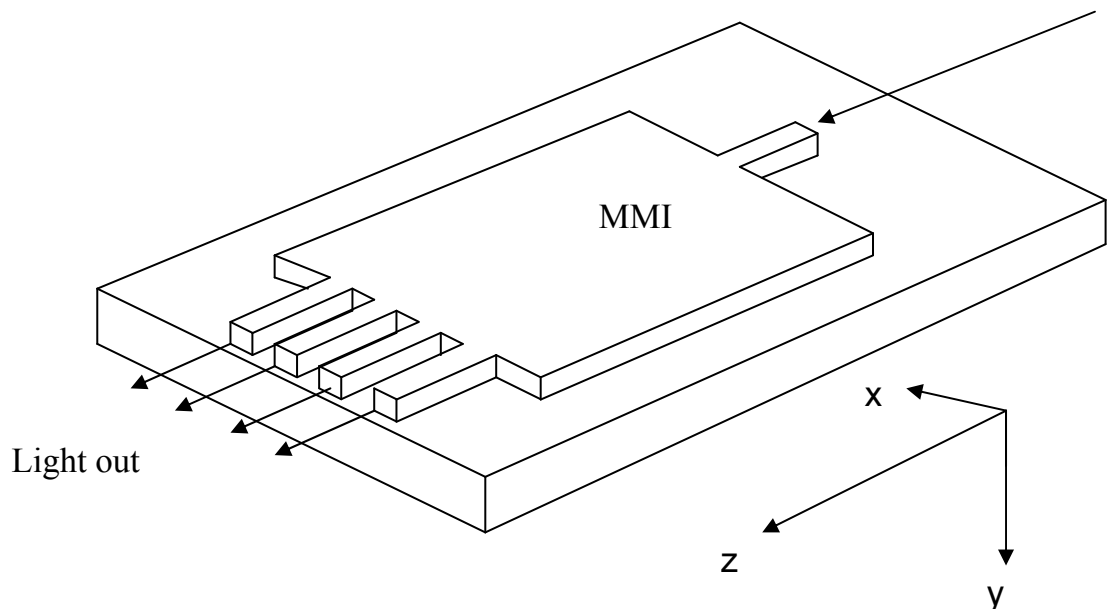


Figure (5.4): 3D-Schematic of the multimode interferometer array laser diode comprising four active gain section and passive MMI with single spatial mode waveguide.

with array laser coupling by the propagating lateral fields. The multimode interferometer structure is used here as a coupling region for the light emitted from the gain sections that should in theory couple all the emitters into one supermode. The reasons for using such structures to couple the light are based on the unique imaging phenomena that MMI passive structures have. They have very low loss, they are compact and the input images are coupled efficiently with good quality to a single image at the output waveguide.

In MMI structures, the total lateral field  $\psi_y(y, z)$  at any position can be expressed by the summation of all the guided mode fields. The total lateral field  $\psi_y(y, z)$  is expressed using equation (5.14) from (196):

$$\Psi(y, z) = \sum_{i=0}^{m-1} c_i \psi_i(y) \exp(j(\omega t - B_i z)) \quad (5.14)$$

The lateral field  $\psi_i(y)$  can be expressed according to excitation of the odd and even modes (198), as follows:

$$\psi_i(y) = \sin \left[ (i+1) \pi \frac{y}{W_{\text{eff}}} \right] \quad \text{for } i = \text{odd.} \quad (5.15)$$

$$\psi_i(y) = \cos \left[ (i+1) \pi \frac{y}{W_{\text{eff}}} \right] \quad \text{for } i = \text{even.} \quad (5.16)$$

$c_i$  in the equation represents the coefficient of each mode. At the entrance of the MMI (where  $z=0$ ), equation (5.14) reduces to:

$$\Psi(y, 0) = \sum_{i=0}^{m-1} c_i \psi_i(y) \quad (5.17)$$

Equation (5.13) represents the decomposition of the input field profile into all possible guided modes.

The coefficients  $c_i$  can be calculated according to (198) using equation (5.18) below. At  $z=0$ , the input field  $\psi(y, 0)$  can be represented as an input field of  $\psi(y)$ :

$$c_i = \frac{2}{W_{\text{eff}}} \int_{-W_{\text{eff}}/2}^{W_{\text{eff}}/2} \psi(y) \cos\left(\frac{(i+1)\pi}{W_{\text{eff}}} \frac{y}{2}\right) dy \quad (5.18)$$

Equation (5.14) can be represented in a more useful form, which can be written as:

$$\Psi(y, z) = \sum_{i=0}^{m-1} c_i \psi_i(y) \exp(j(B_0 - B_i)z) \quad (5.19)$$

By substituting equation (5.13) into (5.19), the image shape at  $z=L$  forms as  $\Psi(y, L)$ , as described by equation (5.20):

$$\Psi(y, L) = \sum_{i=0}^{m-1} c_i \psi_i(y) \exp(j \frac{i(i+2)\pi}{3L\pi} L) \quad (5.20)$$

The image that has been formed  $\Psi(y, L)$  is determined by the excitation coefficients  $c_i$  and the mode phase factor (196) below:

$$\exp(j \frac{i(i+2)\pi}{3L\pi} L) \quad (5.21)$$

There are distinctive types of self imaging;

1) The general interference occurs when there are no conditions placed on the modal excitation at the input. When general interference occurs, the properties of the phase mode factor (equation 5.21) determine the type of the image formed. A self image forms at  $z=L$  if:

$$\exp(j \frac{i(i+2)\pi}{3L\pi} L) = 1 \text{ or } (-1)^i \quad (5.22)$$

From equation (5.22), it is observed that a single image is reproduced such that  $\Psi(y, L)$  is an image of  $\Psi(y, 0)$ . This occurs when (197, 198);

$$L = p(3L\pi) \quad \text{Where } p=0, 1, 2, 3 \dots \dots \dots \quad (5.23)$$

2) Paired Interference occurs for NxN MMI, this configuration of the MMI can still be used for power combining. As the name suggests, NxN MMI means for example 4 inputs and 4 outputs, which entail more complexity in the fabrication. Furthermore, these types of MMI result in substantially longer devices. In a NxN MMI, the length of the central MMI section is 4 times longer (196, 204) than the symmetric interference case of a 1x N MMI. A Good example is the case of the 1x4 MMI integrated array laser, where one of the fabricated devices had MMI length of 617  $\mu\text{m}$  using the 1xN MMI configuration, while using an NxN MMI configuration that could make the MMI length (4x 687  $\mu\text{m}$ = 2468  $\mu\text{m}$ ). This makes the total passive length of the integrated array laser device equivalent to 2793  $\mu\text{m}$  assuming an output waveguide length of 325  $\mu\text{m}$ . In theory, an NxN MMI array laser configuration can be used for coherent coupling.

3) The symmetric interference for 1xN combiners is very important. This interference is realized, where the N fold image occurs at:

$$L = \frac{p}{N} \left( \frac{3L\pi}{4} \right), \text{ where } p=0, 1, 2, 3 \dots \dots \dots (5.24)$$

The N images of the input field  $\Psi(y, 0)$  are symmetrically located along the y-axis with equal spacing of  $W_e/N$ .

For the MMIs that have been used in high brightness lasers, the output waveguide is placed in the middle of the waveguide. Insertion of the waveguide in the centre excites only the even modes (197, 198, 199). An example of this is a simple 1xN (N=2) MMI, where the MMI ports work as the gain sections.

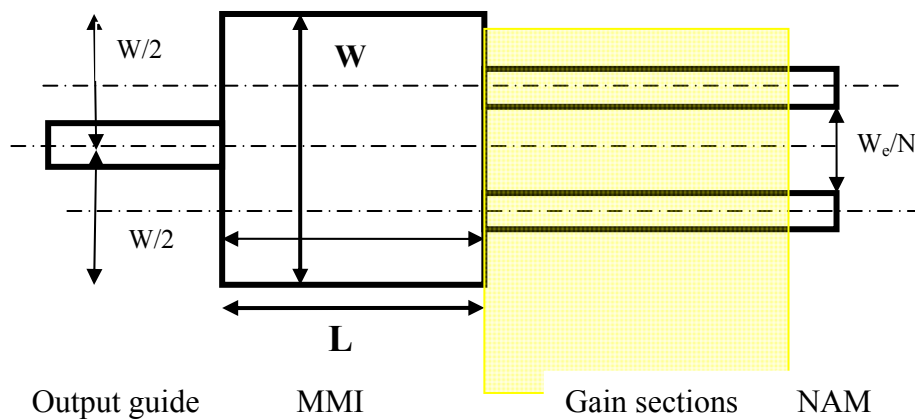


Figure (5.5): Schematic diagram for a 1x2 MMI symmetrical interference splitter/combiner. The device has gain sections, which are the lasers with NAMs (with dimensions of 50-150 $\mu$ m), MMI section and output waveguide.

In the symmetric interference case shown in figure (5.5), where the MMI is centre fed, the even modes are excited. Thus, the equation (5.15) can be written as follows:

$$\Psi(y, z) = \sum_{i=0,2,4}^{m-1} c_i \cos \left[ (i+1)\pi \frac{y}{W_{eff}} \right] \exp \left( j \left( \frac{i(i+2)\pi}{3L\pi} \right) L \right) \quad (5.21)$$

In figure (5.5), where symmetric interference is the dominant, the first single image can be found at:

$$L = \frac{3L\pi}{4N}, \text{ (N=1) corresponds to a single image} \quad (5.22)$$

The self-imaging in the multimode interference coupler is comparable to the Talbot effect. However, there are some differences. The Talbot effect refers to a diffraction phenomenon and consists of a reproduction of the field of an illuminated periodic object at certain distances away from the object plane. These distances are multiples of the Talbot distance  $Z_T = 2d^2/\lambda$ , (87, 111) where  $d$  is the spatial periodicity of the object (emitters) and  $\lambda$  is the wavelength.

The Talbot distance is a minute for a small centre to centre spacing. Specially, that is valid for the monolithic configuration. If we assume a 4 array laser, which has spacing of  $6\mu\text{m}$  (measured from between the centres of two adjacent emitters), then the Talbot distance is  $Z_T = 2d^2/\lambda = (2*6^2/0.83) = 86.75 \mu\text{m}$ .

In the Talbot effect, the image plane is superimposed with the object and induces coherent coupling between the lasers. The mirror is placed at a Talbot distance of ( $Z_T$ ), where the return of the light is maximum. The in-phase mode for all the emitters and the out-of-phase modes compete against each other. In order to select the in-phase mode, where the phase difference between the adjacent emitters is zero, the output mirror with certain reflectivity is placed at a Talbot distance of ( $Z_T/4$ ) with an angle of ( $\alpha = \lambda/2d$ ) (111, 205). In this way, the in-phase mode is selected, whereby the phase locking is achieved. The far-field pattern width at the FWHM for the phase locked operation would be equivalent to the diffraction limited of ( $\lambda/N.d$ ).

Let us return to the 1x2 MMI array laser. For the two images, where ( $N=2$ ) corresponds to two images. Therefore, equation 5.22 becomes:

$$L = \frac{3L\pi}{4N}, \text{ for N=2 this leads to:}$$

$$L = \frac{3L\pi}{8} \quad (5.23)$$

In Figure 5.5, which represents the design for a 1x2 MMI array laser, if we assume that the waveguides are  $3\mu\text{m}$  wide ( $w$ ) (this waveguide width still

supports single mode), the spacing is  $3.5 \mu\text{m}$  and the waveguide distance from the edge of the MMI say  $(w/2)$ . In this case, the minimum design width of the MMI would be  $13 \mu\text{m}$ . This depends on the condition that it supports more than three modes to have useful interference. Simulation for  $1 \times 2$  MMI structures using the BPM method is discussed in section (5.7.3). This is used to verify the number of modes supported by the MMI as well as the correct design length. For proper design, the position of the gain sections should be placed where the maximum imaging quality is obtained with minimum losses. We see in this equation that only the even modes are supported and this leads to a four times shorter MMI structure (196). This feature is particularly useful for a  $1 \times N$  MMI array laser, which favours using shorter MMI with lower losses because the MMI used here is a passive combiner.

### **5.6.1 MMI design rules in high power array lasers**

The design rules for MMIs that are used as combiners for high power lasers will be different from those MMIs that are used for power splitting. The main difference is that optimised coupling must exist in order to couple the light into a single image at the output waveguide. An important aspect of the single image output waveguide where the light is collected is that it has the same dimensions as the input waveguides (gain sections). If the input guide width is different from that of the output guide, it will result in an un-optimised image at the output guide. This means higher losses and a lower power will be achieved. The reason for this is that the image spot size becomes larger than the waveguide width.

The MMIs that are used in combining optical modes are in the form of  $N \times 1$  couplers,  $N$  being the number of gain sections. Number (1) represents the single output waveguide where the power is collected. The maximum number of gain sections selected must avoid the dropping out of the lock mechanism. This occurs at the edge of the array- the first and last gain sections in conventional array lasers. Therefore, the maximum number of gain sections used in this research was fixed at 4 gain sections. Using a number of gain sections less than 4 has also been investigated and devices fabricated.

### 5.6.1.1 4x1 MMI array laser design

The number of gain sections selected was set to a maximum of 4, as indicated in the previous section. The MMI section is designed to be sufficiently wide although this is determined by simulation. Narrow MMIs are avoided because reducing the width of the MMI decreases the number of guided modes, which can increase the losses of the MMIs.

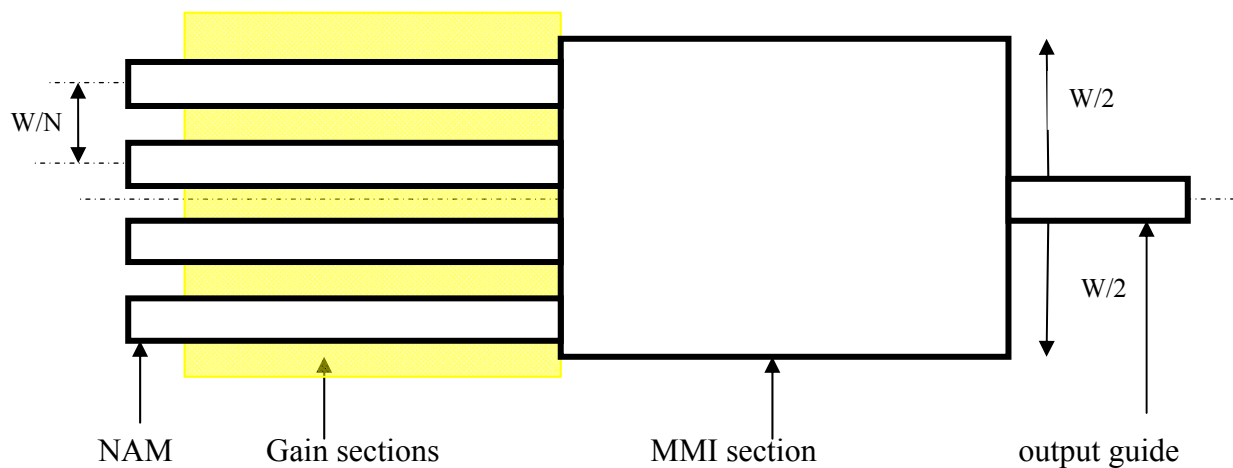


Figure (5.6): schematic of 4x1 MMI array laser device.

The width of the MMI in the case of the 4x1 MMI array laser is also dictated by the width of the individual gain section and the separation between neighbouring gain sections. The separation between the gain sections is an important design factor, which has been optimised from the modelling, as discussed in the next few sections. The separation distance (inter-element spacing) has been modelled and optimised. The results of the simulation can be seen in section (5.7.5). In this design, the spacing is equal to  $W_0/N$  namely  $3.5 \mu\text{m}$ . It was shown by the work in reference (201) that the inter-element spacing between the gain sections is very important for achieving optimum coupling between the gain sections. In the design by (201), the spacing was selected to be  $> 5 \mu\text{m}$ , which proved to be too large for 2x1 MMI array laser devices to work effectively.

In this work, the length of gain section was selected to be at least equivalent to the length of the passive section, which consists of the MMI section and the output waveguide. Longer passive sections will result in increased losses. Therefore, the gain section should be at least equivalent in length to the passive section in order to have sufficient gain to obtain high power at the

output waveguide. A length of 1 mm was selected for the gain section. The width of the gain section is designed to be 2.5  $\mu\text{m}$ , which ensures that single mode gain sections feed the MMI. The width of the gain sections was kept identical for uniform spatial mode and coupling coefficients.

The other important design factor regarding the MMI structure are deep etching of passive MMI, which results in lower losses at the side walls and improved image quality. Therefore, the MMI section was etched through the core. There is one limiting factor for deeply etched MMI's, which is the reflectance at the edge of the deep to shallow interface between the MMI section and single mode output waveguide, which is much shallower than the MMI.

The other parameters that have been selected in the design have been optimised by modelling using BPM and are discussed in the next sections.

## 5.7 Multimode interference coupler modelling

The self-imaging principle causes the input field to reproduce as either single or multiple images at regular intervals along the length of the MMI device.

As seen in previous sections of this chapter, symmetrical multimode interference devices, single and multiple images of the input field occur at distances given by integer and odd-half integer values of  $3L_\pi$ . 3 fold images of the input field also occur at  $L_\pi/4$ , where  $L_\pi$  is the beat length of the two lowest order modes in the MMI device. Recalling equation (5.6) which is:

$$L_\pi = \frac{\pi}{\beta_0 - \beta_1} = \frac{4nW_e^2}{3\lambda_0} \quad ,$$

where  $W_e$  is the effective width of the MMI (as in figure (5.8)),  $n$  is the effective index of the MMI and  $\lambda_0$  is the free space wavelength.

From the equation above, we infer that the imaging length is a strong function of  $W_e$  (the effective MMI width) and the effective refractive index. The imaging length varies if the core waveguide index is changed. To explain this, a simple scan of the MMI core waveguide has been carried out. There is an imaging length variation of around 100  $\mu\text{m}$  for a change of the core refractive index from 3.5 to 3.9. Therefore, selecting the optimum core refractive index ensures an accurate design. The value of the refractive index ( $n_c$ ) has been calculated to be 3.6713 in Chapter 3.

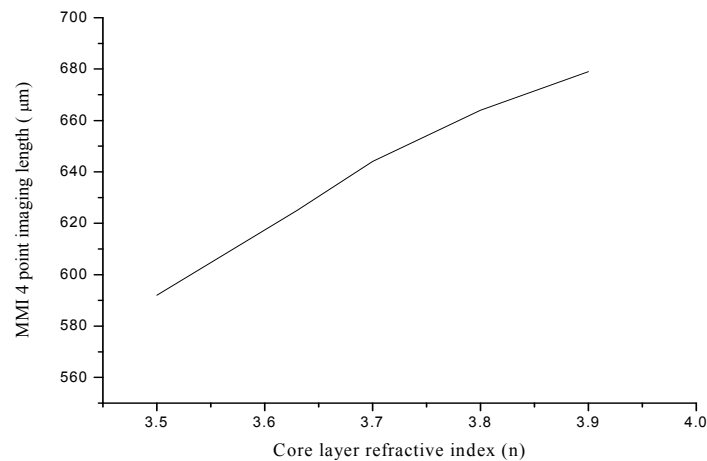


Figure (5.7): 1x4 MMI simulated imaging length with respect to core layer refractive index for GaAs/AlGaAs material.

In selecting an optimum value of the refractive index, the imaging length variation can be affected by the fabrication tolerances. Thus, any deviation during fabrication of the MMI width from the design value would affect the imaging length and results in a lower image quality at the output waveguide. Consequently, the poorer image quality will result in higher losses inside the MMI cavity. Similarly, the collective change in the effective index difference ( $\Delta n$ ) during device operation due to injected carrier, free carriers and temperature variations will also have a considerable effect on the imaging length of the MMI.

Figure (5.8) represents a 1x4 MMI. For the purpose of the simulation, we used a 1x4 MMI. A fundamental mode is launched at path (1). The spacing is between two adjacent waveguides is  $3.5 \mu\text{m}$ .

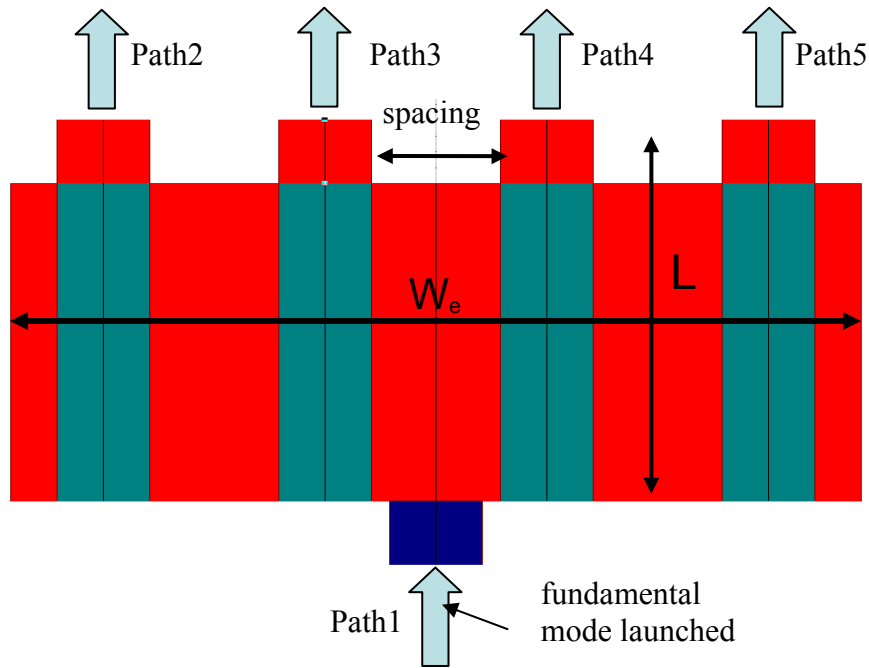


Figure (5.8): 1x4 MMI computed fundamental mode is launched at path1, so the input signal will go through the MMI guide, multiple images are formed. Naming the path in the software makes it easier to monitor each path during simulation.

As the mode is launched in the centre of the waveguide, the symmetrical interference mechanism is the dominant one. In this case, only the even modes are excited in the guide. Table (5.1) below summarises the symmetric characteristics for the MMI. It can be seen that for symmetric interference in the 1xN MMI, the first image can be calculated to be at  $(3L_\pi/4)$ . In addition, the N fold image will be located at  $(3L_\pi/4N)$ . A summary of the characteristics of the symmetrical 1xN MMI are given in the table below:

Interference mechanism	Symmetric
Inputs $\emptyset$ outputs	1 $\emptyset$ N
First single image distance	$(3L_\pi)/4$
First N fold image distance	$(3L_\pi)/4N$

Table (5.1): symmetric 1xN multimode interference coupler characteristics.

In the following sections, the mode solver package (BPM) is used to simulate the 4x1 MMI, 3x1 MMI and 2x1 MMI configurations. Selecting the MMI width is very important because the number of guided modes must be  $>3$  for

good imaging. Therefore, a simple simulation using BPM provides an indication of the number of guided modes inside the MMI. Fifteen guided modes are identified by BPM for an MMI width of  $24\ \mu\text{m}$ , which is ideal for the proper functioning of the MMI, as illustrated in figure (5.9).

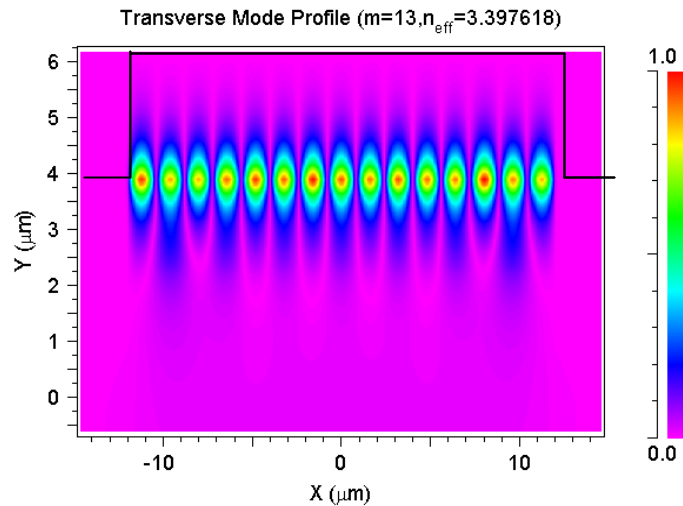


Figure (5.9): Highest order mode for  $24\ \mu\text{m}$  wide multimode interference (MMI) section.

At the start of the simulation, the fundamental mode of a  $2.5\ \mu\text{m}$  wide input guide is computed by the BPM, as shown in figure (5.10) below. The computed mode was launched at the centre of the MMI in Figure (5.8).

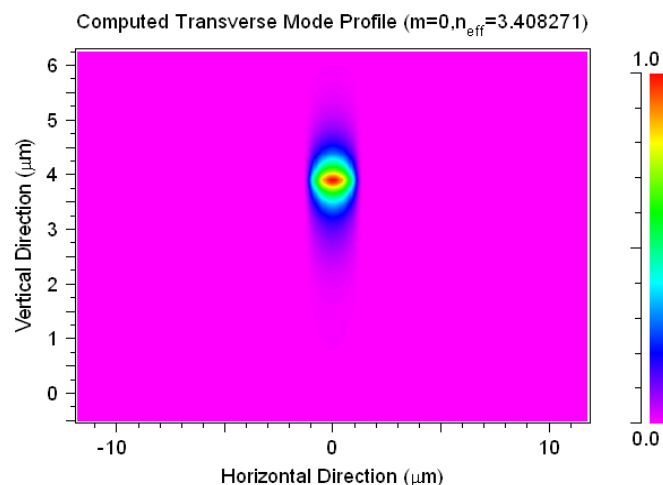


Figure (5.10): Computed fundamental mode profile obtained using BPM for  $2.5\ \mu\text{m}$  waveguide.

For this example, the MMI consists of an input access waveguide of  $2.5\ \mu\text{m}$ , centred symmetrically in an MMI waveguide of width  $24\ \mu\text{m}$  and length of  $700\ \mu\text{m}$ . This length is selected to be greater than the predicted MMI length to

show the extended mode interference. This is used to accurately obtain the MMI length where the images are formed.

Figure (5.11) shows the results of the simulation. Four images can be seen as marked, in the left side of the figure. The corresponding monitored paths are shown on the right. The four equivalent images of the input field are located at  $625\mu\text{m}$ .

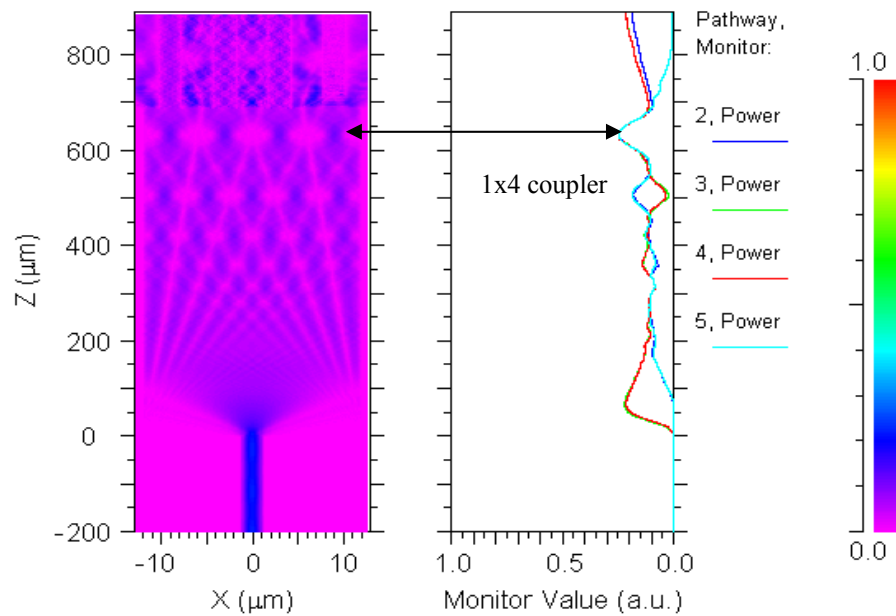


Figure (5.11): Simulation for a 1x4 MMI for  $700\mu\text{m}$  length using BPM mode solver.

The length of the MMI is then adjusted to  $625\mu\text{m}$  and the simulation is repeated. The result of this simulation can be seen in figure (5.12), which shows the MMI mode interference and the images with equal intensities. This can be seen clearer in figure (5.13), which shows that the intensity of the images is equal to 0.25 each. This makes the total optical power or light propagation inside the MMI equivalent to the input power, which is unity. This has been verified in Figure (5.14), which shows the equal intensities at the four gain sections. In order to calculate the equal intensities accurately, a cross sectional view for the simulation of a 1x4 MMI array laser can be seen in Figure (5.15), which shows the equal mode profile for the four gain sections.

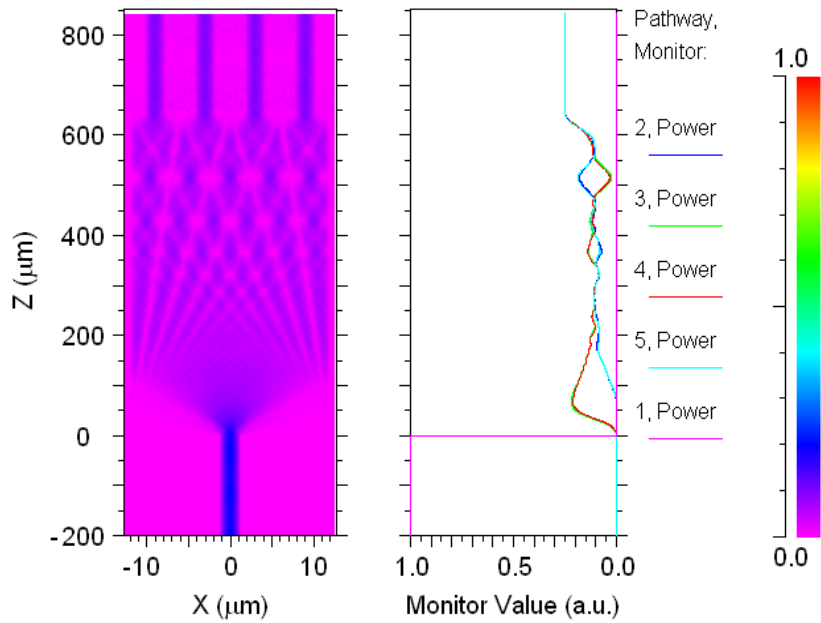


Figure (5.12): Simulation for a 1x4 MMI coupler, it can be seen that at distance 625 $\mu\text{m}$  the power is equal for the four waveguides. The waveguide width is 2.5 $\mu\text{m}$  and the MMI width is 24 $\mu\text{m}$ .

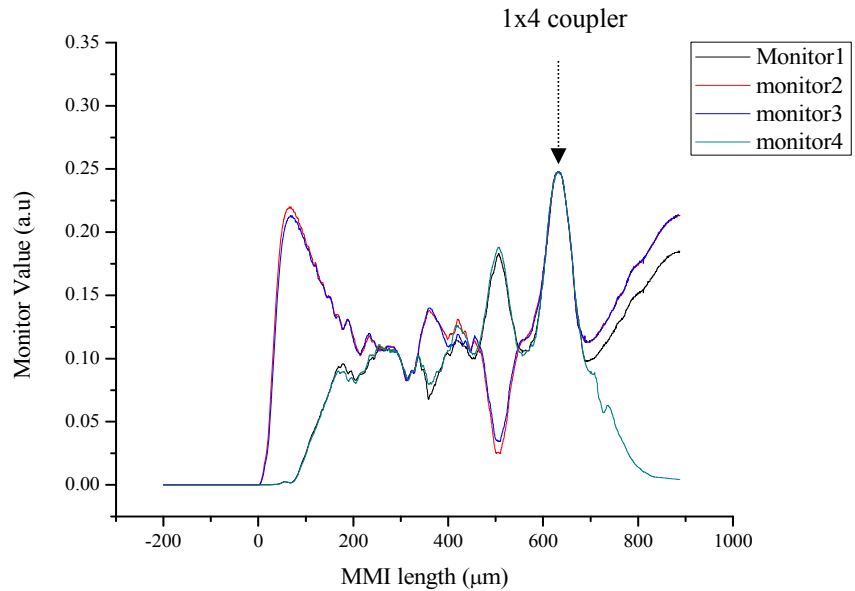


Figure (5.13): Monitored optical power value for a 1x4 MMI GaAs/AGaAs array laser diode. The four image location is marked, as in the graph. Inspection of the graph shows that the monitored value is 0.25.

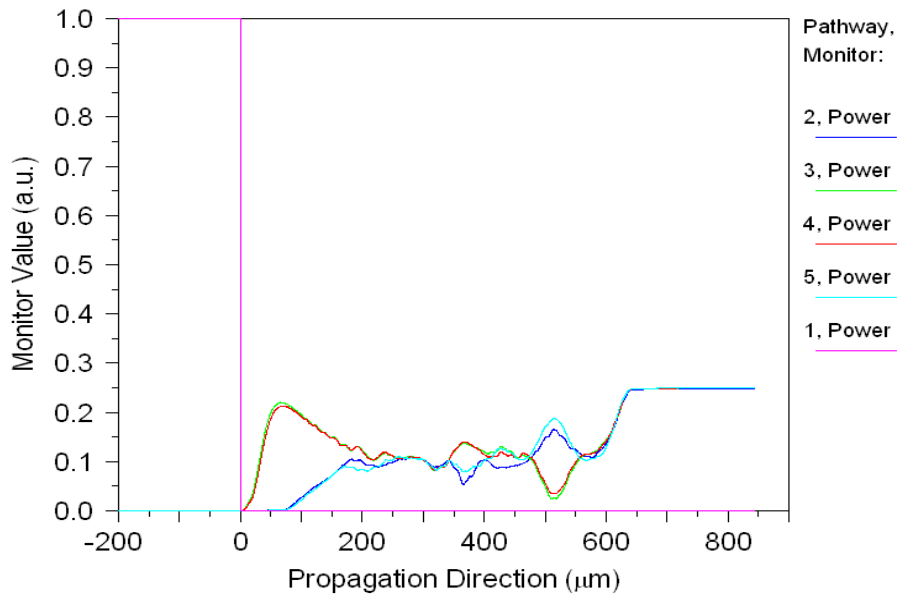


Figure (5.14): Simulation of a 4x1 MMI array laser diode using Rsoft BPM software. Equal power is verified as MMI length of 625  $\mu\text{m}$ .

This mode profile was attained by scanning with BPM. Thus, the optimum image was at the 617  $\mu\text{m}$  plane. It is worth indicating that the image quality is affected by the length of the MMI as well as any fabrication errors, whereby the width variation effect is the largest. The MMI length is usually optimised experimentally by fabricating several different MMI lengths. The MMI length is the MMI with the best image quality at the output waveguide (i.e. the device

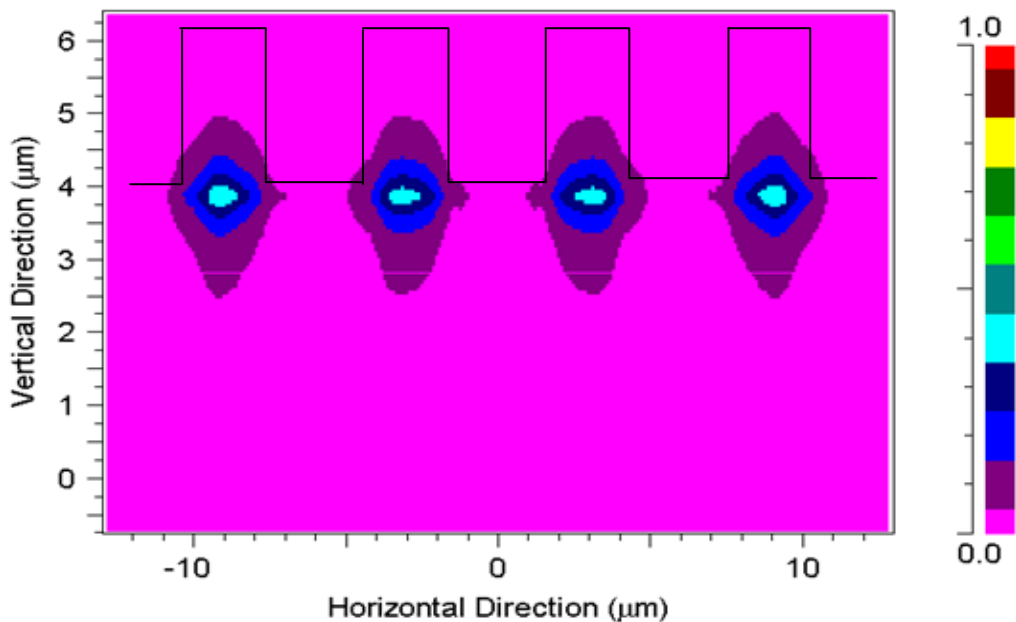


Figure (5.15): Cross sectional view of the simulated 4x1 MMI array laser illustrating the optical mode profile in each gain section at MMI length ( $L=617 \mu\text{m}$ ).

with highest output power). This means the experimentally attained optimum image must have the least loss, so the coupling to the output waveguide is maximised.

So, we have an optimised a 1x4 MMI with a length of 617 $\mu\text{m}$ , 24 $\mu\text{m}$  width and a spacing of 3.5 $\mu\text{m}$  between two adjacent waveguides. The same BPM method is used to simulate 1x3 and 1x2 multimode interference couplers, where the correct imaging length has also been calculated.

### 5.7.1 Optical field phase simulation for Nx1 MMI array laser

The light generated from current injection into the gain sections propagates and couples inside the MMI and then into the output waveguide. At the interface between the gain sections and the MMI, the phase relationship of the gain section must be known for effective coupling of light inside the MMI. Thus, if the light in each of the arms is in an anti-phase relationship with its neighbouring arms, then no light will propagate. However, if the arms are in phase, constructive interference occurs inside the MMI cavity and a higher power is achieved. Therefore, careful analysis of the phase relations should be carried out. In this section, BPM is used to calculate the relative phase relations between each of the gain sections.

For example, for the symmetrical 4x1 MMI array laser shown in Figure (5.16), assume that the phases at the edge of the four gain sections are denoted by  $\Phi_1$ ,  $\Phi_2$ ,  $\Phi_3$  and  $\Phi_4$ , respectively. The ideal phase relationship for the 1x4 MMI should be:

$$\Phi_1 = \Phi_2 = \Phi_3 = \Phi_4$$

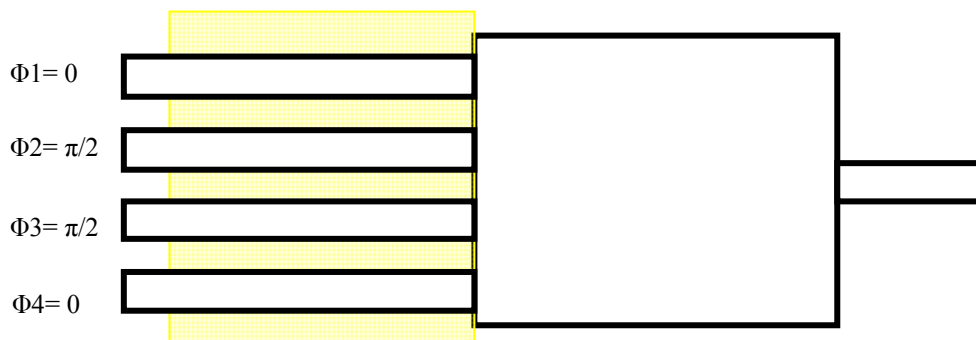


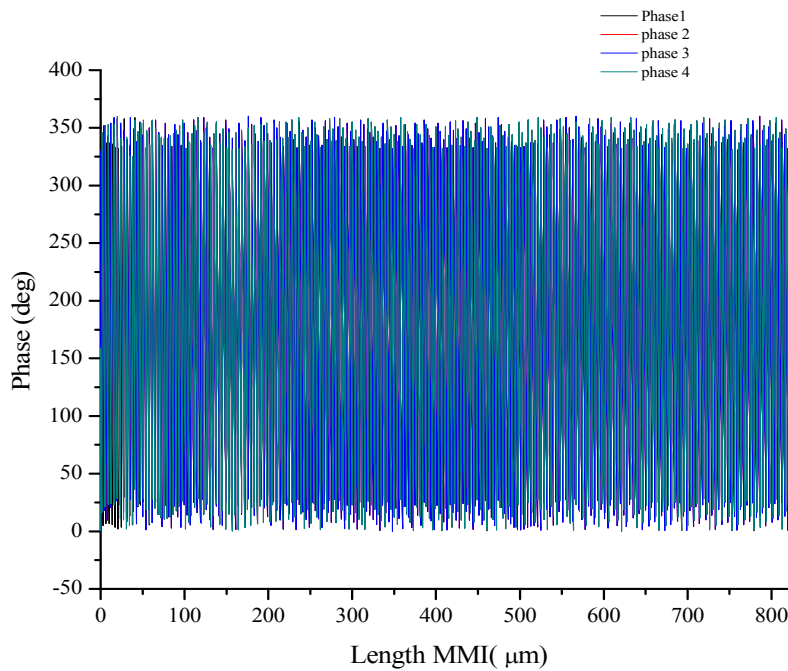
Figure (5.16): Phase relationship for symmetrical 1x4 MMI array laser. The spacing between the emitters is the same. The emitters have the same length. BPM calculations show that arms one and four have the same phase and arms two and three have the same phase. The relative phase difference between these two groups is  $\pi/2$ .

In reality, a phase difference exists between each of the individual gain sections. Therefore, BPM now is used to estimate the relative phase change between the adjacent gain sections.

Figure (5.17) below shows the phase modelling using BPM for the 1x4 MMI. The model does look as if it is unexplainable. However, by using the zoom tool we can easily deduce the relative phase difference between each of the four MMI sections.

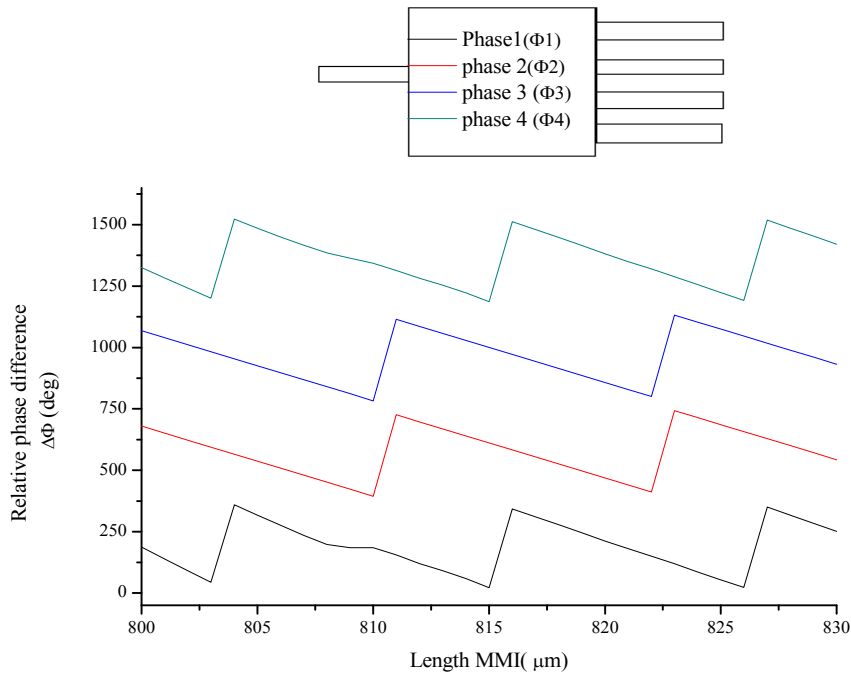
$$\Phi_2 = \Phi_3, \Phi_1 = \Phi_4$$

$$\Delta \Phi = (\Phi_2 = \Phi_3) - (\Phi_1 = \Phi_4) = \pi/2$$

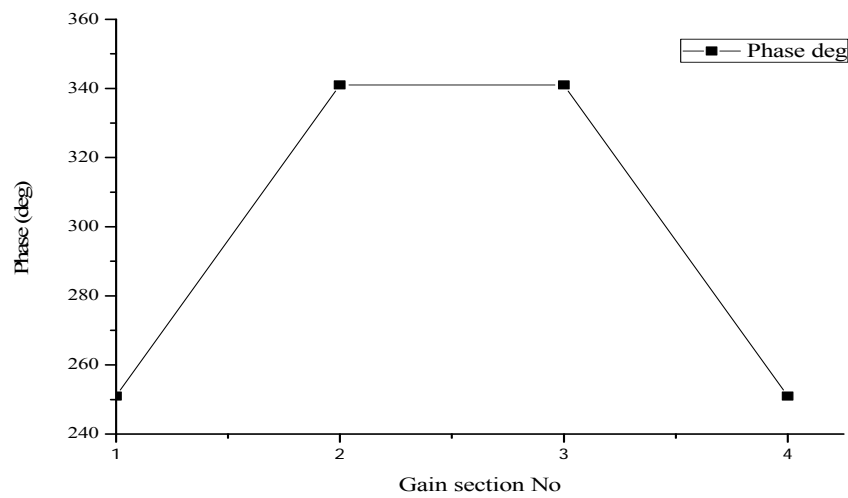


Graph (5.17): BPM phase Modelling for the optical field for 1x4 MMI laser

The relative phase difference between the inner gain sections and the outer gain sections is  $\pi/2$ . This can be seen in figures (5.18) and in more detailed manner in figure (5.19). The phase relations for the 1xN MMI have been studied by (203), which confirmed the results obtained in this modelling. The relative phase relations in the MMI are inherent to this type of device. However, the phases relationship can be changed by changing the relative optical path lengths by changing the position of the waveguides.



Graph (5.18) Magnified version of graph (5.17), which shows the relative phase difference between two adjacent gain sections.



Graph (5.19): Phase simulation for a 1x4 MMI array laser versus the gain section number. There is a relative phase difference equal to  $(\pi/2)$  between gain sections (1) and (2) and (3) and (4). Gain section (1) and gain section (4) have equal phases and similarly (2) and (3) have equal phases.

The process is repeated for the 1x3 MMI and 1x2 MMI array lasers. A schematic of the 1x3 MMI array laser is shown in figure (5.20), which shows the relative phase relations for the gain sections (emitters). The actual simulation results are illustrated in figure (5.21). The outer gain sections have

equal phases, but the middle gain section has a relative phase shift of  $(\pi/3)$  with the respect to the outer gain sections. In the case of the 1x2 MMI array laser, there is no phase shift provided the output waveguide is placed in the centre and the MMI is symmetrical.

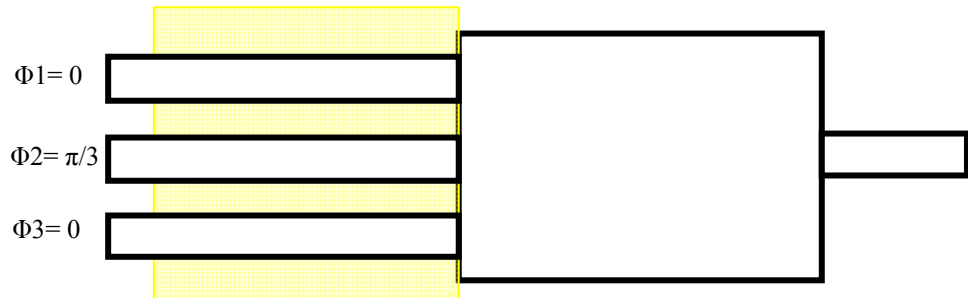
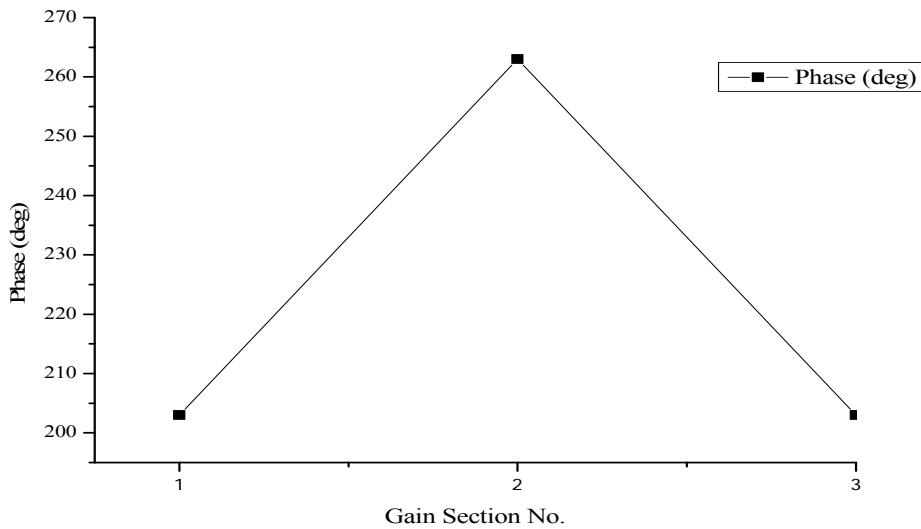


Figure (5.20): Schematic diagram of a 1x3 MMI array laser. The phase relations are shown for a symmetrical 1x3 MMI. The phases of the two outer arms are equal, but the middle arm has a relative phase shift of  $\pi/3$ .



Graph (5.21): Phase simulation for a 1x3 MMI array laser versus the gain section number. There is a relative phase difference equal to  $(\pi/3)$  between gain section (2) and each of gain sections (1) and (3). Gain section (1) and gain section (3) have equal phases.

### 5.7.2 Simulation of 3x1 MMI array laser.

A similar method was used for design and simulation of 1x3 and 1x2 MMI array laser diodes. In this simulation, a single mode was launched in the centre of the MMI as shown in figure (5.22) below. The single mode waveguide width used was 3  $\mu\text{m}$ . A single spatial mode for 3  $\mu\text{m}$  waveguide is shown in figure (5.22). The complete simulation for a 1x3 MMI array laser can be seen in figure (5.23), which shows a 1x3 MMI coupler length of 566  $\mu\text{m}$ .

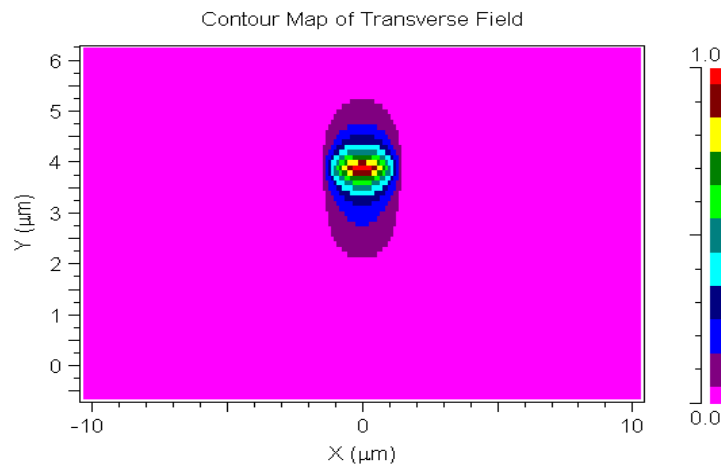


Figure: (5.22): BPM simulation showing the fundamental mode for a 3  $\mu\text{m}$  waveguide, which is launched at the centre of a 1x3 MMI array laser.

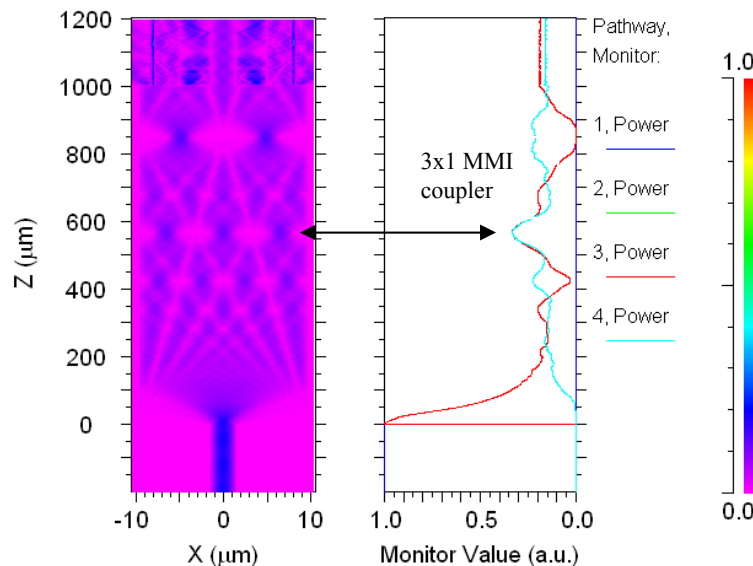


Figure (5.23): 1x3 MMI simulation using the BPM method. By Inspection of the figure above, 3 images are seen at a Z distance of 566 $\mu\text{m}$ . The corresponding monitor values are 0.333. This means an equal power splitting ratio. The MMI width in this simulation was 19.5  $\mu\text{m}$ . The waveguide spacing is 3.5  $\mu\text{m}$ .

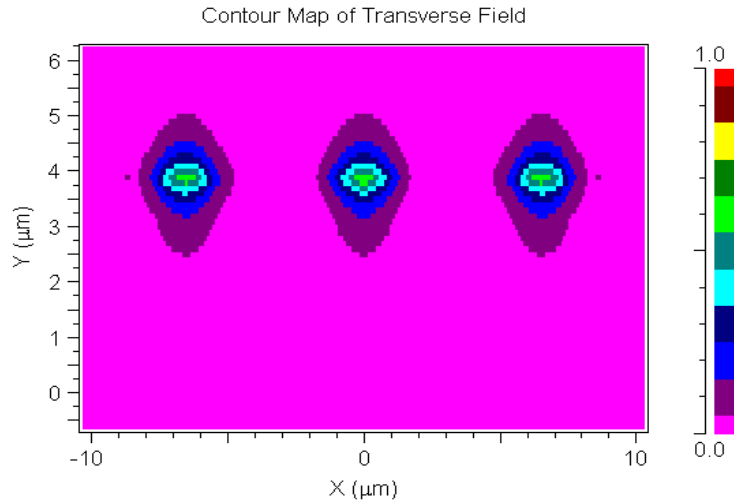


Figure (5.24): Cross sectional view of the simulated 3x1 MMI array laser illustrating the optical mode profile in each gain section at an MMI length ( $L=566 \mu\text{m}$ ).

The cross section of the 1x3 MMI coupler in figure (5.24) shows equivalent spot profiles for the images at  $Z=566 \mu\text{m}$ .

### 5.7.3 Simulation of 2x1 MMI array laser.

In this section, the simulation of a 1x2 MMI array laser is summarised. The spacing for the 1x2 array laser is selected to be  $3.5 \mu\text{m}$ . The simulation for a 1x2 MMI array laser diode can be seen in Figure (5.25), which is carried out for

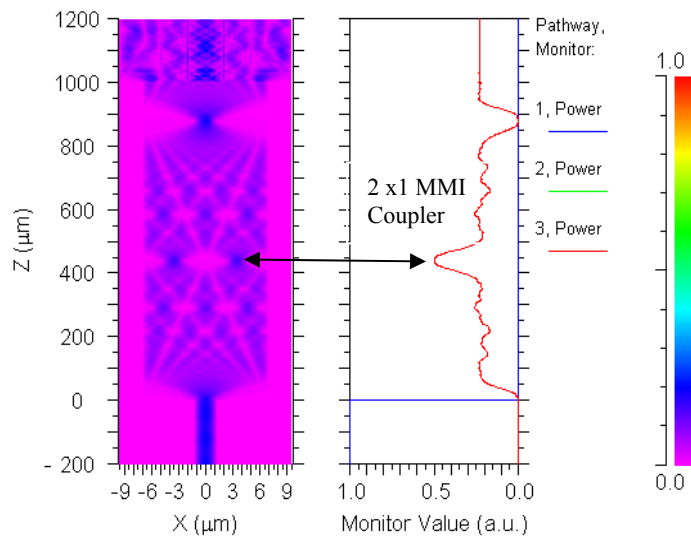


Figure (5.25): 1x2 MMI simulation using BPM method. By Inspection of the figure above, 2 images are seen at a Z distance of  $465 \mu\text{m}$ . The corresponding monitor values are 0.5. This means an equal power splitting ratio. The MMI width in this simulation was  $15 \mu\text{m}$ . The waveguide spacing was  $3.5 \mu\text{m}$ .

1000  $\mu\text{m}$ . Different couplers are observed. For example, a 1x2 MMI coupler is located at length of 465  $\mu\text{m}$ , while the 1x3 MMI coupler is located at 590  $\mu\text{m}$ . The single image (1x1 coupler) is located at 879  $\mu\text{m}$ . The MMI length is then adjusted and the simulation is repeated. The cross section of the equivalent spot profiles is observed in Figure (5.26) below.

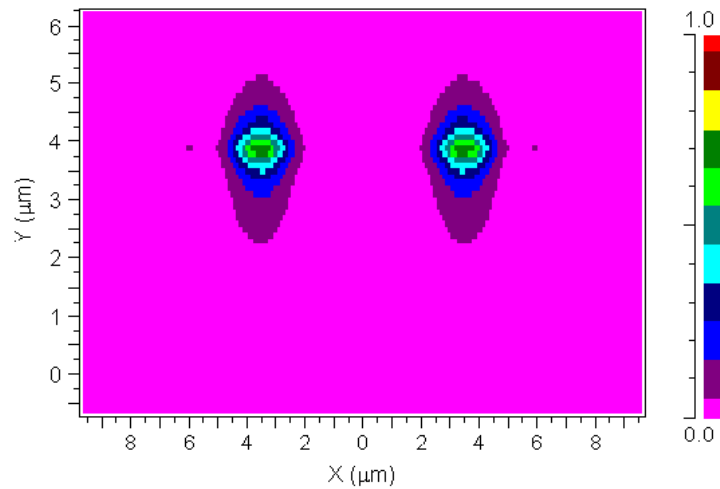


Figure (5.26): Cross sectional view of the simulated 2x1 MMI array laser illustrating the optical mode profile in each gain section at MMI length ( $L=465 \mu\text{m}$ ).

#### 5.7.4 Modelling of 1xN tapered MMI array laser

In Figure (5.27), a schematic of a 1x 4 tapered MMI array laser is shown. For the design of the tapered section of the 1xN MMI array device, several criteria were taken into consideration:

1. The taper angle ( $\theta$ ) is selected to be larger than the divergence angle of the light. Since the entering light will not interact immediately with the side walls of the MMI coupler, self-imaging properties are not affected. The length of the tilted section (taper) is then calculated, based on the angle ( $\theta$ ).

Tapered ends of the MMI were made, whereby the angle of the taper is larger than the angle of the light emission of the individual waveguide in the MMI. MMI Tapers with different angles were simulated. The angles of the taper were varied in a range of (5-40  $^\circ$ ). Angles below (5 $^\circ$ ) resulted in a very long taper length, which led to non-functioning MMI. The values of the simulated angles of the tapered MMI and the corresponding taper lengths are illustrated in table (5.2) for an MMI width of 22  $\mu\text{m}$ . The tapers at the waveguides-MMI interface were very small, because the waveguide (emitter) was 2.5  $\mu\text{m}$  wide.

Taper angle	Main Taper length ( $\mu\text{m}$ )
5	120
10	59.5
15	39.2
20	28.8
25	22.5
30	18.2
40	15.0

Table (5.2) Taper angles and the corresponding length of the tapers for the 1x4 tapered MMI array laser

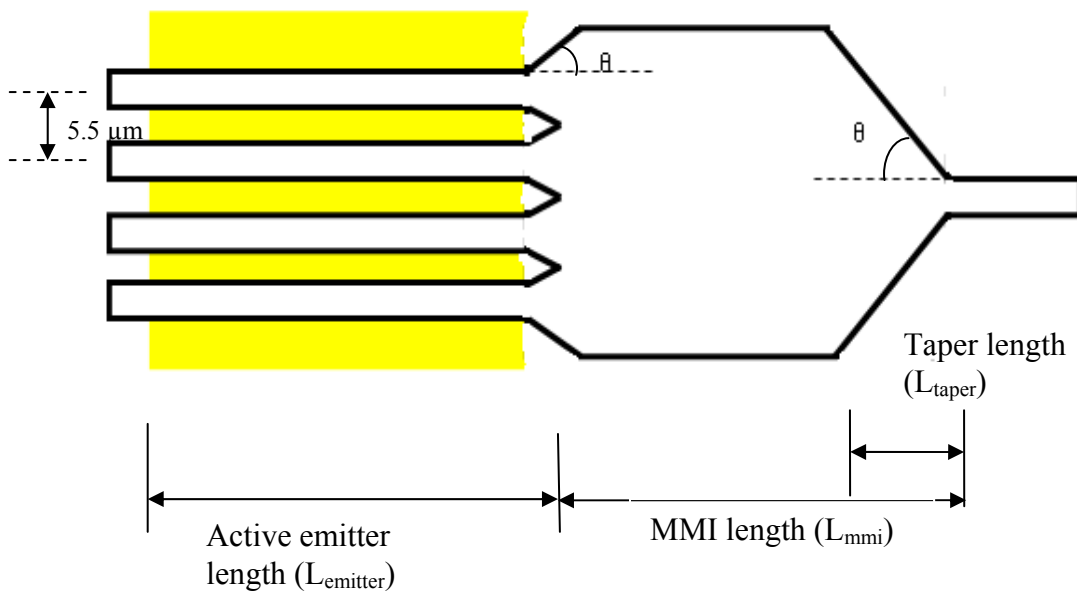


Figure (5.27): A schematic of 1x4 tapered MMI array laser. 1x4 tapered MMI array laser with parameters as follows: taper length ( $L_{\text{taper}}$ ) was  $28.8 \mu\text{m}$  for  $\theta = 20^\circ$ , MMI spacing was  $3 \mu\text{m}$  (centre to centre  $=5.5 \mu\text{m}$ ), the optimum MMI length was  $520 \mu\text{m}$ , the waveguide width was  $2.5 \mu\text{m}$  and the MMI was  $22 \mu\text{m}$  wide.

The results of the simulation of the optimum dimensions were as follows: the total MMI length was  $520 \mu\text{m}$ , spacing was  $3 \mu\text{m}$  (equivalent to a centre to centre pitch of  $5.5 \mu\text{m}$ ), and the taper length ( $L_{\text{taper}}$ ) was  $28.8 \mu\text{m}$  for an angle  $\theta$  of  $20^\circ$ . During fabrication, different MMI lengths were selected around the optimum dimensions. The simulations for this tapered device are illustrated in the figures (5.28) and (5.29). A simulation example for a taper angle of  $3^\circ$  is shown in Figures (5.30) and (5.31). At a taper angle of  $3^\circ$ , the self imaging effect of the tapered MMI is not sustainable because of the large taper length of  $200 \mu\text{m}$ . The same procedure above was repeated for 1x2 tapered MMI array laser.

2. The MMI taper must be considered as part of the design length of the MMI.

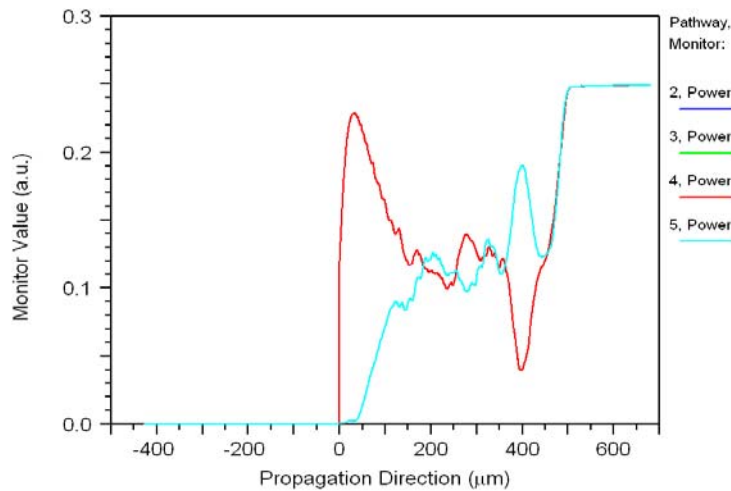


Figure (5.28): Simulation of 1x4 tapered MMI array laser with parameters as follows: taper length ( $L_{\text{taper}}$ ) was  $28.8 \mu\text{m}$  for angle  $\theta$  of  $20^\circ$ , MMI spacing of  $3 \mu\text{m}$  (equivalent to a centre to centre pitch of  $5.5 \mu\text{m}$ ), the optimum MMI was  $520 \mu\text{m}$  in length, the waveguide width was  $2.5 \mu\text{m}$  and the MMI was  $22 \mu\text{m}$  wide. This figure shows the monitored power in each guide.

Otherwise, the taper could affect the accurate design length. This was confirmed during the simulation.

3. In figure (5.29), a phase locked horizontal far-field pattern was simulated. It is evident that central lobe width at FWHM is compatible with theory for a diffraction limited beam of  $2.16^\circ$  (i.e.  $\lambda/N.p$ ). Furthermore, the side lobe separation is equivalent to  $8.6^\circ$  (i.e.  $\lambda/p$ ). The simulation of a 1x4 tapered MMI array laser with a taper divergence angle of  $3^\circ$  is shown in figures (5.30) and

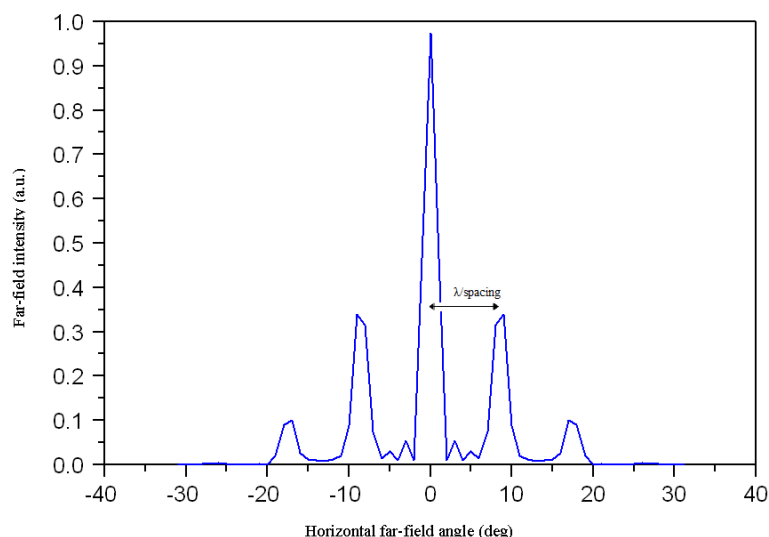


Figure (5.29) Simulation of the far-field pattern for the 1x4 tapered MMI array laser parameters were as follows: the taper length ( $L_{\text{taper}}$ ) was  $28.8 \mu\text{m}$  for an angle  $\theta$  of  $20^\circ$ , the MMI spacing was  $3 \mu\text{m}$  (equivalent to a centre to centre pitch of  $5.5 \mu\text{m}$ ), optimum MMI length was  $520 \mu\text{m}$ , the waveguide width was  $2.5 \mu\text{m}$  and the MMI width was  $22 \mu\text{m}$ . The angular separation between individual peaks is ( $\lambda$  spacing), which is  $8.6^\circ$ , the central lobe width at FWHM equals ( $\lambda$   $N$ \*spacing), which is  $2.16^\circ$ . These values are for a laser that is phase locked.

(5.31). A taper divergence angle of  $3^\circ$  results in a very long taper length of around  $200\ \mu\text{m}$ . At this angle, the  $1 \times 4$  tapered MMI does not function due to the non-optimised taper length, whereby self-imaging is no longer sustainable at this angle. The phase locked far-field pattern is simulated, which it does not coincide with the regular diffraction pattern that is anticipated from a  $1 \times 4$  tapered

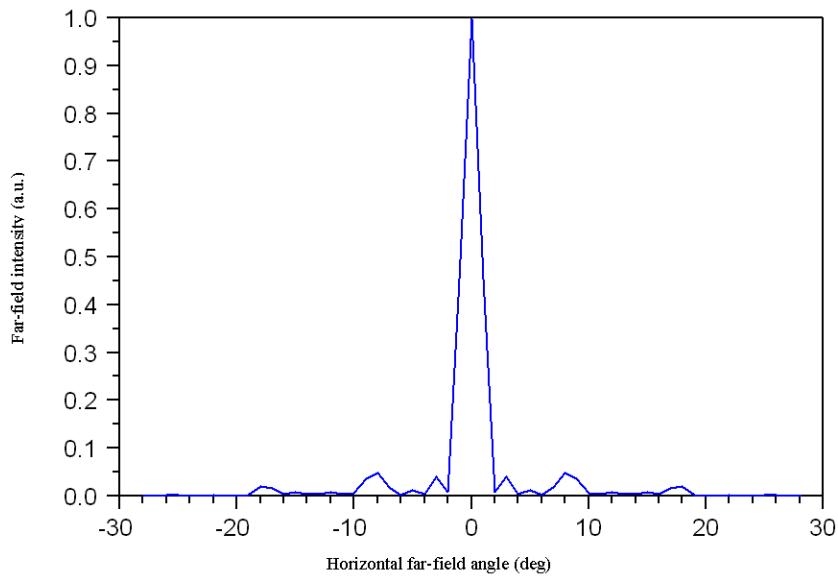


Figure (5.30): Simulation of a far-field pattern of the  $1 \times 4$  tapered MMI array laser with following parameters: the taper length ( $L_{\text{taper}}$ ) was  $200\ \mu\text{m}$  for an angle  $\theta$  of  $3^\circ$ , the MMI spacing was a  $3\ \mu\text{m}$  (equivalent to a centre to centre pitch of  $5.5\ \mu\text{m}$ ), the optimum MMI length was a  $520\ \mu\text{m}$ , the waveguide width was  $2.5\ \mu\text{m}$  and the MMI was  $22\ \mu\text{m}$  wide. The individual peaks in this simulation disappear due to non optimised taper.

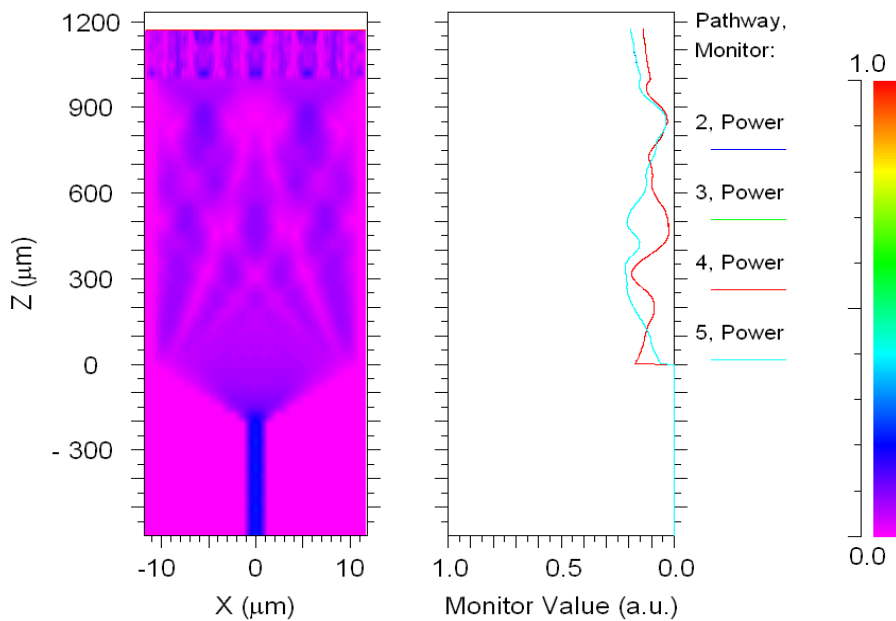


Figure (5.31): Simulation of  $1 \times 4$  tapered MMI array laser with parameters as follows: taper length ( $L_{\text{taper}}$ ) =  $200\ \mu\text{m}$  for  $\theta = 3^\circ$ , MMI spacing of  $3\ \mu\text{m}$  (centre to centre =  $5.5\ \mu\text{m}$ ), MMI length of  $1000\ \mu\text{m}$ , waveguide with  $2.5\ \mu\text{m}$ , MMI width =  $22\ \mu\text{m}$ . This figure shows the monitored power in each waveguide.

MMI array. In figure (5.31), it is noticed that even if the tapered MMI was increased to 1000  $\mu\text{m}$  in length, still the 1x4 coupler could not be formed.

4. The design length of the 1x4 tapered MMI was optimized. Optimization of the MMI length results in decreasing the number of design lengths that are selected for fabrication. The length scan was performed using the BPM for the following parameters: the taper length ( $L_{\text{taper}}$ ) was 28.8  $\mu\text{m}$  for an angle  $\theta$  of 20  $^\circ$ , the MMI spacing was 3  $\mu\text{m}$  (equivalent to a centre to centre pitch of 5.5  $\mu\text{m}$ ), the waveguide was 2.5  $\mu\text{m}$  wide and the MMI width was 22  $\mu\text{m}$ . The optimization was also performed for a standard 1x4 MMI laser array that includes an MMI with spacing of 3.5  $\mu\text{m}$  (equivalent to a centre to centre pitch of 6  $\mu\text{m}$ ), a waveguide width of 2.5  $\mu\text{m}$  and an MMI width of 24  $\mu\text{m}$ . The results of the design length optimization are illustrated in Figure (5.32). In this figure, the upper and lower limits for the MMI design length are shown.

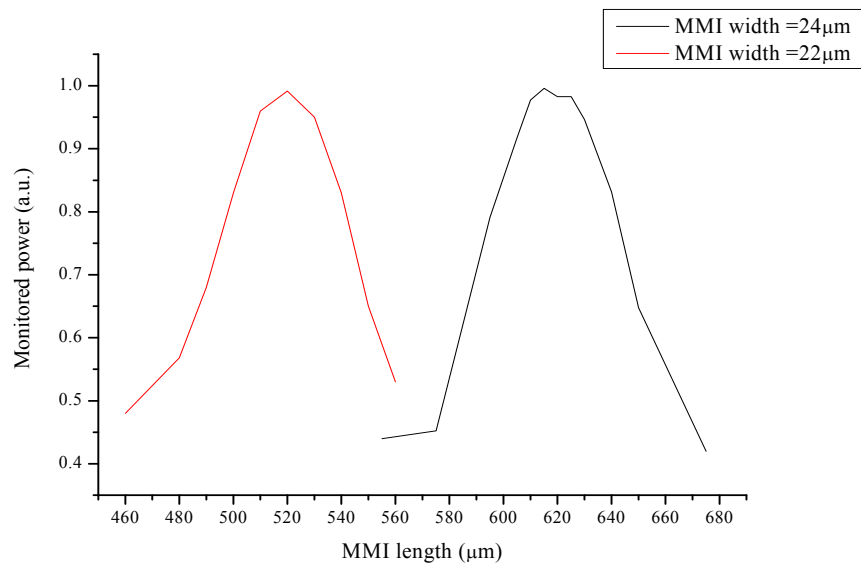


Figure (5.32): Simulation of the monitored power for different 1x4 MMI lengths. The parameters for the 1x4 tapered MM are: Tapered MMI length was varied within a range of 460  $\mu\text{m}$  to 560  $\mu\text{m}$  (red curve), The MMI width was 22  $\mu\text{m}$ , the spacing was a 3  $\mu\text{m}$  (equivalent to a centre to centre pitch of 5.5  $\mu\text{m}$ ) and the length of the taper was 28.8  $\mu\text{m}$  for an angle of 20  $^\circ$ . The 1x4 not tapered MMI have parameters, which are: MMI length was varied within a range of 560  $\mu\text{m}$  to 680  $\mu\text{m}$ . 617  $\mu\text{m}$ , MMI width of 24  $\mu\text{m}$ , the spacing was a 3.5  $\mu\text{m}$  (equivalent to a centre to centre pitch of 5.5  $\mu\text{m}$ ) and the MMI width was 24  $\mu\text{m}$ .

The MMI length design limits depend on the monitored power factor. From the simulation, it is anticipated that the MMI length for the best performing device should be in the range given as in table (5.3). This range for the tapered MMI length is between (505  $\mu\text{m}$  -534  $\mu\text{m}$ ), while the range of the standard 1x4 MMI

array with no taper is between (601  $\mu\text{m}$ -634  $\mu\text{m}$ ). Therefore, several MMI lengths should be chosen during fabrication to obtain the best results.

The simulation of the several design length of the MMI with monitoring the power reveal that there is a range, whereby the power is maximum. This indicates that the length of the MMI is optimum. It also means that any loss due different factors inside the MMI like mode or an image mismatch with coupling waveguide are the least possible. Moreover, the accurate MMI length results in the phase locking through the combination of self-imaging effect and the lateral coupling between the adjacent emitters. A phase locked operation should in theory lead to a single wavelength emission with a very narrow spectral width of  $\ll 1\text{nm}$ .

1x4 tapered MMI array			
Monitored power (a.u.)	The upper limit for tapered MMI designed length ( $\mu\text{m}$ )	The lower limit for tapered MMI designed length ( $\mu\text{m}$ )	
0.9	505	534	
0.95	510	530	
0.975	514	523	
1x4 standard MMI array (with no taper)			
Monitored power (a.u.)	The upper limit for MMI designed length ( $\mu\text{m}$ )	The upper limit for MMI designed length ( $\mu\text{m}$ )	
0.9	601	634	
0.95	607	630	
0.975	610	624	

Table (5.3) Simulation results of the MMI lengthy scans using BPM. The simulation was performed for 1x4 tapered MMI laser array and 1x4 MMI laser array. The data are a direct interpretation of the figure (5.32).

### 5.7.5 MMI Modelling parameter scan for the MMI width, length and gain section spacing for 1x4 case.

In the previous section, the theory and modelling of the MMI structure has been studied with an emphasis on using the MMI to form part of the cavity of a high brightness laser. In this section, the BPM modelling tool is utilised to predict the optimum device performance. This is done by scanning the parameters for the MMI across a range of MMI parameters that are likely to include the optimum. Thus, the parameter scanner function in the BPM software has been used to carry out a mapping of the parameters in order to optimise the simulation. The optimisation by the simulation is used to reduce

the number of fabrication experiments. Ultimately, the goal is to identify the device parameters that provide maximum output power from the output waveguide. Therefore, the transmitted power is monitored in the simulation.

The refractive index used for the GaAs layer in this simulation was 3.6713 for an operating wavelength of 830 nm.

The parameters for the modelling are identified in figure (5.33) below, which represents a 1x4 MMI array coupler.  $d$  is the spacing of between the gain sections ( $d$  is defined here to be the distance from the edge to edge),  $W_e$  is the width of the MMI and  $L$  is the length of the MMI.

These parameters will be optimised, by varying each one of them while keeping the other parameters fixed. The percentage of the transmitted power in a fundamental TE mode is calculated each time. The value of the transmitted power is calculated.

The simulation assumes that the ridge width of the input waveguides is  $2.5\ \mu\text{m}$ . This ridge dimension of the input waveguide supports a single fundamental mode. The results of this simulation are summarised in figures (5.34) and (5.35). Inspection of figure (5.34) shows that for a spacing  $d < 3\ \mu\text{m}$  between the input waveguides (gain sections), the percentage of the transmitted power in the fundamental mode is the highest for a spacing of  $2.92$

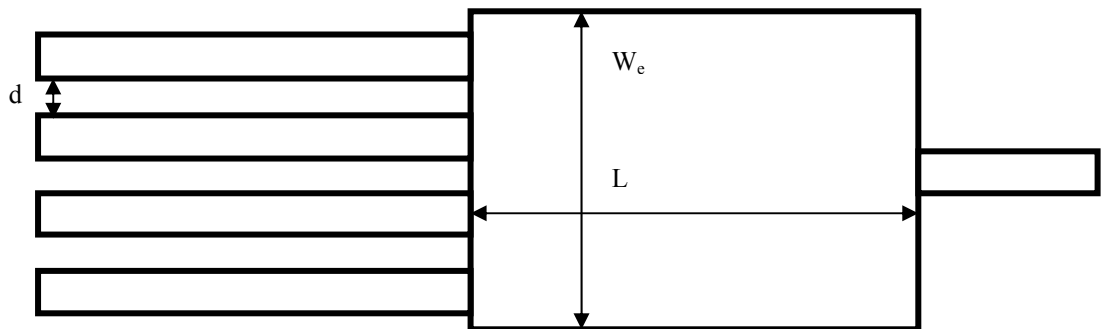


Figure (5.33): Represent 1x4 multimode interference coupler. Design parameters to be optimised are input waveguide spacing ( $d$ ), the width of the MMI ( $W_e$ ) and the length of the MMI section ( $L$ ).

$\mu\text{m}$  with corresponding width of the MMI ( $W$ ) of  $24.36\ \mu\text{m}$  and corresponding length of  $625\ \mu\text{m}$ . Thus, the optimum values for the dimensions of the MMI can be easily mapped. The higher the values of the percentage of the transmitted power in the fundamental mode, the more accurate the beat length calculation. The position of the optimum MMI length for 1x4 MMI is

$(3L_\pi/16)$ . Recalling equation (5.12) the beat length ( $L_\pi$ ) is calculated from the equation:

$$L_\pi = (4 * 3.409 * 24.36^2) / 3 * 0.83 = 3249.69 \mu\text{m}$$

$$\text{Position of N fold image (4 image)} = 3L_\pi/4 * 4 = 609.31 \mu\text{m}$$

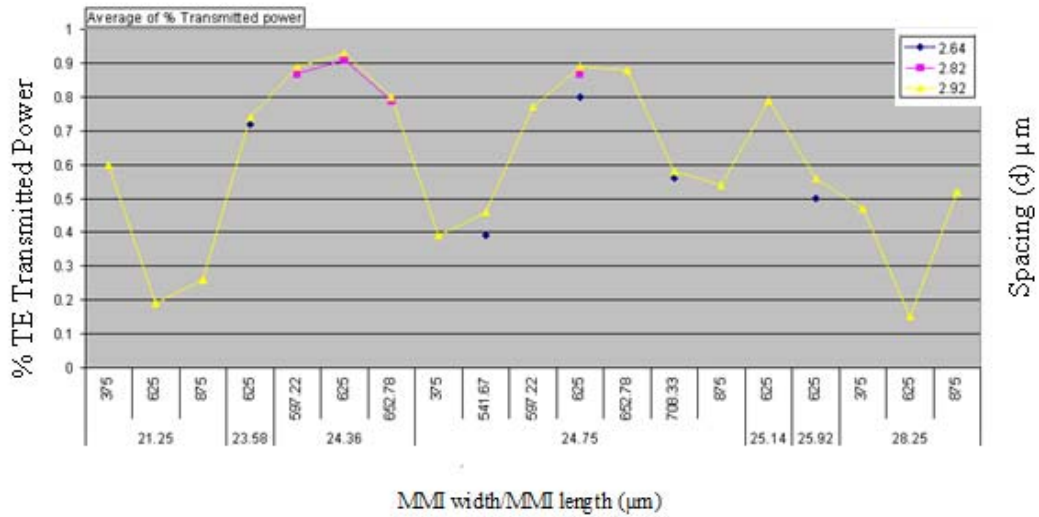


Figure (5.34): Optimisation data for a 1x4 MMI simulation using BPM. Percentage of transmitted power in TE mode plotted for different input waveguide spacing versus MMI width/length.

This calculated value for the position of four fold image is very close to the value in the simulation, as some losses could be due to the reflections as a percentage of the optimum power transmitted is not 100 %. Inspection of figure (5.35) shows that for a spacing range between (3 μm-3.75 μm), there is a high degree of flexibility in selecting the design parameters for the MMI. This provides a higher fabrication tolerance. The graph shows the results of the optimisation for MMI widths between 24 μm and 24.75 μm.

The percentage of transmitted power was highest for a range of different MMI lengths. Therefore, the optimum design parameters can be predicted easily. Since the percentage of transmitted power in the fundamental mode is  $\geq 90\%$  for different MMI widths/ lengths as observed from the figure (5.35), this value should be the criterion to select the device design parameters. Percentage of transmitted power  $< 90\%$  should be excluded from the design for best possible results. For example, for an MMI width of 24.36 μm and spacing of 3.07 μm, the percentage of transmitted power is 95 %. The beat length is equal to 3249.69 μm and the optimum 1x4 MMI coupler length is 609 μm. From figure (5.35), the values for the MMI length are in the range of 615 μm- 625 μm. The calculations are in agreement with the simulation results.

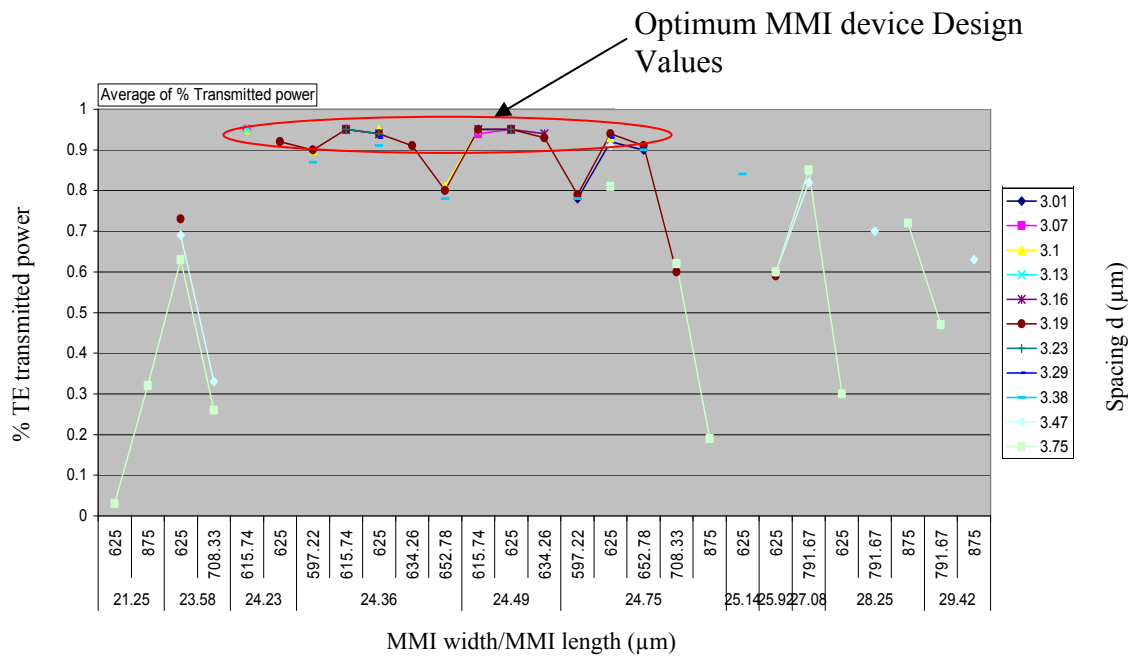


Figure (5.35): Optimisation data for 1x4 MMI simulation using BPM method. Percentage of transmitted power in TE mode plotted for different input waveguide spacings versus MMI width/ length.

The transmitted power is less than 100 %, which could be due to the fact that not all the transmitted power is observed. The transmitted power is less than 100 % due the MMI operation efficiency and any possible internal reflections inside the MMI. The conclusions of the parameter scan are that MMI dimensions exist with maximum output power on the condition that certain rules in the design of MMI array laser are adhered to, such as:

1. The length of the gain section must be greater than the overall passive sections length. A longer gain section is vital in increasing the output power of the device, particularly in structures with high  $d/\Gamma$  and low loss.
2. The evanescent coupling strength depends on the pitch between neighbouring waveguides of the array. More specifically, the power or energy transfer from one waveguide to another varies exponentially with the pitch. The waveguide spacing should not be increased beyond 3.5  $\mu\text{m}$ . Higher spacing values will result in the lasers operating independently with no coupling. It is shown in the simulation, that spacing values between 2.5 to 3.5  $\mu\text{m}$  ensure maximum coupling, so that maximum power is achieved. If we to come up with numbers for the coupling strength for the 1x4 MMI array laser, we notice that for a pitch of 2.6  $\mu\text{m}$  between the adjacent

waveguide, MMI width of 24.75  $\mu\text{m}$ , the combined coupling strength is 0.8 (a.u.). The coupling strength of a pitch of 3.2  $\mu\text{m}$  between the adjacent waveguide, MMI width of 24.75  $\mu\text{m}$ , the combined coupling strength is 0.94 (a.u.).

3. There is a range of MMI lengths for each MMI width, whereby the power is maximized and the loss is minimized. The length of the MMI section is related to the spacing or pitch between the gain sections.

### **5.8 Far field modelling for 1xN MMI laser**

The criteria for determining if an array of lasers is coherent have been explored in Chapter 2 of this thesis. In the array supermode theory in Chapter 2, the details of the diffraction patterns were studied and two models were briefly discussed. The criteria for array phase locking are used here, when discussing the far-field.

The far-field modelling study is very important for determining the phase locking of a 1xN MMI array laser diode. This is the reason for carrying out the simulation. The BPM is used in this section to model the far-field from the array side of the MMI (i.e. from the gain section side).

The far-field profile provides information for the locked supermode of the entire structure. Indeed, the shape of the far-field profile gives a strong indication if the array is coherent and the emitters are coupled with each other. The far-field pattern for a phase locked array of laser is diffraction limited, whereby the central lobe width at the FWHM is equivalent to  $(\lambda/N.p)$ . Moreover, the side lobe angular separation is equivalent to  $(\lambda/p)$ . Therefore, it is not necessarily the case that the phase locked far-field pattern results in a single lobed peak. Furthermore, as indicated in section (2.4.1.4) from chapter 2, the quality factor ( $M^2$ ) for the single emitter and the quality factor ( $M^2$ ) of the bar should be measured during the assessment of the phase locking. Visibility of the far-field pattern and the spectral output are the essential criteria for measuring the degree of coherence of an array of lasers.

The vertical far-field pattern for the array is dictated by the epitaxial layers and hence is not affected by the array design. The criteria for phase locking have been explained in detail with examples in Chapter 2. To explain this further, the lateral far-field for a 1x4 MMI integrated array laser was performed. This simulation is illustrated in figure (5.36), whereby  $N=4$ , the

spacing is a  $3.5 \mu\text{m}$  (equivalent to a centre to centre pitch of  $6 \mu\text{m}$ ), the MMI is  $24 \mu\text{m}$  wide and the length of the MMI that supports single image with is  $617 \mu\text{m}$ . The examples in this section utilise the same BPM method, as set out in the preceding sections of this chapter.

For a coherent array of  $1 \times 4$  MMI integrated array lasers, the intensity distribution of the far-field should have a central peak width equivalent to  $(0.83/4 \times 6)$ , which is  $1.98^\circ$ . That is the diffraction limit. The angular separation of individual peaks is equivalent to  $(\lambda/p)$ , which is around  $(0.83/6) = 7.9^\circ$ , as observed from the graph. The far field intensity distribution of this coherent array lies in the envelope of the individual emitters, which is equivalent to the  $(2\lambda/\pi w)$  at  $1/e^2$  for a Gaussian beam propagation.

The horizontal far-field pattern for the phase locked supermode is very much affected by the array being in a phase-locked state or not. Inspection of the simulation of the far-field from the array side for  $1 \times 4$  MMI array laser shows a narrow central peak with a FWHM close to 2.5 degrees, as well as two secondary peaks, where intensity is below 50 % of that of the central lobe,

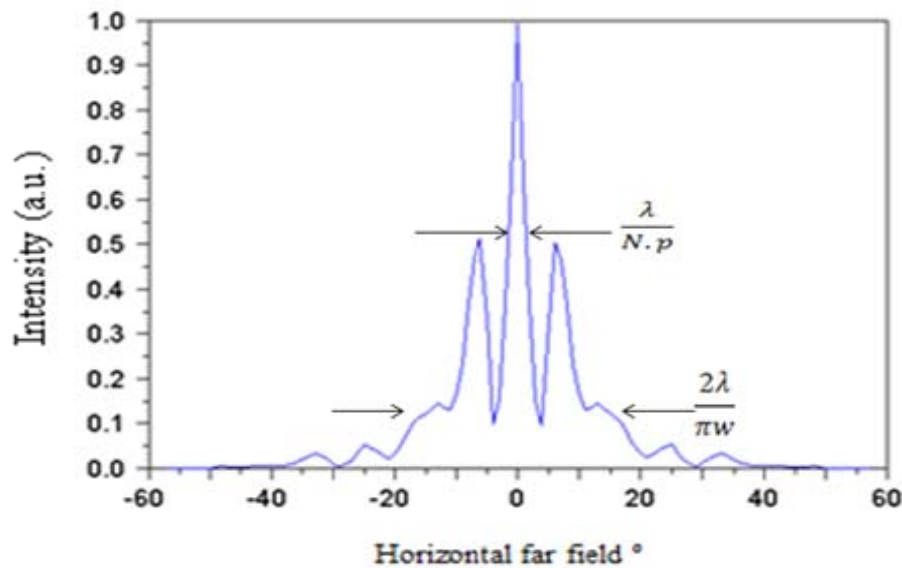


Figure (5.36): Horizontal far-field simulation for a  $1 \times 4$  MMI array laser from the array side. The dimensions of the MMI laser array are as follows: the MMI length is  $617 \mu\text{m}$ , the inter-element spacing is  $3.5 \mu\text{m}$  (equivalent to a pitch  $p$  of  $6 \mu\text{m}$  that is measured from the centre of one emitter to the next one) and the MMI width is  $24 \mu\text{m}$ . This same device has been fabricated and the results will be discussed in Chapter 6. The fill factor ( $f$ ) in this example is (41.6 %). The width of the central peak is  $(\lambda/N \cdot p)$  and the width at  $1/e^2$  is comparable to envelope of individual emitter. The angular separation of individual peaks is equivalent to  $(\lambda/p)$ .

Which are positioned approximately at  $(7.9^\circ)$  or  $(\lambda/p)$ . In this simulation, the MMI design parameters were  $617 \mu\text{m}$  for the length,  $24 \mu\text{m}$  for width and  $3.5 \mu\text{m}$  for the spacing between the gain sections. If we examine the degree of

coherence in the simulation, we can estimate that the visibility of the pattern ( $V$ ) is around 0.8, measured simply from  $V = ((I_{max} - I_{min}) / (I_{max} + I_{min}))$ .

This is obviously a simulation; the real value of the pattern visibility can only be confirmed once the devices are tested. The results of these tests are presented in Chapter 6 of this thesis.

The far-field pattern for a 1x3 MMI array laser has been also simulated and the FWHM of the horizontal far-field pattern is about 2 degrees. In this simulation, the spacing between the gain sections was kept at 3.5  $\mu\text{m}$  (similar to the 1x4 MMI case). This structure has smaller side lobes than the 1x4 MMI structure, as shown as in figure 5.37.

The case of a 1x2 MMI array laser has been studied as well. The far field appears to be comb like, with the side lobes intensity being close to 0.6 (a.u.), while the horizontal far-field FWHM is 4  $^\circ$  (approximately equivalent  $\lambda/N.p$ ), as shown in figure (5.38). The case of the 1x2 MMI array laser diode is an interesting one, because the relative phase difference is zero and theoretically phase locking should be achieved when using an MMI cavity. However, the simulation revealed that if it is to maintain useful transmitted power through the MMI, the spacing should be  $\leq 3.5 \mu\text{m}$ . In the case of the 2x1 MMI array laser, which is a special case, the spacing should not be reduced to a level that requires a reduction of the MMI width to a value lower than 14  $\mu\text{m}$ . A smaller

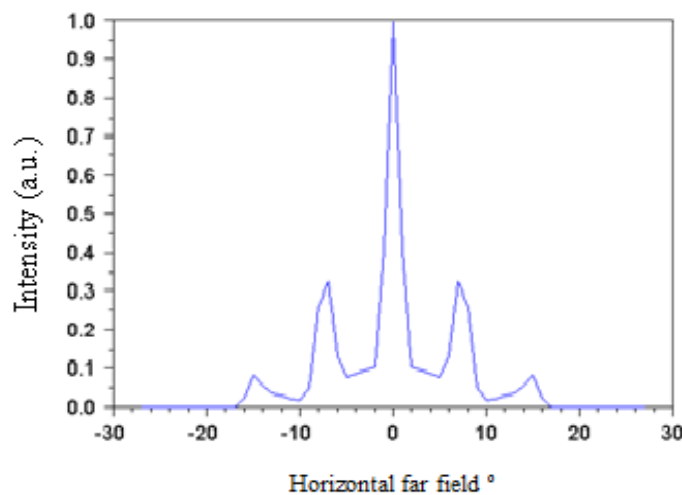


Figure. (5.37) Horizontal far-field simulation for a 1x3 MMI array laser for the array side. The dimensions of the MMI laser array are as follows: MMI length (566 $\mu\text{m}$ ), inter-element spacing (3.5  $\mu\text{m}$ ), MMI width of (19.5  $\mu\text{m}$ ) and gain sections widths of (3.0  $\mu\text{m}$ ). The fill factor ( $f$ ) in this example is (41.6 %).

MMI width means the device will be susceptible to the effects of fabrication errors. For example, a small deviation of the MMI width will cause the

imaging length to change massively, which in return results in higher losses (see figure 5.32). Furthermore, a narrower MMI leads to a reduction in the number of supported modes. Therefore, a lower imaging quality and lower output power are achieved for the device. As explained in Chapter 2, by using an MMI array configuration, the width of the MMI section is a constriction.

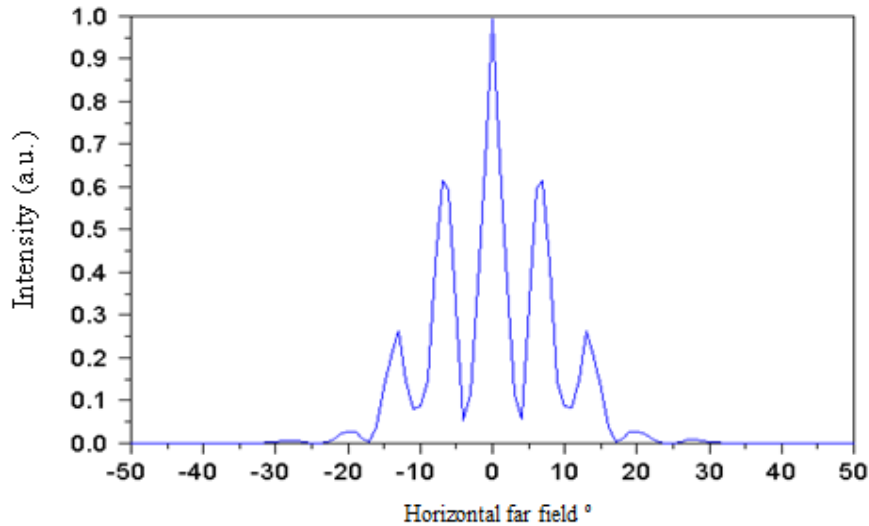


Figure (5.38): Horizontal far-field simulation for a 1x2 MMI array laser from the array side. The dimension of the MMI laser array is as follows: The MMI length is ( $465 \mu\text{m}$ ), the inter-element spacing is ( $3.5 \mu\text{m}$ ), the MMI width is ( $15\mu\text{m}$ ), the gain sections width is ( $3.0 \mu\text{m}$ ) and the fill factor ( $f$ ) in this example is ( $46\%$ ).

The centre to centre pitch between the neighbouring emitters is related to the MMI width required. For example, if a pitch of  $12.46 \mu\text{m}$  is used, this implies the use of an MMI width of  $50 \mu\text{m}$  (see figure 2.8 from Chapter 2). The 1x4 MMI coupler length in this case is  $2770 \mu\text{m}$ . The total 1x4 MMI array laser device would be about 4.195 millimeters (assuming that the gain section is 1 mm in length, the length of the output waveguide is  $325 \mu\text{m}$ , while the NAM section is  $100 \mu\text{m}$  long). Therefore, a device length of 4.195 mm is impractical.

# Chapter 6

## MMI Array Laser Device Results and Discussion

### 6.1 Introduction

As we have seen from the previous chapters, the goal in this work is to design and fabricate high brightness lasers based on the use of multimode interference couplers to couple the light into a single image and to be collected from the fundamental spatial mode of the output waveguide. Let us see the concept briefly for the devices that have been fabricated. The basic concept is shown in figure 6.1.

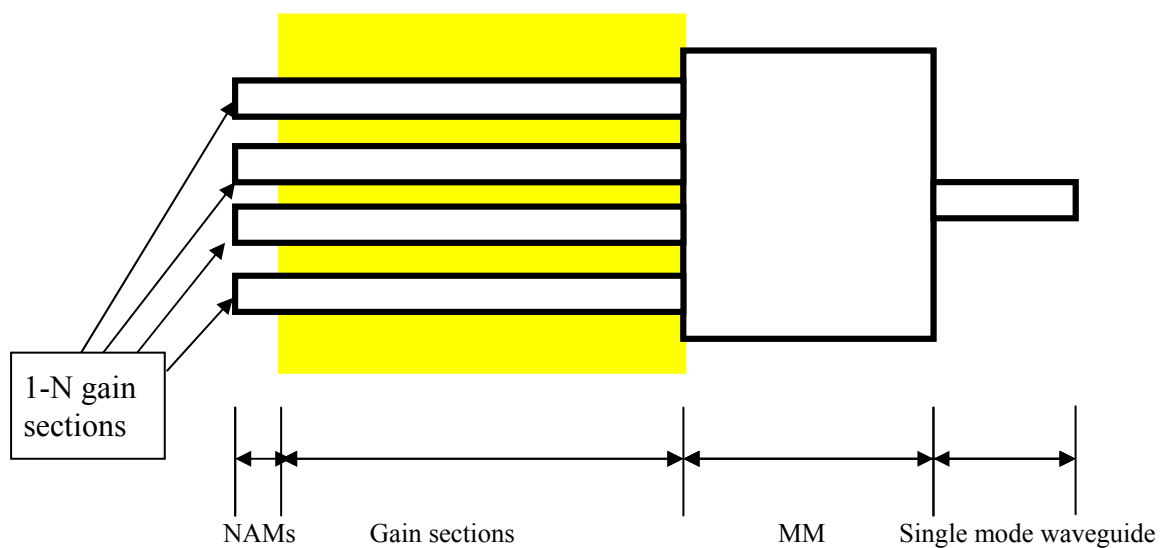


Figure (6.1) Concept for a 1x4 MMI array laser diode, which is comprised of NAMs, gain sections, MMI coupler and single mode output waveguide.

The number of gain sections has been selected to be a maximum of four (206, 207). Increasing the number of gain sections will result in a very complicated array laser, which manifests itself as a loss of the locking mechanism of array laser. Specifically, the edge lasers easily drop out of phase locking. Furthermore, the relative phase relationship becomes complicated.

This chapter is organised as follows: In section 6.2, a 1x4 array laser diode design is discussed. This section itself is divided into sub-sections, which are related to a summary of the 1x4 fabrication, followed by all of the results relevant to the 1x4 MMI laser. In section 6.3, further analysis and discussion is conducted. Specifically, this section compares the results in this thesis to what has been reported and the description of additional improvement work that has been carried out during this research. In section 6.4, the design and the results for the 1x2 MMI array laser are discussed.

## **6.2 1x4 MMI array laser device**

The device is comprised of four main sections, as seen in figure (6.2a, b). The first section of the device is the non-absorbing mirror, which is adjacent to the facets. The NAMs have been fabricated using the quantum well intermixing technique, which is detailed in chapter four. The wavelength shift produced is blue shifted by 58 nm to maintain low absorption at the facets and thus increase the maximum power prior to COMD. The second section of the device is the pumped area, which consists of four single spatial mode ridge waveguides, where the etch depth is 1.84  $\mu\text{m}$  to maintain the single mode behaviour. The separation between the ridge waveguides is set at 3.5  $\mu\text{m}$  from the edge of a waveguide to the edge of the adjacent waveguide. The modelling in chapter 5 shows that this separation gives the optimum lateral coupling, which along with the mode mixing in the MMI through self imaging, should maximise the output power of the device. Furthermore, a wider separation distance (pitch) results in a considerably longer MMI section, as shown in the simulation example in Chapter 2 in figure (2.8). When the pitch is increased to 12.46  $\mu\text{m}$ , the length of the 1x4 coupler is 2770  $\mu\text{m}$ . The total device length is around 4.195 mm, which is impractical. It is found from the simulation that a higher separation distance will result in the deterioration of the lateral coupling, resulting in lower output power. This is reported to be the case in

gain guided laser array (211) and 1x2 MMI array laser diode (201). This has been studied by Walker (201), where he fabricated a 1x2 MMI array laser and indicated that the low transmitted power achieved at the output waveguide was due to the large lateral separation distance used. The third section of the device is the multimode interference coupler region, which is responsible for maintaining the constructive interference of the light injected by the gain section elements. The dimensions of the MMI are a critical factor, where a single image is achieved at the output waveguide when a suitable MMI length is employed.

In order to ensure the optimum length of the MMI, several lengths have been fabricated close to the optimum length. These MMI lengths were calculated using the BPM simulation detailed in Chapter 5, namely, 617  $\mu\text{m}$ , 644  $\mu\text{m}$ , 665 $\mu\text{m}$ , 687  $\mu\text{m}$  and 709  $\mu\text{m}$  as seen in Table 6.1. The optimum length of the MMI is affected by the etched depth of the MMI and is therefore sensitive to variations introduced in the fabrication process. The design parameters are summarised in Table 6.1 below.

<b>Design Parameters for MMI 1x4 array laser</b>		
<b>NAM length</b>	75	$\mu\text{m}$
<b>Gain section length</b>	975	$\mu\text{m}$
<b>MMI length</b>	617,644,665 687,709	$\mu\text{m}$
<b>MMI width</b>	24	$\mu\text{m}$
<b>Ridge width (gain section width)</b>	2.5	$\mu\text{m}$
<b>Spacing</b>	3.5	$\mu\text{m}$
<b>Output waveguide length</b>	309	$\mu\text{m}$
<b>Output waveguide width</b>	2.5	$\mu\text{m}$

Table (6.1) Design Parameters chosen for the 1x4 MMI array laser diode

The schematic for the array laser device is shown in figure (6.2a). The length of the passive non-absorbing mirror section (NAM) is 30-100  $\mu\text{m}$ . The length can be increased up to 150  $\mu\text{m}$ . The longer the NAM, the easier the mechanical cleaving process.

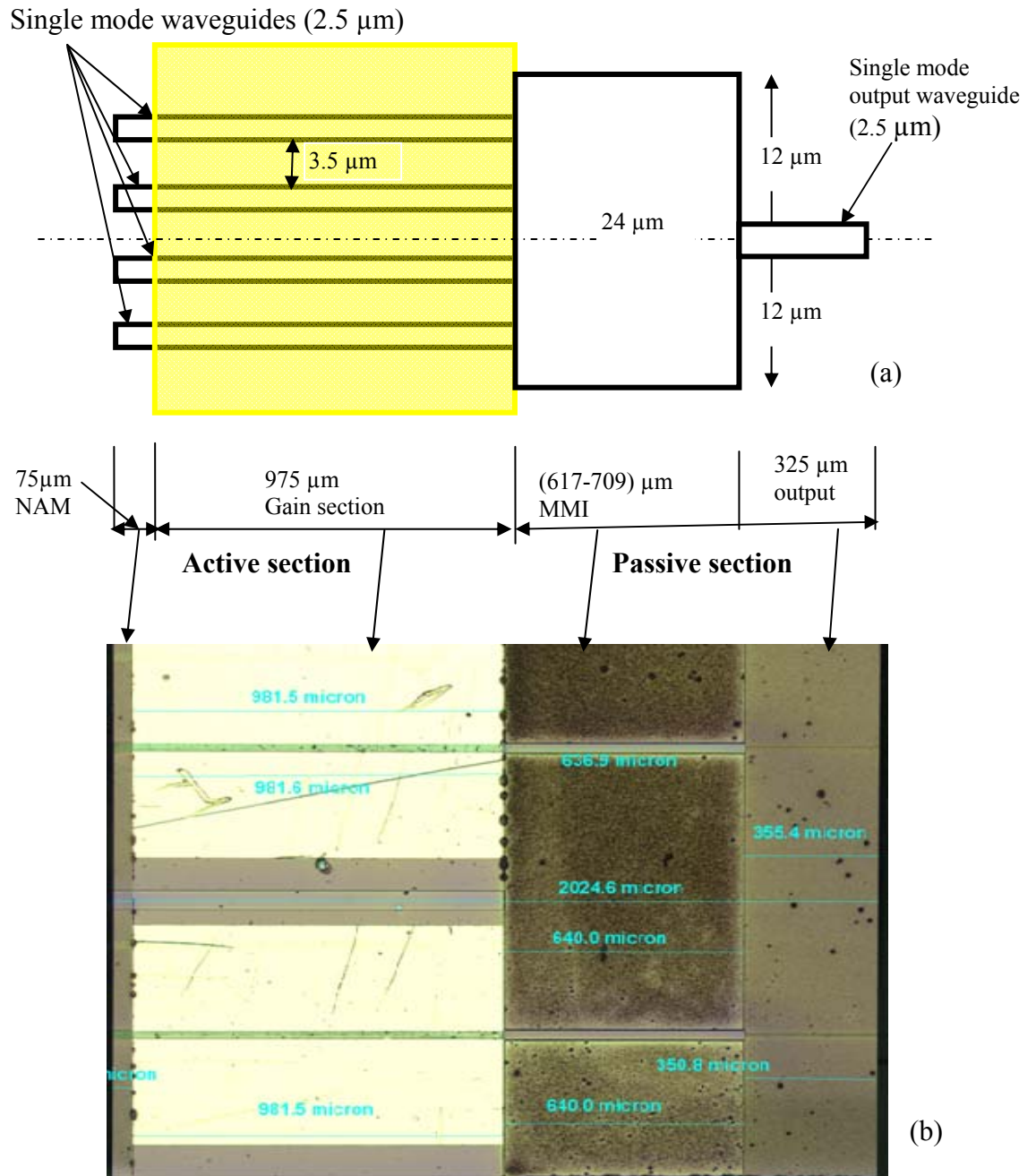


Figure (6.2): a) Schematic diagram of the 1x4 MMI coupler array laser. The devices were etched up to 300 nm above the quantum well. The MMI section is etched again through the waveguide core. The gain sections are electrically connected with a single contact. b) Image taken of the array laser by optical microscope, showing the four sections of the integrated device.

An optical microscope image in figure (6.2b) shows the four sections of the integrated 1x4 array laser device. The length of the gain sections is 975  $\mu\text{m}$ . The length of the active section can be made longer to increase the output power. The width of the MMI section is very critical and is the most important parameter in the design. This has been verified from the simulation, where a small deviation from the fabrication increases or decreases the true imaging length, thereby resulting in high losses inside the MMI or losses generated at the output waveguide. However, the deviation in the width of the MMI can be compensated for by fabricating different MMI lengths (196), as described in the previous section.

The MMI was etched through the waveguide core to increase the number of guided modes and increase the quality of the image. The image quality in the MMI is a measure of the efficiency of converting the input field from the gain sections to an image field at the output section (i.e. the single mode waveguide). The gain sections and the output waveguide are single mode waveguides designed to maintain a single spatial mode output. The electrical contact to the gain sections is common for all the gain sections, so the devices are not individually addressable. Individually addressable gain sections would have provided more flexibility during testing as well as the possibility of injecting different current levels into each gain section. However, difficulties with the metallisation process made it unattainable to fabricate MMI array lasers with individually addressable gain sections.

### 6.2.1 1x4 MMI array laser device fabrication summary

Following the design, the device was fabricated. The difficulty with the fabrication of individually addressable gain sections (emitters) was caused by the less than 2  $\mu\text{m}$  gap between adjacent contacts. This separation distance was not large enough to obtain good metal lift off. The devices fabricated suffered shorting due to uncleaned metallisation debris.

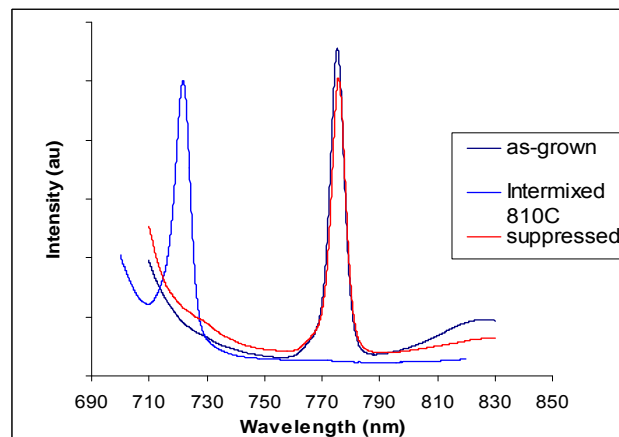
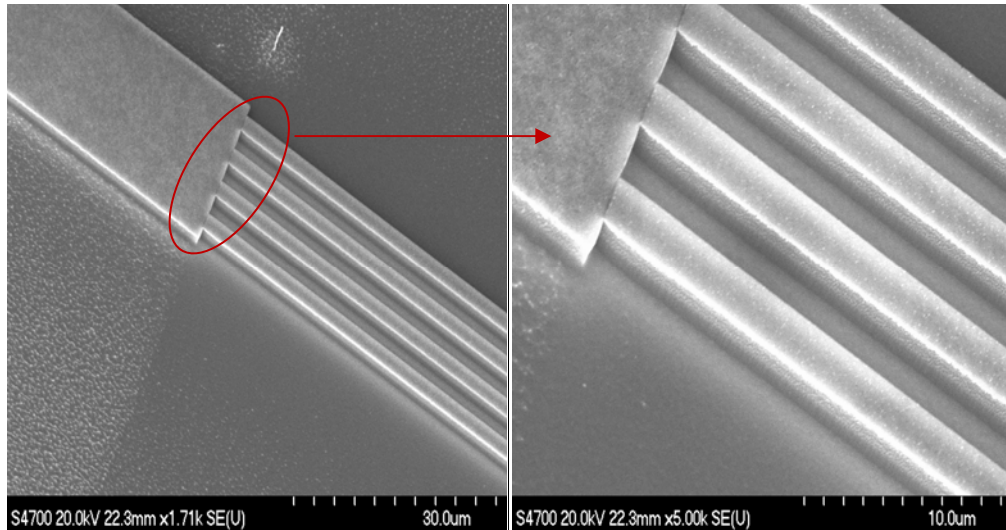


Figure: 6.3 Photo-luminescence spectra from the as-grown, suppressed and intermixed device. A wavelength shift of 58 nm is observed. The non-intermixed areas are suppressed by using a layer of protective silica.

The details of the fabrication process are discussed in Chapter 4, but it useful to summarise the specific details of the device fabrication in this section.

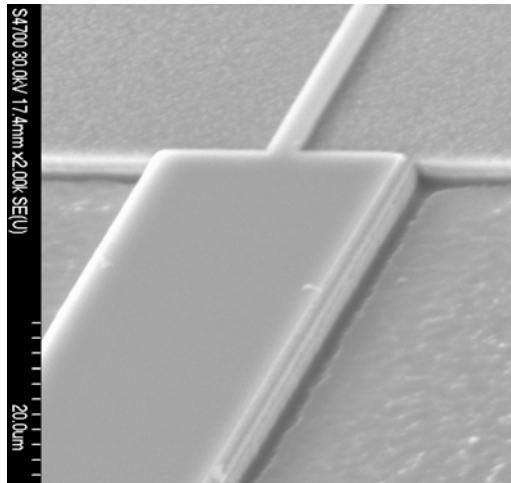
- 1) Etch markers: The etched markers have been used in e-beam lithography using the deep etch process for GaAs/AlGaAs material.
- 2) Quantum well intermixing: The QWI stage is very important, as it is an integrated device, where the (non-absorbing mirrors) NAMs, the MMI and output waveguides are defined at this stage. The photoluminescence spectra for the intermixed sample are shown in figure 6.3.
- 3) Definition of the waveguides and etch.

In this step, the waveguides are defined and etched to a depth of 1.84  $\mu\text{m}$ . This is the depth that supports a single spatial mode. This is followed by a second deeper etch for the MMI region to achieve lower losses. The SEM image in figure 6.4 shows the etched devices.



(a)

(b)



(c)

Figure: 6.4 (a) This SEM image shows a 1x4 etched waveguide with well defined waveguides. (b) This SEM image is a magnified image of (a), which shows a well etched waveguide with a good interface between the MMI and gain sections. (c) The SEM image shows the deeper etch used for the MMI section.

#### 4) Contacts

The final step in the laser fabrication is the metallisation. A single contact pad was used for all the gain sections as can be observed in SEM image in figure (6.5). By using a single p-metal contact metallisation, it became difficult to control the phase of the laser array. The complete laser bar on the Cu type carrier can be seen in Figure (6.6).

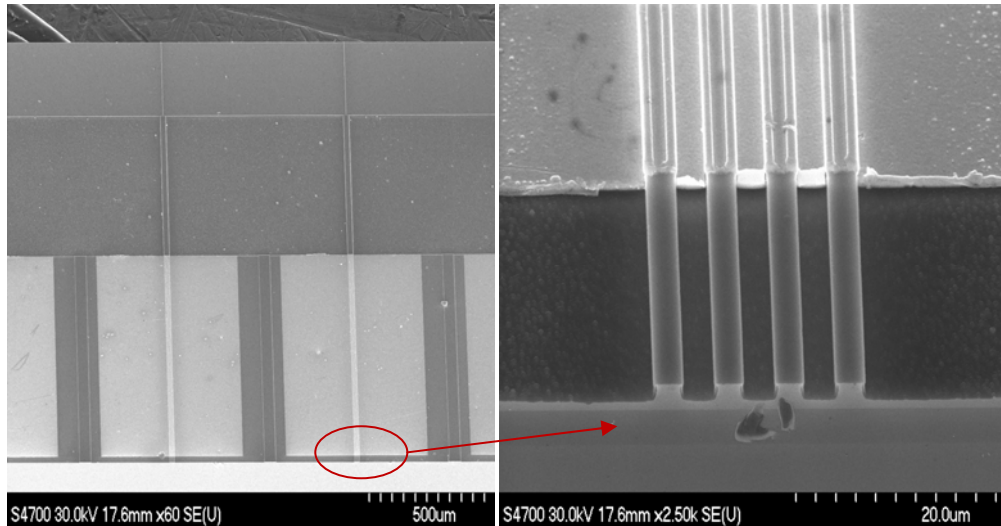


Figure: 6.5 This SEM image (left) shows a bar of 1x4 MMI array devices mounted on a brass sub-mounts. The magnified image (right) shows the cleaved facets. The p-metallisation which covers all the four gain sections is well defined. The non-coated area represents the NAM area.

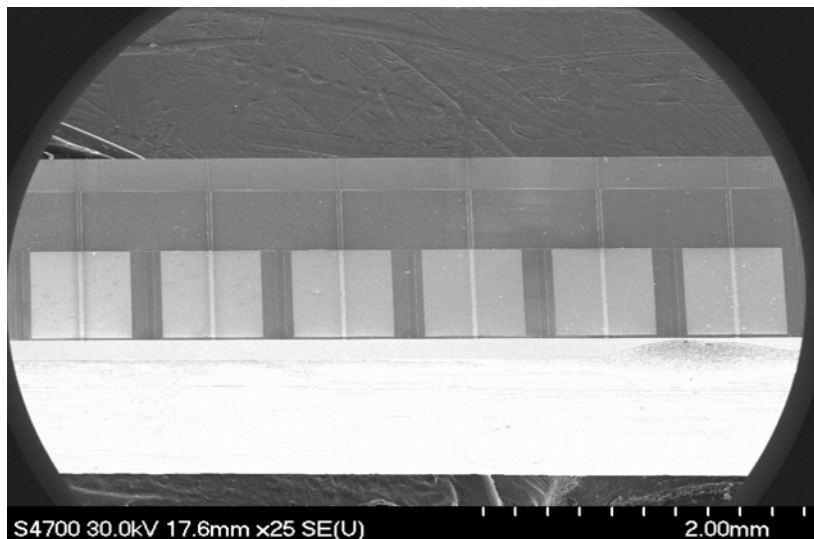


Figure: 6.6: Complete bar of 1x4 MMI laser arrays, which is mounted on a brass sub-mount, where six devices are visible.

### 6.2.2 1x4 MMI array laser device testing

The devices were tested electrically in pulsed mode. The tests were performed using a pulsed current source using 10  $\mu$ s pulses and a 1 KHz repetition rate, while the device was held at 25° C. 10 $\mu$ s pulses do not suppress self-heating but increase the lifetime of the device. As explained in the previous section, all of the gain sections are electrically connected, so the current applied will be split between the four gain sections. The current injection may have been split non-uniformly into the gain sections due to non-uniformities in the material and fabrication. This could have an effect on the amount of the light generated in each gain section. The current injection may have been split non-uniformly

due to the single contact for all the emitters in the array. The factors that can affect the current splitting can be several. Firstly, the series resistance nonuniformity of the devices, which is due to variation of the temperature across the array. Secondly, a variability in the spatial distribution of the injected carriers, which determines the lateral gain profile (208). Thirdly, current splitting between emitters is also influenced by both the current and carrier profiles beneath each emitter and neighbouring emitters (209, 210). Fourthly, current spreading is another important issue in the determination of the current splitting. Lastly, the current splitting between the emitters is influenced by different stimulated emission rates, which is caused by supermode competition between the locked and unlocked states. Furthermore, the current splitting is also affected by the quasi - supermode operation, where different supermode exists for each emitter. Each emitter in this case, emits at different wavelengths.

The results for a 1x4 array laser device with the parameters tabulated in table 6.1 are shown in figure (6.7a). The device was tested up to  $(20 \times I_{th})$  and no COMD was observed. This demonstrates that the quantum well intermixing process has worked and that the non-absorbing mirrors (NAMs) prevented the destruction of the facet. The maximum power achieved for the device was close to 440 mW per facet at  $20 \times I_{th}$  in pulsed mode. The power was measured from the single output waveguide, as shown in figure (6.7a). This power is equivalent to an optical intensity of  $17.6 \text{ MW/cm}^2$  (for a mode area of  $1 \mu\text{m} \times 2.5 \mu\text{m} = 2.5 \mu\text{m}^2$ ). Even at this intensity, there was no sign of COMD. The threshold current for the device was 145 mA. The threshold current was equal for all of the devices, despite the differences in the MMI length. This means that optical loss in the MMI was very small in the passive sections. This also means that the quantum well intermixing process has been excellent in reducing the optical losses in the passive sections to a minimum. The wavelength measured was 824 nm for this particular device, as shown in the inset of figure (6.7a). The threshold current for a single ridge waveguide fabricated from the same material and equivalent gain section length with no absorbing mirrors has a threshold current of 33 mA. For a 1x4 MMI array laser, an average threshold current of 36 mA for single active ridge waveguide is reasonable assuming that all the gain sections have the same threshold.

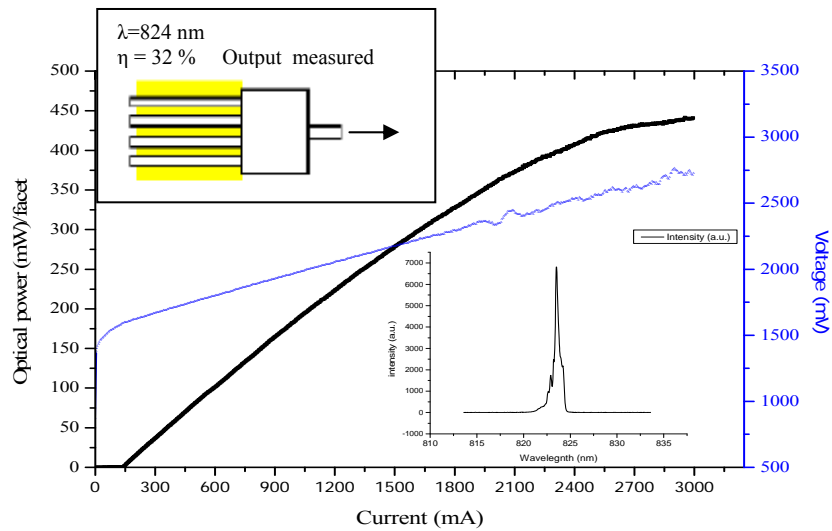


Figure (6.7a) Front facet (power per facet) light current/voltage (LIV) test results for a 1x4 MMI array laser. The devices were tested pulsed up to  $(20 \times I_{th})$ . The MMI length was  $(617 \mu\text{m})$ , the gain section length was  $(975 \mu\text{m})$ , the NAM length was  $(100 \mu\text{m})$  and output waveguide length was  $325 \mu\text{m}$ . The MMI length is very close to the simulated MMI length of  $617 \mu\text{m}$ . The operating wavelength was  $824 \text{ nm}$ , as shown in the inset.

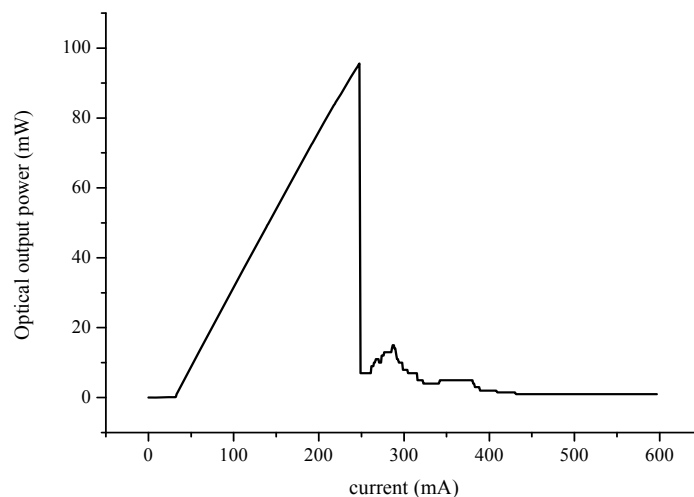


Figure (6.7b) LI curve for  $2.5 \mu\text{m}$  single ridge waveguide performance. The length of the device was  $1.5 \text{ mm}$ . There was no facet coating and no NAM which was fabricated using the same Intense Ltd material. The device suffered COMD at  $98 \text{ mW}$  at this particular example.

This would mean an increase from the standard ridge waveguide laser by  $3 \text{ mA}$ . The increase in threshold current is probably due to the additional losses introduced in the passive section of the device. In figure (6.7b), an LI characteristic is shown for a ridge waveguide laser fabricated from the same material with a length of  $1.5 \text{ mm}$ . The device has no facet coating and no NAMs suffered COMD at around  $98 \text{ mW}$  for this particular example.

In the 1x4 MMI array laser, as predicted, the highest power achieved was for the device whose MMI length was very close to the precise imaging length,

where four equivalent intensity images are located. The output power was measured for devices with different MMI lengths. Figure (6.8a) shows the maximum power level versus MMI length at an injection current of 3.0 A. The devices with an MMI length of 617  $\mu\text{m}$  achieved higher powers than devices with longer MMI sections. From the simulations in Chapter 5, we saw that the

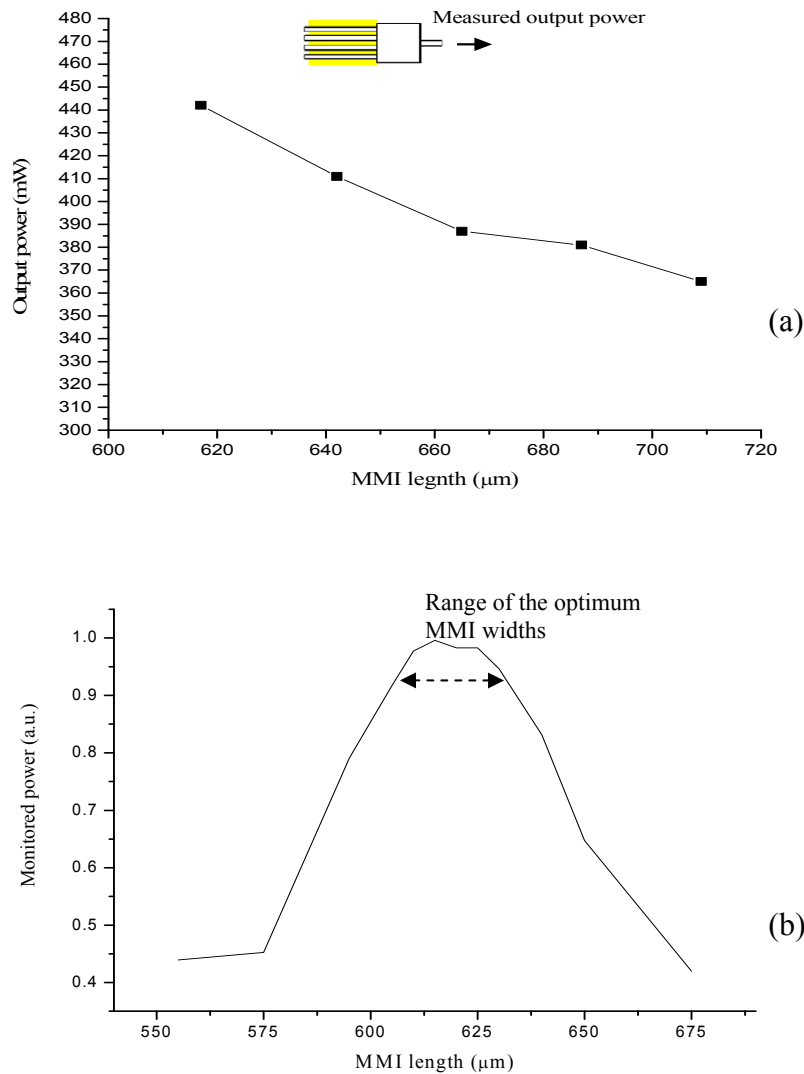


Figure (6.8) a) Maximum power values measured at 3.0 A current for devices with different MMI length. The optimum MMI length from the simulations was 615  $\mu\text{m}$ . The device with highest power has an MMI length of 617  $\mu\text{m}$ . b) BPM Simulation resulted for the monitored power of a 1x4 MM array laser. The array laser dimensions are as follows: the MMI width was 24  $\mu\text{m}$ , the ridge waveguide width was 2.5  $\mu\text{m}$  and the emitter separation distance was 3.5  $\mu\text{m}$  (equivalent to a centre to centre spacing of 6  $\mu\text{m}$ ). The MMI length was varied for optimisation. MMI window for a monitored power of 0.95 (a.u.) is in the range of (607 $\mu\text{m}$  -630  $\mu\text{m}$ ) optimum MMI length was 617  $\mu\text{m}$ . The length can be slightly longer or shorter due process variations during fabrication. Recalling the simulation for

monitored MMI power versus the MMI length from Chapter 5, it is clear from the figure (6.8b) that the trend for the monitored power in the simulation matches the experimental result. The simulation revealed that there is an optimum window of MMI length for each MMI width that could result in higher power. The range for the optimum window is around (607 $\mu\text{m}$ -630 $\mu\text{m}$ ). Therefore, it is no coincidence that the best performing 1x4 MMI array is the device whose MMI length is 617  $\mu\text{m}$ . It is very important to match the image spot size and shape to the mode size and the shape of the output waveguide. This is attained by the selection of the accurate MMI length, which is the case here. Inspection of the graph (6.7a) shows that good light current characteristics are observed with a minimum kink in the LI curves. However, the LI curve obtained for this optimised device shows that the slope efficiency is 0.24 W/A per facet or about 32 % external quantum efficiency, which is rather low. However, if we take into account that the devices are actually uncoated, this is quite a reasonable efficiency. If the devices' facets are coated with an anti-reflection coating and a highly reflective coating, this would result in doubling the output power obtained. This can increase the external quantum efficiency. The present result obtained is good, especially if it is compared to what has been reported by for example Camacho *et. al.* (3) who fabricated a similar device. The slope efficiency of their device did not exceed (0.10 W/A) and the maximum output power obtained was only 180 mW. However, the output power for the device in this research is almost 2.5 times more than what was achieved before using the same material system. If the gain sections here were increased beyond 975  $\mu\text{m}$  for example to 2000 or 3000  $\mu\text{m}$ , the output power would have increased significantly. One reason why we can afford to do that with the GaAs/AlGaAs material that has been used in the design, is that the material has a low propagation loss (1.59  $\text{cm}^{-1}$ ), which was measured in Chapter 3. Furthermore, the epitaxial design utilises the d/T property, which allows the fabrication of longer devices without paying a penalty in increasing the propagation loss. For a more detailed discussion of this issue, see Chapter 3, section (3.5.2).

The wall plug efficiency (also known as the power conversion efficiency) of the device is plotted in figure (6.9). The low external quantum efficiency is reflected, as expected in a reduced WPE.

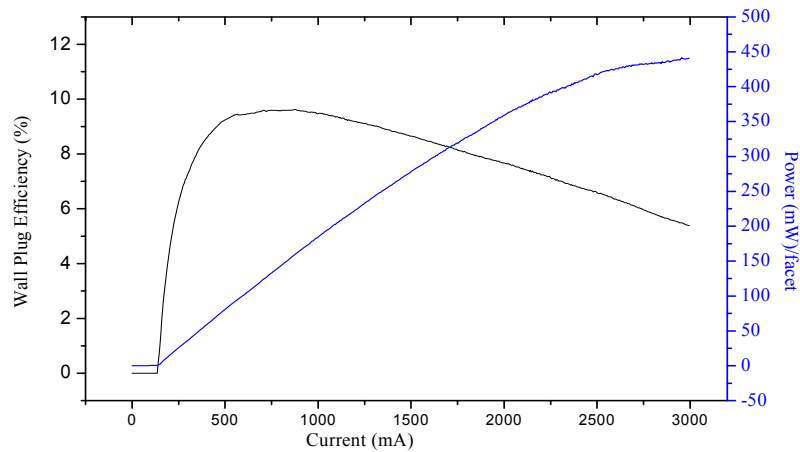


Figure (6.9) Wall plug efficiency (WPE) and output power vs. drive current for an uncoated 1x4 MMI array laser with MMI length of  $617\mu\text{m}$ . The power was measured from the single output waveguide side.

It was calculated directly from the LI curve from figure (6.7a). The wall plug efficiency of the 1x4 MMI array laser device was 9.6 % per facet for a drive current of 900 mA. At this current, the optical power was 165 mW per facet. At a high current of 2.75 A, the WPE was decreased to 6%, while the output power per facet was increased to 430 mW per facet, as seen in figure (6.9).

The operation of the 1x4 MMI array laser device is optimised. Optimisation means that the lateral coupling and the imaging length is accurate. Therefore, good quality imaging is obtained at the end of the single output waveguide. A comparison between the results for an optimised device and non-optimised one can be seen in figure (6.8a). The output power measured from the single output waveguide decreases from the highest level of 442 mW for the optimum length of  $617\mu\text{m}$  to 365 mW for the much longer length of  $709\mu\text{m}$ . This shows a reduction of (21.9 %) in the optical output power per facet for the non-optimised device, which is substantial.

If we look at another example for a device with the same parameters, but longer MMI length by  $27\mu\text{m}$  (MMI length was  $644\mu\text{m}$ ), as result the loss is expected to be higher due to poor quality imaging at the output waveguide. This resulted in a reduction of the output power by (6.5 %) per facet, as can be seen in figure (6.10). This is very considerable, so it is imperative that the length of the MMI section is optimised. The argument is true for devices with a longer or shorter MMI section.

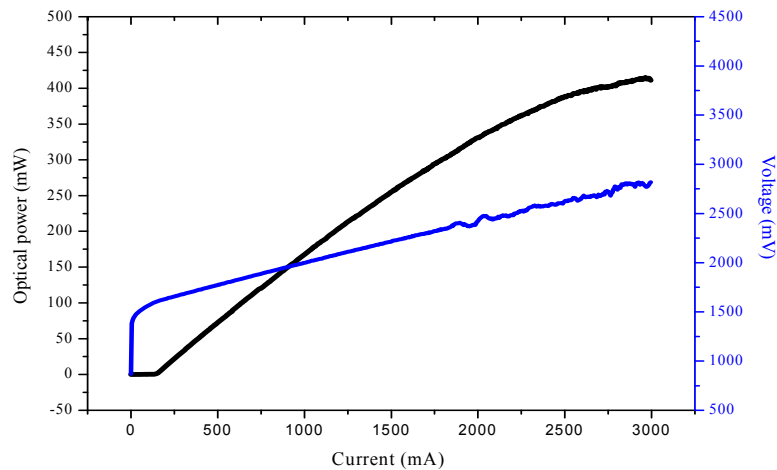


Figure (6.10) Front facet light current/voltage (LIV) test results for a 1x4 MMI array laser. The devices were tested pulsed up to  $(20 \times I_{th})$ . The MMI length was  $(642 \mu\text{m})$ , the gain section length was  $(975 \mu\text{m})$ , the NAM length was  $(100 \mu\text{m})$  and output waveguide length was  $325 \mu\text{m}$ . The MMI length is longer than the simulated MMI length by  $25 \mu\text{m}$ .

The phase relationship in the case of a non-ideal MMI would be affected as well, due to differences in the imaging length. We infer that once the length of the MMI section deviates from the optimum imaging length, there will be a reduction in the output power achieved. Furthermore, when the  $665 \mu\text{m}$  MMI length device was measured, the drop in the optical output power was  $(14.7 \%)$  per facet, as in figure (6.11). The largest drop in power observed was for the device with the longest MMI length of  $709 \mu\text{m}$ . The drop of the output power is

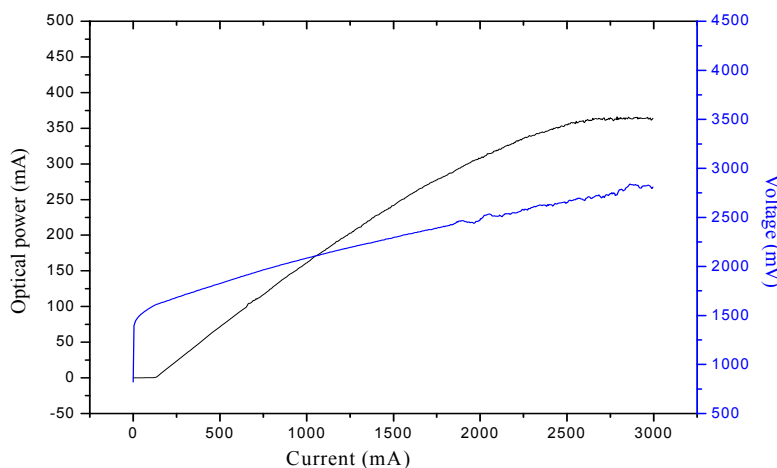


Figure (6.11) Front facet light current/voltage (LIV) test results for a 1x4 MMI array laser. The devices were tested pulsed up to  $(20 \times I_{th})$ . The MMI length was  $(665 \mu\text{m})$ , the gain section length was  $(975 \mu\text{m})$ , the NAM length was  $(100 \mu\text{m})$  and output waveguide length was  $325 \mu\text{m}$ . The MMI length is longer than the simulated MMI length by  $48 \mu\text{m}$ .

due to the incorrect imaging length and phase. This led to a mode mismatch, which resulted in higher losses. An incorrect imaging length means that the spot size is larger than the waveguide width, thus results in increased losses.

### 6.2.3 Single lateral mode operation of the 1x4 MMI array laser

For studying single lateral mode operation, the far field was measured for a 1x4 MMI array laser from the single output facet. The test results for the vertical and horizontal far field patterns of the device with an MMI length of  $617\ \mu\text{m}$  can be seen in figure (6.12). Inspection of the horizontal far-field graph

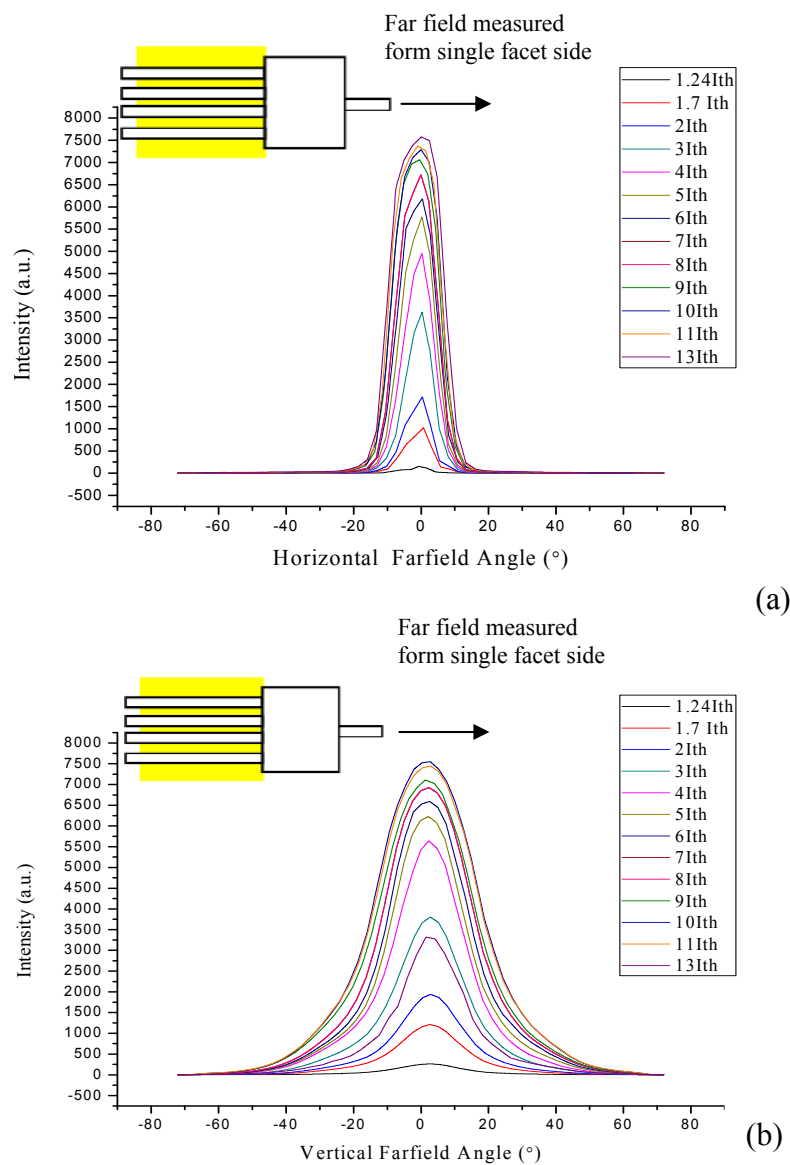


Figure (6.12) a) Vertical and far field for 1x4 MMI array laser from single output facet side. b) Horizontal far field. The far field was measured from  $(1.24I_{th})$  mA up to  $(13I_{th})$  mA, which corresponds to 180 mA up to 1900 mA.

shows a single-lobed far field pattern for  $1.24I_{th} = 180$  mA. Moreover, when the current is increased to 1900 mA ( $13xI_{th}$ ), the far-field profile remains single-lobed with a width of about  $11.7^\circ$  at the FWHM. However, the far-field at  $1/e^2$  is about  $23.2^\circ$ . The values of the far-field measurement at ( $13xI_{th}$ ) are comparable with what has been observed in the simulation of a  $2.5\ \mu\text{m}$  single spatial mode waveguide, as shown in figure (6.13) below.

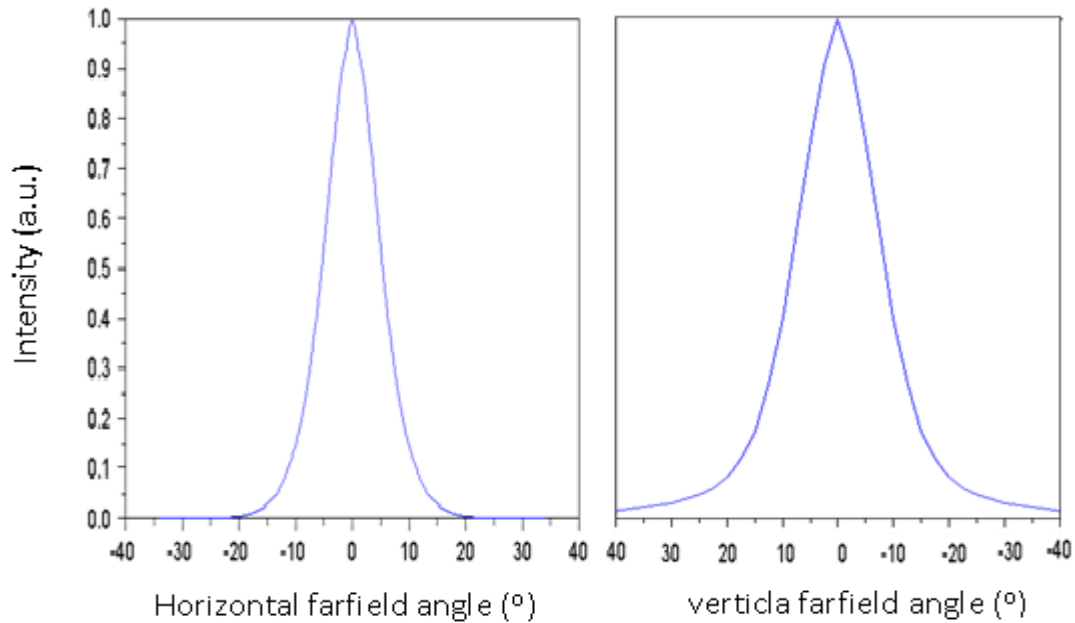


Figure (6.13) a) Horizontal far-field BPM simulation for the  $1x4$  MMI single output side. Ridge depth of a  $1.84\ \mu\text{m}$  and waveguide width of a  $2.5\ \mu\text{m}$  is used. The FWHM is  $9.3^\circ$  at  $3I_{th}$ . The far-field was measured at  $3I_{th}$ , which was  $9.4^\circ$  at FWHM. The far-field at  $1/e^2$  is  $23.2^\circ$  when measured at  $13I_{th}$ . The value of the far-field from the simulation above is  $21^\circ$ . b) The BPM simulation of the vertical far-field for a  $1x4$  MMI single output side shows a FWHM of  $22^\circ$ . The vertical far-field increases to  $23^\circ$  FWHM at  $3I_{th}$ . A ridge depth of  $1.84\ \mu\text{m}$  and waveguide width of  $2.5\ \mu\text{m}$  are used.

The FWHM values of the horizontal far-field are often optimistic. The far-field pattern observed in Figure (6.12a) resembles the divergence for a single emitter (i.e.) the width is comparable to  $(2\lambda/\pi w)$  at the  $1/e^2$ . Obviously, in this example there is no phase locking. A phase locked array should have far field pattern properties, as indicated in section (2.4.1.4) from Chapter 2 as well as an optical spectrum with single wavelength peak with  $\text{FWHM} \ll 1\text{nm}$ .

In theory, the output from the  $2.5\ \mu\text{m}$  single mode waveguide should be single mode, but this cannot be guaranteed at high output powers. This is because increasing the current injection, causes device heating and leads to temperature and carrier induced refractive changes, which reduces the

effective index. The reduction of the effective index may result in a change from index guiding regime to gain guiding, as explained in section 3.5.3.2 in Chapter 3. Furthermore, the coherence of the array may be lost. Although the device showed single lobed far-field behaviour to about 2000 mA, this does not mean that the device operates in single mode, whereby the device might be emitting in several wavelengths from the single ridge waveguide side. The heat generated and the onset of higher order modes becomes apparent if the current is increased to 2500 mA. This means the sought after phase-locking is very difficult to achieve at high injection currents for this particular device. The operation and the coupling of the laser gain sections is not simple to explain due to different factors that affect the collective mode behaviour, which we called the supermode.

To achieve stable phase locking between all the gain sections, the phase should be equal in all the gain sections. This was investigated by the simulations in Chapter (5), which showed a phase difference between the inner arms ( $\Phi_2=\Phi_3$ ) and the outer arms ( $\Phi_1=\Phi_4$ ) is  $(\pi/2)$ . However, the power extracted from a single output waveguide is usable and is much higher than that from a standard uncoated single ridge waveguide. The device performance would have been improved, if the phase locking was achieved at high injection currents. However, the limited slope efficiency is due the fact that the locking is unstable. The slope efficiency is higher when phase locking is achieved. Moreover, the lower slope efficiency is due to the heating effects which cause an increase in the junction temperature at high injection currents. The reduction of the threshold current density is very important for improving the device performance. The performance of the device will improve dramatically if a facet coating is applied and the power would certainly double. In return, this may improve the phase locking through a process called self adjustment (3, 212, 213), whereby the laser adjusts the laser phases. This results in the selection of the supermode with the lowest loss (lowest threshold), which emits in one single lateral supermode for the whole 1x4 MMI array structure. To further study the phase locking, the MMI array laser was characterised from the array facets side. The light power characteristics were measured and the results from this measurement can be seen in figure (6.14). The light current characteristics in figure (6.14) confirm clearly that the power

measured from the array side is lower than the power obtained from the single output waveguide. The maximum power measured was 400 mW from the four array facets side. This power is lower than that from the single wavelength side by about 10 %. Nevertheless, this power level is very good- meaning that

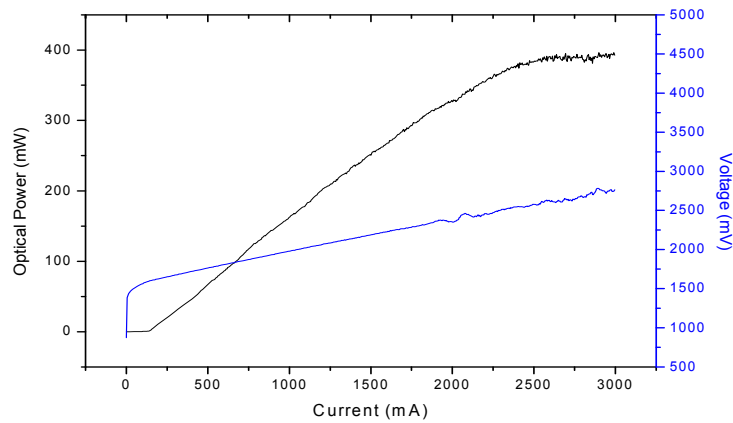


Figure: (6.14) Back facet (array side) light current/voltage (LIV) test results for a 1x4 MMI array laser. The devices were tested pulsed up to  $(20 \times I_{th})$ . The MMI length was  $(617 \mu\text{m})$ , the gain section length was  $(975 \mu\text{m})$ , the NAM length was  $(100 \mu\text{m})$  and output waveguide length was  $325 \mu\text{m}$ . The MMI length is very close the simulated MMI length of  $617 \mu\text{m}$ .

the whole device is behaving like an ordinary single ridge waveguide laser. However, the difference in power from the two sides could be explained by the different geometry and the possible leakage of light from the passive integrated cavities. The efficiency of the MMI operation can be another reason for this behaviour. Optimisation of the MMI is vital for the reduction of the losses due mode mismatch between the MMI and the output waveguide. Thus, if we look at the power from the array side of the 1x4 MMI array laser, we see that the maximum power was achieved for the MMI with optimised length, as seen in figure (6.15). In figure (6.15), the optimized MMI device has a minimum mode and image mismatch. This is verified by the low lost power observed. The lost power is the difference between the measured optical power from the single output waveguide and the power measured from the array facets side. This lost power can be due to scattering of light as well as leakage from the passive guides. The power loss is around 10 % per facet for the optimised device. There is a clear trend in Figure (6.15), whereby the lost power increases as the deviation in the MMI length increases. This loss can also be attributed to the leakage of light from the waveguide at the interface between the MMI and the single output waveguide at the combiner mode.

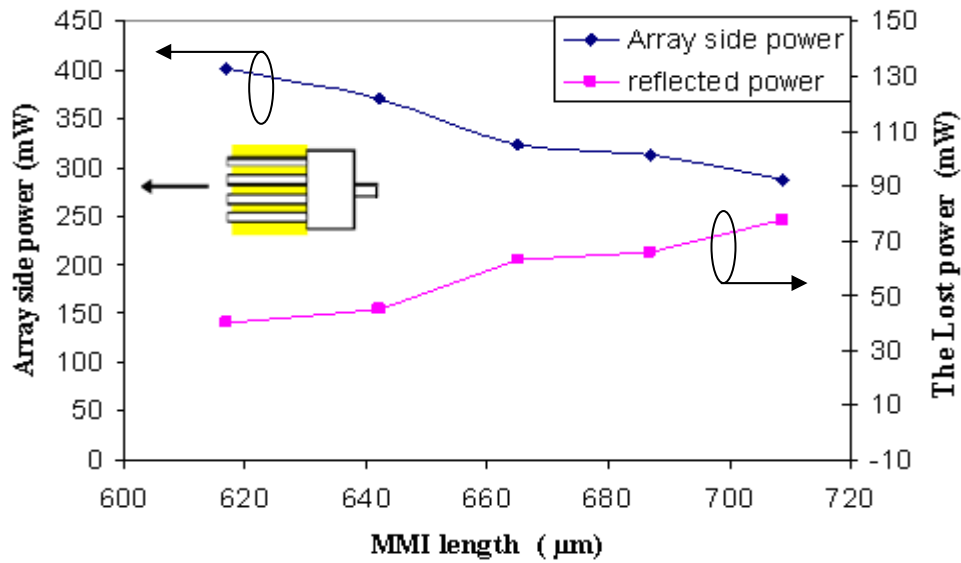


Figure: (6.15) Output power of 1x4 MMI array lasers with different MMI lengths for 3 A pulsed current measured from the gain section side. From the simulation, the designed length of 617  $\mu\text{m}$  was in the range of optimum MMI lengths. The effect of mode mismatch and phase difference increased, as the MMI length deviation from optimum range increased.

#### 6.2.4 Far-field measurement and analysis of array side facets for 1x4 MMI array lasers

To confirm a form of supermode locking of the MMI array laser diode, far-field measurements were conducted for the array facets side of the device. The horizontal far field pattern was measured, as shown in figure (6.16). The measurement was performed from  $2 I_{\text{th}}$  to  $7 I_{\text{th}}$ . Inspection of the horizontal far-field pattern for the array facet shows that there is indeed strong phase locking of the supermode. This is evident from the narrow full width half maximum of  $2.1^\circ$  at  $2xI_{\text{th}}$ , when the current is increased to  $4.0 \times I_{\text{th}}$ , the horizontal far-field width did not increase and remained  $2.0^\circ$  at FWHM. As the current is increased further to  $7xI_{\text{th}}$ , the horizontal far field (HFF) at FWHM remained  $2.0^\circ$ . These results suggest that the phase locking is stable, whereby the high gain supermode is selected. What happens in this case suggests that the laser adjusts the gain and minimize the losses, which result from carrier density perturbations and the heating of the centre of the array (213). Thus, this enhances the selection of the supermode with the lowest threshold, so that phase locking occurs.

There is no evidence of emission in the double lobed pattern, which is always a result of the presence of a  $\pi$  phase shift between the neighbouring emitters. However, the increase in the side lobe intensity, as illustrated in figure (6.16)

is not an indication of reduced phase-locking, but represents an increase in the far-field emission angle of the constituent emitters. This increase in the far-field emission angle is due carrier induced lensing effects, like spatial hole burning. However, the phase locking is stable up to  $7xI_{th}$ , which means that the phase relationship between the emitters remains fixed. Moreover, the evidence of the strong phase locking for this particular device is confirmed by the measurement of the array spectra. The lasing spectra were measured from the four back facets side, as can be seen in figures (6.17) and figure (6.19).

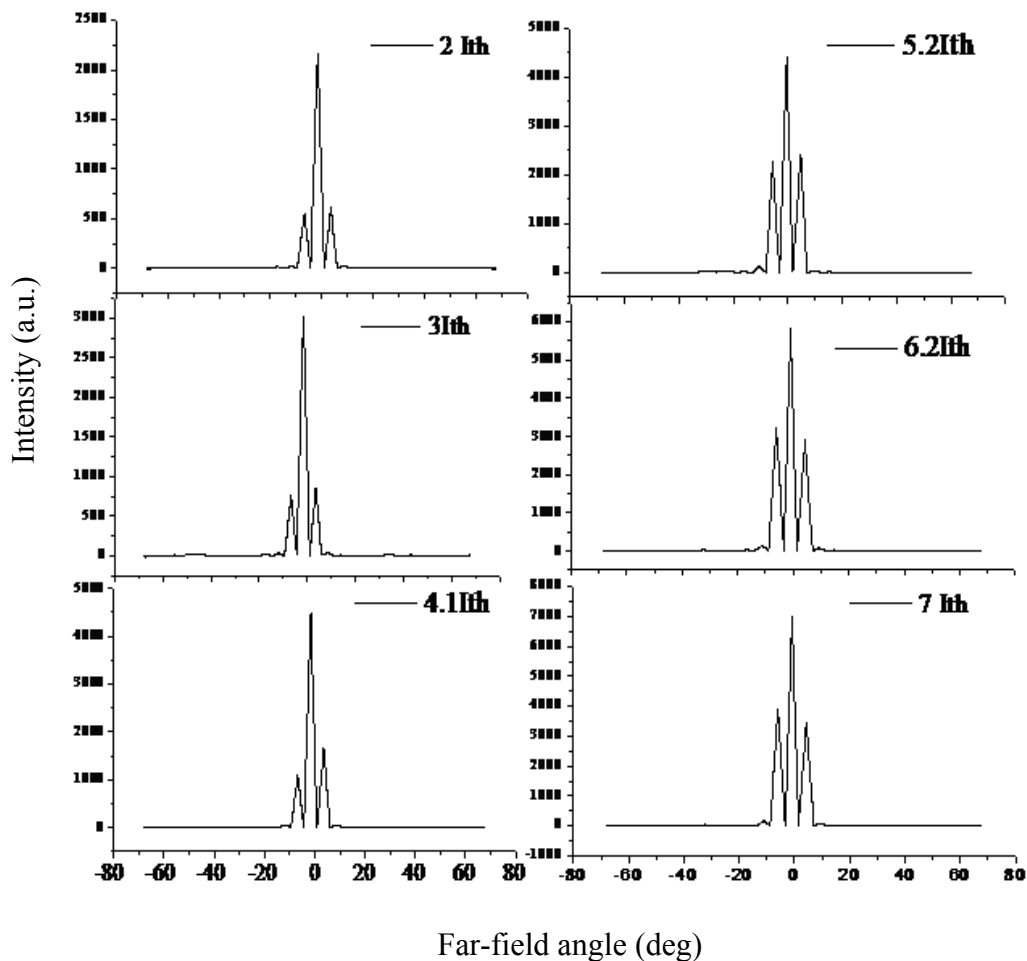


Figure: (6.16) Horizontal far-field pattern for a  $1 \times 4$  MMI array laser from the array side. The horizontal far-field pattern has been measured for  $2I_{th}$  up to  $7 I_{th}$ . The far-field pattern is a phase locked, which is very close to a diffraction limit of  $(\lambda/N.p)$  at the centre. The angular separation matches the pattern from a phase locked pattern. This angular separation equals to  $\lambda/p$ . In this example,  $N=4$ ,  $p= 6\mu\text{m}$ , the width of individual emitter is ( $2w = 2.5 \mu\text{m}$ ) and operating wavelength of  $0.822 \mu\text{m}$ .

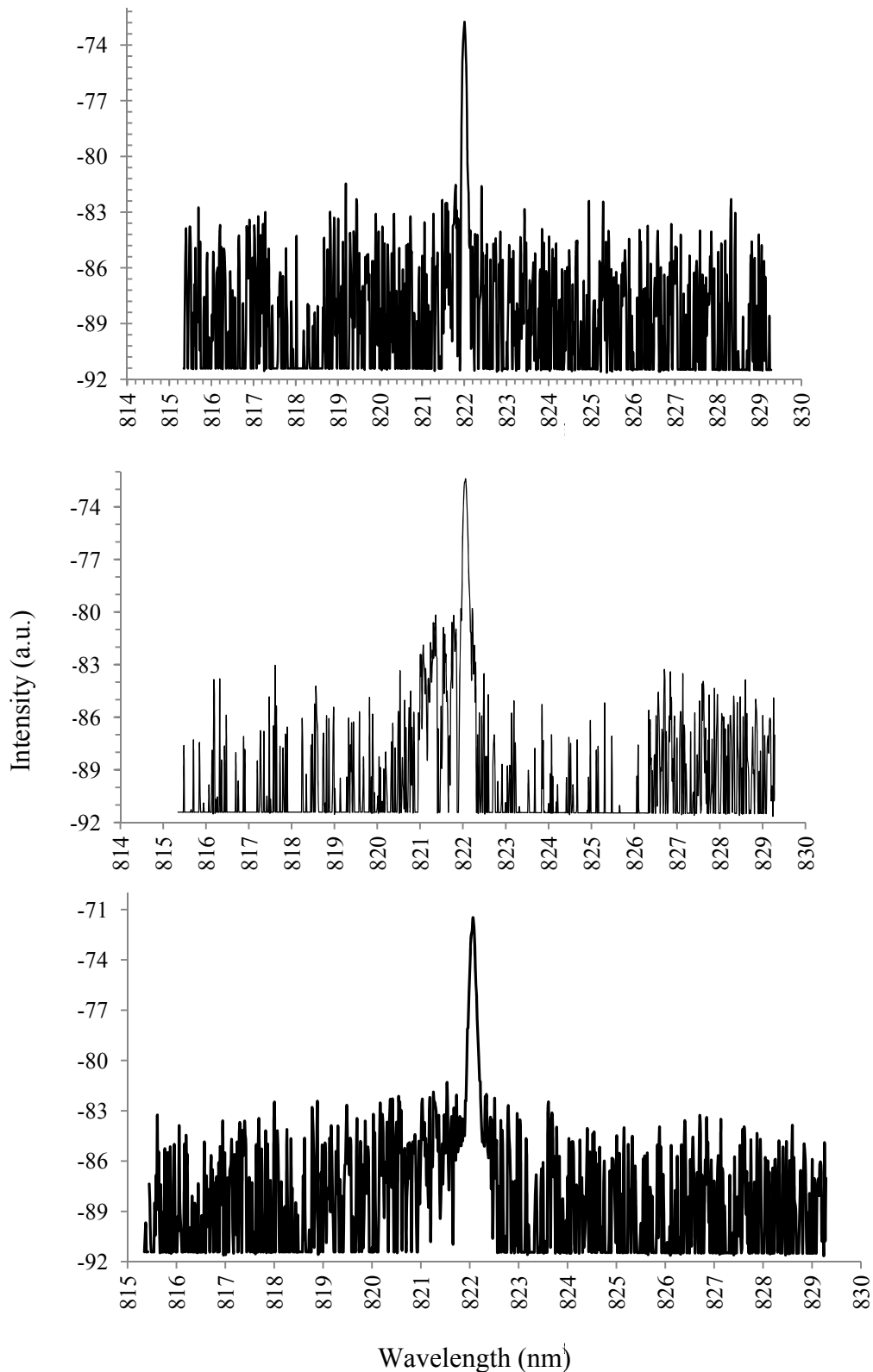


Figure 6.17: (a) The measured spectra from the back facet of a 1x4 MMI array laser show a single wavelength emission for an applied current of  $2xI_{th}$ . The peak wavelength is 822.0 nm and the spectral width ( $\Delta\lambda$ ) is 0.13nm at the FWHM. (b) The measured spectra from the back facet of a 1x4 MMI array laser show a single wavelength emission for an applied current of  $4xI_{th}$ . The peak wavelength is 822.04 nm and the spectral width ( $\Delta\lambda$ ) is 0.18nm at the FWHM. Figure (c) shows the measured spectra from the back facet of a 1x4 MMI array laser, whereby single wavelength emission is visible for a  $5.2xI_{th}$ . The peak wavelength is 822.09 nm and the spectral width ( $\Delta\lambda$ ) is 0.22nm at FWHM for an applied current of  $5.2xI_{th}$ . The power at  $5.2xI_{th}$  is 152 mW per facet.

The optical spectra measurements were conducted in a pulsed mode using 5  $\mu$ s pulse with a repetition rate of 1 kHz. In figure (6.17), a single wavelength emission is unambiguous, which is measured from the back facets of a 1x4 MMI array laser for an applied current of  $2xI_{th}$ . The peak wavelength is centred at 822.0 nm and the width at the FWHM ( $\Delta\lambda$ ) is 0.13 nm at the FWHM. It is clear that the device is phase locked, where the spectral width (FWHM) slightly increased to 0.22nm ( $\Delta\lambda \ll 1$ nm) for an applied current of a  $5.2xI_{th}$ . The peak emission wavelength shifted to 822.09 nm, whereas the power at  $5.2xI_{th}$  was 152 mW per facet. The single longitudinal mode can be explained by the fact that the array oscillation frequency is determined by strong coherent coupling between the array units rather than by the nonlinear effects for the single device (60, 214, 215). Other criteria were examined to validate the phase locking, as indicated in Chapter 2. The far-field FWHM of the phase locked pattern should be equivalent to the diffraction limited. The width of the central peak of the diffraction limited pattern is equivalent to  $(\lambda/N.p)$ . Furthermore, the angular separation of the side lobes for a phase locked pattern is equivalent to  $(\lambda/p)$ . The width of the central peak in the far field pattern in Figure (6.16) is 2.1°, which is slightly higher than the diffraction limited of (1.96 °) by a minute amount. The pattern is a 1.07 x diffraction limit. The other important parameter is the degree of coherence, which is measured by determining the visibility of the interference pattern. Recalling the visibility parameter using the equation from Chapter 2:

$$\text{The visibility (V)} = \frac{I_{max} - I_{min}}{I_{max} + I_{min}}$$

The visibility of the far field pattern is very close to unity, as seen from the figure (6.16). To verify that what is produced here is valid, careful inspection of the simulation using the BPM propagation tool shows a similar profile for the far-field. This is illustrated in figure (6.18) taken from Chapter 5. The width at FWHM of the horizontal far-field pattern is 2.5 ° in the simulation, which is very close to the measured value of 2.1 ° at FWHM. Furthermore, in the simulation of a 1x4 MMI array laser, as in figure (6.18) the visibility of the pattern is 0.8. This value of the visibility is actually lower than the experimental result, which is near unity. This higher visibility established in the experiment can be due to the strong cross coupling between the emitters and due to the gain competition favouring the coherent mode over that of the

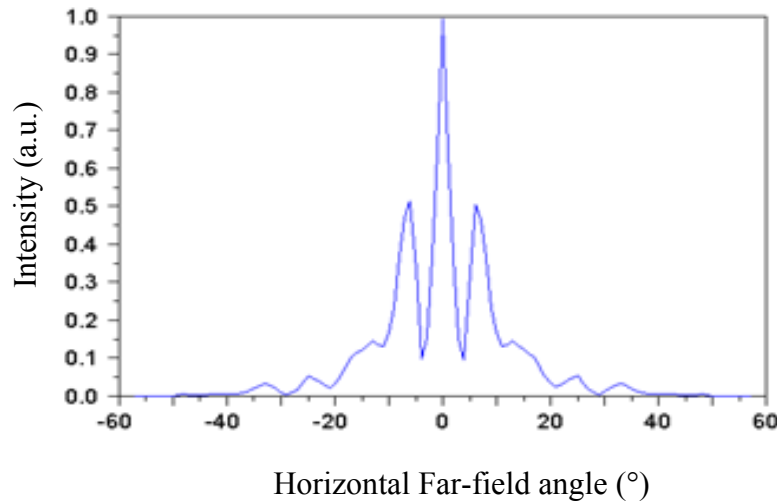


Figure: (6.18) Simulation of the horizontal far-field from the array facet side of a 1x4 MMI laser diode. A very similar pattern can be seen from the measurement in figure (6.15), which was measured from the array facet side. The far-field FWHM in this simulation is 2.5 degrees, which is very close to the measured value of 2.1 degrees. Overall, there is a good agreement between experiment and the simulation.

incoherent mode(s). The beam quality of the 1x4 MMI array laser array is very important for validating the phase locking operation. The beam quality for an emitter is estimated as indicated from Chapter 2:

$$M^2_{emitter} = \frac{2\Delta\theta}{\lambda/\pi w},$$

$M^2_{emitter}$  is the quality factor of the individual emitter,  $2\Delta\theta$  is the total width of the pattern at  $1/e^2$ , therefore quality factor for the emitter is easily found to be 1.

The beam equality for an array laser bar can be estimated from the following relation from Chapter 2:

$$M^2_{bar} = 2\delta\theta \frac{Np}{\lambda} = (2.1^\circ/1.96^\circ) = 1.07,$$

$M^2_{bar}$  is the quality factor of the bar,  $2\delta\theta$  is the total width of the central peak. This quantity can be considered as a quality factor for the bar. The width of the central peak is compared with the diffraction limit for the bar. The beam quality ( $M^2_{bar}$ ) was estimated to be 1.07. The brightness can also be estimated for the array laser bar, recalling the relation from Chapter 1:

$$B_{NDL} = \frac{P}{M_x^2 \cdot M_y^2 \cdot \lambda^2}$$

The  $B_{NDL}$  is the brightness of non-Gaussian beams. The brightness is estimated using the parameters, which are: power (P) at  $5.2 \times I_{th} = 152.0$  mW,  $M_x = 1.07$ ,  $M_y = 1$  and  $\lambda = 0.822$   $\mu\text{m}$  and the Brightness =  $19.60$  MW/cm<sup>2</sup>.sr

If we are to compare these results with single emitter with single mode spatial mode results, we see that Intense Ltd (1) has a single mode ridge waveguide laser with a power of 200 mW at an operating current of 250 mA, a brightness of 29 MW/cm<sup>2</sup>.sr and an  $M_{em}^2$  of 1.0. Some of the reported results are described in table (6.2) along with additional results are tabulated in section (2.8) from Chapter 2 of the thesis.

Device type	Power mW	Brightness MW/cm <sup>2</sup> .sr	Characteristics	Reference
1x4 MMI array, $\lambda = 0.822$ $\mu\text{m}$	152mW per Facet @ 754 mA	19.6	$M_{bar}^2 = 1.07$ $M_{emitter}^2 = 1.0$ Visibility (V)=1.0 $\Delta\lambda = 0.22$ nm	This work
Single Ridge waveguide $\lambda = 0.83$ $\mu\text{m}$ , width= 2 $\mu\text{m}$	200 mW@ 250 mA	29	$M_{em}^2 = 1.0$	Ref (1)
Single SCOWL width= 3 $\mu\text{m}$ , $\lambda = 0.83$ $\mu\text{m}$	1 W	100	$M_{em}^2 = 1.1$	Ref (100)

Table (6.2): The 1x4 MMI array laser characteristics compared with different single mode ridge waveguide examples. The beam characteristics are recorded.

When the optical spectra were measured for an injection current of  $6.2 \times I_{th}$ , four emission peaks become visible at  $\lambda_1 = 821.35$  nm,  $\lambda_2 = 821.59$  nm,  $\lambda_3 = 821.83$  nm and  $\lambda_4 = 822.08$  nm, respectively. These emission peaks correspond to the four individual lasers of the 1x4 MMI array laser. They started to emit independently at current of  $6.2 \times I_{th}$ . In this case, the phase locking is lost. The spectral separation is around 0.24 nm between the individual laser emission peaks. The width of the spectrum at FWHM of individual peaks is 0.22 nm. Such a very narrow spectral width for a phase locked semiconductor laser array is very problematic to stabilise without a

wavelength stabilisation technique. The wavelength stabilisation can be enhanced if a volume Bragg grating is used (63, 68).

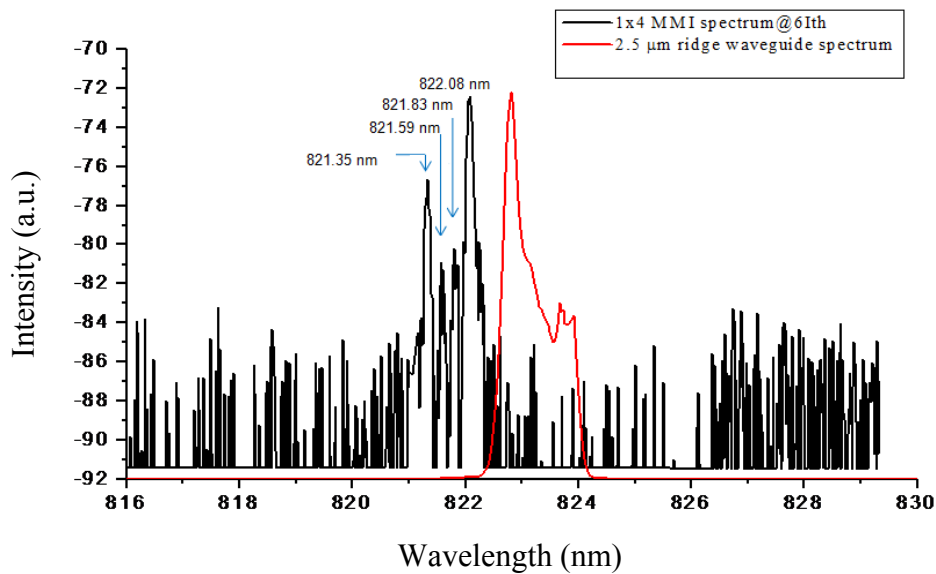


Figure 6.19 : (a) The measured spectrum from the back facet of 1x4 MMI array laser shows multiple wavelength emission for 6.2xIth. At this current, the phase locking is lost. An evidence of that is the four wavelength peaks, which are visible as follows:  $\lambda_1=821.35$  nm,  $\lambda_2=821.59$  nm,  $\lambda_3=821.83$  nm and  $\lambda_4=822.08$  nm, respectively. The  $\Delta\lambda$  width at FWHM is around 0.22 nm for the each of the individual peaks. (b) The spectrum in red colour represents the emission spectra for 2.5  $\mu\text{m}$  wide and 1000  $\mu\text{m}$  uncoated ridge waveguide laser. It was measured at 200 mA in pulsed mode of 5  $\mu\text{s}$  and a repetition rate of 1 KHz. The spectral width at FWHM is around 0.65 nm.

The emission spectrum from a 2.5  $\mu\text{m}$  ridge waveguide laser is also plotted for an applied current of 200 mA. It was measured in a pulsed mode of 5  $\mu\text{s}$  and 1 KHz repetition rate. In this particular example, the spectral width ( $\Delta\lambda$ ) of the ridge waveguide laser is 0.65 nm at the FWHM.

It is noteworthy that the different array modes give rise to a cluster of resonances for each longitudinal mode, which is a direct consequence of the different propagation constants. The wavelength separation between two neighbouring modes becomes larger with increasing mode order. More array modes emit simultaneously, as the current is increased and the array is no longer phase locked. This is illustrated in Figure (6.20), whereby the current is increased to 9xIth.

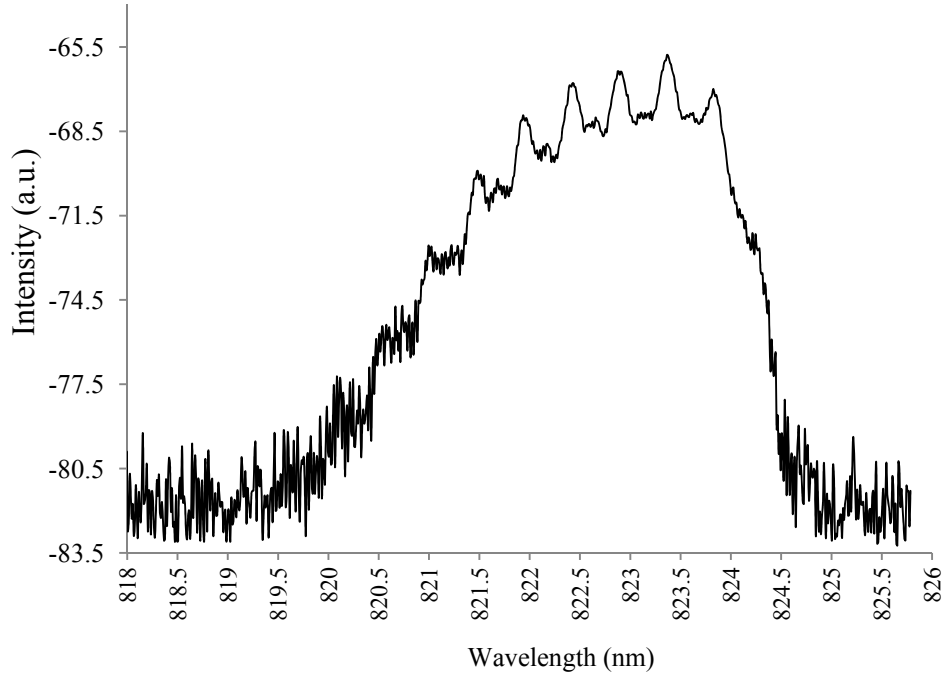


Figure 6.20: The measured spectrum from the back facet of 1x4 MMI array laser shows lasing spectra at 9xIth (Ith=145 mA). More array modes are visible with different wavelength separation between array modes. The phase locking is lost at this current level, whereby each mode consists of clusters of resonances.

The resonant wavelength separation between two neighbouring array modes  $i$  and  $i+1$  is much smaller than the Fabry-Perot longitudinal mode spacing. This is given by:

$$\Delta\lambda_{i,i+1} = \frac{\lambda^2 \cdot \Delta\beta_{i,i+1}}{2\pi n^*}$$

where  $\Delta\beta_{i,i+1}$  is the difference between the propagation constants of the two neighbouring array modes and  $n^*$  is the effective longitudinal mode index of the laser array, which is given by:

$$n^* = n - \lambda \frac{\partial n}{\partial \lambda}$$

The Fabry Perot mode spacing between adjacent longitudinal modes is found from the equation below:

$$\Delta\lambda_{FP} = \frac{\lambda^2}{2Ln^*} \quad ,$$

where  $\Delta\lambda_{FP}$  the FP longitudinal-mode spacing,  $L$  is the cavity length and  $\lambda$  is the operating wavelength. In Figure (6.20), the FP mode spacing is  $4.9 \text{ \AA}$ , while the resonant wavelength separation between two neighbouring array modes ( $\Delta\lambda_{i,i+1}$ ) is  $0.14 \text{ \AA}$ . This results in a  $\Delta\beta_{i,i+1}$  of  $9.87 \times 10^{-5}$ , which is the difference between the propagation constants of the two neighbouring array modes. Additional measurements for 1x4 MMI array lasers with an MMI

lengths of  $617 \mu\text{m}$  are found in Appendix A. The results shown include the far-field measurement from both facets and the lasing spectra.

The other observation that has been noticed from the back facet far-field is that the other devices showed different behaviour, as can be seen from figure (6.21). Inspection of figure (6.21) shows that the FWHM for  $1.7I_{\text{th}}$  is  $5.3^\circ$ , which remains stable up to  $4 I_{\text{th}}$  with a FWHM of  $5.8^\circ$ . The FWHM increases

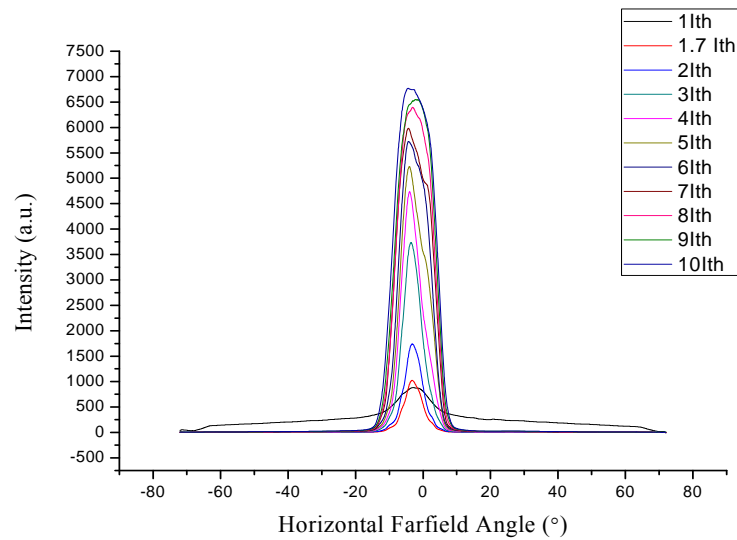


Figure: (6.21) Measurement of the horizontal far-field from the array facets side of a  $1 \times 4$  MMI laser diode for the optimum device with an MMI length of  $617 \mu\text{m}$

to  $9^\circ$  at  $7I_{\text{th}}$ . The reason for this behaviour is attributed to complete lack of phase locking. The far-field pattern in this case is consistent with the far-field pattern of individual emitter and there is absolutely no phase locking in this particular example. The spectral width at  $7 \times I_{\text{th}}$  is 4.6 times the diffraction limit. The broadening in the spectra can be explained that by the increase in the far-field of constituent emitters in the array due to spatial hole burning effects. The reason for emphasizing the phase locking is that, if phase locking is achieved, higher power devices with higher efficiency can be achieved. However, the  $1 \times 4$  array laser would always emit in single lateral mode because of the single mode output waveguide.

### 6.2.5 Far-field measurement and analysis of array side facets for $1 \times 4$ MMI Array lasers with non-optimised MMI lengths

In this section, a representative data for devices with MMI length that deviates from the optimum (i.e.  $>617 \mu\text{m}$ ) are presented. If we investigate the characteristics of the far-field profile for a device with an MMI section, which

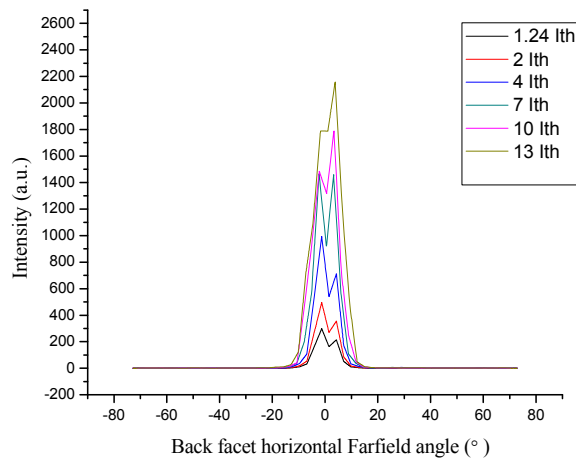


Figure: (6.22) Measurement from the horizontal far-field array facets side for a 1x4 MMI laser diode with an MMI length of  $665\mu\text{m}$ . The  $180^\circ$  out of phase is visible, which is the reason for the double lobed far-field. It is a typical example of an array laser where the elements operate in anti-phase.

is much longer than the optimum design ( $617\mu\text{m}$ ). Thus, the far-field was measured for the device with an MMI length of  $665\mu\text{m}$ . The results of this measurement are observed in figure (6.22). The  $180^\circ$  out of phase mode (double lobed far-field feature) is very prominent when measured from the array side. The double lobed far-field can be seen for drive currents ranging from  $1.24 I_{\text{th}}$  up to  $13 I_{\text{th}}$ , which is the typical double lobed pattern for an array laser, whereby the adjacent elements are operating in anti-phase. This means there is a large phase difference between the array emitters and it is always locked in the out of phase mode (i.e. a phase difference of  $180^\circ$ ). The comparison therefore is very clear between a phase locked device, as in figures (6.16) and the locked device in an anti-phase, as in figure (6.22), which has dominantly double lobed far field. It is noteworthy that this device is still susceptible to distortion of the far-field because of temperature rise at the junction and carrier induced lensing effect.

If we look at another example, all the dimensions are the same apart from the MMI length, which is  $644\mu\text{m}$ . The far-field was measured for the device with an MMI length of  $644\mu\text{m}$ . The results of this measurement are observed in figure (6.23). If we examine the far-field pattern, there is evidence of two fully unresolved lobes at about ( $7.8^\circ$ ) at  $2xI_{\text{th}}$ . These lobes are in agreement with angular side lobes separation of  $(\lambda/p)$ . The side lobes are still visible at  $5xI_{\text{th}}$ . The width of the central peak of the far-field pattern at  $2xI_{\text{th}}$  ( $I_{\text{th}} = 145\text{ mA}$ ) is

2.8 times the diffraction limit ( $\lambda/N.p$ ). In this case, the phase locking is imperfect with the broadening of the array pattern far-field due to an increase of the constituent emitter far-field. Moreover, the phase locking is affected by non-precise imaging at the output waveguide.

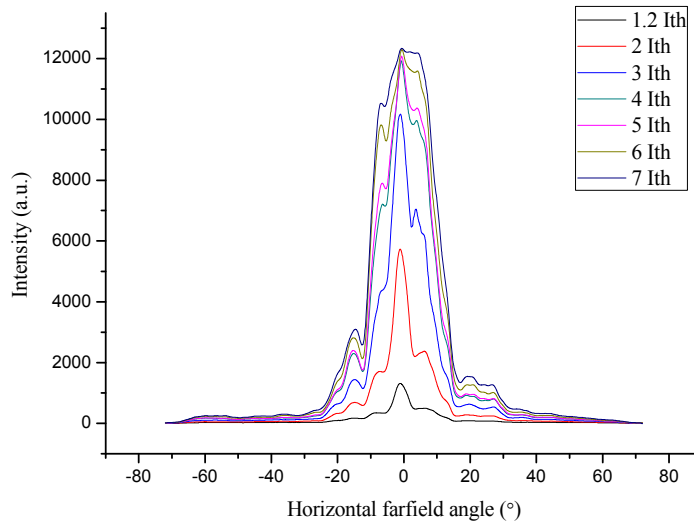


Figure: (6.23) Measurement from the horizontal far-field array facets side for a 1x4 MMI laser diode with an MMI length of 644 $\mu$ m. The fully unresolved side lobes are in agreement with angular side lobes separation of ( $\lambda/p$ ).

The emission spectra were measured for the 1x4 MMI array laser device with an MMI length of 644  $\mu$ m. It was tested in pulsed mode of 5  $\mu$ s width and a repetition rate of 1 KHz. Figure (6.24) shows the evolution of the optical spectra with respect to an increasing drive current for a 1x4 MMI array laser. It is measured from the array facets side for drive currents in the range of 1.4xIth to 4xIth. At a current of 1.4xIth, four wavelength peaks are visible as follows:  $\lambda_1=820.5$  nm,  $\lambda_2=820.8$  nm,  $\lambda_3=821.1$  nm and  $\lambda_4=821.31$  nm. These emission peaks corresponds to the four individual emitters of the array. At higher currents, the emission spectra were broadened. The broadening in the spectral can be explained by the increase in the far-field of constituent emitters in the array due to spatial hole burning effect, as we have seen previously. Different peaks appear due to the non linear effects. At a current of 4xIth, all the peaks merge into one single wide spectrum with a FWHM of around 2 nm. So, in this case the phase locking is absent.

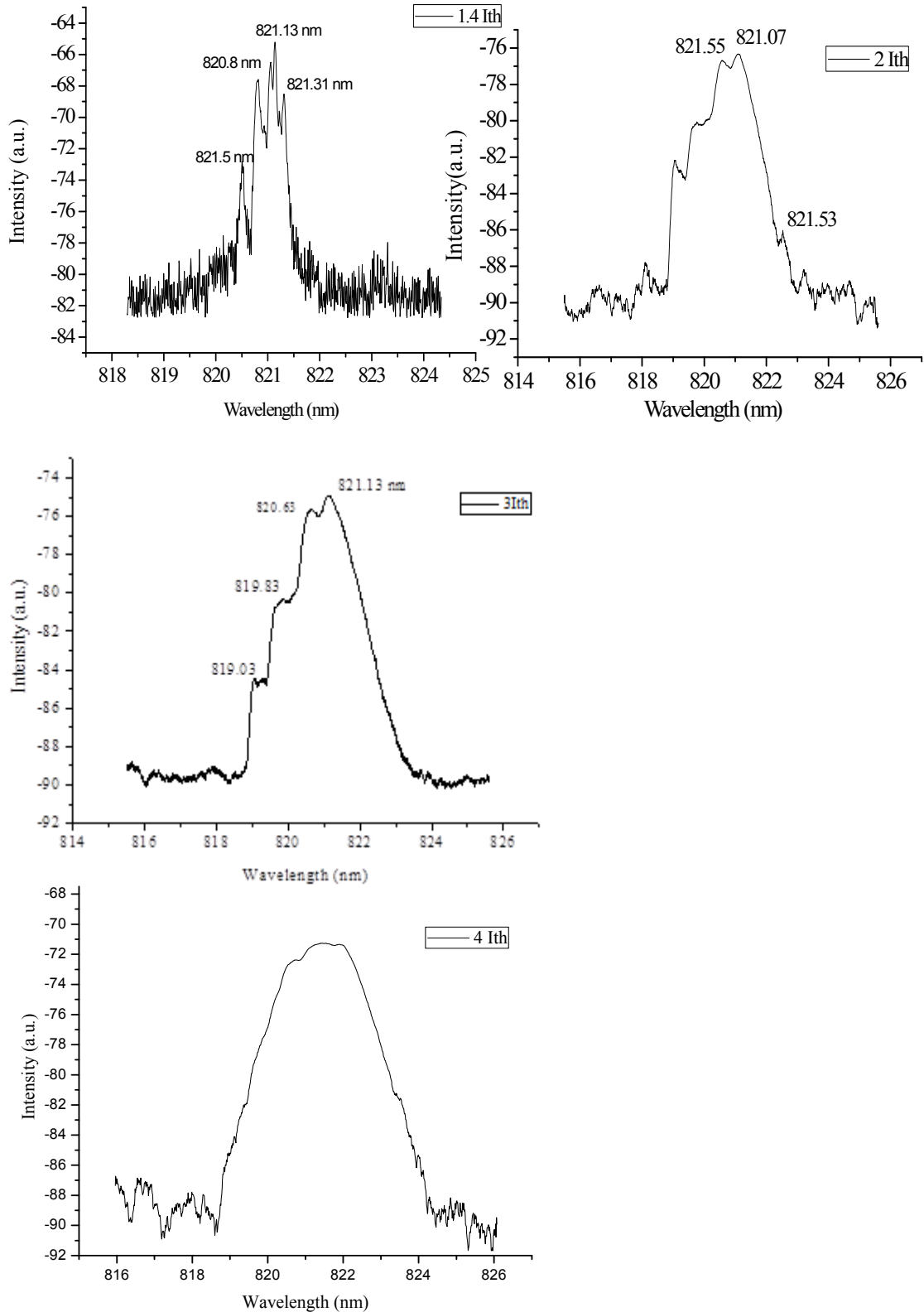


Figure (6.24) : (a)-(d) Evolution of the optical spectra with an increasing drive current from 1.4xIth to 4xIth for a 1x4 MMI array laser. The MMI length is 644  $\mu\text{m}$ . (a) The measured spectrum from the back facet of a 1x4 MMI array laser shows a multi-wavelength emission for a 1.4xIth. Four wavelength peaks are visible, which correspond to the four emitters as follows:  $\lambda_1=820.5$  nm,  $\lambda_2=820.8$  nm,  $\lambda_3=821.1$  nm and  $\lambda_4=821.31$  nm, respectively. In figures (b-d), the emission spectra broaden due to the spatial hole burning. The emission spectra were measured at a pulsed mode of 5  $\mu\text{s}$  width and a repetition rate of 1 KHz.

### 6.3 Further discussion and analysis

The motivation behind using array laser diodes to form a high brightness laser is because of the narrow far field that is obtained from a phase locked set of lasers. As explained in the literature review of this thesis, a series of designs were proposed. However, the solutions that have been provided have not been a great success. Every design has its own flaw and limitation. Firstly, using a conventional array of ridge index guided lasers results always in locking of the anti-phase mode. Secondly, a leaky wave concept worked to a certain level, but it was not practical due to complexity and cost. Thirdly, gain guided designs like coupled parabolic guided cavity suffer from filamentation. Lastly, devices integrated with Talbot cavities do offer phase locking to a limited power range, unless external cavities (62, 68, 70) are used, which adds more complexity. In this research work, we used an MMI coupler in a form of a 1xN combiner to maintain phase locked operation. Banjiri (216) conducted a theoretical comparison between an Nx1 coupled array laser and Talbot cavity designs, which predicted superior performance for the MMI coupled array laser over the Talbot array laser. The importance of Nx1 MMI array laser is that the output is always a single spatial mode, so single Gaussian beam is always achieved from the single mode passive waveguide.

The improved operating characteristics demonstrated by the results in this chapter for the Nx1 MMI array laser can be also attributed to the uniform coupling coefficients between the emitters. Those coupling coefficients are the criteria for how well the inter-element coupling occurs within the device. These coupling coefficients are uniform for a limited number of emitters. If the number of emitters is increased to eight, for example, the distant emitters do not couple at all. In this case, the loss of the locking mechanism is greater than for four emitters. The results obtained during this research are very interesting, as it is the first time that phase locking is observed. Lasing in a single wavelength emission was attained with a high degree of coherence. An evidence of this was the high visibility of the pattern of near unity. The overall power achieved in a single spatial mode was 152 mW per facet at 754 mA. The beam quality factor ( $M^2_{\text{bar}}$ ) was 1.07 for the whole array, while the brightness was 19.60 MW/cm<sup>2</sup>.sr. The optical spectra of the array confirmed single wavelength emission with a narrow spectral width ( $\Delta\lambda$ ) of 0.22 nm and

a central peak wavelength of a 0.822  $\mu\text{m}$  at an operating current of 5.2 Ith, although with limited power of 152 mW per facet. But, the maximum power achieved was over 440 mW per facet. Therefore, the power here is much higher than that from a single ridge uncoated waveguide laser. As seen in section (6.2.2), the slope efficiency was 0.24 W/A.

Other integrated devices have been fabricated during this research. For example, the devices that have been fabricated to reduce the problem of the reflections were made similar to the present design, but tapering has been used. Tapering the interface between the gain sections and the MMI improves device operation and may reduce reflections (217-219). Although the devices did not function properly due to another problem with the fabrication process, the threshold current obtained for the 1x4 MMI array laser diode was around 75.0 mA. This is much lower than the threshold for the devices reported in section 6.2.2, which the threshold was 145 mA. The majority of the fabricated 1x4 and 1x2 MMI tapered laser devices suffered COMD immediately after the test and the other remaining devices did not function due to the unsuccessful QWI process for this particular batch. The reason for that (as indicated in the Chapter 4) is the QWI process repeatability problem. Moreover, other problems

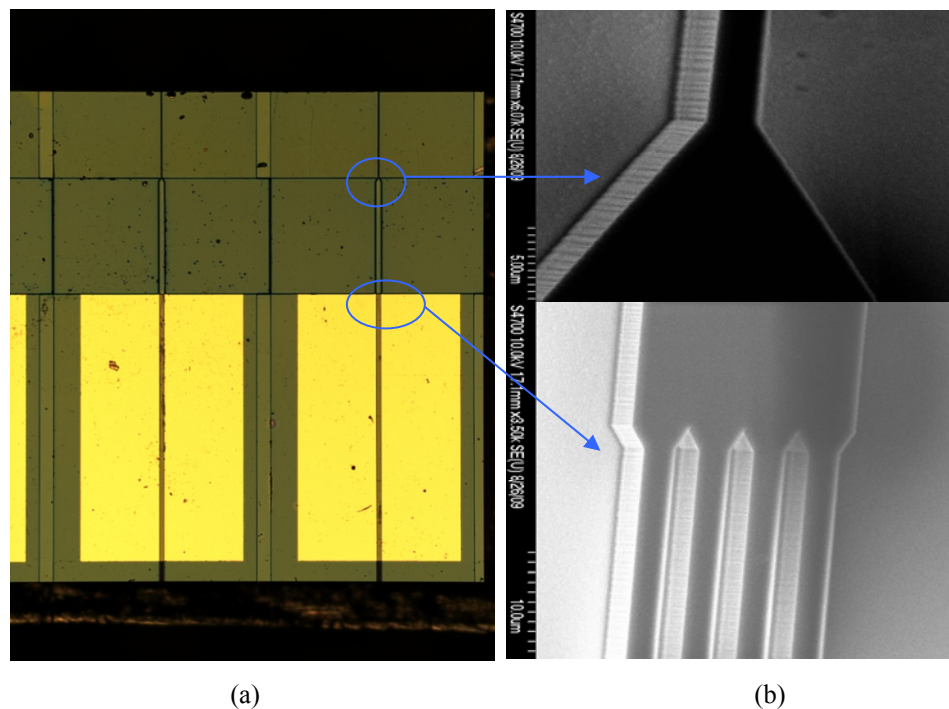


Figure: (6.25) a) Optical microscope image for a 1x4 tapered array MMI, which shows two complete devices comprising the NAM, gain section, tapered MMI and output waveguide. b) SEM images for the interfaces between the gain section and the MMI and the MMI with the output waveguide. The MMI is deeply etched although it is not shown in this particular SEM image.

occurred during the fabrication of this batch, such as sputtering machine contamination issues. The cross contamination of the process originates from the frequent use of the sputtering machine for the deposition of various metals like (Au, Cu, SiO<sub>2</sub>, Ti, Ni, Al, Pt, Ge).

The unsuccessful QWI process for this particular batch caused higher losses in the passive section, so that the devices did not function properly. This was confirmed by the higher threshold currents observed, especially when the length of the passive section of the devices was increased. The scanning electron microscopy images in figure (6.25) show two devices and their corresponding etch profile. The LI characteristics for the device can be seen in figure (6.26) for the device. It is worth indicating that with improved tapered sections at the interfaces; the device had a shorter MMI with compared with the device in section 6.2.2. The length of the MMI is designed shorter because the MMI width in these devices was 22  $\mu\text{m}$ . The spacing between the emitters was set at 3  $\mu\text{m}$  from the edge of one waveguide to the edge of next waveguide. However, the results here were not as hoped for, due to processing problems at the time when this batch of devices was fabricated. If the work conducted during this research is compared with what is reported in literature, we can see that similar devices were reported by Camacho (1998) (3). They used

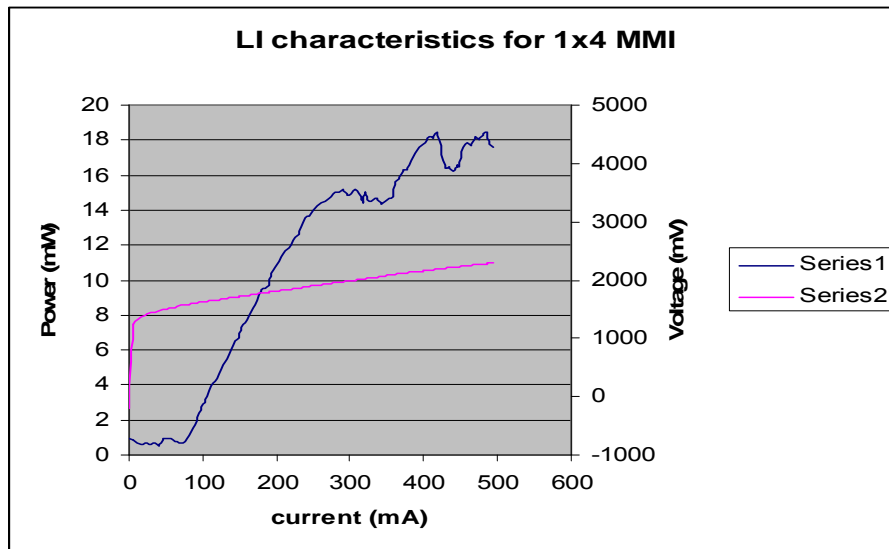


Figure: (6.26) Light current characteristic for 1x4 tapered array MMI laser. NAM length 75  $\mu\text{m}$ , 975  $\mu\text{m}$  gain section, MMI length 440  $\mu\text{m}$ , width 22  $\mu\text{m}$ , the separation distance between gain sections is 3  $\mu\text{m}$  and output waveguide is 325  $\mu\text{m}$ . The angle of the taper was set at 31°, which was designed wider than the divergence angle of the laser to reduce any possibility of reflections.

a 1x4 MMI device and achieved a maximum power of 180 mW, but no evidence of phase locking was observed. The emitter separation was 2.5  $\mu\text{m}$  and the ridge waveguides were shallowly etched, which suggests more coupling. However, this does not mean uniform coupling across the array. This means that the device did not operate to good level, which was seen in the low slope efficiency achieved of 0.10 W/A, although the device was stable. The problems with Camacho's device were firstly due to the fact that the MMI was shallowly etched. A shallow etched MMI has a poor imaging quality, due to the reduced number of modes inside the MMI. The MMI in this case will be longer, which increases the passive length of the devices. Thus, the actual output power is reduced. Thus, a reduction in the power and the slope efficiency was observed. Other investigations into this type of device have focused on optimising the phase relationship between the individual emitters. Avrutin (1999) (220) suggested introducing a gentle bend in one of the emitters, which may adjust the phase by the virtue of changing the optical path length. The bend in the waveguides to adjust the phase has been reported by (116), where the device 1x2 and 1x3 active MMIs devices were fabricated using InGaAsP. The problem with the active MMI is that the refractive index changes with the carrier contribution, which affects the operation of the device. Using the bend for phase adjustment is possible. The phase adjustment occurring in the 1x4 MMI array described in section 6.2 is due to optimised lateral coupling. The optimised lateral coupling occurs in the MMI array laser device through two mechanisms. Firstly, there is an evanescent field coupling between the neighbouring emitters. The narrower the separation distance between the emitters, the stronger the lateral coupling. In this thesis, the maximum separation distance (measured from the edge of one waveguide to the next waveguide) used was 4.5  $\mu\text{m}$ . Secondly, the longitudinal and lateral coupling provided by the integrated MMI cavity through self-imaging must be stronger than the evanescent coupling between the neighbouring emitters. If a large separation distance was used, then that enforces using a very wide MMI. Therefore, wider MMI necessitates using a very long MMI, which could be a few millimetres long and this is impractical. The reader is referred to section 2.4.1.3 in Chapter 2, whereby a simulation example was presented for an MMI width of 50  $\mu\text{m}$  and a pitch of 12.46  $\mu\text{m}$

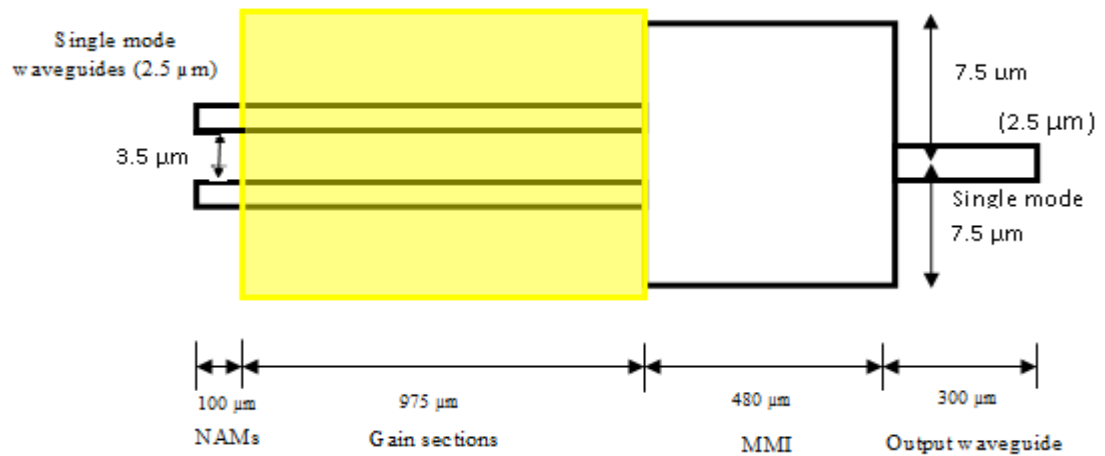
## 6.4 1x2 MMI array laser device

The device is similar to the 1x4 MMI array laser, but in this case two gain sections have been used. These devices were fabricated on the same chip as the 1x4 MMI array laser. Since the devices were on the same chip as the 1x4 MMI array laser, the quantum well intermixing shift was the same at 58 nm. The pumped area of the device consists of two single spatial mode ridge waveguides, where the etch depth has been kept at 1.84  $\mu\text{m}$  to maintain the single mode behaviour. The separation between the ridge waveguides was set at 3.5  $\mu\text{m}$  from the edge of a waveguide to edge of the adjacent waveguide. The dimensions of the MMI are a critical factor, where a single image is achieved at the output waveguide when a suitable MMI length is selected. In order to optimise the length of the MMI, a few lengths have been selected, namely 500  $\mu\text{m}$ , 480  $\mu\text{m}$ , 460, 440  $\mu\text{m}$  and 420  $\mu\text{m}$ . The design parameters are summarised in Table (6.2).

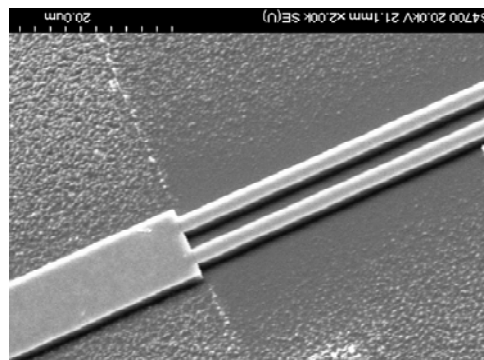
<b>Design Parameters for MMI 1x2 array laser</b>		
<b>NAM length</b>	75	$\mu\text{m}$
<b>Gain section length</b>	975	$\mu\text{m}$
<b>MMI length</b>	500,480,460,444, 420	$\mu\text{m}$
<b>MMI width</b>	15	$\mu\text{m}$
<b>Ridge width (Gain section width)</b>	2.5	$\mu\text{m}$
<b>Spacing</b>	3.5	$\mu\text{m}$
<b>Output waveguide length</b>	309	$\mu\text{m}$
<b>Output waveguide width</b>	2.5	$\mu\text{m}$

Table 6.2: Design Parameters for 1x2 MMI array laser diode

The best length will be where the highest power is achieved due to optimised imaging at the output waveguide. The length of the MMI is affected by the depth of the etched MMI. The schematic for the array laser device is shown in figure (6.27a) and an etched 1x2 MMI is seen in figure (6.27b). The length of the non-absorbing mirror (NAM) section is  $75\mu\text{m}$ . Although the length can be shortened to around  $30\mu\text{m}$ , the longer NAM simplifies the mechanical cleaving process. The NAM can be made very long between two adjacent devices, once that happened, the desired length of the cleave can be selected. So, the NAM length can be decided at the cleaving process. This makes it easier to cleave the devices accurately. The length of the gain sections was  $975\mu\text{m}$ . This length can be lengthened to increase the output power.



(a)



(b)

Figure 6.27: (a) Schematic for a 1x2 MMI array laser design. The MMI comprises of NAMs, gain section, MMI, and output waveguide. (b) Example of an etched 1x2 MMI array laser, which shows the ridge waveguides and the MMI.

The width of the MMI section is very critical, as seen from the simulations. A small deviation from the designed length during the fabrication can increase or decrease the true imaging length. The MMI is etched through the core for proper imaging quality and lower losses inside the MMI.

G. Walker (3, 16) worked on a 2x1 MMI array laser. The devices had a slope efficiency of around 0.05 W/A, which was due to inefficient lateral coupling between the gain sections. The devices made by (3) had a high threshold current of 250 mA, accompanied by a low slope efficiency and a very low power. Hence, the devices did not function at all. No phase locking was observed in the devices reported by (3). In this section, a demonstration of phase locking in a 1x2 MMI array laser is also provided. To the best of my knowledge this is the first time that the phase locking has been achieved using a monolithically integrated MMI laser cavity.

#### **6.4.1 Light current characteristics of 1x2 MMI array laser devices**

The devices were tested electrically at 25° C in pulsed mode using 10  $\mu$ s pulses and a 1 KHz repetition rate. The tests were performed on 1x2 array laser devices with parameters tabulated in Table 6.2 and corresponding schematic in figure (6.27a). The device was tested up to  $(30 \times I_{th})$  and there was no COMD. The maximum power achieved for the device was close to 332 mW per facet at  $(24 \times I_{th})$  in pulsed mode. The power was measured from the single output waveguide. The threshold current for the device was 85 mA. The threshold current per gain section was about 42.5 mA. The light current characteristics for this device can be seen in Figure (6.28). The device with an MMI length of 480  $\mu$ m was the best device in terms of the slope efficiency and performance. The slope efficiency was (0.25 W/A) and the external quantum efficiency was (33.0 %). The LI rolled over when tested at around  $(30 \times I_{th})$  as can be seen in figure (6.28). This is an indication that the quantum well intermixing was successful, so that no COMD was observed. Furthermore, the roll-over is due to increased heating at high injection currents.

If we compare the performance of this device to that of the 1x4 MMI array laser, we see that the slope efficiency is slightly higher and the amount of power achieved per gain section is much higher and exactly is (total power/2),

which is equivalent to 166 mW. The power per gain section for the 1x4 MMI array laser is 110 mW per gain section. The maximum wall plug efficiency attained for a 1x2 MMI array laser was higher than that for a 1x4 MMI array laser. In figure (6.9), the maximum computed WPE for a 1x4 MMI array laser measured from the single output waveguide side was about 9.6 % for an injection current of 900 mA, while the maximum WPE for a 1x2 MMI array laser

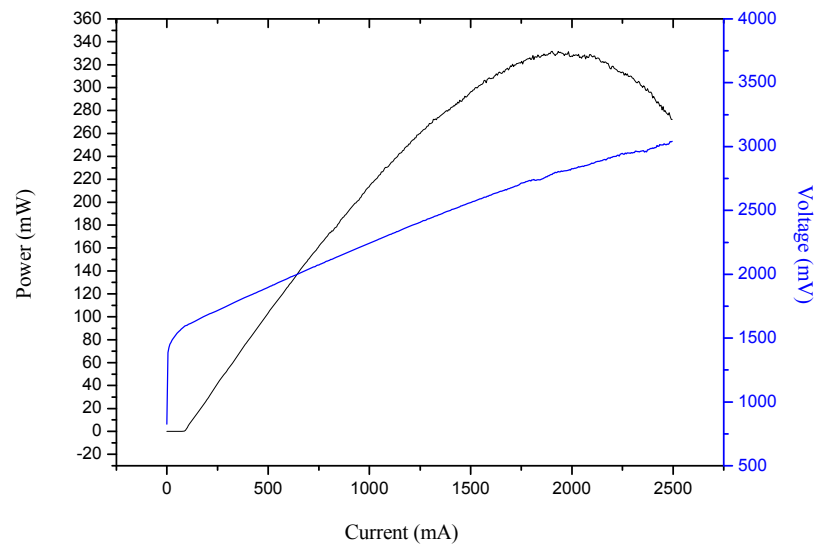


Figure: (6.28) Front facet light current/voltage (LIV) test results for the 1x2 MMI array laser. Devices tested pulsed up to  $(30 \times I_{th})$ . The MMI length was  $(480 \mu\text{m})$ , the gain section length was  $(975 \mu\text{m})$ , the NAM length was  $(75 \mu\text{m})$  and output waveguide length  $(325 \mu\text{m})$ .

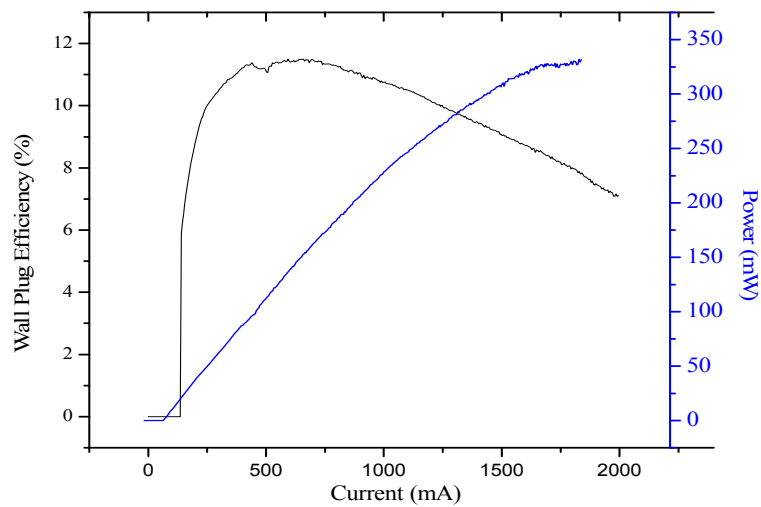


Figure (6.29) Wall plug efficiency (WPE) and output power vs. drive current for a 1x2 MMI array laser with MMI length of  $480\mu\text{m}$ . The power was measured from the single output waveguide side.

laser device was 11.5 % for a drive current of 618 mA, as can be observed from the figure (6.29).

The configuration for the 1x2 MMI array laser has a unique feature where no adjustment for the phase is required between the two gain sections because they have equal phases. This has been verified by simulation and the optical path length for them is the same. The 1x2 MMI array laser has less lateral coupling than the 1x4 MMI array laser due to reduced number of coupled gain

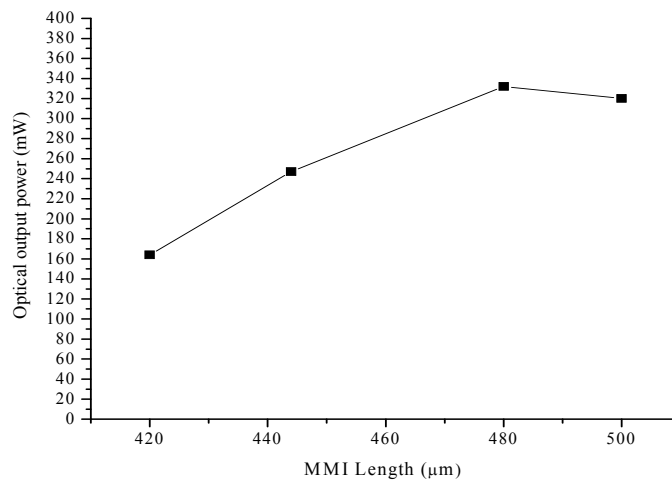


Figure (6.30) Maximum power values measured at 2.0 A current for devices with different MMI length. The devices with highest power had an MMI length of 480  $\mu\text{m}$ .

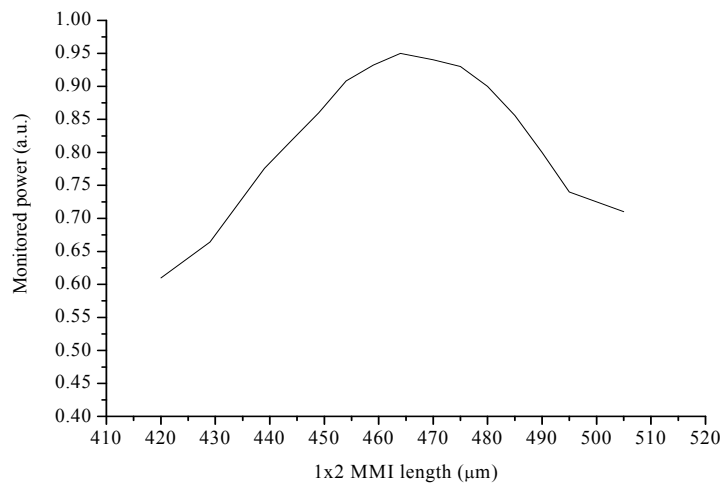


Figure (6.31) BPM simulation for 1x2 MMI array laser where an MMI length scan was performed using the following parameters: MMI length was 15  $\mu\text{m}$ , ridge waveguide width was 2.5  $\mu\text{m}$  the pitch was 3.5  $\mu\text{m}$  and the length of the MMI was varied. The range of the optimum lengths is between (456-482  $\mu\text{m}$ ). This is based on an optimum power value of (0.9 a.u.).

sections. As explained, if the imaging length is not accurate, higher losses can undermine the laser operation. Figure (6.30) shows the optical power measured from the single output waveguide for different MMI lengths. Inspection of the figure shows that the closer you approach the optimum imaging length, the higher the optimum power. Therefore, it is imperative to fabricate few different lengths of the MMI to map the optimum MMI dimension. This is verified by BPM simulations, where an MMI length scan was performed for a 1x2 MMI array laser, as shown in figure (6.31). The simulation predicts an optimum MMI range of (456 – 482  $\mu\text{m}$ ) for a power value of 0.9 (a.u.). The simulation is in good agreement with the results obtained from experiment represented by the figure (6.30).

If we examine the light current result obtained from the 1x2 MMI array laser with an MMI length of 420  $\mu\text{m}$ , as shown in figure (6.32), we see that the power is halved at about (164 mW) with a reduced slope efficiency of 0.15 W/A. This is due to the incorrect imaging length and phase as a result of poor imaging and mode mismatch at the output waveguide.

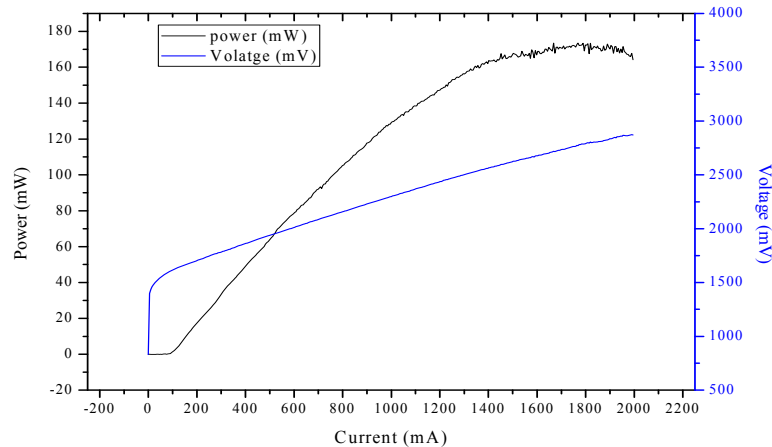


Figure: (6.32) Front facet light current/voltage (LIV) test results for a 1x2 MMI array laser. Devices tested pulsed up to ( $30 \times I_{th}$ ). The MMI length was (420  $\mu\text{m}$ ), gain section length was (975  $\mu\text{m}$ ), the NAM length was (75  $\mu\text{m}$ ) and output waveguide length was 325  $\mu\text{m}$ .

If we compare the MMI length for the best performing device with the simulation results, we see that there is a difference of around 15  $\mu\text{m}$  with simulated imaging length of 465  $\mu\text{m}$  (calculated simply from  $3L_{\pi}/2N$ ). This difference between the optimum MMI length and the one with highest performance is within the simulation range of (10-15)  $\mu\text{m}$  of best performing devices. In the BPM simulation in figure (6.31), this range of optimum MMI

lengths for maximum power is 456  $\mu\text{m}$ - 482  $\mu\text{m}$ . The modelling gives a prediction of the best parameters for the design. These parameters should be very close to the real practical values of the device. However, the difference of 15  $\mu\text{m}$  between the simulated imaging length of the MMI and the experimental value can be due to processing issues and the deviation of the width of the simulated MMI from the fabricated one. If we assume that the problem was because of the deviation of the MMI width, we can estimate that the fabricated width of the MMI was wider than the design by around 125 nm on both sides of the MMI. The 125 nm figure for the fabrication error was estimated as follows:

If the fabricated MMI width deviated from the design by 250 nm, so the width of the fabricated MMI was 15.25  $\mu\text{m}$  instead of 15  $\mu\text{m}$ . The optimum imaging length of a 1xN MMI structure is calculated using  $3L\pi/4N$ . In the case of the 1x2 MMI array, the 1x2 MMI coupler is two image point position. This is located at MMI length of  $3\frac{L\pi}{4N}$ , where N=2 and  $L\pi$  can be calculated from the equation below:

$$L\pi \cong \frac{\pi}{B_0 - B_1} \cong \frac{4n_{eff}W_{mmi}^2}{3\lambda_0} .$$

To calculate  $L\pi$ , we have from the simulation  $n_{eff}=3.418$ ,  $W_{mmi}=15.25 \mu\text{m}$ ,  $\lambda_0=0.830$ , and therefore  $L\pi$  is estimated as follows:

$$L\pi = 4*3.418*(15.25)^2/3*0.83 = 1276.94 \mu\text{m}.$$

The optimum MMI length for two image positions for an MMI width ( $W_{mmi}$ ) of 15.25  $\mu\text{m}$  equals  $3\frac{L\pi}{4N}$ . Therefore, MMI length equals  $(3*1270.22/4*2)$ , which is 478.84  $\mu\text{m}$ . This calculated MMI length of 478.84  $\mu\text{m}$  is a very close to the best performing 1x2 MMI laser device with an MMI length of 480  $\mu\text{m}$ .

If the width of the MMI ( $W_{mmi}$ ) is 15  $\mu\text{m}$  (i.e. fabricated length is identical to simulated MMI length) and all the other parameters have the same values, then, the MMI length is calculated as follows:

The MMI length for two image positions for an MMI width of 15  $\mu\text{m}$  equals  $3\frac{L\pi}{4N}$ .  $L\pi$  is calculated as follows:

$$L\pi \cong \frac{\pi}{B_0 - B_1} \cong \frac{4n_{eff}W_{mmi}^2}{3\lambda_0} = 4*3.418*(15.00)^2/3*0.83 = 1235.42 \mu\text{m}.$$

The optimum MMI length for an MMI width ( $W_{\text{mmi}}$ ) of  $15.00 \mu\text{m}$  equals  $3\frac{L\pi}{4N}$ . Therefore, MMI length equals  $(3*1228.91/4*2)$  which is  $463.28 \mu\text{m}$ .

The optimum MMI length of  $463.26 \mu\text{m}$  is very close to  $465 \mu\text{m}$ , which is the original value in the main simulation. This analysis assumes the deviation in the fabricated MMI width, but there could be deviations in the other parameters of the MMI array laser. There are other factors in this deviation of the imaging length, such as uniformity of the etch process. Furthermore, in the BPM simulation in figure (6.31), the range of optimum MMI length for maximum power is  $(456 \mu\text{m}- 482 \mu\text{m})$  for a power of 0.9 (a.u.). The  $1 \times 2$  MMI devices with maximum power had an MMI length of  $480 \mu\text{m}$ , which still lies within this range.

#### 6.4.2 Far-field analysis of array facets side for the $1 \times 2$ MMI array laser

In this section, we detail the measurement of the far-field characteristics of the  $1 \times 2$  array lasers. The far-field was measured using the same method used for the  $1 \times 4$  MMI array laser. In these devices, the separation between the ridge waveguides is  $3.5 \mu\text{m}$ , which is critical. The coupling that is provided by the MMI section would strengthen the overall coupling for the global cavity. To study the phase locking behaviour, a far-field scan of the back facet can be seen in figure (6.33). The inspection of the horizontal far-field pattern of the back facets (array side) of the figure shows single lobed far-field behaviour up to  $300 \text{ mA}$  ( $3.1 I_{\text{th}}$ ). The far-field at FWHM is  $7.6^\circ$ . When the current is increased to  $7.0 I_{\text{th}}$ , a single peak is still observed. The device stayed at the  $7.6^\circ$ .

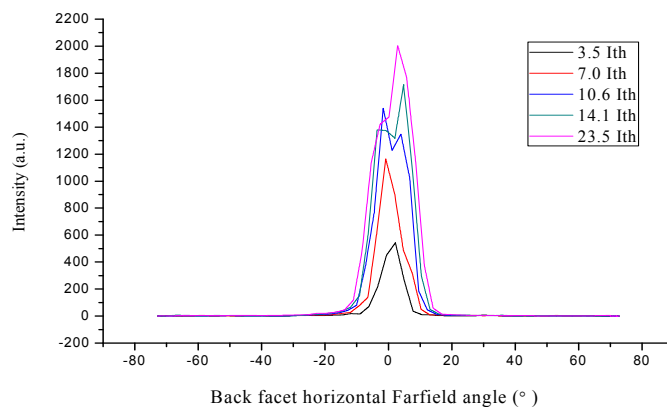


Figure (6.33): Horizontal far-field pattern from a  $1 \times 2$  MMI array laser measured from the array side (back) facets.

The width of the far-field at FWHM is broad, which resembles the far field of a single emitter. However, there is an overlap between the far-field of the two emitters. However, this far-field pattern is broad and it is 2.25 times the diffraction limit of  $(\lambda/N.p)$ . This suggests that the two gain sections are not phase locked. There is a contribution from the free running mode; this is affected by the difference in intensities of the two lasers due to the common contact. The common contact does not guarantee equal injection of the current applied to the device. Furthermore, heating effects appear, which cause the far-field to be even broader at currents of  $(10 \times I_{th})$ .

To corroborate a form of phase locking of the 1x2 MMI array laser diode, far-field measurements were conducted from the array facets side for additional devices with the same MMI length of  $480 \mu\text{m}$ . The horizontal far-field pattern was measured, as shown in figure (6.34). The measurement was performed from  $3.2 I_{th}$  CW to  $21.0 I_{th}$  CW. The horizontal far-field pattern of the array facets demonstrates that there is a degree of phase locking of the 1x2 MMI array. However, as explained in Chapter 2 different criteria are required to validate the phase locking of an array of lasers. The far-field pattern for a current value of  $(3.2 \times I_{th})$  ( $I_{th} = 85 \text{ mA}$ ) is re-plotted in figure (6.35) along with the simulation of the 1x2 MMI array taken from Chapter 5. In figure 6.35,

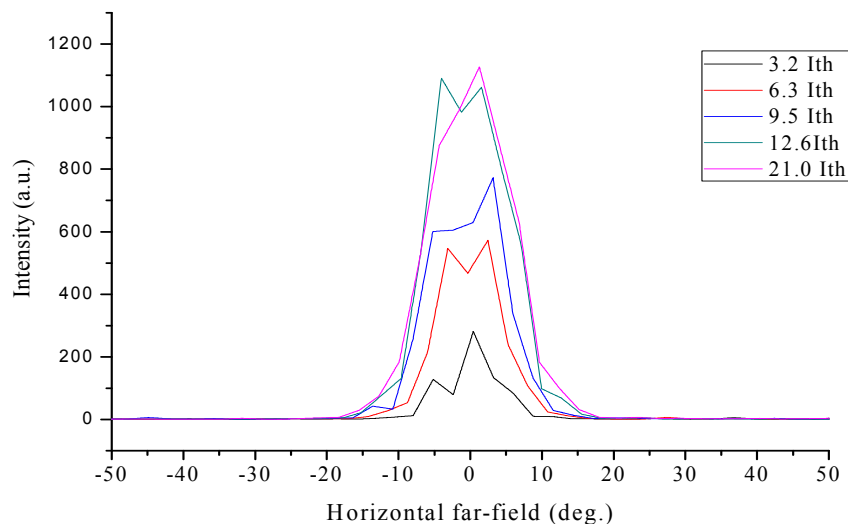


Figure (6.34): Horizontal far-field pattern for a 1x2 MMI array laser measured from the array side (back) facets. The MMI length for this device was  $480 \mu\text{m}$ . The far-field pattern was measured for a current injection of  $3.2 \times I_{th}$  to  $21.0 \times I_{th}$  in CW mode. The threshold current ( $I_{th}$ ) for 1x2 MMI array laser was  $85 \text{ mA}$ .

there is a reasonable correlation between the far-field pattern from the measurement and the far-field pattern from the simulation. The side lobes are identical except that one of the side lobes is hidden by the broadening of the pattern due to carrier induced lensing effect. Furthermore, the width of the central lobe was measured to be equivalent to  $1.3 \times (\lambda/Np)$ , where  $(\lambda/Np = 3.37^\circ)$ . This means that the measured far-field is  $1.3 \times$  diffraction limit. In Figure (6.34), it is evident that the far-field pattern broadened at injection currents higher than  $3.2 \times I_{th}$  due to spatial hole burning and lensing effects. This means that the phase locking was lost at current higher than  $3.2 \times I_{th}$  for  $1 \times 2$  MMI array laser. The quality factors for the array can be estimated.

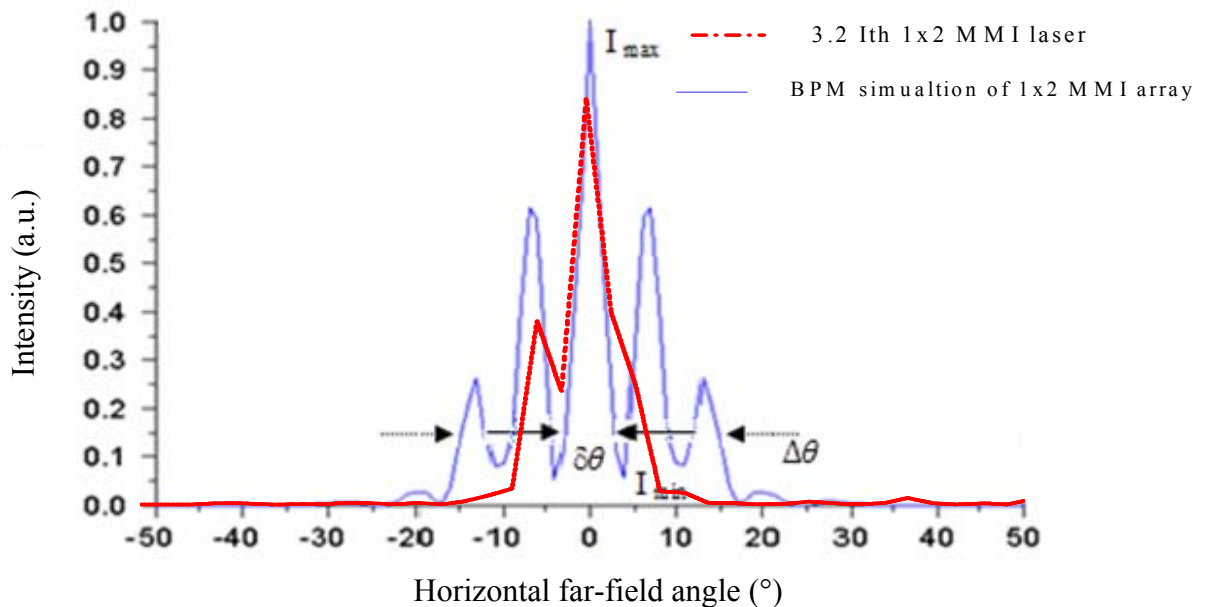


Figure (6.35): Dotted graph in red shows the horizontal far-field pattern for a  $1 \times 2$  MMI array laser measured from the array side (back) facets for an injection current of  $3.2 \times I_{th}$  CW. The far-field pattern in blue colour show the simulation results for the  $1 \times 2$  MMI array taken from Chapter 5. The MMI length for this device was  $480 \mu\text{m}$ . The  $I_{th}$  for this  $1 \times 2$  MMI array laser was  $85 \text{ mA}$ .

The emitter quality factor ( $M^2_{\text{emitter}}$ ) is measured to be 1.0 and the array quality factor ( $M^2_{\text{bar}}$ ) is calculated to be 1.33. The visibility ( $V$ ) of the pattern in figure (6.35) can be easily estimated, which was around 0.5. The brightness can also be estimated to be  $5.02 \text{ (MW/ cm}^2 \cdot \text{sr)}$  for a modest power of  $60 \text{ mW}$  CW at  $3 \times I_{th}$ . This phase locking is validated by the optical spectrum measured from single waveguide side. In figure (6.36), the optical spectrum for a  $1 \times 2$  MMI array laser diode is measured for different injection currents for an MMI

length of 480  $\mu\text{m}$ . The emission spectrum broadens and clearly shifts to a longer wavelength due higher current injection and operating temperature. The typical value for wavelength shift with an increase in the junction temperature is 0.3 nm/ $^{\circ}\text{C}$  (221), so the broadening is expected at high currents injection. If we re-plot the spectrum for a current injection of  $3.2I_{\text{th}}$ , as in figure (6.37) below, it indicates clearly a single wavelength emission with a peak of 823.55 nm and a very narrow spectrum of 0.3 nm at the FWHM. The optical power at an injection current of  $3.2I_{\text{th}}$  was a mere 60 mW.

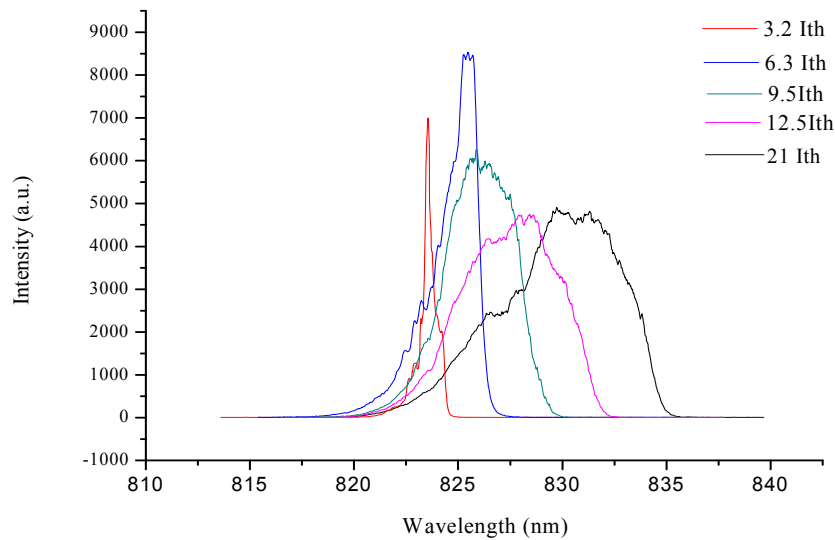


Figure (6.36) Measured optical spectra in CW mode from the single facet side for a 1x2 MMI array laser diode. The figure shows a very narrow spectrum of 0.3 nm at FWHM for an applied current of  $3.2I_{\text{th}}$ . The spectrum broadens to several nanometres at  $6.3I_{\text{th}}$ .

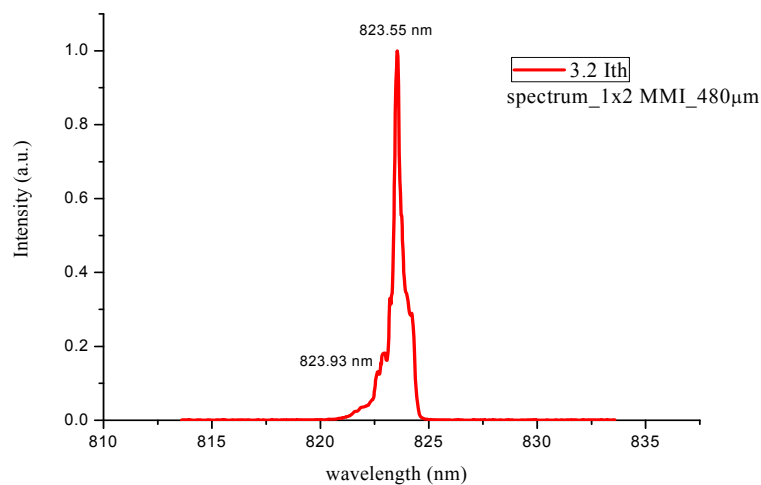


Figure (6.37) Optical spectra measured from the single facet side for a 1x2 MMI array laser diode. The length of the MMI was 480  $\mu\text{m}$ . The figure illustrates a very narrow spectral width ( $\Delta\lambda$ ) of 0.3 nm at the FWHM for an applied current of  $3.2I_{\text{th}}$  ( $I_{\text{th}}= 85 \text{ nm}$ ). The power at  $3.2I_{\text{th}}$  was around 60 mW per facet.

### 6.4.3 MMI operation effect on the phase locking and correlation with optical spectra.

The phase locking in a 1xN MMI array laser diode is induced by two mechanisms. Firstly, the lateral coupling between the constituent emitters through the evanescent interaction of propagating fields. Secondly, the longitudinal cross coupling provided by the MMI cavity through the self imaging phenomenon. The MMI cross coupling induces stronger phase locking than evanescent coupling when the waveguide gap is above 2.5  $\mu\text{m}$ . If we explore the 1x2 MMI array laser device, as in the figure (6.38) below; the phase locking region of the device is located at the interface between the MMI and the single output waveguide.

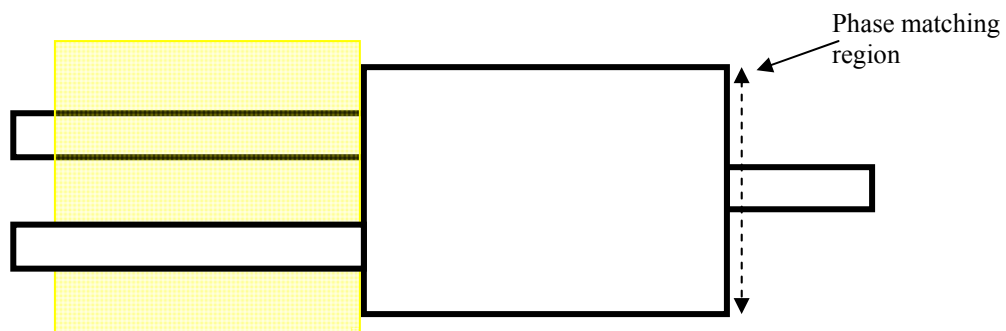


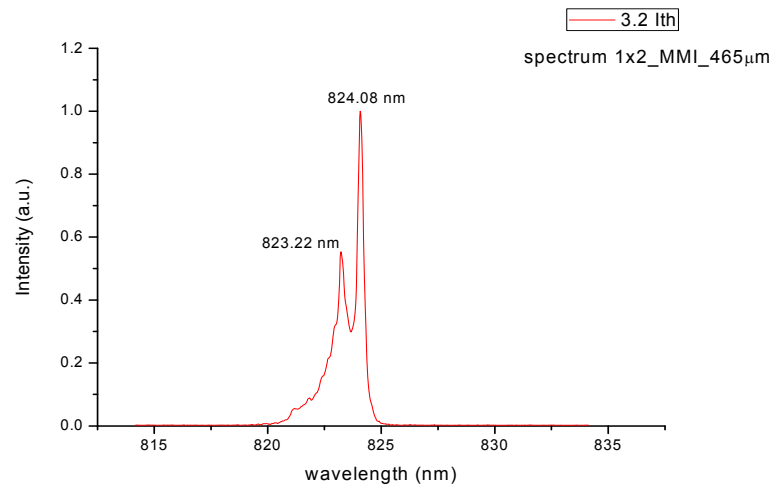
Figure (6.38) A schematic for 1x2 MMI array laser, which shows the phase matching region.

This phase locking region is very important, where single self-image field is coupled into the single output waveguide. Therefore, the length of the MMI must be optimised to achieve phase locking.

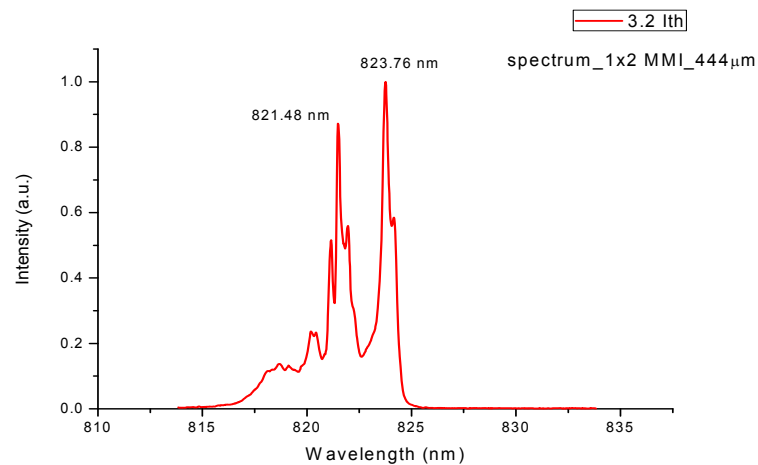
In figure (6.37) and (6.39a,b), the optical spectra of 1x2 MMI array lasers are illustrated for three different MMI lengths, 480  $\mu\text{m}$ , 465  $\mu\text{m}$  and 444  $\mu\text{m}$ . The spectral width for the 1x2 MMI array laser device was 0.3 nm at FWHM and the central peak wavelength was 823.55 nm for an injection current of ( $3.2 \times I_{\text{th}} = 272 \text{ mA}$ ). The device had an MMI length of 480  $\mu\text{m}$  and it happened to be the best performing device in terms of phase locking and the overall power. The device clearly emits in a single mode, as seen from the figure (6.37). This is the design with accurate phase matching at the output waveguide.

If the MMI length was deviated from this optimum value, the phase locking is not sustainable due to the phase mismatch of the self-image at the output waveguide. The MMI device with a length of 465  $\mu\text{m}$  had two clear oscillating

modes:  $\lambda_1 = 824.08$  nm and  $\lambda_2 = 823.22$  nm with a  $\Delta\lambda$  of 0.86 nm, as indicated in figure (6.39a). As the MMI length was varied much further to a length of 444  $\mu\text{m}$ , we see that there are few modes oscillating due to higher difference in the phase matching. Thus, the FWHM for the spectrum was 3.1 nm, as shown in figure (6.39b).



(a)



(b)

Figure (6.39): (a) Spectra of a 1x2 MMI array laser measured at 3.2xIth in CW mode. The device length was 465  $\mu\text{m}$ . Two modes are oscillating one at 824.08 nm and the other mode at 823.22 nm with a spectral width ( $\Delta\lambda$ ) of 0.86 nm at FWHM. (b) Spectra of a 1x2 MMI array laser measured at 3.2xIth CW. Device length was 444  $\mu\text{m}$ . It is clearly two modes are oscillating one at 823.76 nm and the other mode at 821.48 nm with spectral width ( $\Delta\lambda$ ) of 3.1 nm at the FWHM. There are cluster of resonances for each oscillating mode. In these two examples, there is no phase locking.

In Figure (6.40), the spectral bandwidth is plotted for 1x2 MMI array laser devices with different MMI length. The spectral width ( $\Delta\lambda$ ) was enlarged with a reduction of the MMI length. Once the MMI length deviates from the optimum value, the coherence of the pattern is lost due un-optimised self-imaging.

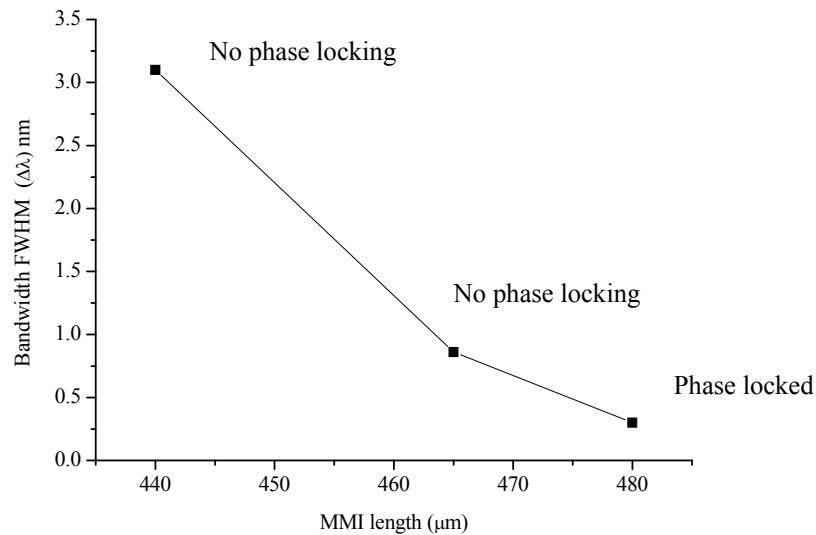


Figure (6.40): The spectral bandwidth versus MMI cavity length for a 1x2 MMI array laser devices. Phase locking was achieved for the device with optimum self imaging with the accurate phase matching region, which was the device with a 480  $\mu\text{m}$ .

The phase locking in these devices is much weaker than that for the 1x4 MMI array lasers- even though the phase difference is equal for the 1x2 MMI array laser configurations. The reason for this is that less efficient lateral coupling exists in the two gain section laser. It could also be the case that the 1x4 MMI array laser introduces a higher losses for the free-running modes of the individual array lasers. Therefore, the overall coupling in the 1x2 array laser device is much weaker. Although the phase is equal initially in the two gain sections, this phase is not guaranteed to remain the same when high injection currents are applied, which reduces the effective index steps at the gain sections.

# Chapter 7

## Conclusions and Future Work

This Chapter presents a summary of the research work presented in this thesis and also provides some suggestions for future work. This thesis was mainly focused on the design, fabrication and characterisation of monolithically integrated 1xN MMI array lasers diode in GaAs/AlGaAs material system for an increased brightness and performance using quantum well intermixing. To do this, a lot of work, including the development of RIE process, the QWI process, fabrication of a wide range of devices, such as low loss waveguides, NAMs, broad area lasers, TLMs, MMI coupler combiners, ridge waveguide lasers, monolithically integrated tapered/standard 1x2 MMI array laser diode, monolithically integrated tapered/standard 1x4 MMI array laser diode, was been carried out. The conclusions of this study are summarised below:

- 1) The development of reactive ion etching process to facilitate the fabrication of various devices. Etching profile of  $> 89^\circ$  was essential to obtain devices with low loss. Problems with micro-masking were studied and solved with reduced dry etching damage. The fluorocarbon polymer formation using  $\text{CHF}_3$  at the hard mask etching stage, (prior to ridge waveguide etch using  $\text{SiCl}_4$ ) was found to be responsible for the micro-masking issue in GaAs/AlGaAs.
- 2) The development of new quantum well intermixing process (QWI), which included technology development and transfer from Intense Ltd. The maximum band gap blue shift of 68 nm was realized for a Cu sputtering

time of 25 seconds and a thickness of 2-3 nm, 200 nm sputtered silica capped with 200 nm PECVD, annealing temperature of 825 ° C and annealing time of 90 seconds. However, this temperature was found to be high for non-intermixed quantum wells. Therefore, an annealing temperature of 810 ° C was used for 90 seconds, which resulted in a blue shift of 58 nm. The optical loss was measured to be as low as 4.48 dB/cm for an intermixed 830 nm passive ridge waveguide. This QWI shift was adequate for the fabrication of high brightness 1xN MMI array laser diode.

- 3) Broad area laser and ridge waveguide laser fabrication and characterisation for material evaluation purpose for use in the development of high brightness laser. Tests showed that the material loss for the high power structure was 1.59/cm, which was much less than the value of 18/cm for the standard laser. Uncoated ridge waveguide laser suffered COMD at around 98 mW. The ridge waveguide laser had a spectral width of a 0.65 nm at FWHM. This spectral width was measured for a current of 200 mA in pulsed mode with a 5 µs pulse width.
- 4) 1x2 integrated phase locked MMI array laser diodes have been modelled, designed, fabricated and tested. The phase locking has been successfully demonstrated in this type of devices with a degree of coherence with a visibility of 0.5. The 1x2 MMI array devices were tested in a pulsed mode up to  $30 \times I_{th}$ . The power was  $> 332$  mW from the single output waveguide and the corresponding slope efficiency was 0.25 W/A. Threshold current was 85 mA. The optical output power was 332 mW from the single output waveguide side. This power is equivalent to an optical intensity of  $11.06$  MW/cm<sup>2</sup> (for a mode area of  $1 \mu\text{m} \times 3 \mu\text{m} = 3.0 \mu\text{m}^2$ ). The result was best for an MMI length of 480 µm and a width of 15 µm. The phase locking was only evident up to  $3 \times I_{th}$  ( $I_{th} = 85$  mA). The width of the central lobe of the far-field pattern was 4.49 ° (equivalent to 1.33x the diffraction limit). The beam quality factor of the array (bar) ( $M_{bar}^2$ ) was estimated to be 1.33. There was some correlation between the far-field pattern from the measurement and the far-field pattern from the simulation. The side lobes are identical, but one of the side lobes is hidden by the broadening of the pattern due to the carrier induced lensing effect. The phase locking is validated by the lasing spectra measured from single waveguide side. The

lasing spectra showed a single wavelength emission with a peak of 823.55 nm and a very narrow spectral width of 0.3 nm at the FWHM for an MMI length of 480  $\mu\text{m}$ . The optical power at an injection current of  $3.2xI_{th}$  was a mere 60 mW per facet. The results for a 1x2 MMI laser array indicated that the length of the MMI section promoted the phase locking.

- 5) 1x4 monolithically integrated phase locked MMI array laser diodes have been modelled, designed, fabricated and tested. The phase locking has been successfully demonstrated in this type of devices with high degree of coherence with perfect visibility of unity and a brightness of 19.60 MW/cm<sup>2</sup>.sr. It was found that the correct design length of the self imaging structure (MMI) is of great importance for the phase locking process. Furthermore, the lateral coupling between the emitters was also important. Such level of lateral coupling was obtained through maintaining a pitch of 6  $\mu\text{m}$  between the emitters. The quality factor for the emitter ( $M^2_{emitter}$ ) was 1, whereas the beam quality factor of the bar ( $M^2_{bar}$ ) was estimated to be 1.07. The single emission wavelength was measured from the four array side with a narrow spectral width ( $\Delta\lambda$ ) of 0.22 nm at the FWHM for an operating current of  $5.2x I_{th}$ . The narrow spectral width of 0.22 nm for the array was a much smaller than that for a ridge waveguide laser.

An overall power of  $> 440$  mW per facet was achieved when measured from the single output waveguide in pulsed mode at current  $20I_{th}$ . There was no sign of COMD. The threshold current was 145 mA. The slope efficiency was 0.24 W/A and the external quantum efficiency was 32.1 %. The operating wavelength for a 1x4 MMI laser diode array was 0.822  $\mu\text{m}$ . The highest power was achieved for an MMI width of 24  $\mu\text{m}$ , length of 617  $\mu\text{m}$  and gain section spacing of 3.5  $\mu\text{m}$ . The power associated with this design was in good agreement with the results obtained from the BPM simulation.

To set these results into proper perspective, we note that it is the first time to the best of my knowledge that passive phase locking has been achieved using a monolithically integrated 1xN MMI array laser diode. Furthermore, the achieved brightness is comparable to the existing solutions, as illustrated in the table (7.1).

Device type	Power (mW)	Brightness MW/cm <sup>2</sup> . sr	Characteristics	Reference
1x4 MMI array, $\lambda=0.822 \mu\text{m}$	152mW per Facet @ 754 mA	19.6	$M^2_{\text{bar}}= 1.07$ $M^2_{\text{emitter}}= 1.0$ Visibility (V)=1.0 $\Delta\lambda=0.22 \text{ nm}$	This Work
Single Ridge waveguide $\lambda=0.83 \mu\text{m}$ , width= $2\mu\text{m}$	200 mW@ 250 mA	29	$M^2_{\text{emitter}} = 1.0$	Ref (1)
Single SCOWL width= $3\mu\text{m}$ , $\lambda=0.83 \mu\text{m}$	1 W	100	$M^2_{\text{emitter}} = 1.1$	Ref (100)
Talbot Tapered array N=10, p=100 $\mu\text{m}$ $\lambda=976 \text{ nm}$	0.8W @2.5 A	-----	$M^2_{\text{bar}} = 3$ Visibility (V)=0.7	Ref (68)

Table (7.1) The obtained results in this thesis compared with state of the art results for different diode laser configuration.

In this work, the brightness obtained from the uncoated facets was 19.6 MW/cm<sup>2</sup>.sr per facet compared to a brightness of 29 MW/cm<sup>2</sup>.sr from facet coated single ridge waveguide laser made by Intense ltd. (1). The brightness of a 100 MW/cm<sup>2</sup>.sr has been reported when a single SCOWL type laser is used (100) and overall power of 1 W. The beam quality ( $M^2_{\text{emitter}}$ ) in this case was 1.1. In an array form, a power of 0.8 W was reported (68) with a visibility of 0.7, however the beam quality ( $M^2_{\text{bar}}$ ) was 3.0, which is much worse than the results presented in this thesis.

- 6) Considerable modelling work was carried out, including the modelling of 1xN array laser diode using the beam propagation method. This proved very useful tool for predicting the far-field interference pattern for array of coupled emitters as well as design the integrated cavity through passive 3D simulation using BPM.
- 7) Producing functional devices in a form of high brightness 1xN phase locked MMI array requires that all of the modelling work, the design of the devices, QWI intermixing processes, etch processes, wet etching processes, metallisation processes, thinning processes, device mounting and complete device fabrication to be absolutely perfect. Therefore, the outcome was the significantly good results achieved in this thesis.

## 7.1 Future work

The future work in the context of the 1xN MMI array laser could include the following:

1. To further improve the brightness using a 1xN MMI array laser configuration, the number of emitters could be increased to 10 emitters for example. An effort could be made to design individually addressable laser emitters. This arrangement could make it easier to control the phase of each emitter, and hence produce the phase locking.
2. Introduce phase section change region by using current injection just before the MMI cavity. A slight injection current modification will result in a measurable change in the phase region.
3. Epitaxial structure design by increasing the  $d/\Gamma$  value, which should increase the maximum achievable power. All the other parameters need to be measured and controlled. For example, the threshold current, the number of quantum wells and optical confinement, all need to be optimized.

The other types of high brightness laser that can be a point of research are as follows:

1. Investigate a slab coupled optical waveguide laser (SCOWL) epitaxial structure for high power single mode operation. A slab coupled optical waveguide can be integrated with NAMs to increase the COMD level.
2. Design and investigation of optimized GaAs/AlGaAs epi-structures with higher the  $d/\Gamma$  and improve beam circularity. Using a considerably longer device could have the potential of increasing the optical output power without a large increase in the optical loss. Furthermore, a combined use of protective facet coatings and NAMs in high brightness lasers is another area that should be explored for improved COMD-free output power operation.
3. The Photonic band gap crystal waveguide is an emerging technology for high brightness laser, which could operate in very high power and have very low far-field output. This can be a very interesting subject for further development, as the technology is in its early stages.

# Bibliography

- [1] <http://www.intenseco.com/products/hpd/components/series6000.asp>
- [2] [http://www.eagleyard.com/uploads/tx\\_tdoproductstorage/EYP-RWL-0808-00800-4000-CMT04-0000.pdf](http://www.eagleyard.com/uploads/tx_tdoproductstorage/EYP-RWL-0808-00800-4000-CMT04-0000.pdf)
- [3] F. Camacho, C. J. Hamilton, K. McIlvaney, A. C. Bryce, and J. H. Marsh, "Laser structure for generating high optical power in a single mode waveguide," *Electronics Letters*, Vol. 34, 460-461, Mar 5 1998.
- [4] C. L. Walker, A. C. Bryce, and J. H. Marsh, "Monolithically integrated multi-mode interferometer array laser using defect induced quantum well intermixing," 2002 IEEE/LEOS Annual Meeting Conference Proceedings, Vols 1 and 2, 849-850,908, 2002.
- [5] <https://www.cvimellesgriot.com/Products/Documents/TechnicalGuide/Gaussian-Beam-Optics.pdf>
- [6] [http://www.rp-photonics.com/beam\\_divergence.html](http://www.rp-photonics.com/beam_divergence.html)
- [7] H. Wenzel, B. Sumpf, G. Erbert," High brightness diode lasers", *Comptes Rendus Physique*, Vol. 4, No. 6, 649–661, 2003.
- [8] E. Kapon, *Semiconductor Lasers II: Material and structures*. Optics and Photonics Series, Academic Press 1998.
- [9] N. Michel, WWW.BRIGHTER.EU, Recent Solutions for Higher Brightness Laser Sources Tutorial, February 2009.
- [10] John. H Marsh, ‘ Emerging Technologies for high power laser diodes’, *IEEE Photonic Society Newsletter*, 4-7, Dec, 2010.
- [11] S. P. Najda, J. H. Marsh, ‘Laser printing—Laser arrays transform printing’, *Nature Photonics*, Vol 1, No. 7, 387–389, 2007.
- [12] <http://www.lumics.com/Analysis-and-Sensing.364.0.html>.
- [13] INTERNATIONAL STANDARD ISO 11146 -1, “Lasers and laser-related equipment — Test methods for laser beam widths, divergence angles and beam propagation ratios”, 1<sup>st</sup> edition 2005.
- [14] Norman Hodgson and Horst Weber," Optical Resonators: Fundamentals, Advanced Concepts and Applications", (Springer Series in Optical Sciences), 1997.
- [15] Joseph W. Goodman, *Introduction to Fourier Optics*, Roberts and Company Publishers, Technology & Engineering , 2005.

- [16] R. N. Hall, R. O. Carlson, T. J. Soltys, G. E. Fenner, J. D. Kingsley, "Coherent light emission from GaAs junctions," *Physical Review Letters*, Vol. 9, No. 9 366-368, 1962.
- [17] M. I. Nathan, W. P. Dumke, G. Burns, F. H. Dill, G. Lasher, "Stimulated Emission of Radiation from GaAs P-N Junctions," *Applied Physics Letters*, Vol. 1, No.3, 62-64, 1962.
- [18] T. M. Quist, R. H. Rediker, R. J. Keyes, W. E. Krag, B. Lax, A. L. Mcwhorter, H. J. Zeigler, "Semiconductor maser of GaAs," *Applied Physics Letters*, Vol. 1, No. 4, 91-92, 1962.
- [19] D. F. Welch, "A brief history of high-power semiconductor lasers," *IEEE Journal of Selected Topics in Quantum Electronics*, Vol. 6, No. 6, 1470-1477, Nov-Dec 2000.
- [20] N. Holonyak, Jr., R. M. Kolbas, R. D. Dupuis, and P. D. Dapkus, "Quantum well heterostructure lasers," *IEEE Journal of Quantum Electronics*, Vol. QE-16, No. 2, 170-186, Feb 1980.
- [21] C. Weisbuch, "The Development of concept in light emitting devices," *Brazilian Journal of Physics*, Vol. 26, No. 1, 21-42, March 1996.
- [22] N. Chand, E. E. Becker, J. P. Van der Zeil, S. N. G. Chu, and N. K. Dutta, "Excellent uniformity and very low (less-than-50 A/cm<sup>2</sup>) threshold current-density strained InGaAs quantum-well diode-lasers on GaAs substrate," *Applied Physics Letters*, Vol. 58, No. 16, 1704-1706, Apr 22 1991.
- [23] G. P. Agrawal and N. K. Dutta. *Semiconductor Lasers*. New York: Van Nostrand Rienhold, 1993.
- [24] J. Wilson and J.F.B. Hawkes, *Optoelectronics: An Introduction*. Printice-Hall International Inc. , Third Edition, 1998.
- [25] R. Dingle and C. H. Henry, *Quantum effects in heterostructure lasers*. U.S. Patent 3982207, Sept. 1976.
- [26] J. P. Van der Ziel, R. Dingle, R. C. Miller, W. Wiegmann, and W. A. Nordland, "Laser oscillation from quantum states in very thin GaAs-Al<sub>0.2</sub>Ga<sub>0.8</sub>As multilayer structures," *Applied Physics Letters*, Vol. 26, No. 8, 463-465, 1975.
- [27] R. D. Dupuis, P. D. Dapkus, N. Holonyak, E. A. Rezek, and R. Chin, "Room-temperature laser operation of quantum-well Ga<sub>(1-x)</sub>Al<sub>x</sub>As-GaAs laser-diodes

- grown by metalorganic chemical vapor deposition,” *Applied Physics Letters*, Vol. 32, No. 5, 295–297, 1978.
- [28] W. T. Tsang, “Extremely low threshold (AlGa)As graded-index waveguide separate confinement heterostructure lasers grown by molecular beam epitaxy,” *Applied Physics Letters*, Vol. 40, No. 3, 217–219, 1982.
- [29] R. D. Dupuis and P. D. Dapkus, “Very low threshold Ga(1-x)AlxAs-GaAs double heterostructure lasers grown by metal organic chemical vapor deposition,” *Applied Physics Letters*, Vol. 32, No. 8, 473–475, 1978.
- [30] E. J. Thrush, P. R. Selway, and G. D. Henshall, “Metal organic C.V.D. growth of GaAs-GaAlAs double hetero-junction lasers having low interfacial recombination and low threshold current,” *Electronics Letters*, Vol. 15, No. 5, 156–158, 1979.
- [31] W. T. Tsang, “A graded-index waveguide separate-confinement laser with very low threshold and a narrow Gaussian beam,” *Applied Physics Letters*, Vol. 39, No. 2, 134–137, 1981.
- [32] U. Martin, “COMD Behaviour of Semiconductor Laser Diodes,” Annual Report 1999, Dept. of Optoelectronics, University of Ulm, 39-43, 1999.
- [33] J. W. Tomm, M. Ziegler, T. Elsaesser, H. E. Larsen, P. M. Petersen, P. E. Andersen, S. Clausen, U. Zeimer, D. Fendler, "Catastrophic optical mirror damage in diode lasers monitored during single pulse operation," *Novel in-Plane Semiconductor Lasers IX*, Vol. 7616, 328, 2010.
- [34] P. Collot, J. Arias, V. Mira, E. Vassilakis, F. Julien, "Non-absorbing mirrors for AlGaAs quantum well lasers by impurity-free inter-diffusion.," *In-Plane Semiconductor Lasers III*, Vol. 3628, 260-266, 1999.
- [35] M. Silver, O. P. Kowalski, I. Hutchinson, X. Liu, S. D. McDougall, J. H. Marsh, "Theoretical and experimental study of improved catastrophic optical damage performance in 830nm high power lasers with non-absorbing mirrors.," *2005 Conference on Lasers & Electro-Optics (CLEO)*, Vols 1-3, 414-416, 2005.
- [36] C. Lin, *Optoelectronic Technology and Lightwave Communication Systems*. Van Nostrand Reinhold, USA, 1989.
- [37] Carlos A. Barrios “ Gallium arsenide based Buried Heterostructure Laser Diodes with Aluminium-free Semi-Insulating materials Regrowth”, Doctoral

Thesis, Laboratory of Semiconductor Materials Department of Microelectronics and Information Technology Royal Institute of Technology Electrum 229, S-164 40,2002.

- [38] A. Yariv, Optical Electronics, Fourth Edition, Saunders College Publishing, 1991.
- [39] N. W. Carlson, Monolithic Diode-Laser Arrays. Berlin, Germany: Springer-Verlag, 1994.
- [40] Paul W.M. Blom, Pieter J. Van Hall, Jos E.M. Haverkort and Joachim H. Wolter, "Reduction of the threshold current in quantum well lasers by optimization of the carrier capture efficiency", Proceedings of SPIE, Vol. 1677, 130-139, 1992.
- [41] Paul W. M. Blom, Pieter J. Van Hall, Jos E.M. Haverkort and Joachim H. Wolter, "Carrier-carrier scattering induced capture in quantum well lasers", Applied Physics Letters, . 62, No. 13, 1490-1492, 1993.
- [42] Manuela Buda," Low-Confinement High-Power Semiconductor Lasers", PhD Thesis, Eindhoven Technical University, 1999.
- [43] M. Sanchez, P. Diaz, G. Torres, J.C. Gonzales," Influence of cavity length and emission wavelength on the characteristic temperature in AlGaAs lasers", Journal of Applied Physics, Vol. 77, No. 9, 4259-4262, 1995.
- [44] T. Takagi and K. Iga," Temperature dependence of GaAs/AlGaAs multi-quantum barrier lasers", IEEE Photonics Technology Letters, Vol. 4, No. 12, 1322-1324, 1992.
- [45] Teo Jin Wah Ronnie, "Study and development of advanced packaging technique for semiconductor lasers", Ph.D Thesis, Nanyang Technological University, 2007.
- [46] Y. Qu, S. Yuan,C. Yang Liu, B. Bo, G. Liu, and H. Jiang, "High-Power InAlGaAs/GaAs and AlGaAs/GaAs Semiconductor Laser Arrays Emitting at 808 nm", IEEE Photonic Technology Letters, Vol.16, No. 2, 389-391, 2004.
- [47] A. Larsson, S. Forouhar, J. Cody, R. J. Lang, " High-power operation of highly reliable narrow stripe pseudomorphic single quantum well lasers emitting at 980 nm", IEEE Photonic Technology Letters, Vol. 2, No. 5, 307-309, 1990.

- [48] O. J. F. Martin, "Thermal behaviour of visible AlGaInP-GaInP ridge laser diodes", *IEEE Journal of Quantum Electronics*, Vol. 28, No. 11, 2582-2588, 1992.
- [49] Xingsheng Liu, Martin Hai Hu, Hong Ky Nguyen, Catherine G. Caneau, Michael Heath Rasmussen, Ronald W. Davis, Jr., and Chung-En Zah, "Comparison between epi-down and epi-up bonded high-power single-mode 980-nm semiconductor lasers", *IEEE Transactions on Advanced Packaging*, Vol. 27, No. 4, 640-645, 2004.
- [50] V. Spagnolo, M. Troccoli, G. Scamarcio, C. Becker, G. Glastre, and C. Sirtori, "Thermal resistance and temperature characteristics of GaAs/Al<sub>0.33</sub>Ga<sub>0.67</sub>As quantum-cascade lasers", *Applied Physics Letters*, Vol. 78, 1177-1179, 2001.
- [51] M. Leers, C. Scholz, K. Boucke and M. Oudart, "Next generation heat sinks for high-power diode laser bars", *Proceedings of 23rd IEEE SEMI-THERM Symposium*, 105-111, 2007.
- [52] M. Leers, and K. Boucke, "Cooling approaches for high power diode laser bars", *Proceedings of 58th IEEE ECTC*, 1011-1016, 2008.
- [53] E. Kapon, *Semiconductor Lasers II: Material and structures*. Optics and Photonics Series, Academic Press 1998.
- [54] Joseph T. Verdeyen, *Laser Electronics*, Second Edition. Prentice-Hall International Editions, 1989.
- [55] J. K. Butler, D. E. Ackley, and D. Botez, "Coupled-mode analysis of phase-locked injection laser arrays", *Applied Physics Letters*, Vol. 44, 293-295, 1984.
- [56] Dan Botez, "Array-mode far-field patterns for phase-locked diode-laser arrays - Coupled-mode theory versus simple diffraction theory", *IEEE Journal of Quantum Electronics*, Vol. QE-21, No. 11, 1985.
- [57] Y. Twu, K. L. Chen, A. Dienes, S. Wang, J. R. Whinnery, "High-power coupled ridge waveguide semiconductor laser arrays" *Applied Physics Letters*, Vol. 45, No. 7, 709-711, 1984.
- [58] D. F. Welch, P. S. Cross, D. R. Scifres, W. Streifer, R. D. Burnham, "High-power (Cw) in-phase locked Y-coupled laser arrays," *Applied Physics Letters*, Vol. 49, No. 24, 1632-1634, 1986.

- [59] J. Katz, S. Margalit, A. Yariv, J. Katz, "Diffraction coupled phase-locked semiconductor-laser array," *Applied Physics Letters*, Vol. 42, No. 7, 554-556, 1983.
- [60] D. Botez and J.C.Conolly, "High-power phase-locked arrays of index-guided diode lasers," *Applied Physics Letters*, Vol. 43, No. 12, 1096-1098, 1983.
- [61] D. Masanotti and F. Causa, "Optical guiding properties of high-brightness parabolic bow-tie laser arrays," *IEEE Journal of Quantum Electronics*, Vol. 41, No. 7, 909-916, 2005.
- [62] I. Hassiaoui, N. Michel, G. Bourdet, R. McBride, M. Lecomte, O. Parillaud, M. Calligaro, M. Krakowski, and J. P. Huignard, "Very compact external cavity diffraction-coupled tapered laser diodes", *Applied Optics*, Vol. 47, No. 6, 746-750, 2008.
- [63] David Paboeuf, Gaëlle Lucas-Leclin, Patrick Georges, Nicolas Michel, Michel Krakowski, Jun Jun Lim, Slawomir Sujecki and Eric Larkins, "Wavelength-stabilized tapered laser diodes in an external Talbot cavity: simulations and experiments", *Photonics West - LASE 2009*, San Jose, (2009).
- [64] V. V. Apollonov, S. I. Derzhavin, V. I. Kislov, A. A. Kazakov, Y. P. Koval, V. V. Kuz'minov, D. A. Mashkovskii et A. M. Prokhorov, "Phase locking of eight wide aperture semiconductor laser diodes in one-dimensional and two-dimensional configurations in an external Talbot cavity", *Quantum Electronics*, Vol. 28, No. 4, 344-346, 1998.
- [65] C. J. Corcoran and K. A. Pasch, "Modal analysis of a self-Fourier laser cavity", *J. Opt. A: Pure Appl. Opt.* 7, (L1-L7). 2005.
- [66] J. R. Leger, G. J. Swanson et W. B. Veldkamp, "Coherent laser addition using binary phase gratings", *Applied Optics*, Vol. 26, No. 20, 4391-4399, 1987.
- [67] H. Dammann and K. Görtler, "High-efficiency in-line multiple imaging by means of multiple phase holograms", *Journal: Optics Communications - OPT COMMUN*, Vol. 3, No. 5, 312-315, 1971.
- [68] David Paboeuf, Deepak Vijayakumar, Ole Bjarlin Jensen, Birgitte Thestrup, Jun Lim, Slawomir Sujecki, Eric Larkins, Gaëlle Lucas-Leclin, and Patrick Georges, "Volume Bragg grating external cavities for the passive phase locking of high-brightness diode laser arrays: theoretical and experimental study", *JOSA B*, Vol. 28, Issue 5, 1289-1299, 2011.

- [69] R. H. Rediker, R. P. Schloss et L. J. Vanruyven, "Operation of individual diode-lasers as a coherent ensemble controlled by a spatial filter within an external cavity", *Applied Physics Letters* , Vol. 46, No. 2, 133-135, 1985.
- [70] C. J. Chang Hasnain, J. Berger, D. R. Scifres, W. Streifer, J. R. Whinnery and A. Dienes, "High-power with high-efficiency in a narrow single-lobed beam from a diode-laser array in an external cavity", *Applied Physics Letters* , Vol. 50, No. 21, 1465-1467, 1987.
- [71] [http://hal-iogs.archives-ouvertes.fr/docs/00/53/13/49/ANNEX/HPDLS09\\_LucasLeclin\\_Conference.pdf](http://hal-iogs.archives-ouvertes.fr/docs/00/53/13/49/ANNEX/HPDLS09_LucasLeclin_Conference.pdf)
- [72] Y. Twu, K. L. Chen, A. Dienes, S. Wang, J. R. Whinnery, "High-performance index-guided phase-locked semiconductor-laser arrays," *Electronics Letters*, Vol. 21, No. 8, 324-325, 1985.
- [73] E. Kapon, C. Lindsey, J. Katz, S. Margalit, A. Yariv, "Chirped arrays of diode-lasers for supermode control," *Applied Physics Letters*, Vol. 45, No. 3, 200-202, 1984.
- [74] J. S. Tsang, D. C. Liou, K. L. Tsai, H. R. Chen, C. M. Tsai, C. P. Lee, and F. Y. Juang ,” Fundamental mode operation of high power InGaAs/GaAs/AlGaAs laser arrays”, *Journal of Applied Physics*, Vol. 73, No. 9, 4706-4708, 1993.
- [75] C. P. Lindsey, E. Kapon, J. Katz, S. Margalit, and A. Yariv,” Single contact tailored gain phased array of semiconductor lasers”, *Applied Physics Letters*, Vol. 45, No.7, 722-724, 1984.
- [76] K. Hamamoto, E. Gini, C. Holtmann and H. Melchior, “Single transverse mode active multimode interferometer 1.45 $\mu$ m high power laser diode”. *Applied Physics B*, Vol. 73, No. 5-6, 571-574, 2001.
- [77] K. Hamamoto, K.Naniwae, M Ohya. “High power with low electric power consumption active multi-mode interferometer laser diode for fiber amplifier”. *Electronics Letters*, Vol. 38, No. 43, 517, 2002.
- [78] M. Ohya, K Naniwae, S. Sudo, T. Sasaki and K Hamamoto., “Over 1 W output power with low driving Voltage 14xx-nm pump laser diode using active multimode-interferometer, ”. *Electronics Letters*, Vol. 40, No. 17, 1063-1064, 2004.
- [79] D. Botez and L. J. Mawst, “ Phase locked laser arrays revisited,”. *IEEE Circuits and Devices*, Vol. 12, No. 6, 25-31, 1996.

- [80] J. M. Gray, J. H. Marsh and J. S. Roberts., "High-power anti-guided laser array fabricated using a superlattice structure," *Electronics Letters*, Vol. 30, No. 24, 2040-2041, Nov 24 1994.
- [81] J. M. Gray, J. H. Marsh and J. S. Roberts., "High-power anti-guided laser array fabricated without the need for overgrowth," *IEEE Photonics Technology Letters*, Vol. 10, No. 3, 328-330, Mar 1998.
- [82] D. F. Welch, P. Cross, D. Scifres, W. Streifer, R. D. Burnham, "In-phase emission from index guided laser arrays up to 400 mW", *Electronics Letters*, Vol. 22, No.6 293-294, 1986.
- [83] D. Botez, L. Mawst, T. J. Roth, P. Hayashida and G. Peterson, "Two solutions that achieve high-Power (>200 mW) diffraction-limited-beam, array Operation: 1) out of-phase coupled positive index guides, and 2) closely spaced antiguides", *Conference Digest 11th IEEE ISLC Paper B1*, 18-19, Boston, MA, Aug./Sept. 1988.
- [84] J. Z. Wilcox., W. W. Simmons., D. Botez, M. Jansen., L. J. Mawst., "Design considerations for diffraction coupled arrays with monolithically integrated self-imaging cavities", *Applied Physics Letters*, Vol. 54, No. 19, 1848-1850, 1989.
- [85] J. Katz, S. Margalit, A. Yariv, J. Katz, "Diffraction coupled phase-locked semiconductor-laser array," *Applied Physics Letters*, Vol. 42, No. 7, 554-556, 1983.
- [86] M. Jansen, S. S. Ou, J. J. Yang, J. Wilcox, M. Sergant, L. Eaton and W. Simmons, "Large optical cavity (LOC) semiconductor laser arrays," *Electronics Letters*, Vol. 22, No. 20, 1083-1084, 1986.
- [87] D. Yanson, S.D. McDougall, B. Qiu, V. Loyo-Maldonado, G. Bacchin; S. Robertson; S. Bon; J. Marsh., "High-power laser arrays with 100% fill factor emission facet - art. No. 69091B," *Proceedings of SPIE, Novel in-Plane Semiconductor Lasers VII*, B9091-B9091, 2008.
- [88] Robin K. Huang, Leo J. Missaggia, Joseph P. Donnelly, Christopher T. Harris, George W. Turner, Anish K. Goyal, Tso Yee Fan, and Antonio Sanchez-Rubio," High-brightness wavelength beam combined semiconductor laser diode arrays", *IEEE Photonics Technology Letters*, Vol. 19, No. 4, 209-211, 2007.

- [89] W. Kosonock and R. H. Cornely, "GaAs laser amplifiers," *IEEE Journal of Quantum Electronics*, Vol. 4, No. 4, 125-131, 1968.
- [90] K. Kishino, Y. Suematsu, K. Utaka, H. Kawanishi., "Monolithic integration of laser and amplifier / detector by twin-guide structure", *Japanese Journal of Applied Physics*, Vol. 17, No. 3, 589-590, 1978.
- [91] R. Parke, D. Welch, A. Hardy, R. Lang, D. Mehuys, S. O'Brien, K. Dzurko, and D. Scifres, "2 W CW, diffraction-limited operation of a monolithically-integrated master oscillator power amplifier," *IEEE Photonics Technology Letters*, Vol. 5, No. 3, 297-300, 1993.
- [92] R. M. Lammert, E. Ungar, J M. L. Osowski, H. Qi, M. A. Newkirk, N. Bar Chaim, "980-nm master oscillator power amplifiers with non-absorbing mirrors," *IEEE Photonics Technology Letters*, Vol. 11, No. 9, 1099-1101, Sep 1999.
- [93] H. Wenzel, K. Paschke, O. Brox, E. Bugge, J. Fricke, A. Ginolas, A. Knauer, P. Ressel and G. Erbert, "10W continuous-wave monolithically integrated master-oscillator power-amplifier," *Electronics Letters*, Vol. 43, No. 3, 160-162, Feb. 1 2007.
- [94] R. J. Lang, K. Dzurko, A. A. Hardy, S. Demars, A. Schoenfelder and D. F. Welch, "Theory of grating-confined broad-area lasers," *IEEE Journal of Quantum Electronics*, Vol. 34, No. 11, 2196-2210, Nov. 1998.
- [95] K. Paschke, R. Guther, J. Fricke, F. Bugge, G. Erbert, G. Trankle, K. Paschke, "High power and high spectral brightness in 1060 nm alpha-DFB lasers with long resonators," *Electronics Letters*, Vol. 39, No. 4, 369-370, Feb. 20 2003.
- [96] A. Al-Muhanna, L. J. Mawst, D. Botez, D. Z. Garbuzov, R. U. Martinelli, J. C. Connolly, "High-power (> 10 W) continuous-wave operation from 100-  $\mu\text{m}$  - aperture 0.97- $\mu\text{m}$ -emitting Al-free diode lasers," *Applied Physics Letters*, Vol. 73, No. 9, 1182-1184, Aug. 1998.
- [97] D. Garbuzov, M. Maiorov, V. Khalfin, M. Harvey, A. Al-Muhanna, L. Mawst, D. Botez, J. Connolly, "Super high power operation of 0.98  $\mu\text{m}$  InGaAs(P)/InGaP/GaAs broadened waveguide separate confinement heterostructure quantum well diode lasers," *Physics and Simulation of Optoelectronic Devices VII*, Vol. 3625, 803-810, 828, 1999.
- [98] R. K. Huang, J. P. Donnelly, L. J. Missaggia, C. T. Harris, J. Plant, D. E. Mull, W. D. Goodhue, "High-power nearly diffraction-limited AlGaAs-

- InGaAs semiconductor slab-coupled optical waveguide laser," *IEEE Photonics Technology Letters*, Vol. 15, No. 7, 900-902, Jul 2003.
- [99] Shyh Wang, Jaroslava Z. Wilcox, Michael Jansen, and Jane J. Yang," In phase locking in diffraction coupled phased array diode lasers ", *Applied Physics Letters*, Vol. 48, No. 26, 1770-1772, 1986.
- [100] H. Wenzel, E. Bugge, M. Dallmer, F. Dittmar, J. Fricke, K. H. Hasler, G. Erbert, "Fundamental-lateral mode stabilized high-power ridge-waveguide lasers with a low beam divergence," *IEEE Photonics Technology Letters*, Vol. 20, No. 3, 214-216, Jan-Feb 2008.
- [101] J. J. Lee, L. J. Mawst, D. Botez., "Asymmetric broad waveguide diode lasers ( $\lambda=980$  nm) of large equivalent transverse spot size and low temperature sensitivity." *IEEE Photonics Technology Letters*. Vol. 14, No.8, 1046-1048, 2002.
- [102] B. Petrescu-Prahova, P. Modak, E. Goutain, D. Silan, D. Bambrick, J. Riordan, T. Moritz, S. D. McDougall, B. Qiu, J. H. Marsh, "High  $d/\gamma$  values in diode laser structures for very high power", *Proceedings of SPIE* 7198, 71981I, 1-8, 2009.
- [103] B. C. Qiu, S. D. McDougall, X. F. Liu, G. Bacchin, J. H. Marsh, "Design and fabrication of low beam divergence and high kink-free power 980 lasers," *The 17th Annual Meeting of the IEEE Lasers and Electro-Optics Society (LEOS)*, Vol. 2, 477-478, 2004.
- [104] M. V. Maximov, Y. M. Shernyakov, I. I. Novikov, L. Y. Karachinsky, N. Y. Gordeev, V. A. Shchukin, I. Samid, N. N. Ledentsov, "Low divergence edge-emitting laser with asymmetric waveguide based on one-dimensional photonic crystal," *Fourth International Conference on Physics of Light-Matter Coupling in Nanostructures (PLMCN4)*, Vol. 2, 919-922, 208, 2005.
- [105] Mitsuo Fukuda, *Reliability and Degradation of Semiconductor lasers and LEDs*, Artech House Publishers, 1991.
- [106] R. K. Huang, B. Chann, L. J. Missaggia, S. J. Augst, M. K. Connors, G. W. Turner, A. Sanchez-Rubio, J. P. Donnelly, J. L. Hostetler, C. Miester and F. Dorsch,"Coherent combination of slab-coupled optical waveguide lasers", *Proceedings of SPIE*,, paper CMN1, 2008.

- [107] Deepak Vijayakumar, Ole Bjarlin Jensen, Ralf Ostendorf, Thomas Westphalen, and Birgitte Thestrup, "Spectral beam combining of a 980 nm tapered diode laser bar", *Optics Express*, Vol. 18, no 2, 893-898, 2010.
- [108] R. K. Huang, B. Chann, L. J. Missaggia, S. J. Augst, M. K. Connors, G. W. Turner, A. Sanchez-Rubio, J. P. Donnelly, J. L. Hostetler, C. Miester, F. Dorsch, "Coherent combination of slab-coupled optical waveguide lasers", *Proceedings of SPIE*, Vol.7230, 72301G, 1-11, 2009.
- [109] A. Jechow, V. Raab and R. Menzel," Tunable 6.8 W narrow bandwidth emission from a single-stripe continuous-wave broad-area laser diode in a simple external cavity", *Applied Optics*, Vol. 47, No.10, 1447-50. 2008.
- [110] B. Liu, Y. Liu and Y. Braiman, "Coherent addition of high power laser diode array with a V-shape external Talbot cavity", *Optics Express*, Vol. 16, No. 25, 20935-20942, 2008.
- [111] I. Hassiaoui, N. Michel, M. Lecomte, O. Parillaud, M. Calligaro, M. Krakowski, "In-Phase Coherent Coupling of Tapered Lasers in an External Talbot Cavity," *Novel In-Plane Semiconductor Lasers VI*, *Proceedings of SPIE*, Vol. 6485, 64850E, 1-10, 2007.
- [112] <http://arxiv.org/ftp/arxiv/papers/1011/1011.0969.pdf>
- [113] C. Zmudzinski, D. Botez, L. J. Mawst, C. Tu, L. Frantz," Coherent 1 W continuous wave operation of large-aperture resonant arrays of anti-guided diode lasers", *Applied Physics Letters* , Vol. 62, No. 23, 2914-2916, 1993.
- [114] M. Jansen, J. J. Yang, S. S. Ou, D. Botez, J. Wilcox, and L. Mawst, "Diffraction-limited operation from monolithically integrated diode laser array and self-imaging (Talbot) cavity", *Applied Physics Letters*, Vol. 55, No. 19, 1949-1951, 1989.
- [115] <http://www.m2k-laser.de/datasheets/m2k-TAL-0850-2000.pdf>
- [116] T. Fukuda, K. Okamoto, Y. Hinokuma, K. Hamamoto, "Phase-Locked Array Laser Diodes (LDs) by Using 1 x N Active multimode-interferometer (MMI) ", *IEEE Photonics Technology Letters*, Vol. 21, No. 3, 176-178, 2009.
- [117] F. Dittmar, B. Sumpf, J. Fricke, G. Erbert, and G. Tränkle, "High-power 808-nm tapered diode lasers with nearly diffraction-limited beam quality of  $M^2 = 1.9$  at  $P = 4.4$  W, " *IEEE Photonics Technology Letters*, Vol. 18, No. 4, 601-603, 2006.

- [118] N. Michel, M. Lecomte, O. Parillaud, M. Krakowski, J.M. García-Tijero, and I. Esquivias, "Asymmetric Al-free active region laser structure for high-brightness tapered lasers at 975 nm," Proceedings of SPIE, Vol. 6909, 69090R, 2008.
- [119] N. Michel, I. Hassiaoui, M. Calligaro, M. Lecomte, O. Parillaud, M. Krakowski, L. Borruel, J.M. García-Tijero, I. Esquivias, S. Sujecki and E.C. Larkins, "High-power diode lasers with an Al-free active region at 915 nm," Proceedings of SPIE, Vol. 5989, 598909, (2005).
- [120] Ralf Williams, Modern GaAs processing methods, Artech House, London, 1990.
- [121] S. M. Sze, Semiconductor Devices- Physics and Technology, New York, MA: John Wiley and Sons, 2002.
- [122] Safa Kasab and Peter Capper, Springer Handbook of Electronic and Photonic Material, 2006.
- [123] S.L. Chuang, Physics of Optoelectronics Devices, Wiley series in pure and applied optics, 1995.
- [124] D. P. Bour and A. Rosen, "Optimum cavity length for high conversion efficiency quantum well diode lasers", Journal of Applied Physics., Vol. 66, No. 7, 2813-2818, 1989.
- [125] J. Wang, B. Smith, X. Xie, X. Wang and G. T. Burnham, "High-efficiency diode lasers at high output power", Applied Physics Letters, Vol. 74, No. 11, 1525-1527, 1999.
- [126] Friedrich Bachmann, Peter Loosen and Reinhart Poprawe, High Power Diode Lasers Technology and Applications, Springer series in optical Sciences, 2007.
- [127] [www.luxpop.com](http://www.luxpop.com)
- [128] John Gowar, Optical communication systems, Prentice Hall, 2nd Edition, 1993.
- [129] Horace Craig Casey and M. B. Panish, Heterostructure Lasers. Part A: Fundamentals Principles. New York: Academic, 1978.
- [130] John H. Davis, Physics of Low Dimensional Semiconductors; An Introduction, Cambridge University Press, 1<sup>st</sup> Edition, 1998.

- [131] Bocang Qui, "Photonic integration in InGaAs/InGaAsP multiple quantum well laser structures using quantum well intermixing". PhD Thesis, University of Glasgow, 1998.
- [132] H. Okumura, S. Misawa, S. Yoshida, and S. Gonda, "Determination of the conduction-band discontinuities of GaAs/Al<sub>x</sub>Ga<sub>1-x</sub>As interfaces by capacitance-voltage measurements," *Applied Physics Letters*, Vol. 46, No.4, 377-379, 1985.
- [133] Hans P. Zappe, *Introduction to Semiconductor Integrated Optics*, Artech House Publishers, 1995.
- [134] K. Kosiel, J. Muszalski, A. Szerling, and M. Bugajski, "High power (> 1 W) room-temperature (300 K) 980 nm continuous-wave AlGaAs/InGaAs/GaAs semiconductor lasers," *Optica Applicata*, Vol. 37, No. 4, 423-432, 2007.
- [135] Pallab Bhattacharya, *Semiconductor Optoelectronic Devices*, 2<sup>nd</sup> Edition, Prentice Hall, Inc., 132, 1997.
- [136] B. R. Bennett, R. A. Soref, and J. A. Delalano, "carrier-induced change in refractive-index of InP, GaAs, and InGaAsP," *IEEE Journal of Quantum Electronics*, Vol 26, No. 1, 113-122, 1990.
- [137] Y. Suzuki, Y. Horikoshi, M. Kobayashi, and H. Okamoto, "fabrication of GaAlAs window-stripe multi-quantum-well heterostructure lasers utilizing Zn diffusion-induced alloying," *Electronics Letters*, Vol. 20, No. 9, 383-384, 1984.
- [138] C.L. Walker, A.C Bryce, J.H. Marsh, "improved catastrophic optical damage level from laser with non-absorbing mirrors," *Photonics Technology Letters*, (Institute of Electrical and Electronics Engineers, New York, 2002), Vol. 14, No. 10, 1394-1396.
- [139] Yumi Yamada and Yoshikazu Yamada, Tsuyoshi Fujimoto, and Kazuomi Uchida, "High power and highly reliable 980nm lasers with window structure using impurity free vacancy disordering", *Proceedings of SPIE*, Vol. 5738, *Novel In-Plane Semiconductor Lasers IV*, 40-46, 2005.
- [140] J.S. Yoo, H.H. Lee, P. S. Zory," On surface recombination velocity and output intensity limit of pulsed semiconductor lasers", *IEEE Photonic Technology Letters*, Vol. 3, No. 7, 594-596, 1991.
- [141] Roland Diehl, *High-Power Diode Lasers Fundamentals, Technology, Applications*, Series: Topics in Applied Physics, Vol. 78, 2000.

- [142] L. W. Tu, E. F. Schubert, M. Hong, G. J. Zydyk Meyer, "In-vacuum cleaving and coating of semiconductor laser facets using thin silicon and a dielectric", *Journal of Applied Physics*, Vol. 80, No. 11, 6448-6450, 1996.
- [143] P. Collot, S. Delalande, J. Olivier, "Sulphur passivation of dry-etched AlGaAs laser facets", *Electronics Letters*, Vol. 35, No. 6, 506-508, 1999.
- [144] L. J. Mawst, "High power, Al-free active region (ALFA) lasers for the 0.70-0.81  $\mu\text{m}$  wavelength range", *Conference on Electro Optics, CLEO' 99*, 43-44, 1999.
- [145] D. Botez, "Design considerations and analytical approximations for high continuous-wave power, broad-waveguide diode lasers," *Applied Physics Letters*, Vol. 74, No. 21, 3102-3104, 1999.
- [146] M. Buda, T. G. vandeRoer, L. M. F. Kaufmann, G. Iordache, D. Cengher, D. Diaconescu, I. B. Petrescu Prahova, J. E. M. Haverkort, W. vanderVleuten, and J. H. Wolter, "Analysis of 6-nm AlGaAs SQW low-confinement laser structures for very high-power operation," *IEEE Journal of Selected Topics in Quantum Electronics*, Vol. 3, No. 2, 173-179, 1997.
- [147] S. O. Kasap, *Optoelectronics and Photonics: Principles and Practices*, Prentice Hall, 2001.
- [148] B. Qiu, S. D. McDougall, X. Liu, G. Bacchin, and J. H. Marsh, "Design and fabrication of low beam divergence and high kink-free power lasers," *IEEE Journal of Quantum Electronics*, Vol. 41, No. 9, 1124-1130, Sep. 2005.
- [149] G. Yang, Gary M. Smith, Monica K. Davis, David A. S. Loeber and Martin Hu, "Highly reliable high-power 980-nm pump laser", *IEEE Photonic Technology Letters*, Vol. 16, No. 11, 2403-2405, 2004.
- [150] Zuntu Xu, Wei Gao, Brad Siskavich, Alan Nelson, Lisen Cheng, Kejian Luo, Hyo S. Kim, Zhiping Wang, and Aland K. Chin, "Low-divergence-angle 808-nm GaAlAs/GaAs laser diode using an asymmetric-cladding structure", *Proceedings of SPIE*, Vol. 5365, 142-147, 2004.
- [151] G. N. Childs, S. Brand and R. A. Abram, "Intervalence band absorption in semiconductor laser materials", *Journal of Semiconductor Science and Technology*, Vol. 1, No. 2, 116-120, 1986.
- [152] C. H. Henry, R. A. Logan, F. R. Merritt and J.P. Luongo, "The Effect of intervalence band absorption on the thermal behaviour of InGaAsP lasers", *IEEE Journal of Quantum Electronics*, Vol. QE-19, No. 6, 947-952, 1983.

- [153] M. Razeghi and H. Yi, "High power Al-free InGaAsP/GaAs near infrared semiconductor lasers", *Optoelectronics Review*, Vol. 6, No. 2, 81-92, 1998.
- [154] K. A. Bulashevich, V. F. Mymrin, S. Yu. Karpov, D. M. Demidov and A. L. Ter-Martirosyan, "Effect of free-carrier absorption on performance of 808nm AlGaAs-based high-power laser diodes", *Journal of Semiconductor Science and Technology*, Vol. 22, No. 5, 502-510, 2007.
- [155] D. Z. Garbuzov, J. H. Abeles, N. A. Morris, P. D. Gardner, A. R. Triano, M. G. Harvey, D. B. Gilbert and J. C. Connolly. "High power separate confinement heterostructure AlGaAs/GaAs laser diodes with broadened waveguide." *Proceedings of SPIE*, Vol. 2682, 20-26, 1996.
- [156] P. W. McIlroy, A. Kurobe, and Y. Uematsu., " Analysis and application of theoretical gain curves to the design on multi-quantum well laser," *IEEE Journal of Quantum Electronics*, Vol. 21, No. 12, 1958-1963, Dec. 1985.
- [157] M. Asada, A. R. Adams, K. E. Stubkjaer, Y. Suematsu, Y. Itaya, and S. Arai, "The temperature dependence of the threshold current of GaInAsP/InP DH lasers," *IEEE Journal of Quantum Electronics*, Vol. QE-17, 611-619, 1981.
- [158] Levon V. Asryan and Serge Luryi, "Effect of internal optical Loss on threshold characteristics of semiconductor lasers with a quantum-confined active region", *IEEE Journal of Quantum Electronics*, Vol. 40, No. 7, 833-843, 2004.
- [159] A. Kurobe, H. Furuyama, S. Naritsuka, N. Sugiyama, Y. Kokubun, and M. Nakamura, "Effects of well number, cavity length, and facet reflectivity on the reduction of threshold current of GaAs/AlGaAs Multi-quantum well lasers," *IEEE Journal of Quantum Electronics*, Vol. 24, No. 4, 635-639, 1988
- [160] A. G. Baca, Carol I. H. Ashby, "Fabrication of GaAs devices", *Institution of Engineering and Technology, EMIS Processing series 6*, London, 10 Jun. 2005.
- [161] T. C. Shen, G. B. Gao, and H. Morkoc, "Recent developments in ohmic contacts for III-V compound semiconductors," *Journal of Vacuum Science & Technology B*, Vol. 10, No. 5. AVS, 2113-2132, 1992.
- [162] G. Stareev, "Formation of extremely low-resistance Ti/Pt/Au ohmic contacts to P-GaAs," *Applied Physics Letters*, Vol. 62, 2801-2803, 1993. *Applied Physics Letters*, Vol. 62, No. 22, 2801-2803, 1993.

- [163] G. K. Reeves and H. B. Harrison, "obtaining the specific contact resistance from transmission-line model measurements," *Electron Device Letters*, Vol. 3, No. 5, 111-113, 1982.
- [164] N. K. Dutta, N. A. Olsson, and W. T. Tsang, "carrier induced refractive-index change in AlGaAs quantum well lasers," *Applied Physics Letters*, Vol. 45, No. 8, 836-837, 1984.
- [165] J. H. Marsh, "The role of monolithic integration in advanced laser products," *Journal of Crystal Growth*, Vol. 288, 2-6, 2006.
- [166] P. Blood, E. D. Fletcher, K. Woodbridge., "Dependence of threshold current on the number of wells in AlGaAs-GaAs quantum well lasers." *Applied Physics Letters*, Vol. 47, No. 3, 193-195, 1985.
- [167] R. R. Syms and J. R. Cozens, *Optical guided waves and devices*, McGraw-Hill International, 1992
- [168] G. Tandoi, "Monolithic high power mode locked GaAs/AlGaAs Quantum well laser", PhD thesis, University of Glasgow, 2011.
- [169] L.J. Mawst, A. Bhattacharya, M. Nesnidal , J. Lopez , D. Botez, A.V. Syrbu, V.P. Yakovlev, G.I. Suruceanu, A.Z. Mereutza , M. Jansen, R.F. Nabiev, "MOVPE-grown high CW power InGaAs/InGaAsP/InGaP diode lasers" *Journal of Crystal Growth*, Vol. 170, No.1-4, 383-389, 1997.
- [170] L. A. Coldren and S. W. Corzine. *Diode Lasers and Photonic Integrated Circuits*. New York: John Wiley and Sons, 1995.
- [171] Dan Andreyevitch Yanson, "Generation of terahertz-modulated optical signals using AlGaAs/GaAs laser diode", PhD thesis, University of Glasgow, Dec. 2003.
- [172] Vistec Website <http://www.vistec-semi.com/products-applications/products/vistec-vb300/>
- [173] D.Macintyre, *Introduction to electron beam lithography*, University of Glasgow Course, 2009.
- [174] H. Granier, J. Tasselli, A. Marty, H. P. Hu, "A SiCl<sub>4</sub> reactive ion etching and laser reflectometry process for AlGaAs/GaAs HBT fabrication," *Vacuum*, Vol. 47, No. 11, 1347-1351, Nov. 1996.
- [175] K. Maruyama and T. Goto, "Variation of CF<sub>3</sub>, CF<sub>2</sub> and CF Radical Densities with RF ChF<sub>3</sub> Discharge Duration," *Journal of Physics D-Applied Physics*, Vol. 28, No. 5, 884-887, May 1995.

- [176] W. D. Laidig, N. Holonyak, M. D. Camras, K. Hess, J. J. Coleman, P. D. Dapkus, J. Bardeen, "Disorder of an AlAs-GaAs super-lattice by impurity diffusion", *Applied Physics Letters*, Vol. 38, No. 10, 776-778. 1981.
- [177] D.G. Deppe, and N. Holonyak, "Atom diffusion and impurity-induced layer disordering in quantum well III-V semiconductor heterostructures", *Journal of Applied Physics*, Vol. 64, No. 12, R93-R113. 1988.
- [178] J. H. Marsh, "Quantum-well intermixing," *Semiconductor Science and Technology*, Vol. 8, No. 6, 1136-1155, Jun. 1993.
- [179] A. McKee, G. Lullo, C. J. McLean, B. C. Qiu, A. C. Bryce, R. M. De La Rue., "Extended cavity lasers fabricated using photo-absorption induced disordering," 1997 International Conference on Indium Phosphide and Related Materials - Conference Proceedings, 288-291, 680, 1997.
- [180] A. McKee, C. J. McLean, G. Lullo, A. C. Bryce, R. M. De La Rue, J. H. Marsh, C. C. Button, "Monolithic integration in InGaAs-InGaAsP multiple-quantum-well structures using laser intermixing", *IEEE Journal of Quantum Electronics*, Vol. 33, No. 1, 45-55, 1997.
- [181] O. P. Kowalski, C. J. Hamilton, S. D. McDougall, J. H. Marsh, A. C Bryce, R. M. De la Rue, B.Vogele, C. R. Stanley, C. C. Button, J. S. Roberts, "A universal damage induced technique for quantum well intermixing," *Applied Physics Letters*, Vol. 72, No. 5, 581-583, Feb 1998.
- [182] S. D. McDougall, O. P. Kowalski, C. J. Hamilton, F. Camacho, B. C. Qiu, M. L. Ke, R. M. De La Rue, A. C. Bryce, J. H. Marsh, "Monolithic integration via a universal damage enhanced quantum-well intermixing technique," *IEEE Journal of Selected Topics In Quantum Electronics*, Vol. 4, No. 4, 636-646, Jul-Aug 1998.
- [183] A. S. Helmy, A. C. Bryce, D. C. Hutchings, J. S. Aitchison, J. H. Marsh, "Bandgap gratings using quantum well intermixing for quasi-phase-matching," *Journal of Applied Physics*, Vol. 100, No. 12, Dec 2006.
- [184] D. G. Deppe, L. J. Guido, N. Holonyak, K. C. Hsieh, R. D. Burnham, R. L. Thornton, T. L. Paoli, "Stripe-geometry quantum-well heterostructure  $\text{Al}_x\text{Ga}_{1-x}\text{As}$ -GaAs lasers defined by defect diffusion," *Applied Physics Letters*, Vol. 49, No. 9, 510-512, Sep 1 1986.
- [185] Ooi Boon Siew, K. McIlvaney, M.W. Street, A.S. Helmy, S.G. Ayling, A.C. Bryce, J.H. Marsh, J.S. Roberts, "Selective quantum well intermixing in

- GaAs-AlGaAs structures using impurity free vacancy diffusion, " IEEE Journal of Quantum Electronics, Vol. 33, No. 10, 1984-1793, October, 1997.
- [186] R. J. Deri and E. Kapon, "Low-loss III-V semiconductor optical waveguides", IEEE Journal of Quantum Electronics, Vol. 27, No. 3, 626-640, Mar. 1991.
- [187] R. Walker, "Simple and accurate loss measurement technique for semiconductor optical waveguides," Electronics Letters, Vol. 21, No. 13, 581-583, 1985.
- [188] P. A. Andrekson, N.A. Olsson., T. Tanbuk-Ek., R.A. Logan., D. Coblentz, H Temkin, "Novel technique for determining internal loss of individual semiconductor-lasers," Electronics Letters, Vol. 28, No. 2, 171-172, Jan. 16 1992.
- [189] B. R. Pruniaux and A. C. Adams," Dependence of barrier height of metal semiconductor contact (AuGaAs) on thickness of semiconductor surface layer", Journal of Applied Physics, Vol. 43, No. 4, 1980-1982, 1972.
- [190] V. Rideout, "A review of the theory and technology for ohmic contacts to group III-V compound semiconductors," Solid-State Electronics, Vol. 18, No. 6, 554 -550, 1975.
- [191] Steven McMaster, Monolithically Integrated Mode-Locked Ring Lasers and Mach-Zehnder Interferometers in AlGaInAs, Ph.D Thesis, University of Glasgow, May 2010.
- [192] G. P. Agrawal and N. K. Dutta, " Long Wavelegnth Semiconductor Lasers", section 2-5, Van Nostrand Reinhold, New York, 1986.
- [193] O.Bryngdahl., "Image formation using self-imaging techniques," Journal of the Optical Society of America, Vol. 63, No. 4, 416-419, 1973.
- [194] R. Ulrich and G. Ankele, "Self-imaging in homogeneous planar optical-waveguides," Applied Physics Letters, Vol. 27, No. 6, 337-339, 1975.
- [195] T. Niemeier and R. Ulrich, "Quadrature outputs from fiber interferometer with 4x4 coupler," Optics Letters, Vol. 11, No. 10, 677-679, Oct 1986.
- [196] L. B. Soldano and E. C. M. Pennings, "Optical multimode interference devices based on self-imaging - principles and applications," Journal of Lightwave Technology, Vol. 13, No. 4, 615-627, Apr 1995.
- [197] R. M. Jenkins, R. W. J. Deveraux, and J. M. Heaton, "Waveguide beam splitters and recombiners based on multimode propagation phenomena," Optics Letters, Vol. 17, No. 14, 991-993, 1992.

- [198] Katsunari Okamoto, "Fundamentals of Optical Waveguides ", Second Edition, Elsevier Academic Press, 2006.
- [199] Lung-Wei Chung, San-Liang Lee, and Yen-Juei Lin, "Principles and application of reduced beat length in MMI couplers," *Optics Express*, Vol. 14, No. 19, 8753-8764, 2006.
- [200] J. M. Heaton, R. M. Jenkins, D. R. Wight, J. T. Parker, J. C. H. Birbeck, K. P. Hilton, "Novel 1-to-N way integrated optical beam-splitters using symmetrical mode mixing in GaAs/AlGaAs multimode waveguides," *Applied Physics Letters*, Vol. 61, No. 15, 1754-1756, Oct 12 1992.
- [201] C.L. Walker, "Quantum well Intermixing for High Brightness Lasers", Ph.D thesis, University of Glasgow, 2002.
- [202] RSOFTE Design Group commercial BEAM Propagation software package Manual.
- [203] M. Blahut, and A. Opilski, "Multimode interference structures - new way of passive elements technology for photonics," *OPTO-Electronics Review*, Vol. 9, No. 3, 293-300, 2001.
- [204] APSS Apollo application note on multi-mode interference (MMI) devices design, simulation and layout, APN-APSS-MMI, 2003.
- [205] A. F. Glova, "Phase locking of optically coupled lasers," *Quantum Electronics*, Vol. 33, No. 4, 283–306, 2003.
- [206] H. Fujii, I. Suemune and M. Yamanishi, "Analysis of transverse modes of phase- locked multi-stripe lasers," *Electronics Letters*, Vol. 21, No. 16, 713-714, Aug. 1985.
- [207] F. Causa, and D. Masanotti, " High brightness index guided parabolic bow-tie laser arrays," *IEEE Photonics Technology Letters*, Vol. 16, No. 9, 1041-11351, Sep 2004.
- [208] Markus-Christian Amann and F. Kappeler, "Analytical solution for the lateral current distribution in multiple stripe laser diodes", *Applied Physics Letters*, Vol. 48, No. 25, 1710–1712, 23 June 1986.
- [209] G. Lengyel, P. Meissner, E. Patzak, and K-H. Zschauer, "An Analytical solution of the lateral current spreading and diffusion problem in narrow oxide stripe (GaAlAs/GaAs) DH Lasers", *IEEE Journal of Quantum Electronics*, Vol. QE-18, No. 4, April 1982.

- [210] M. Achtenhagen and A. Hardy, "Lateral current spreading in ridge waveguide laser diodes", *Applied Physics Letters*, Vol. 74, No. 10, 1364–1366, 8 March 1999.
- [211] K. J. Beernink, J. J. Alwan, and J. J. Coleman, "InGaAs-GaAs-AlGaAs gain-guided arrays operating in the in-phase fundamental array mode", *Applied Physics Letters*, Vol. 57, No. 26, 2764-2766, 1990.
- [212] H. Bruesselbach, D. Cris Jones, Metin S. Mangir, M. Minden, and Jeffrey L. Rogers, "Self-organized coherence in fiber laser arrays", *Optics Letters*, Vol. 30, No. 11, 1339-1341, June 1 2005.
- [213] Jan P. Van Der Ziel, Robert M. Mikulyak, H. K. Temkin, Ralph A. Logan, Russell D. Dupuis, "Optical beam characteristics of Schottky barrier confined arrays of phase-coupled multi-quantum well GaAs lasers", *IEEE Journal of Quantum Electronics*, Vol. 20, No. 11, 1259 – 1266, Nov 1984.
- [214] D. R. Scifres, R. A. Sprague, W. Streifer, and R. D. Burnham, "Focusing of a 7700Å high power phased array semiconductor laser", *Applied Physics Letters*, Vol. 41, No. 12, 1121-1123, 1982.
- [215] R. F. Kazarinov, C. H. Henry, and R. A. Logan, "Longitudinal mode self-stabilization in semiconductor lasers, " *Journal of Applied Physics*, Vol. 53, No. 7, 4631-4646, 1982.
- [216] J. Banerji, A. R. Davies, and R. M. Jenkins, "Comparison of Talbot and 1-to-N way phase locked resonators," *Applied Optics*, Vol. 36, No. 7, 1604–1609, 1997.
- [217] R. M. Lorenzo, C. Liorente, E. J. Abril, and M. Lopez, "Improved self-imaging characteristics in 1×N multimode couplers," *IEE Proceedings of Optoelectronics*, Vol. 145, No. 1, 65–69, 1998.
- [218] L. Yang, Y. Liu and Q. Wang, "Study on the internal reflection of the multitude-interference-type device", *Optical Engineering*, Vol. 43, No. 10, 2322-2325, 2004.
- [219] R. Hanfoug, L.M. Augustin, Y. Barbarin, J. J. G. M. van der Tol, E.A.J.M. Bente, F. Karouta, D. Rogers, S. Cole, Y. S. Oei, X. J. M. Leijtens and M.K. Smit " Reduced reflections from multimode interference couplers," *Electronics Letters*, Vol. 42, No. 8, 465-466, April 2006.
- [220] E.A. Avrutin, F. Camacho, A.C. Bryce, C.J. Hamilton, D. Yanson, J.M. Arnold, J.H. Marsh, "Analysis of monolithic parallel-compound-cavity

semiconductor lasers for high brightness, single-frequency, and short pulse operation”, Conference of Lasers and Electro-Optics (CLEO), 147, May 25, 1999.

[221] M.L. Osowski, W. Hu, R.M. Lammert, T. Liu, Y. Ma, S.W. Oh, C. Panja, P.T. Rudy, T. Stakelon and J.E. Ungar, “High brightness semiconductor lasers”, High-Power Diode Laser Technology and Applications V, Proceedings of SPIE, Vol. 6456, 64560D, 1-10, 2007.

[222] J. D. Dow and D. Redfield, “Toward a unified theory of Urbach’s rule and exponential absorption edges,” Physics Review. B, Vol. 5, 594-610, 1972.

# Appendix A

The additional results for 1x4 MMI array laser are presented in this appendix.

## 1. Device No. (2) Test Results

- Far-field results for a 1x4 MMI array laser. The dimensions were: the MMI length was (617  $\mu\text{m}$ ), the gain section length was (975  $\mu\text{m}$ ), the NAM length was (100  $\mu\text{m}$ ) and output waveguide length was 325  $\mu\text{m}$ . Far-field pattern was measured from single output waveguide side. ( $I_{\text{th}}=145$  mA).

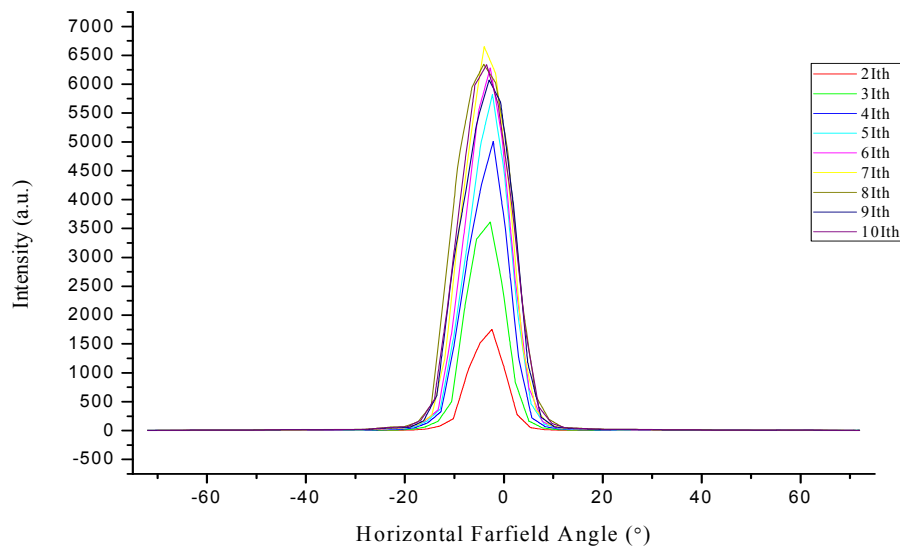


Figure (A1) Single facet side ( $2I_{\text{th}}$ ).

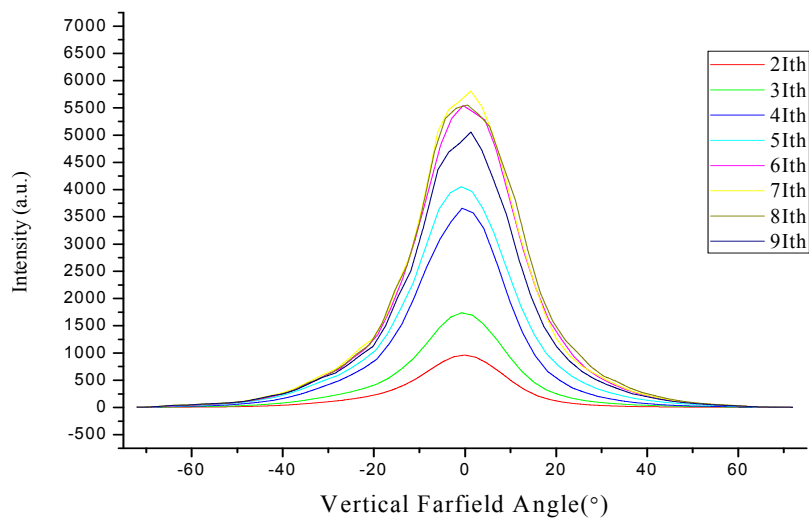


Figure (A2) Single facet side.

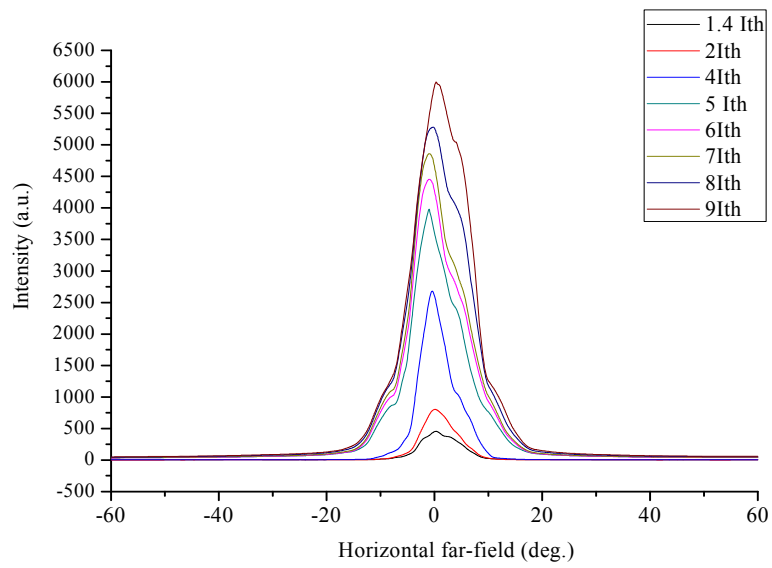


Figure (A3) Four array facets side.

- Spectra measurements for (device-2) from both facets.

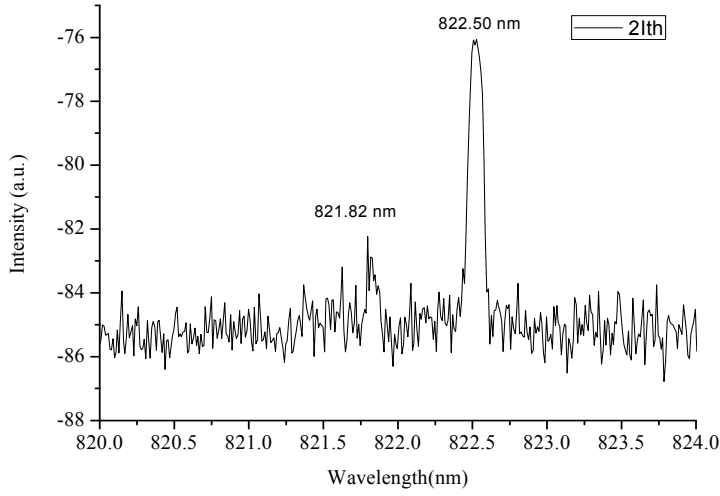


Figure (A4-1): Four array facets side ( $2I_{th}$ ).

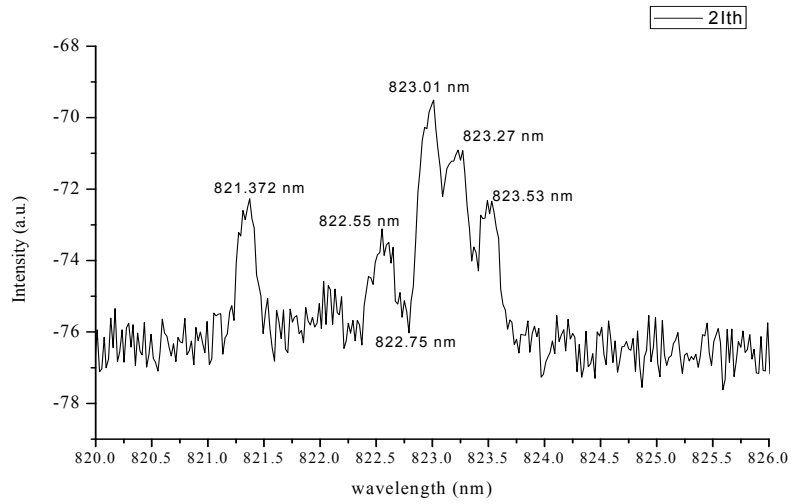


Figure (A4-2): Single facet side ( $2I_{th}$ ).

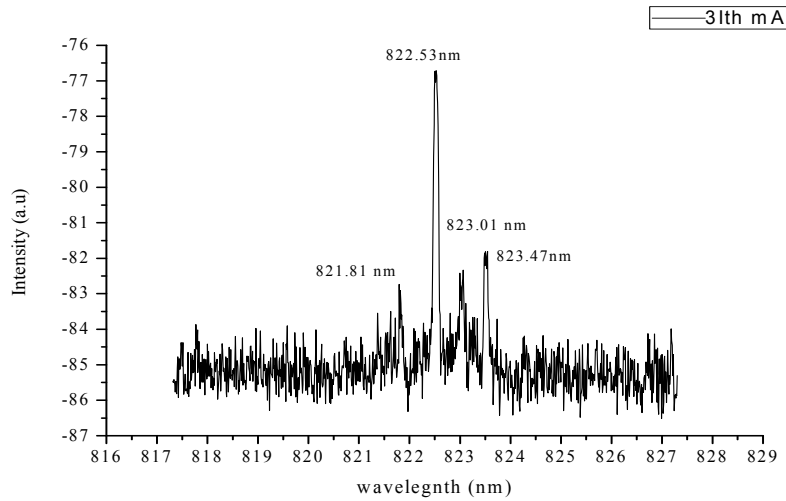


Figure (A5-1): Four array facets side ( $3I_{th}$ ).

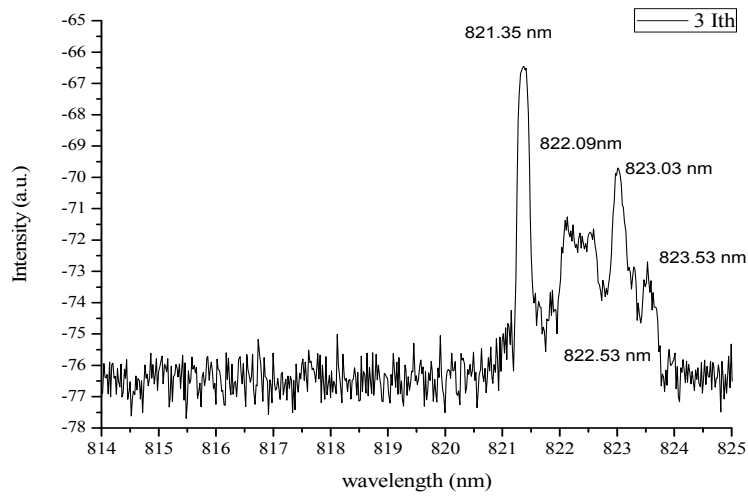


Figure (A5-2): Single facet side ( $3I_{th}$ ).

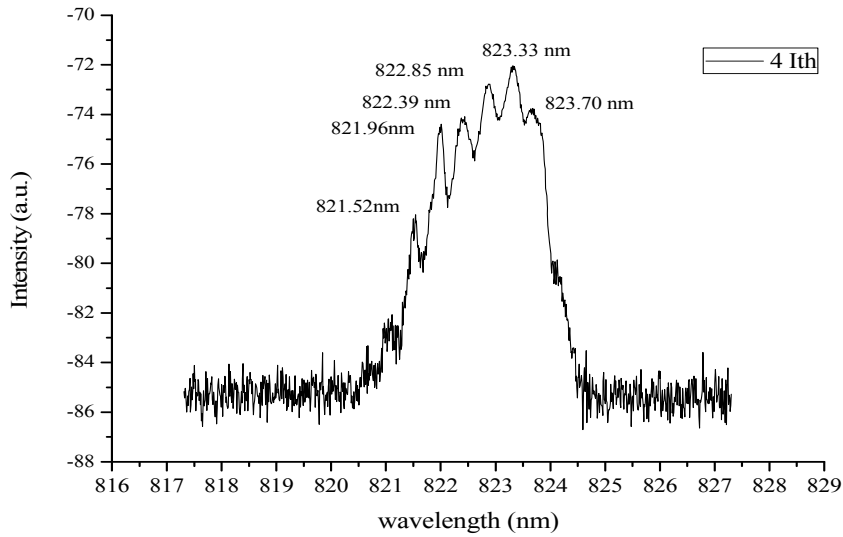


Figure (A6-1): Four array facets side ( $4I_{th}$ ).

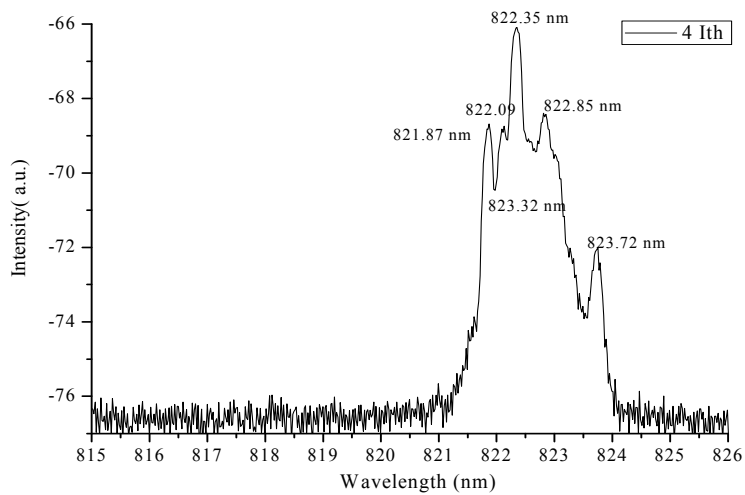


Figure (A6-2): Single facet side ( $4I_{th}$ ).

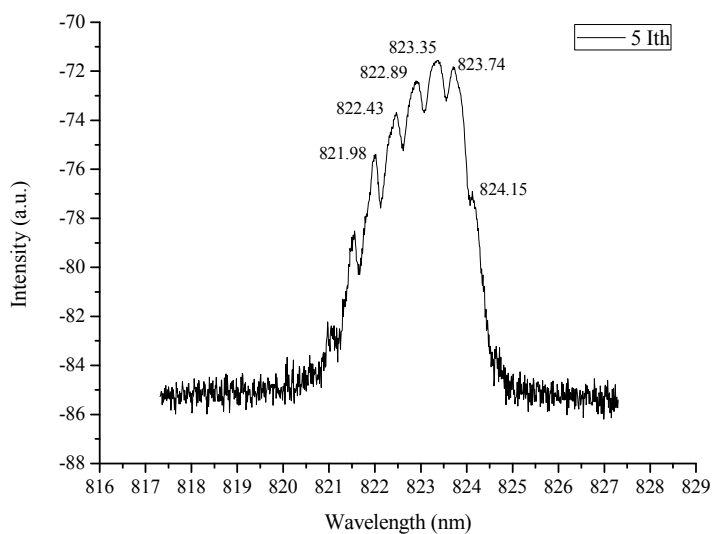


Figure (A7-1): Four array facets side ( $5I_{th}$ ).

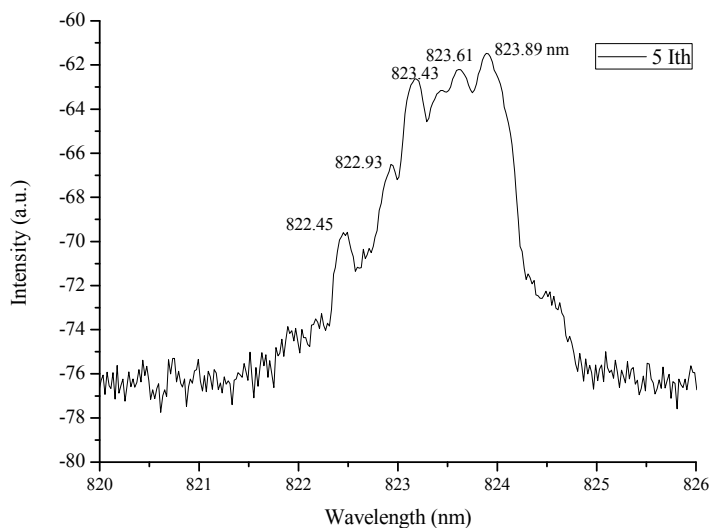


Figure (A7-2): Single facet side ( $5I_{th}$ ).

## 2. Device No. (3) Test Results

- Emission spectra measurements for a 1x4 MMI array laser. The dimensions were: the MMI length was (617  $\mu\text{m}$ ), the gain section length was (975  $\mu\text{m}$ ), the NAM length was (100  $\mu\text{m}$ ) and the output waveguide length was 325  $\mu\text{m}$ . Spectra were measured in CW mode for device number 3 from single output facet side.

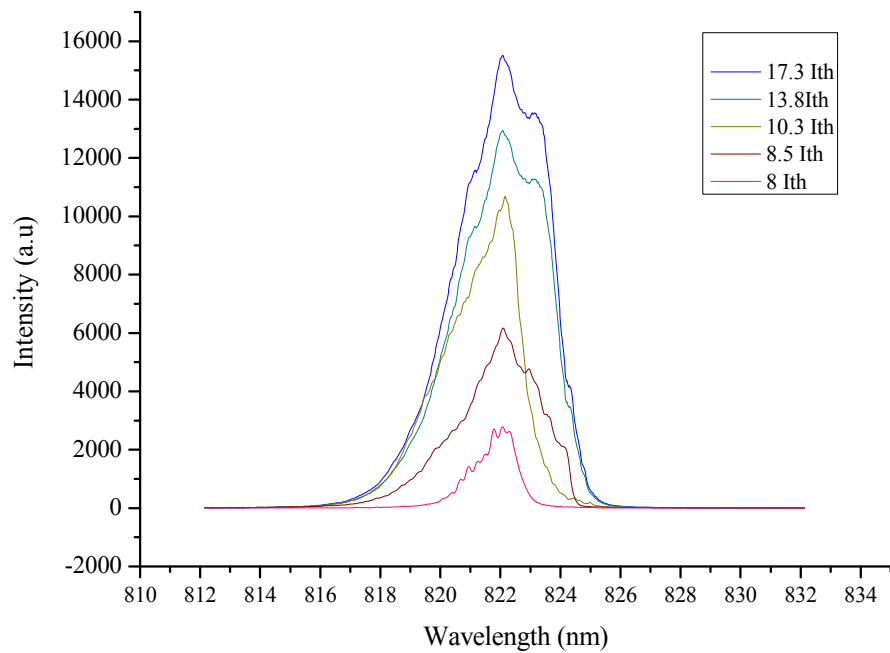


Figure (A8-1): Single facet side

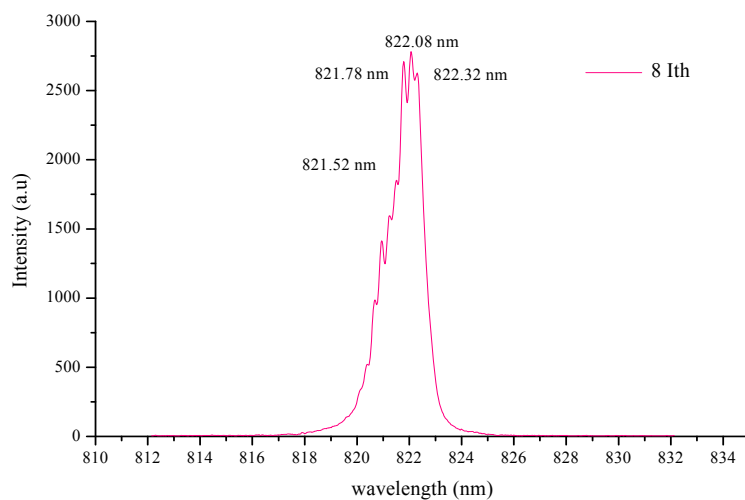


Figure (A8-2): Single facet side ( $8I_{th}$ )